Elucidating the Effects of Different Aging-Delaying Interventions on the Cellular Lipidome and Metabolome of Budding Yeast

Karamat Mohammad

A Thesis
In the Department
Of
Biology

Presented in Partial Fulfillment of the Requirements
For the Degree of
Doctor of Philosophy (Biology) at
Concordia University
Montreal, Quebec, Canada

June 2021

CONCORDIA UNIVERSITY

School of Graduate Studies

This is to certify that the thesis prepared

By: Karamat Mohammad

Entitled: Elucidating the Effects of Different Aging-Delaying Interventions on the Cellular Lipidome and Metabolome of Budding Yeast

and submitted in partial fulfillment of the requirements for the degree of

DOCTOR OF PHILOSOPHY (Biology)

complies with the regulations of the University and meets the accepted standards with respect to originality and quality.

Signed by the final Examining Committee:

_____ Chair
Dr. David Mumby

_____ External Examiner
Dr. Troy Harkness

_____ External to Program
Dr. Dajana Vuckovic

_____ Examiner
Dr. Aashiq H. Kachroo

_____ Examiner
Dr. Alisa Piekny

_____ Thesis Supervisor
Dr. Vladimir Titorenko

Approved by _____
Dr. Robert Weladji, Graduate Program Director

July 08, 2021 _____
Dr. Pascale Sicotte, Dean
Faculty of Arts and Science

ABSTRACT

Elucidating the Effects of Different Aging-Delaying Interventions on the Cellular Lipidome and Metabolome of Budding Yeast

Karamat Mohammad, Ph.D.
Concordia University, 2021

In studies presented in this Thesis, I developed novel methods of liquid chromatography coupled with tandem mass spectrometry for the identification and quantitation of the cellular lipidomes and metabolomes of budding yeast. Both these methods are versatile, robust, and sensitive. They provide several other advantages over the advanced methods currently employed for the mass spectrometry-based quantitative analyses of cellular lipids and water-soluble metabolites. Using the mass spectrometry-based methods of quantitative lipidomics and metabolomics, I investigated mechanisms through which several aging-delaying (geroprotective) interventions extend the longevity of budding yeast by specifically targeting the metabolism and transport of cellular lipids and water-soluble metabolites. My studies provided evidence that the extract from Salix alba's bark, called PE21, slows the chronological aging of budding yeast because it lowers the intracellular concentrations of free fatty acids below a toxic threshold. The resulting weakening of an aging-associated liponecrotic form of regulated cell death increases the probability of cell survival during the entire process of chronological aging. My studies suggested two additional mechanisms by which a PE21-dependent reorganization of the cellular lipidome delays the chronological aging of budding yeast. In one of these additional mechanisms, the PE21-dependent rise in the concentrations of endoplasmic reticulum-generated phospholipids activates the pro-longevity process of unfolded protein response in the endoplasmic reticulum. In the other additional mechanism, the PE21-dependent changes in the composition of mitochondrial

membrane lipids create a pro-longevity pattern of mitochondrial functionality. I also applied the mass spectrometry-based lipidomics to assess how three different geroprotectors (namely, caloric restriction, *tor1Δ* mutation and lithocholic acid) influence the lipidomes of quiescent and nonquiescent yeast cells purified using Percoll density gradient centrifugation. My data showed that caloric restriction reorganizes the lipidomes of these cells differently than two other geroprotectors. I proposed two mechanisms by which the caloric restriction-specific lipidome reorganization might slow the chronological aging of quiescent and nonquiescent yeast cells. Moreover, I used my non-targeted metabolomics method to investigate how three different geroprotective interventions (i.e., caloric restriction, *tor1Δ* mutation and lithocholic acid) affect the intracellular water-soluble metabolome of chronologically aging budding yeast. My findings provide evidence that the three different geroprotectors create distinct metabolic patterns throughout the budding yeast's entire chronological lifespan. My study identified a distinct metabolic pattern created by the caloric restriction geroprotector. I found two characteristic features that distinguish the caloric restriction-specific metabolic pattern from the cellular metabolism patterns created by the *tor1Δ* and lithocholic acid geroprotectors. One characteristic feature that distinguishes the caloric restriction-specific metabolic design is its ability to suppress the biosynthesis of methionine, S-adenosylmethionine and cysteine from aspartate, sulfate and 5-methyltetrahydrofolate throughout the chronological lifespan. The other characteristic feature of the caloric restriction-specific metabolic pattern is a decline in the intracellular concentration of ATP, a rise in the intracellular concentrations of AMP and ADP, and an increase in the ADP:ATP and AMP:ATP ratios at various phases of chronological aging.

Acknowledgments

I am thankful to my supervisor, Dr. Vladimir Titorenko, for inspiring my interest in cell biology. I highly appreciate the continuous guidance and support of Dr. Titorenko throughout my graduate studies in his laboratory. I would also like to thank my committee members Dr. Alisa Piekny and Dr. Aashiq H. Kachroo, for their expert advice and valuable guidance that contributed to my research and learning experience. I am grateful to the Centre for Biological Applications for Mass Spectrometry team for their outstanding expertise and valuable advice throughout the years. My thanks go to the members of the Titorenko lab, past and present, Anthony Arlia-Ciommo, Anna Leonov, Vicky Lutchman, Melissa McAuley, Darya Mitrofanova, Younes Medkour, Pamela Dakik, Monica Enith Lozano Rodriguez, Jennifer Anne Baratang Junio, Emmanuel Orfanos, Tala Tafakori and Christine Abd El Malek for their kindness and support. I am thankful to the numerous undergraduate students for their valuable help with the experiments. Lastly, I would like to thank and acknowledge the constant support of my family members, particularly of my mom Simin Akbari, throughout the endeavors of my graduate studies.

Table of Contents

List of Figures and Tables

Abbreviations

ABC, ammonium bicarbonate

Acc1, acetyl-CoA carboxylase 1

ACN, acetonitrile

ADP, adenosine diphosphate

AGC, automatic gain control

Ale1, acyltransferase for lysophosphatidylethanolamine 1

AmAc, ammonium acetate

AmAc/AA, ammonium acetate with acetic acid

AmAc/FA, ammonium acetate with formic acid

AmF, ammonium formate

AmF/FA, ammonium formate with formic acid

AMP, adenosine monophosphate

App1, actin patch protein 1

Are1/2, acyl-coenzyme A: cholesterol acyl transferase-related enzymes 1 and 2

Asn, asparagine

Asp, aspartate

ATG, autophagy-related genes

ATP, adenosine triphosphate

Aur1, aureobasidin A resistance 1

Ayr1, acyl-dihydroxyacetone-phosphate reductase 1

°C, degrees Celsius

CDP, cytidine diphosphate

CDP-DAG, cytidine diphosphate-diacylglycerol

Cds1, CDP-diacylglycerol synthase 1

CER, ceramide

CerS, ceramide synthase complex

CFU, colony-forming units

Cho1/2, choline requiring 1 and 2

CID, collision-induced dissociation

CL, cardiolipin

CLS, chronological lifespan

CR, caloric restriction

Csg1/2, calcium-sensitive growth 1 and 2

CSH, charged-surface-hybrid

Csh1, CSG1/SUR1 homolog1

CW, cell wall

Cys, cysteine

D, diauxic shift

Da, Dalton

DAG, diacylglycerol

DDA, data-dependent acquisition

Dga1, diacylglycerol acyltransferase 1

$\Delta\Psi m$, the electrochemical potential across the inner mitochondrial membrane

Dgk1, diacylglycerol kinase 1

DHAP, dihydroxyacetone phosphate

dhCer, dihydroceramide

DHS, 3-ketodihydrosphingosine into dihydrosphingosine

DNA, deoxyribonucleic acid

Dpp1, diacylglycerol pyrophosphate phosphatase 1

ER, endoplasmic reticulum

ESI, electrospray ionization

ETC, electron transport chain

Faa1/4, fatty acid activation 1 and 2

FA-CoA, fatty acyl-CoA esters

FAD, flavin adenine dinucleotide

$FADH_2$, flavin adenine dinucleotide reduced

Fas1/2, fatty acid synthetases 1 and 2

Fat1, fatty acid transporter 1

FFA, free (unesterified) fatty acids

FMN, flavin mononucleotide

Fox1/2/3, fatty acid oxidation 1, 2 and 3

FTMS, Fourier transform mass spectrometry

FWHM, full width at half maximum

g, gravity

G1, growth phase 1 of the cell cycle

Gln, glutamine

Glu, glutamate

Gpd1/2, glycerol-3-phosphate dehydrogenases 1 and 2

Gpt2, glycerol-3-phosphate acyltransferase

Gro, glycerol

Gro-3-P, glycerol-3-phosphate

h, hour

H_2O, water

H_2S, hydrogen sulfide

HCD, higher-energy collisional dissociation

HD, high density

HESI, heated electrospray ionization

Hom3, aspartate kinase

HPLC, high pressure liquid chromatography

IMM, the inner mitochondrial membrane

IMS, intermembrane space

IPODs, insoluble protein deposits

IPC, inositol-phosphorylceramide

Ipt1, inositolphosphotransferase 1

Isc1, inositol phosphosphingolipid phospholipase C 1

3-KDHS, 3-ketodihydrosphingosine

Kei1, Kex2-cleavable protein essential for inositol-phosphorylceramide synthesis 1

kV, kilovolt

L, Logarithmic

Lac1, longevity-assurance gene cognate 1

Lag1, longevity assurance gene 1

LC, liquid chromatography

LCA, lithocholic acid

Lcb1/2, , long-chain base proteins 1 and 2

LC-MS/MS, liquid chromatography coupled with tandem mass spectrometry

LDP, lipid droplet

LD, low density

Lip1, Lag1/Lac1 interacting protein 1

Loa1, lysophosphatidic acid: oleoyl-CoA acyltransferase 1

LPA, lysophosphatidic acid

LPC, lysophosphatidylcholine

LPE, lysophosphatidylethanolamine

LPG, lysophosphatidylglycerol

LPI, lysophosphatidylinositol

Lpp1, lipid phosphate phosphatase 1

LPS, lysophosphatidylserine

LTQ, linear trap quadrupole

M, molecular ion (neutral)

MAGs, monoacylglycerols

Met, methionine

Met6, a cobalamin-independent methionine synthase involved in Met and Sam biosynthesis

Met7, folylpolyglutamate synthetase indirectly involved in Met, Cys and Sam biosynthesis

Met17p, an *O*-acetyl homoserine-*O*-acetyl serine sulfhydrylase indirectly involved in Met, Cys and Sam biosynthesis

MFQL, molecular fragmentation query language

ml, microliters

ml, milliliters

min, minutes

MIPC, mannosyl-inositol-phosphorylceramide

M(IP)2C, mannosyl-di-inositol-phosphorylceramide

MLCL, monolysocardiolipin

MS, mass spectrometry

MS/MS, tandem mass spectrometry

MSn, multi-stage mass spectrometry

MS1, parent ions

MS2, product ions

MTBE, methyl-tert-butyl-ether

5-Mtf, 5-methyltetrahydrofolate

N, nucleus

NaCl, sodium chloride

NAD^+, nicotinamide adenine dinucleotide

NADH, nicotinamide adenine dinucleotide hydride

$NADP^+$, nicotinamide adenine dinucleotide phosphate

NADPH, nicotinamide adenine dinucleotide phosphate hydride

non-CR, non-caloric restriction conditions

NQ, non-quiescent

NQ^{HD}, high density non-quiescent cells

NQ^{LD}, low density non-quiescent cells

Opi3, overproducer of inositol 3

Orm1/2, orosomucoid 1 and 2

PA, phosphatidic acid

Pah1, phosphatidic acid phosphohydrolase 1

PC, phosphatidylcholine

PCA, principal component analysis

PD, post-diauxic shift

PE, phosphatidylethanolamine

PE21, plant extract 21

PG, phosphatidylglycerol

PGP, phosphatidylglycerol-phosphate

PHC, phytoceramide

PHS, phytosphingosine

phytoCer ,phytoceramide

PI, phosphatidylinositol

PID, propidium iodide

PKA, protein kinase A

Pkh1/Pkh2, Pkb-activating kinase homolog proteins 1 and 2

PM, plasma membrane

POA, palmitoleic acid

Ppa2, inorganic pyrophosphatase 2

ppm, parts per million

PS, phosphatidylserine

Psd1, phosphatidylserine decarboxylase 1

PSGs, proteasome storage granules

OMM, outer mitochondrial membrane

Q, quiescent

Q^{HD}, high-density Q cells

Q^{LD}, low-density Q cells

RCD, regulated cell death

RLS, replicative lifespan

RNA, ribonucleic acid

ROS, reactive oxygen species

RP, reverse phase

RT, room temperature

RTT, retention time

S. cerevisiae, Saccharomyces cerevisiae

Sac1, suppressor of actin 1

Sam, S-adenosylmethionine

Sam1/2, *S*-adenosylmethionine synthetases 1 and 2

Sct1, suppressor of choline-transport mutants 1

sec, second

SEM, standard error of the mean

Slc1/4, sphingolipid compensation 1 and 4

Snf1, sucrose non-fermenting complex 1)

SPOTS, serine palmitoyltransferase, Orm1/2 and Sac1

SPT, serine palmitoyltransferase

ST, stationary phase

Sur2, suppressor 2 of Rvs161 and rvs167 mutations

TAG, triacylglycerol

TCA, tricarboxylic acid

Tgl1/3/4/5, triglyceride lipases 1, 3, 4 and 5

TOF, quadrupole flight time

Tor1, target of rapamycin complex 1

Tsc3/10, temperature-sensitive suppressors of Csg2 mutants 3 and 10

UPR, unfolded protein response

UPR^{ER} , unfolded protein response in the ER

YNB, yeast nitrogen base

YP, yeast extract, peptone

WT, wild type

Chapter 1: Introduction.

1.1 The budding yeast *Saccharomyces cerevisiae* is a model eukaryotic organism commonly used in the research on aging and longevity.

An overwhelming body of evidence supports the notion that the mechanisms underlying aging and longevity of eukaryotic organisms have been conserved in evolution [1-5]. Studies in the budding yeast *Saccharomyces cerevisiae*, a unicellular eukaryote, have provided strong evidence in favor of this notion. These studies have discovered many genes that influence cellular aging's pace and contribute to organismal longevity assurance not only in *S. cerevisiae* but also in multicellular eukaryotes [6-10]. Studies in budding yeast have also identified a distinct set of the signaling pathways that, in response to changes in nutrient availability and energy supply, regulate longevity-defining cellular processes in budding yeast and other eukaryotic organisms [11-15]. Moreover, studies in budding yeast have revealed many small molecules that slow aging, prolong longevity and postpone the onset of aging-associated pathologies in *S. cerevisiae* and other eukaryotes [16-20]. All these advances in using *S. cerevisiae* to dissect the fundamental mechanisms underlying biological aging and its delay are due to several advantages this yeast offers for aging research. These advantages include the following. Both replicative and chronological lifespans (RLS and CLS, respectively) of budding yeast are comparatively short and easy to measure [6, 8, 21, 22]. Furthermore, the complete sequencing of the budding yeast's genome has allowed the commercial production and extensive use of various mutant libraries for exploring the involvement of many genes and their protein products in cellular aging [6, 8, 21-23]. Moreover, a plethora of intricate molecular analyses can be used for examining the complexity of the aging process in budding yeast [6, 8, 21-23].

1.2 Replicative and chronological aging of budding yeast.

Two different modes of budding yeast's aging are known. One of these modes is the so-called chronological aging (Figure 1.1) [24, 25]. A quantitative measure of chronological aging under laboratory conditions is for how long a post-mitotic yeast cell exited the cell cycle in the G_1 phase because it consumes the exogenous carbon source (or other nutrients) retains the ability to re-enter the cell cycle. To assess this ability, the post-mitotic yeast cell is transferred from a nutrient-depleted medium to a medium rich in the supply of all nutrients (Figure 1.1) [6, 8, 26].

Because a nutrient supply-dependent cell cycle arrest in the G_1 phase elicits the entry of a budding yeast cell into a G_0 state of quiescence, the ability of a quiescent cell to re-enter the mitotic cell cycle after such transfer serves as the criterium for its viability (Figure 1.1) [6, 8, 26]. The liquid culture's aliquots are recovered on different culturing days to assess the chronological aging of budding yeast under laboratory conditions. Each aliquot is then plated on a solid medium containing all nutrients, and the ability of many individual cells to form a colony is visually assessed (Figure 1.1) [6, 8, 24-26]. The more time budding yeast cells spent in a nutrient-depleted liquid culture, the lower percentage of cells in the culture remains quiescent (i.e., capable of forming a colony) [6, 8, 24-26]. Several high-throughput assays have been recently developed for quantifying the chronological aging of budding yeast [26-29]. A consensus is that the chronological mode of budding yeast's aging mimics the aging of neurons and other post-mitotic cells of humans [6, 8, 24-26, 30-33].

The other mode of budding yeast's aging is called replicative aging (Figure 1.1) [34-37]. A quantitative measure of this aging mode under laboratory conditions is what number of daughter bud cells a mother cell can generate before it becomes unable to replicate by budding [34-37]. This definition does not specify if, after losing the ability to form a daughter bud, the mother cell remains quiescent (i.e., capable of creating a colony) for a certain time or immediately escapes quiescence to become senescent. This is a highly debated topic, including whether a cell remains quiescent (i.e., capable of forming a colony after being transferred to certain nutrient-rich media) if it can no longer produce a daughter cell in a nutrient-deprived medium [38-46]. To measure the pace of budding yeast's replicative aging under laboratory conditions, the daughter bud cells are separated from a mother cell with the help of a micromanipulator [34-37]. The average number of mitotic divisions that a mother cell can undergo before becoming unable to replicate by budding is counted for many mothers [34-37]. Akin to the chronological aging measurement under laboratory conditions, several assays for quantifying the budding yeast's replicative aging exist in a high-throughput format [47-53]. A commonly accepted viewpoint is that the replicative mode of budding yeast's aging mimics the aging of lymphocytes and other mitotically active cells of humans [6, 35, 54-57].

Although the replicative and chronological modes of budding yeast's aging are traditionally assessed separately from each other in different types of laboratory assays, a growing body of evidence indicates that a single aging process integrates both these aging modes in the

wild or even in a laboratory yeast culture [38-46].

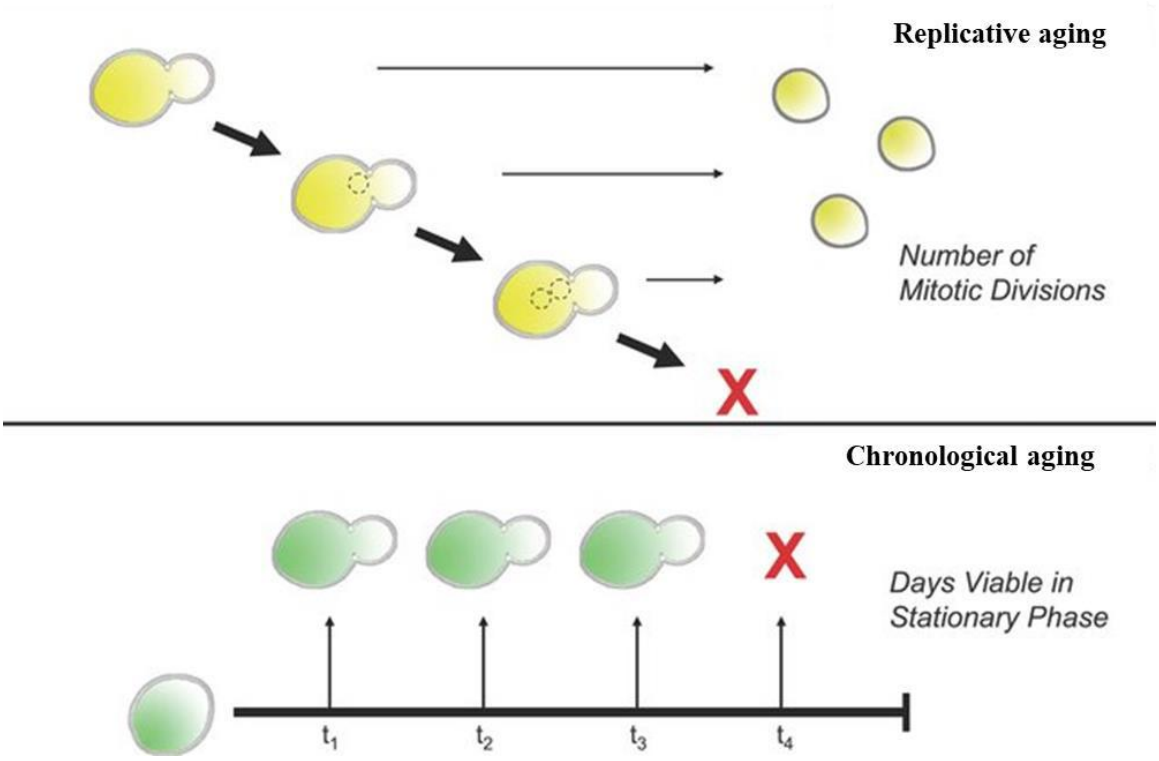

Figure 1.1. Replicative and chronological aging of budding yeast under laboratory conditions. Replicative aging of budding yeast under laboratory conditions is assessed by determining the maximum number of daughter bud cells that a mother cell can generate before it becomes unable to replicate by budding. Chronological aging of budding yeast under laboratory conditions is examined by assessing the time during which a post-mitotic yeast cell exited the cell cycle because it consumes the exogenous carbon source (or other nutrients) retains the ability to re-enter the cell cycle if it is transferred from a nutrient-depleted medium to a medium that contains all nutrients. From: Reference [58. Kaeberlein et al. PLoS Genet. 2007; 3: e84].

1.3 A link between chronological aging and a cellular quiescence program in budding yeast.

One way of studying budding yeast cells' chronological aging is to culture them under aerobic conditions in a complete, nutrient-rich medium initially containing 2% glucose as the only exogenous source of carbon [59]. These yeast cells are not limited in calorie supply and grow under the conditions for which the term "non-caloric restriction conditions (non-CR)" was coined

[59]. After consuming the exogenously added glucose, the budding yeast cells amass ethanol and a diauxic (D) shift period begins [59-61]. The growth of yeast culture is decelerated as the cells catabolize ethanol [59-61]. During the subsequent post-diauxic (PD) shift, mitochondrial respiration is enhanced, and yeast culture's growth is further slowed [59-61].

In some cells within the yeast culture initially grown under non-CR conditions, the PD shift is marked by the cell cycle arrest at the nutrient-sensing "START A" checkpoint in the late G_1 phase [62]. Two cell populations become detectable within the culture at that point. One of these populations is a population of quiescent (Q) cells whose cell cycle is arrested [62, 63]. Because Q cells do not have bud scars on their surface, these cells are daughter cells separated by budding from the mother cell [62, 63]. Of note, as discussed below, both Q and NQ cells can senesce. Q cells' two hallmarks are their clonogenicity and ability to divide synchronously. These and other properties of Q cells are detailed in the next section of my thesis introduction chapter. The other cell population includes non-quiescent (NQ) cells whose cell cycle is not arrested [62, 63]. The presence of one or more bud scars on the surface of NQ cells or the appearance of a separating daughter bud indicates that the NQ cells are the mother cells of the first and other generations [62, 63]. As described in the next section of my thesis introduction chapter, depending on cell age, some of these NQ cells are clonogenic and can divide synchronously, whereas others are not [62, 63]. An intricate signaling network, which integrates a distinct set of signaling pathways and protein kinases, controls the development of the diverse properties of Q and NQ cells [64].

After ethanol, a product of glucose fermentation, is consumed, the culture initially grown under non-CR conditions moves into the stationary (ST) phase of culturing [59, 60]. The cell-division cycles of all yeast cells in the culture are getting arrested at the nutrient-sensing "START A" checkpoint in the late G_1 phase [62, 63]. The chronological aging of Q cells begins [6, 8, 62, 63]. An aging-associated process in which a gradually increasing number of initially Q cells lose their clonogenicity and ability to divide synchronously to become NQ cells [62, 63].

1.3.1 Q and NQ cells that are aging chronologically under non-CR conditions differ from each other in their properties and fates.

The cell division cycles of all mother and daughter cells under non-CR conditions are arrested at the "START A" checkpoint in the late G_1 phase. For some mothers and daughters, this cell cycle arrest occurs during the PD shift, whereas for others, it happens at the beginning of the

ST phase of culturing [62, 63]. These mother and daughter cells become Q cells. A distinct set of properties exhibited by the Q cells under non-CR conditions and their fates are described in this section. The cell-division cycles of some mother cells under non-CR conditions are arrested during the PD shift; for other mothers, the cell-division cycle arrest under these conditions occurs at the beginning of the ST phase of culturing [62, 63]. All these mother cells give rise to the three populations of NQ cells. The properties of each of these NQ cell populations under non-CR conditions and their fates are also discussed here.

The two properties of Q cells most relevant to chronological aging are their clonogenicity and ability to divide synchronously (Figure 1.2) [62-67]. The clonogenicity is tested by plating a cell aliquot recovered from the ST phase culture on a nutrient-rich solid medium and assessing the cells' ability to form a colony clone [62-67]. The ability to divide synchronously is examined by transferring a cell aliquot taken from the ST phase culture to a nutrient-rich liquid medium and evaluating the cells' ability to undergo synchronous mitotic divisions [62-67]. Q cells under non-CR conditions are uniformly sized cells that do not form buds and lack bud scars on their surface (Figure 1.2) [62-67]. A thick cell wall of Q cells is responsible for their ability to refract light upon phase-contrast microscopical examination (Figure 1.2) [62-67]. Although most Q cells under non-CR conditions have high buoyant density, some are low-density cells (Figure 1.2) [62-68]. The increased metabolic activity, build-up of the glycogen and trehalose storage reserves, and elevated mitochondrial respiration and membrane potential are distinctive properties of Q cells under CR conditions (Figure 1.2) [62-68]. These cells possess low reactive oxygen species (ROS) concentrations and do not display significant oxidative damage to their proteins, nucleic acids and lipids (Figure 1.2) [62-68]. The high resistance to exogenous stresses, low rates of mutations in the nuclear and mitochondrial genomes, and the postponed onsets of apoptosis and necrosis are distinguishing Q cells' properties under CR conditions; this is likely because many of these cells are brand new daughter cells. (Figure 1.2) [62-68]. Q cells under non-CR conditions display a relocation of some heat-shock proteins from the cytosol to the nucleus and a build-up of other heat-shock proteins within the cytosolic foci and filaments (Figure 1.2) [69]. These cells exhibit substantial changes to the processes confined to their nucleus, including altered nuclear morphology, the topology of nuclear chromosomes and transcription of nuclear genes (Figure 1.2) [69]. The proteostatic capacity of Q cells under non-CR conditions is significantly enhanced due to a build-up of P-bodies and stress granules in the cytosol, relocation of inactive proteasome

subunits from the nucleus to the insoluble protein deposits, and transfer of active proteasome subunits from the nucleus to the proteasome storage granules (Figure 1.2) [69]. The re-arrangement of actin cytoskeleton and microtubules, the disintegration of the tubular mitochondrial network, and deposition of many small and globular mitochondria at the cell periphery are characteristic of Q cells under non-CR conditions (Figure 1.2) [69].

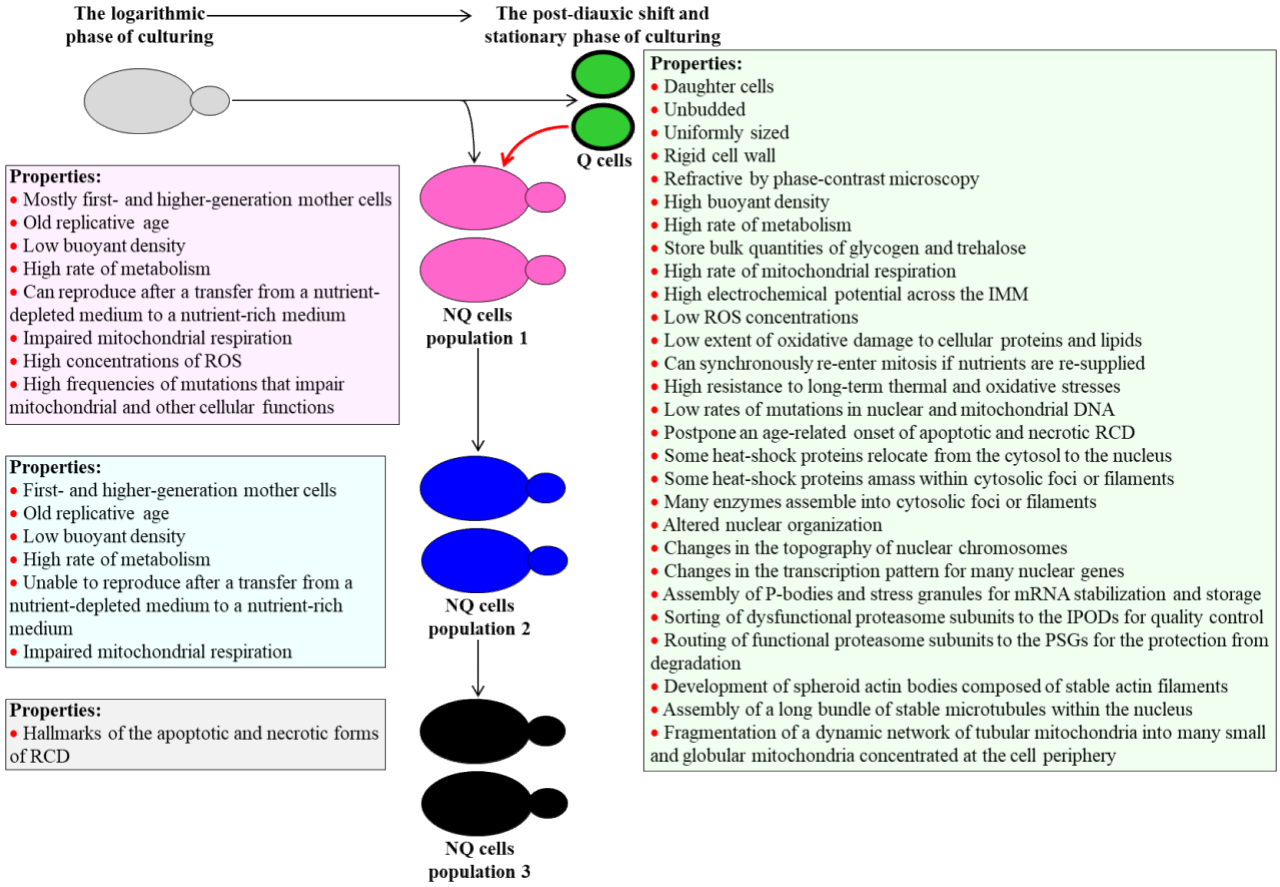

Figure 1.2. The properties and fates of Q and NQ cells of budding yeast cultured under non-CR conditions are different. NQ cells of population 1 originate from Q cells. The cells of NQ population 1 are predecessors of NQ population 2, the direct ancestors of NQ population 3. See the text for more details. Abbreviations: IMM, the inner mitochondrial membrane; IPODs, insoluble protein deposits; PSGs, proteasome storage granules; RCD, regulated cell death; ROS, reactive oxygen species From: Reference [70. **Mohammad** et al. Int J Mol Sci. 2020; 21: 4717].

Some of the above properties of Q cells under non-CR conditions are essential contributors to their abilities to retain a Q state when the nutrient supply is limited and withdraw from this state

to resume proliferation when nutrients become available again (Figure 1.2) [62-69]. Therefore, a commonly accepted viewpoint is that these properties of Q cells under non-CR conditions are also essential contributing factors to the assurance of their longevity in the wild and under laboratory conditions [62-69].

The mother cells that undergo cell-division cycle arrest under non-CR conditions give rise to the three populations of NQ cells (Figure 1.2) [62-67]. Only one of these cell populations, known as the NQ cell population 1, includes clonogenic cells that can divide synchronously (Figure 1.2) [62-67]. Therefore, it has been suggested that all NQ cells in this population are the direct descendants of Q cells (Figure 1.2, red arrow) [62-67]. Unlike most Q cells, the cells in NQ population 1 have low buoyant density (Figure 1.2) [62-67]. Moreover, the cells in NQ population 1 exhibit lower mitochondrial respiration, higher intracellular ROS, and lesser spontaneous mutations' frequencies than Q cells (Figure 1.2) [62-67]. Thus, it is conceivable that the changes in these Q cells' properties might be responsible for their conversion to the cells of NQ population 1.

Because the cells of NQ population 2 are not clonogenic and cannot divide synchronously, it is believed that they originate from the cells of NQ population 1 (Figure 1.2) [62-67]. Furthermore, the cells of NQ population 3 are not only non-clonogenic and incapable of dividing synchronously but also display major hallmarks of the apoptotic and necrotic forms of cell death (Figure 1.2) [62-67]. Therefore, it was suggested that the cells of NQ population 3 are the direct descendant of NQ population 2 cells (Figure 1.2) [62-67].

1.3.2 CR alters the properties of Q and NQ cells and slows their chronological aging.

CR is a robust aging-delaying (geroprotective) dietary regimen [71-73]. It reduces the supply and intake of calories but provides enough vitamins, amino acids and other essential nutrients [71-73]. CR slows aging and prolongs longevity in organisms across species, including replicative and chronological aging in budding yeast [2, 6, 8]. This dietary intervention delays the onset of aging-associated pathologies in budding yeast and metazoans [72-76].

The Q and NQ cell populations have been purified from chronologically aging budding yeast cultured under CR conditions and recovered on different days of the aging process [68]. The CR conditions were administered by culturing yeast in a nutrient-rich medium supplemented with 0.2% glucose. In contrast, the traditional non-CR conditions were implemented by culturing yeast

in a nutrient-rich medium initially containing 2% glucose [68]. These studies enabled the detailed comparative analyses of the properties exhibited by Q and NQ cells that are aging chronologically under CR or non-CR conditions [68, 70, 77]. This section of my thesis introduction chapter summarizes the findings of such comparative analyses.

As discussed in the previous section, the cell-division cycle arrest in budding yeast cells that are aging chronologically and consume glucose under non-CR conditions occurs at the "START A" checkpoint in the late G_1 phase; this cell cycle arrest coincides with the appearance of the high- and low-density populations of Q and NQ cells [62, 63, 65-67]. This is unlike the cell-division cycle arrest in budding yeast cells that consume glucose when they are aging chronologically under CR conditions. The arrest of their cell cycle happens at a checkpoint in the early G_1 phase, and it is also coincidental with the emergence of Q and NQ cells of different densities (Figure 1.3A) [68, 70, 77].

In yeast cultures aging chronologically under non-CR conditions, the low-density Q cells become the most abundant cell population during the ST phase of culturing [68, 70, 77]. If yeast cells are aging chronologically under CR conditions, a peak in the abundance of the low-density Q cell population is observed during the PD phase of culturing (Figure 1.3B) [68, 70, 77].

As discussed before, clonogenicity and the ability to divide synchronously are the two distinguishing features of Q cells [62-67]. Although Q cells under non-CR conditions retain both these abilities for a comparatively brief time (Figure 1.3C) [68, 70, 77], Q cells under CR conditions remain clonogenic and capable of dividing synchronously much longer (Figure 1.3D) [68, 70, 77].

The two major forms of glucose storage in budding yeast are glycogen and trehalose [60, 78]. The other essential roles of trehalose include proteostasis maintenance and stress protection [79-81]. The intracellular concentrations of glycogen and trehalose in the Q and NQ cell populations of budding yeast cultured under CR conditions exceed those found under non-CR conditions (Figure 1.3E) [68, 70, 77].

Triacylglycerols (TAG) constitute the primary form of lipid storage in lipid droplets (LDP) of budding yeast [82, 83]. These so-called neutral lipids are the intracellular source of free fatty acids (FFA) for generating energy and providing the precursors for phospholipid synthesis [82, 83]. The intracellular concentrations of TAG in the Q and NQ cell populations of budding yeast cultured under CR conditions are significantly lower than those observed in the corresponding cell

populations under non-CR conditions (Figure 1.3F) [68, 70, 77].

Cardiolipins (CL) are the lipids confined to the inner mitochondrial membrane (IMM) [83-86]. They define mitochondrial morphology and play essential roles in maintaining the mitochondria's proper functional state [83-86]. The Q and NQ cell populations of budding yeast cultured under CR conditions possess higher CL concentrations than the corresponding cell populations recovered from yeast under non-CR conditions (Figure 1.3G) [68, 70, 77].

The longevity of chronologically aging budding yeast cells depends on the rate of respiration and electrochemical membrane potential ($\Delta\Psi_m$) exhibited by their mitochondria [59, 87-90]. These essential features of mitochondrial functionality are activated in the Q and NQ cell populations of yeast cultured under CR conditions compared to the control non-CR conditions (Figure 1.3H) [68, 70, 77].

The intracellular ROS, which are produced mainly as by-products of respiration in mitochondria, contribute to longevity regulation in chronologically aging budding yeast [91-95]. ROS concentrations in Q and NQ cells that do not reach the ST phase of culturing under CR conditions are lower than those in the corresponding cell populations under non-CR conditions (Figure 1.3I) [68, 70, 77]. A reverse trend is observed in the Q and NQ cell populations recovered from yeast cultures that entered the ST phase (Figure 1.3I) [68, 70, 77].

The oxidative damage to cellular proteins, nucleic acids and lipids is an essential contributor to longevity regulation in chronologically aging budding yeast [90, 95-98]. The extent of oxidative damage to these macromolecules in the Q and NQ cell populations of yeast cultured under CR conditions is substantially lower than that found in the corresponding cell populations under non-CR conditions (Figure 1.3J) [68, 70, 77].

The dietary, genetic and pharmacological interventions that make eukaryotic cells more tolerant to chronic (long term) exogenous stresses slow down cellular aging [97-101]. The Q and NQ cell populations of budding yeast cultured under CR conditions are more resistant to chronic thermal and oxidative stresses than the corresponding cell populations recovered from yeast under non-CR conditions (Figure 1.3K) [68, 70, 77]. Q cells under CR conditions tolerate both these stresses better after the culture reaches the ST phase, whereas NQ cells under CR exhibit high stress resistance during PD shift [68, 70, 77].

When the chronologically aging cells die of old age, they exhibit the hallmarks of apoptotic and/or necrotic death [102-108]. The onsets of chronological aging-associated apoptosis and

necrosis in Q and NQ cells of budding yeast cultured under CR conditions occur later in the CLS than their onsets in the corresponding cell populations under non-CR conditions (Figure 1.3L) [68, 70, 77]. Moreover, under CR conditions, Q and NQ cells are more resistant to both forms of cell death elicited by exogenous stimuli than Q and NQ cells under non-CR conditions (Figure 1.3M) [68, 70, 77].

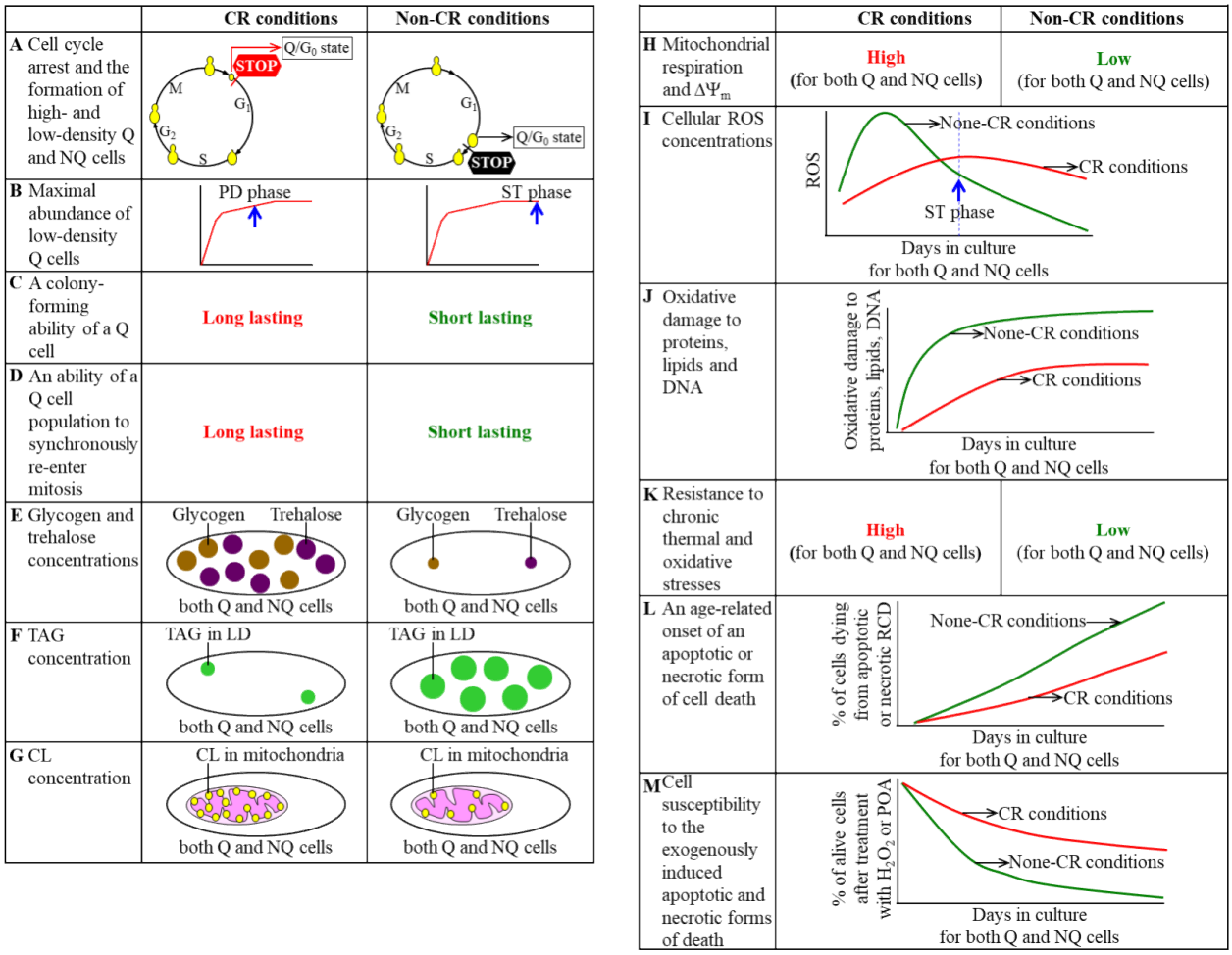

Figure 1.3. CR alters the properties of Q and NQ cells during the chronological aging of budding yeast. The CR-dependent changes in properties of Q and NQ cells are provided in different panels of the figure. See the text for more details. Abbreviations: CL, cardiolipins; LDP, lipid droplets; POA, palmitoleic acid; ROS, reactive oxygen species; TAG, triacylglycerols; $\Delta\Psi_m$, the electrochemical potential across the inner mitochondrial membrane. From: Reference [70. **Mohammad** et al. Int J Mol Sci. 2020; 21: 4717].

1.3.3 A possible mechanism that links chronological aging of budding yeast to properties of Q and NQ cells.

As described above, CR slows the chronological aging of budding yeast and changes Q and NQ cell populations' properties in chronologically aging yeast cultures. Many of these CR-driven changes in Q and NQ cells' properties have been previously implicated in the CR-dependent delay of budding yeast's chronological aging. Altogether, these observations suggest a mechanism that might link the chronological aging of budding yeast to some properties of Q and NQ cell populations. CR slows the chronological aging of budding yeast in the proposed mechanism because this geroprotective diet influences four essential processes within Q cells (Figure 1.4). These processes are integrated into a program of cellular quiescence operating during the chronological aging of budding yeast.

One of the cellular quiescence-related processes whose regulation by CR might be responsible for the CR-dependent delay of chronological aging is the positioning of a checkpoint in the G_1 phase at which the cell-division cycle is arrested during the PD shift and ST phase entry (Figure 1.4, process 1) [68, 70, 77]. Of note, this cell-division cycle arrest yields the high-density population of Q cells (Q^{HD}) (Figure 1.4, process 1). The cell cycle arrest resulting in Q^{HD} cells' formation under non-CR conditions occurs at a checkpoint in the late G_1 phase and creates large Q^{HD} cells (Figure 1.4, process 1). In contrast, the cell cycle arrest leading to Q^{HD} cells' creation under CR conditions occurs at a checkpoint in the early G_1 phase and creates small Q^{HD} cells (Figure 1.4, process 1). It is tempting to speculate that the small size of Q^{HD} cells formed under CR conditions contributes to some of the pro-longevity properties of these cells, including a rise in their reproductive competence (i.e., clonogenicity and synchronous division), an increase in their tolerance to chronic stresses, and a decline in their susceptibility to aging-associated apoptosis and necrosis (Figure 1.4).

A cellular quiescence-related process that leads to the conversion of Q^{HD} cells into low-density Q (Q^{LD}) cells is another CR-regulated event that might contribute to the CR-dependent delay of chronological aging (Figure 1.4, process 2) [68, 70, 77]. CR expedites the Q^{HD}-into-Q^{LD} conversion during chronological aging of budding yeast [68, 70, 77]. One may speculate that this CR-driven acceleration of the Q^{HD}-into-Q^{LD} conversion plays an essential role in developing some of the pro-longevity biochemical and cell biological properties of Q^{LD} cells. These properties are

named in the box for process 3 (Figure 1.4).

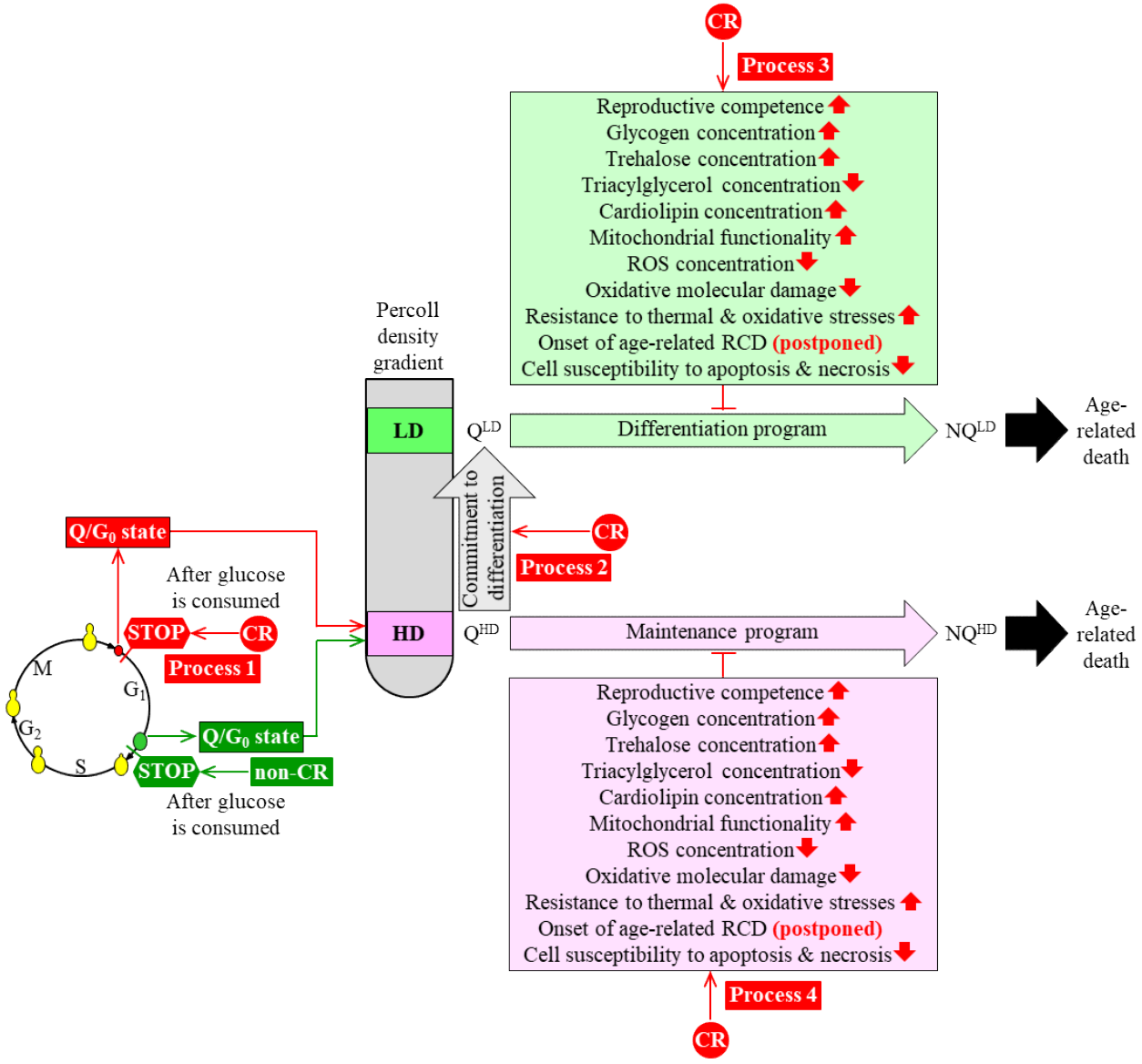

Figure 1.4. A mechanism that might link budding yeast's chronological aging to some properties of Q and NQ cells. In the proposed mechanism, CR slows the chronological aging of budding yeast because this geroprotective diet influences four essential processes within Q cells. See the text for more details. Abbreviations: HD, high density; LD, low density; Q, quiescent cells; NQ, non-quiescent cells; ROS, reactive oxygen species. ↑ Increased by CR; ↓ Decreased by CR; ⊣ Slows the Q^{LD}-into-NQ^{LD} or Q^{HD}-into-NQ^{HD} cell conversion. From: Reference [70. **Mohammad** et al. Int J Mol Sci. 2020; 21: 4717].

CR slows down another cellular quiescence-related process, the conversion of long-lived

Q^{LD} cells into short-lived NQ^{LD} cells (Figure 1.4, process 3) [68, 70, 77]. It is conceivable that this effect of CR on the Q^{LD}-into-NQ^{LD} conversion (which delays budding yeast's chronological aging) is due to CR's ability to affect some of the cell properties termed in the box for process 3 (Figure 1.4) [68, 70, 77].

CR also decelerates a cellular quiescence-related process of transforming long-lived Q^{HD} cells into short-lived NQ^{HD} cells (Figure 1.4, process 4) [68, 70, 77]. Akin to process 3, the CR-driven slowdown of process 4 (which slows the chronological aging of budding yeast) may be elicited because CR alters some of the cell properties indicated in the box for process 4 (Figure 1.4) [68, 70, 77].

As mentioned above, among cell properties altered by CR are those related to the intracellular concentrations of two lipid classes, TAG and CL. The low-calorie diet decreases TAG concentration and has the opposite effect on the concentration of CL in Q and NQ cells [68, 70, 77]. It would be interesting to assess the impact of CR on the intracellular concentrations of the lipid classes other than TAG and CL. These other lipid classes include FFA, sphingolipids and various phospholipid classes. All these other lipids have been implicated in the regulation of many essential cellular processes. Another interesting direction of future research is investigating how the geroprotective interventions other than CR (including genetic and pharmacological ones) influence the concentrations of all these lipid classes in Q and NQ cells.

1.4 Geroprotective phytochemicals extend the longevity of chronologically aging budding yeast.

Plants have evolved metabolic pathways for synthesizing a variety of secondary metabolites collectively known as phytochemicals [109, 110]. Phytochemicals synthesized by the host plants do not provide the energy needed for these plants' development, growth, and functional activities [109, 110]. The host plants do not use phytochemicals as the precursors or intermediates for synthesizing complex chemical compounds required for the development, growth and functionality of these plants [109, 110]. A body of evidence indicates that phytochemicals' primary role is to help the host plant synthesizing and releasing them into the ecosystem to survive and reproduce in this ecosystem [109, 110]. There are several ways through which phytochemicals can contribute to the host plant's ability to survive and reproduce within the ecosystem it inhabits. These different ways have been described elsewhere [109-123]. They include protecting plants

from various environmental stresses and pollutants, defending plants from microbial and other infections, attracting pollinators to plants and many other ways [109-123].

After phytochemicals are produced and released into the ecosystem by autotrophic organisms (i.e., by plants) to help the plants to survive and reproduce within the ecosystem, some of these phytochemicals can delay aging and extend the longevity of various heterotrophic organisms (e.g., of animals or yeasts) living in this ecosystem. This section of my Thesis Introduction chapter describes several known mechanisms by which geroprotective phytochemicals synthesized by different plant species can slow down the chronological aging of budding yeast and prolong budding yeast's longevity.

Quercetin is a flavonol phytochemical that is abundant in many fruits and vegetables [124]. When the cells of a budding yeast's laboratory strain were pre-treated for 15 min with 0.1 mg/ml quercetin, then washed with water and incubated in water, their mean CLS (i.e., the number of days needed for 50% of cells in a culture to become non-clonogenic) increased by 60% [125]. The quercetin-driven extension of the budding yeast's mean CLS coincided with a quercetin-dependent rise in cell resistance to exogenous oxidative stress inflicted by exposure to exogenous hydrogen peroxide [125]. Quercetin treatment reduced intracellular ROS, decreased glutathione oxidation, and lowered the extent of oxidative damage to proteins and lipids [125]. The quercetin-dependent increase in cell resistance to oxidative stress was not caused by the activation of the antioxidant enzymes (i.e., glucose-6-phosphate dehydrogenase, superoxide dismutase or catalase) or iron chelation in quercetin-treated yeast cells [125]. Therefore, it was suggested that quercetin slows the chronological aging of budding yeast cells and prolongs their longevity because it functions as the direct scavenger of cellular ROS, thereby sustaining the redox homeostasis and preventing oxidative macromolecular damage within the chronologically aging yeast cell [125].

Caffeine is an alkaloid phytochemical present in *Coffea* plants [126]. The addition of 0.2 – 0.4 mM caffeine to the exponentially grown culture of a budding yeast's laboratory strain significantly extended the longevity of chronologically aging yeast [127]. The longevity-extending effect of caffeine in budding yeast was due to this phytochemical ability to target the TORC1–Sch9–Rim15 cascade of nutrient-sensing protein kinases [127]. In the absence of caffeine, TORC1 phosphorylates and activates Sch9 [127, 128]. Sch9 then phosphorylates Rim15 in the cytosol [128]. The Sch9-dependent, site-directed phosphorylation of Rim15 suppresses its import into the nucleus [128]. The nuclear import of Rim15 is needed to phosphorylate and activate (directly or

indirectly) several nuclear transcription factors that promote transcription of many genes encoding pro-longevity proteins [128]. These proteins are essential contributors to protein folding, stress resistance, ROS detoxification, reserve carbohydrates synthesis, cell cycle arrest in G_1 and quiescence entry [127, 128]. Caffeine binding to TORC1 inhibited the TORC1-dependent phosphorylation and activation of Sch9, thereby preventing Sch9-driven suppression of Rim15 import into the nucleus [127]. After being imported into the nucleus of caffeine-treated yeast cells, Rim15 stimulated transcription of many nuclear pro-longevity genes and prolonged the longevity of chronologically aging budding yeast [127].

Cryptotanshione, a quinone from the roots of *Salvia miltiorrhiza* Bunge (also known as Danshen) [129], significantly extended the longevity of chronologically aging budding yeast if a cell culture entering stationary phase was supplemented with 78-313 nM of this phytochemical [130]. Although cryptotanshinone lowered intracellular ROS in wild-type (WT) strain, it did not affect ROS concentrations in a mutant strain lacking a pro-longevity gene for the mitochondrial manganese superoxide dismutase SOD2 [130]. Yet, cryptotanshinone significantly prolonged the CLS of this mutant strain [130]. Thus, the longevity-extending effect of cryptotanshinone was unlikely to be directly caused by its ability to decrease intracellular ROS. Moreover, the longevity-extending ability of cryptotanshinone was impaired by mutations eliminating genes for nutrient-sensing protein kinases Tor1, Sch9 and Gcn2 and by the amino acid limitation in a minimal growth medium [130]. It is known that Tor1 and Sch9 are pro-aging protein kinases activated in amino acid-rich media, whereas Gcn2 is an anti-aging protein kinase stimulated in response to amino acid limitation [128, 131]. Therefore, a mechanistic link between the high longevity-extending efficiency of cryptotanshinone and the cellular amino acid homeostasis remains unclear.

Spermidine is a polyamine phytochemical that is most abundant in wheat germ and soybean seeds [132, 133]. When exogenous spermidine was added to a WT culture of budding yeast on day 1 of culturing at a final concentration of 4 mM, it significantly extended yeast CLS [134]. Spermidine treatment increased budding yeast's resistance to chronic thermal and oxidative stresses and decreased yeast cells' susceptibility to an aging-associated necrotic death [134]. The histone acetyltransferases' activities decreased, and the extent of histone H3 deacetylation increased in long-lived budding yeast treated with spermidine [134]. The transcription of several genes implicated in the autophagic degradation of dysfunctional macromolecules and organelles was enhanced in spermidine-treated budding yeast [134]. The assessment of several hallmarks

events of autophagy has revealed that spermidine stimulates this essential mechanism of cell protection from aging-associated macromolecular and organellar damage [134]. A knock-out mutation in a gene encoding an autophagy-related protein impaired spermidine's longevity-extending ability [134]. Therefore, it was concluded that spermidine-induced autophagy is an essential contributor to a spermidine-depended extension of budding yeast's CLS [134]. Such an essential contribution of spermidine to longevity extension of chronologically aging yeast is likely due to the spermidine-dependent delay in the onset of aging-associated necrotic death [134].

4,4'-dimethoxychalcone is a flavonoid phytochemical found in the plant *Angelica keiskei koidzumi* [135]. The addition of 100 μM 4,4'-dimethoxychalcone to budding yeast 12 h after cell inoculation slowed down a chronological aging-associated decline in cellular health [135]. Indeed, 4,4'-dimethoxychalcone treatment increased plasma membrane (PM) integrity, reduced intracellular ROS, prolonged yeast CLS, and delayed the onset of the age-related forms of apoptotic and necrotic forms of cell death [135]. Akin to spermidine, 4,4'-dimethoxychalcone activated autophagy, and this activation was essential for the 4,4'-dimethoxychalcone-dependent extension of budding yeast's CLS [135]. Unlike spermidine, the CLS-extending effect of 4,4'-dimethoxychalcone depended on its ability to suppress Gln3 [135]. Gln3 is a 5'-GATAAG-3' sequence-binding transcriptional activator of genes subjected to nitrogen catabolite repression [136]; Gln3 also negatively regulates autophagy in a TORC1-independent manner [135].

In sum, the above examples indicate that diverse geroprotective phytochemicals target different proteins and cellular processes to extend the longevity of chronologically aging budding yeast. The Titorenko laboratory has recently discovered 21 geroprotective plant extracts that significantly increase this yeast CLS [137, 138]. It would be interesting to investigate the mechanisms through which these geroprotectors of plant origin prolong the longevity of chronologically aging *S. cerevisiae*.

1.5 Lithocholic acid (LCA), a natural geroprotector synthesized by intestinal bacteria and released by animals and humans, extends the CLS of budding yeast.

LCA was discovered in a high-throughput chemical genetic screen for small molecules that can extend the longevity of chronologically aging budding yeast [139]. After being synthesized from the primary chenodeoxycholic bile acid by intestinal bacteria, LCA, the most hydrophobic secondary bile acid is released into the environment by animals and humans [140,

141]. When commercial LCA was added to a budding yeast's culture limited in calorie supply at a final concentration of 50 μM, this bile acid crossed the cell wall (CW) and plasma membrane (PM) [142]. After LCA got into the cell, it was sorted mainly into the IMM [142]. LCA's minor quantities were also delivered to the outer mitochondrial membrane (OMM) [142].

Of note, all mitochondrial proteins involved in the phospholipid transport into and phospholipid metabolism in yeast mitochondria reside in the OMM and IMM, respectively [143, 144]. This explains why LCA's build-up in the OMM and IMM elicited a remodeling of their lipidomes (Figure 1.5) [142, 145-148].

A hallmark of the LCA-driven remodeling of the OMM and IMM lipidomes was a substantial rise in these membranes' phospholipid/protein ratio (Figure 1.5) [142]. This led to a significant increase in mitochondria' size within LCA-treated yeast cells (Figures 1.5 and 1.6) [142].

Another characteristic change in the OMM and IMM lipidomes within LCA-treated yeast was an increase in the concentration of phosphatidic acid (PA) (Figure 1.5) [142, 147]. It is conceivable (but still needs to be confirmed) that the observed rise in mitochondrial PA was due to the LCA-dependent promotion of PA movement through the contact sites linking the ER to OMM and/or subsequent PA transfer from the OMM to the IMM by the PA-binding proteins in the intermembrane space (Figure 1.5) [142, 147]. Noteworthy, PA is known for its propensity to promote mitochondrial fusion [149]. Therefore, it was suggested that the LCA-driven rise in the mitochondrial membrane PA is responsible for decreasing the number of mitochondria seen within LCA-treated yeast cells (Figures 1.5 and 1.6) [142, 147].

LCA treatment also altered the concentrations of other mitochondrial membrane lipids. The concentrations of phosphatidylserine (PS), phosphatidylglycerol (PG) and phosphatidylcholine (PC) were increased in the membranes of mitochondria within yeast cells treated with LCA (Figure 1.5) [142, 147]. LCA treatment of yeast cells had the opposite effects on the concentrations of phosphatidylethanolamine (PE), cardiolipin (CL) and monolysocardiolipin (MLCL) in the mitochondrial membranes (Figure 1.5) [142, 147]. It was suggested that the most reasonable explanations for the observed effects of LCA on the above mitochondrial membrane lipids are that LCA inhibits the enzymatic activities of Psd1 (which is known to accelerate the PS-into-PE conversion) and Crd1 (which is known to promote the PG-into-CL transformation) (Figure 1.5) [142, 147].

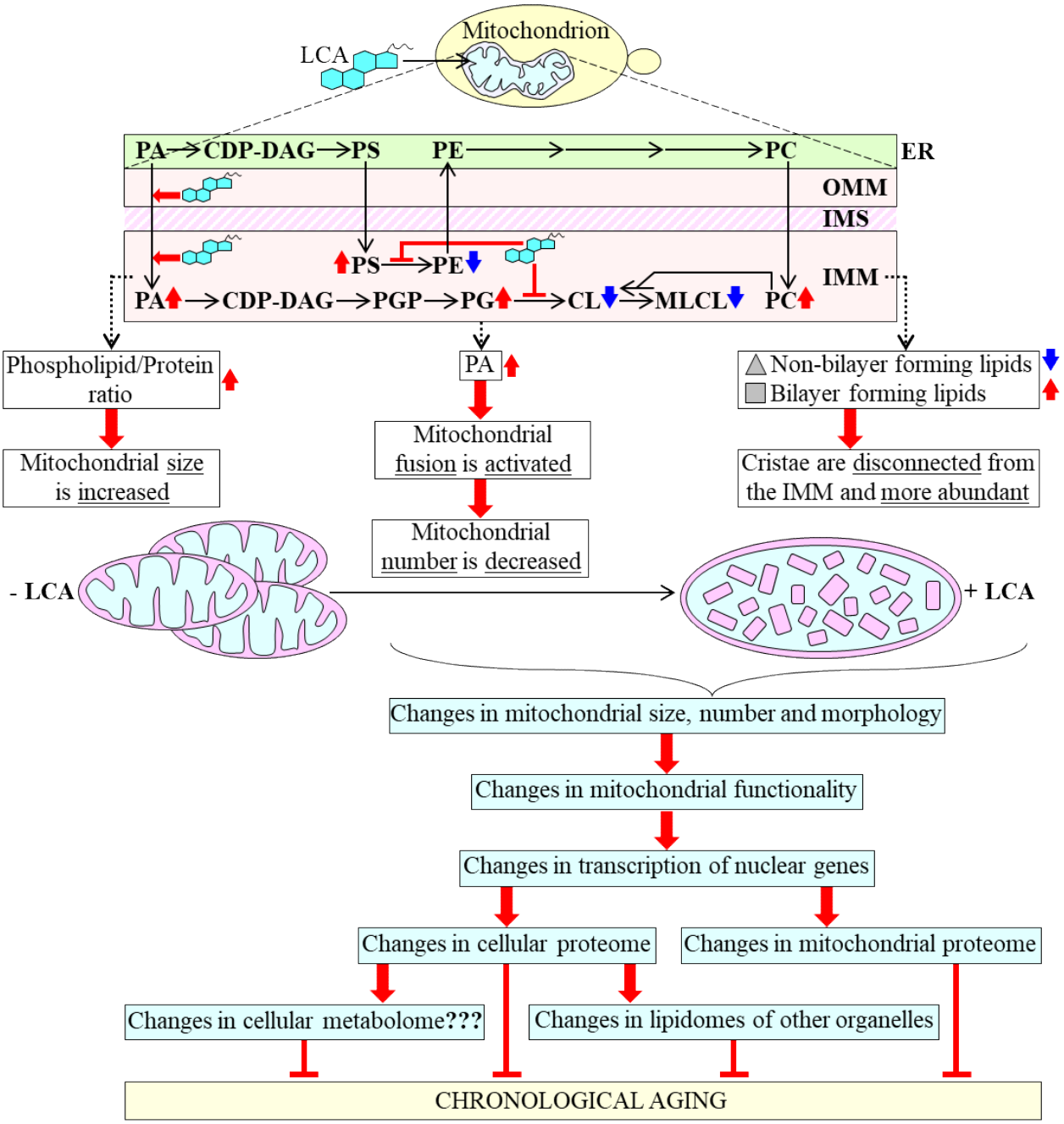

Figure 1.5. After exogenous lithocholic acid (LCA) gets into the yeast cell, it is sorted into the outer and inner mitochondrial membranes (OMM and IMM, respectively). Because all mitochondrial proteins involved in the phospholipid transport into and phospholipid metabolism within yeast mitochondria reside in the OMM and IMM, the build-up of LCA in these membranes elicits a remodeling of their lipidomes. The LCA-dependent remodeling of mitochondrial membrane lipidomes gradually changes mitochondrial size, number, morphology, proteome and functionality. Due to these changes, mitochondria become an organelle that helps organize a pro-

longevity cellular pattern and prolong the longevity of chronologically aging yeast. See the text for more details. Abbreviations: CDP-DAG, cytidine diphosphate-diacylglycerol; Cl, cardiolipin; ER, endoplasmic reticulum; OMM, outer mitochondrial membrane; IMM, inner mitochondrial membrane; IMS, intermembrane space; MLCL, monolysocardiolipin; PA, phosphatidic acid; PC, phosphatidylcholine; PE, phosphatidylethanolamine; PG, phosphatidylglycerol; PS, phosphatidylserine; PGP, phosphatidylglycerol-phosphate. From: Reference [83. Mitrofanova D, Dakik P, McAuley M, Medkour Y, **Mohammad K**, Titorenko VI. Lipid metabolism and transport define the longevity of the yeast Saccharomyces cerevisiae. Front Biosci (Landmark Ed). 2018; 23:1166-1194] with modifications.

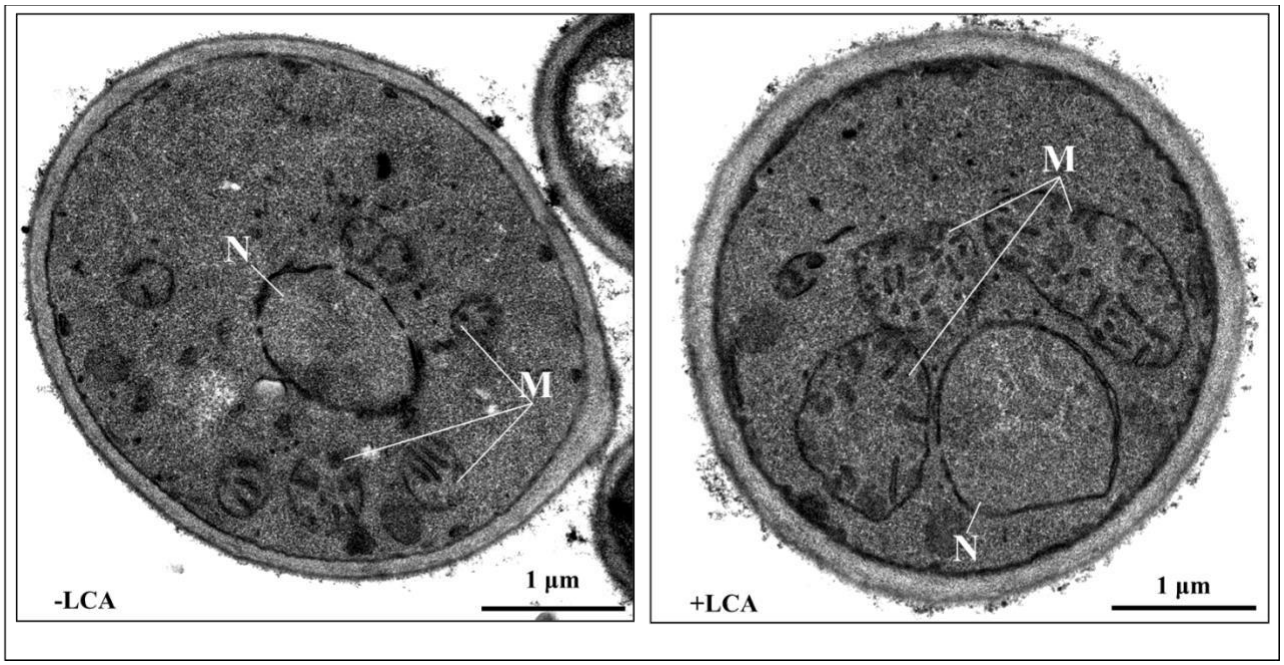

Figure 1.6. After LCA is sorted into the OMM and IMM, it increases mitochondrial size, decreases the mitochondrial number and alters mitochondrial cristae morphology. Transmission electron micrographs of budding yeast cells. The cells were cultured in a liquid medium without LCA or with 50 µM LCA. The cells were recovered on day 7 of cell culturing. M, the mitochondrion. N, the nucleus. Bar, 1 µm. From: Reference [142. Beach A, Richard VR, Leonov A, Burstein MT, Bourque SD, Koupaki O, Juneau M, Feldman R, Iouk T, Titorenko VI. Mitochondrial membrane lipidome defines yeast longevity. Aging (Albany NY). 2013; 5:551-574].

Of note, PS, PG and PC are known as the bilayer-forming phospholipids that decrease the

extent of membrane curving for the IMM [142, 150-152]. In contrast, PE, CL and MLCL are called the non-bilayer-forming phospholipids because they increase the degree of membrane curving for the IMM [142, 150-152]. The LCA-dependent rise in the concentrations of the bilayer-forming phospholipids (i.e., PS, PG and PC) and decline in the concentrations of the non-bilayer-forming phospholipids (i.e., PE, CL and MLCL) satisfactorily explains the observed changes in cristae morphology within mitochondria of LCA-treated yeast. Indeed, the flat membrane bilayers of cristae were detached from the IMM and accumulated in the matrix of these mitochondria, thereby increasing the surface area of the mitochondrial cristae (Figures 1.5 and 1.6) [142, 145-148].

The LCA-dependent changes in the size, number, and morphology of mitochondria alter these organelles' functionality (Figure 1.5) [142, 147, 153]. Some of the LCA-induced alterations in the mitochondrial functionality (including a decline in the mitochondrial membrane potential in the LCA-treated yeast cells before entry into the ST phase of culturing or a rise in the mitochondrial ROS in the LCA-treated yeast cells that have entered the ST phase of culturing) stimulate a distinct set of transcription factors [153]. These transcription factors include Rtg1, Rtg2, Rtg3, Sfp1, Aft1, Yap1, Msn2, Msn4, Skn7 and Hog1 [153]. They all are activated in response to the LCA-inflicted changes in specific aspects of mitochondrial functionality [153]. After being activated, these transcription factors regulate the expression of nuclear genes whose protein products are essential contributors to longevity assurance in budding yeast [153]. Some of these protein products are localized to mitochondria, whereas others reside in the cytosol, ER, lipid droplets (LPD) and peroxisomes [147, 153, 154]. The resulting remodeling of mitochondrial and cellular proteomes elicits the development of a pro-longevity cellular pattern and allows to sustain this pattern throughout the lifespan (Figure 1.5) [147, 153, 154]. This pro-longevity cellular pattern includes a specific remodeling in the lipidomes of cellular organelles other than mitochondria (Figure 1.5) [154]. The LCA-dependent cellular pattern that enables the deceleration of budding yeast's chronological aging exhibits several characteristic features. These features include a specific remodeling of lipid and carbohydrate metabolism in mitochondria and other cellular locations, re-arrangement of the ER-LD, ER-mitochondria and mitochondria-peroxisome intercompartmental communications, and delay in the onsets of apoptotic and necrotic forms of age-related cell death [147, 153, 154].

Altogether, the above findings suggested a mechanism underlying LCA's aging-delaying action in chronologically aging budding yeast (Figure 1.5). Of note, a critical process integrated

into this mechanism is a substantial remodeling of the mitochondrial lipidome and the lipidomes of other organelles (Figure 1.5) [147, 153, 154]. Although the proteomic analysis revealed the significant changes in the abundance of proteins implicated in the metabolism of water-soluble metabolites, it would be interesting to assess whether LCA inflicts substantial alterations in the water-soluble metabolome of chronologically aging budding yeast (Figure 1.5).

1.6 The integration of lipid metabolism in the cytosol, ER, Golgi apparatus, mitochondria, LD and peroxisomes maintains cellular lipid homeostasis in budding yeast.

The preservation of lipid homeostasis in *S. cerevisiae* cells requires integrating chemical reactions for the biosynthesis and catabolism of several lipid classes, including phospholipids, TAG, FFA, ceramides and sphingolipids [155-159]. These biosynthetic and catabolic reactions are catalyzed by the enzymes in the cytosol, ER, Golgi apparatus, mitochondria, LD and peroxisomes [155-159]. Moreover, the maintenance of cellular lipid homeostasis in budding yeast depends on some lipids' interorganellar transport via contact sites between different organelles [159-163].

The biosynthesis of phospholipids begins when the glycerol-3-phosphate dehydrogenases Gpd1 and Gpd2 in the cytosol catalyze a reversible redox conversion of the glycolytic intermediate dihydroxyacetone phosphate (DHAP) to glycerol-3-phosphate (Gro-3-P) (Figure 1.7) [60]. DHAP and Gro-3-P can enter the biosynthetic pathway for phospholipids only after the cytosolic acetyl-CoA is converted to fatty acyl-CoA esters (FA-CoA) and these esters are transported into the ER (Figure 1.7). The acetyl-CoA conversion to FA-CoA is catalyzed by the acetyl-CoA carboxylase Acc1 and fatty acid synthetase complex Fas1/Fas2 in the cytosol (Figure 1.7) [164, 165]. After the transport of FA-CoA into the ER, the FA-CoA molecules are used as co-substrates in the Gpt2- and Sct1-catalyzed reactions leading to the formation of acyl-DHAP from DHAP and lysophosphatidic acid (LPA) from Gro-3-P (Figure 1.7) [166, 167]. An Ayr1-dependent reduction of acyl-DHAP to LPA further increases LPA concentration in the ER (Figure 1.7) [168]. The FA-CoA molecules transported into the ER can also be used as co-substrates in the reaction leading to PA formation (Figure 1.7). This reaction is catalyzed by Loa1, Ale1, Slc1, Slc4, Loa1 and Ale1 [169-171].

After being formed in the ER, PA can enter two different biosynthetic branches for other phospholipid species. The initial reaction of one of these branches generates CDP-DAG and is catalyzed by the CDP-DAG synthase Cds1 (Figure 1.7) [156-159, 172]. CDP-DAG is then

converted to phosphatidylinositol (PI) and PS in the reactions catalyzed by the ER enzymes Pis1 and Cho1, respectively (Figure 1.7) [156-159]. PS is transferred from the ER to the OMM through mitochondria-ER contact sites and then to the IMM across the IMS (Figure 1.7) [159-163]. In the IMM, PS is converted into PE in the Psd1-dependent reaction (Figure 1.7) [159-163]. The PE formation in the IMM is followed by its transfer, initially to the OMM and then to the ER via mitochondria-ER contact sites (Figure 1.7) [160-163]. The first biosynthetic branch for the PA conversion to other phospholipid species is completed when the Cho2- and Opi3-catalyzed reactions generate PC from PE (Figure 1.7) [156-159]. The second biosynthetic branch for converting PA to other phospholipid species includes a phosphatase-dependent reaction that generates DAG and is catalyzed by the PA phosphatases App1, Dpp1, Lpp1 and Pah1 in the ER (Figure 1.7) [156-159]. The biosynthesis of TAG from DAG in the ER is completed in two reactions. Each of these reactions is catalyzed by different enzymes that use different co-substrates for converting DAG to TAG. Are1, Are2 and Dga1 use FA-CoA as a co-substrate to catalyze one of these reactions (Figure 1.7) [173, 174]. Lro1 uses PE and PC as the co-substrates to catalyze the other reaction (Figure 1.7) [175]. The TAG molecules' formation in the ER is followed by their transfer to and accumulation in the LD (Figure 1.7) [157-159].

The TAG molecules can be stored in LD as a reserve for the formation of FFA and DAG, the source of energy and biosynthetic precursors of more complex lipids. In the budding yeast cells that rapidly proliferate, the TAG lipases Ayr1, Tgl1, Tgl3, Tgl4 and Tgl5 hydrolyze TAG in LD to form FFA and DAG (Figure 1.7) [176-180]. The Tgl3-driven hydrolysis of DAG generates monoacylglycerols (MAGs), which can be further hydrolyzed to form glycerol (Gro) in a Yju3-catalyzed reaction; both these hydrolytic reactions lead to the formation of more FFA in LD (Figure 1.7) [179, 181]. The FFA molecules formed during TAG, DAG and MAG hydrolysis in LD can be converted to FA-CoA in the reaction that is catalyzed by the complex of the long-chain acyl-CoA synthetases Faa1, Faa4 and Fat1 in the LD (Figure 1.7) [182, 183]. The FA-CoA molecules produced in LD can be directed to the ER for phospholipid and TAG synthesis (Figure 1.7) [166, 167]. The FA-CoA molecules generated in LD can also be subjected to beta-oxidation in the peroxisomes adjacent to the LD (Figure 1.7) [184-188]. Peroxisomal beta-oxidation of these FA-CoA in the Fox1-, Fox2- and Fox3-dependent reactions yields acetyl-CoA (Figure 1.7). This acetyl-CoA can be used for mitochondrial energy production. It can also be used for FA-CoA formation in the reactions catalyzed by the cytosolic acetyl-CoA carboxylase Acc1 and fatty acid

synthetase complex Fas1/Fas2 (Figure 1.7) [164, 165].

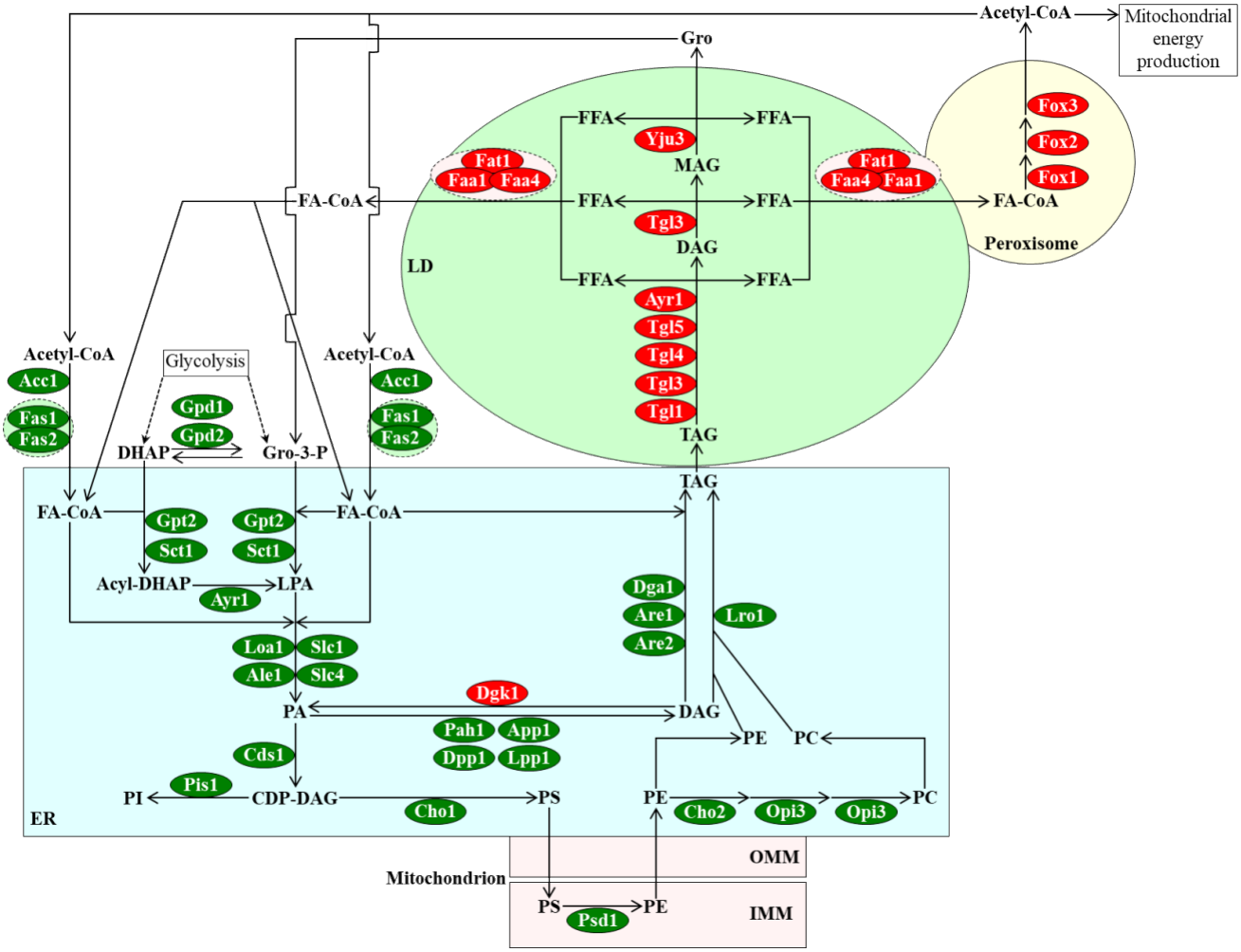

Figure 1.7. The biosynthetic and catabolic pathways of phospholipid and TAG metabolism in the cytosol, ER, mitochondria, LD and peroxisomes. Enzymes that catalyze reactions of the biosynthetic pathways are shown in green. Enzymes that catalyze reactions of the catabolic pathways are shown in red. See the text for more details. Abbreviations: Acc1, acetyl-CoA carboxylase 1; Ale1, acyltransferase for lysophosphatidylethanolamine 1; App1, actin patch protein 1; Are1/2, acyl-coenzyme A: cholesterol acyl transferase-related enzymes 1 and 2; Ayr1, acyl-dihydroxyacetone-phosphate reductase 1; CDP, cytidine diphosphate; Cds1, CDP-diacylglycerol synthase 1; Cho1/2, choline requiring 1 and 2; DAG, diacylglycerol; Dga1, diacylglycerol acyltransferase 1; Dgk1, diacylglycerol kinase 1; Dpp1, diacylglycerol pyrophosphate phosphatase 1; DHAP, dihydroxyacetone phosphate; Faa1/4, fatty acid activation 1 and 2; FA-CoA, fatty acyl-CoA ester; Fas1/2, fatty acid synthetases 1 and 2; Fat1, fatty acid

transporter 1; FFA, free fatty acid; Fox1/2/3, fatty acid oxidation 1, 2 and 3; Gpd1/2, glycerol-3-phosphate dehydrogenases 1 and 2; Gpt2, glycerol-3-phosphate acyltransferase; Gro, glycerol; Gro-3-P, glycerol-3-phosphate; OMM, outer mitochondrial membrane; IMM, inner mitochondrial membrane; Loa1, lysophosphatidic acid: oleoyl-CoA acyltransferase 1; Lpp1, lipid phosphate phosphatase 1; LPA, lysophosphatidic acid; Lro1, lecithin cholesterol acyl transferase related open reading frame 1; MAG, monoacylglycerol; Opi3, overproducer of inositol 3; PA, phosphatidic acid; Pah1, phosphatidic acid phosphohydrolase 1; PC, phosphatidylcholine; PE, phosphatidylethanolamine; PS, phosphatidylserine; Psd1, phosphatidylserine decarboxylase 1; Sct1, suppressor of choline-transport mutants 1; Slc1/4, sphingolipid compensation 1 and 4; Tgl1/3/4/5, triglyceride lipases 1, 3, 4 and 5. From: Reference [83. Mitrofanova D, Dakik P, McAuley M, Medkour Y, **Mohammad K**, Titorenko VI. Lipid metabolism and transport define the longevity of the yeast Saccharomyces cerevisiae. Front Biosci (Landmark Ed). 2018; 23:1166-1194] with modifications.

The biosynthesis of sphingolipids begins when the serine palmitoyltransferase (SPT) protein complex in the ER membrane catalyzes the formation of 3-ketodihydrosphingosine from serine and palmitoyl-CoA (Figure 1.8) [189-191]. The SPT complex contains the catalytic subunits Lcb1 and Lcb1 and the activating subunit Tsc3 (Figure 1.8) [189-191]. The SPT complex associates with the Orm1 and Orm2 proteins and the phosphatidylinositol phosphate phosphatase Sac1 to form the SPOT (serine palmitoyltransferase associated with Orm proteins) protein complex; the Orm1, Orm2 and Sac1 subunits of the SPOT complex are responsible for the regulation of sphingolipid biosynthesis by the intracellular concentrations of sphingolipids and phosphatidylinositol phosphates (Figure 1.8) [192, 193].

The 3-ketosphinganine reductase Tsc10 catalyzes the conversion of 3-ketodihydrosphingosine into dihydrosphingosine (DHS), a long-chain sphingolipid base (Figure 1.8) [190, 194]. DHS is then transformed into phytosphingosine (PHS), another long-chain sphingolipid base; this reaction is catalyzed by the sphinganine C4-hydroxylase Sur2 (Figure 1.8) [190, 195]. The acylation reaction between $C_{26:0}$ FA-CoA and DHS or PHS leads to the synthesis of dihydroceramide (dhCer) or phytoceramide (phytoCer), respectively (Figure 1.8). The acylation of DHS and PHS is catalyzed by the ceramide synthase (CerS) complex in the ER; the CerS complex contains the Lac1, Lag1 and Lip1 subunits (Figure 1.8) [195-200].

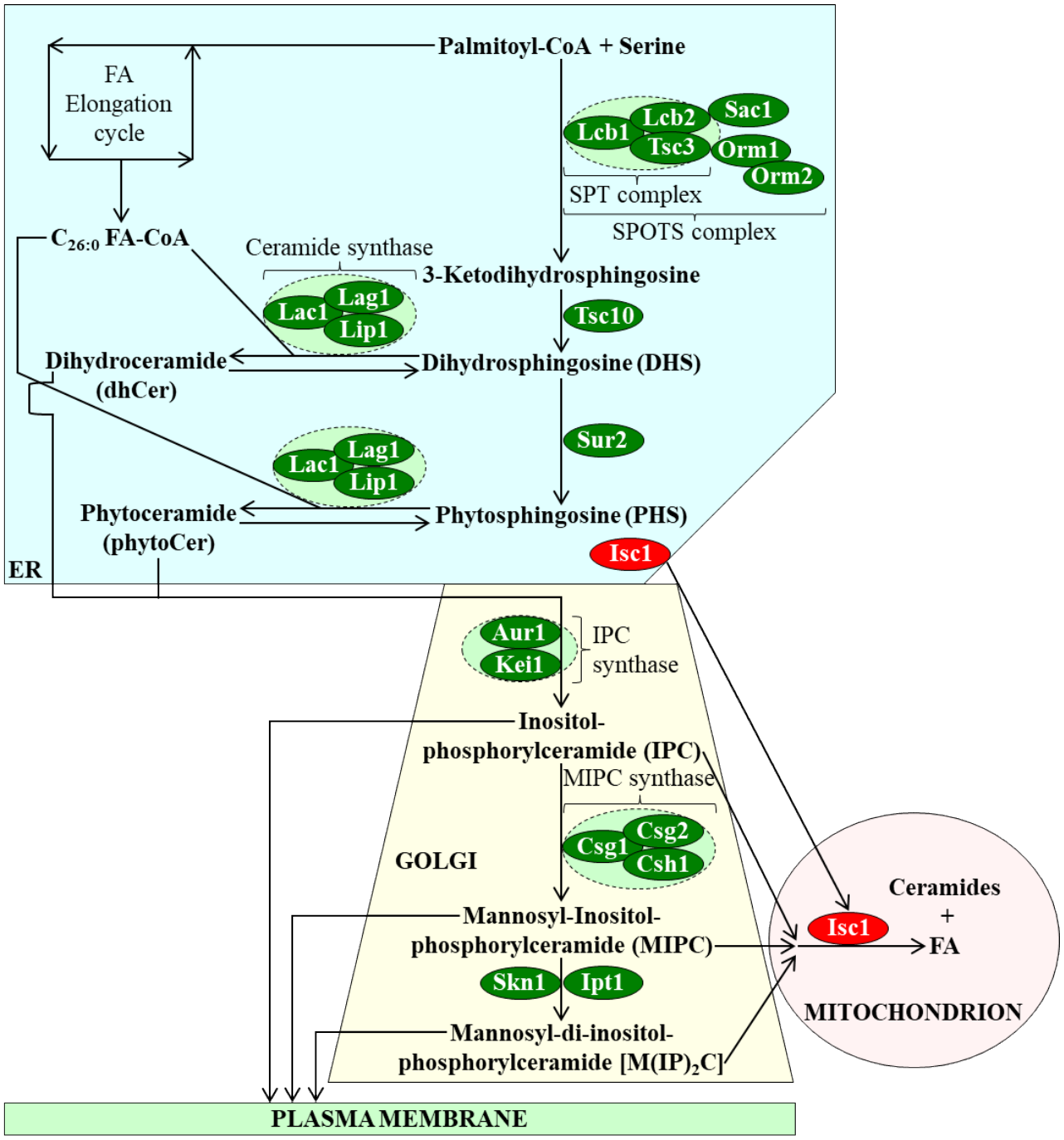

Figure 1.8. The biosynthesis of sphingolipids in the ER and Golgi apparatus and the catabolism of complex sphingolipids in mitochondria. Enzymes that catalyze reactions of sphingolipid biosynthesis are shown in green. The Isc1 enzyme, which catalyzes the hydrolysis of complex sphingolipids to regenerate ceramide, is shown in red. See the text for more details. Abbreviations: Aur1, aureobasidin A resistance 1; Csg1 and Csg2, calcium-sensitive growth 1 and

2 (respectively); Csh1, CSG1/SUR1 homolog1; ER, endoplasmic reticulum; FA, fatty acid; Ipt1, inositolphosphotransferase 1; IPC, inositol-phosphorylceramide; Isc1, inositol phosphosphingolipid phospholipase C 1; 3-KDHS, 3-ketodihydrosphingosine; Kei1, Kex2-cleavable protein essential for inositol-phosphorylceramide synthesis 1; Lac1, longevity-assurance gene cognate 1; Lag1, longevity assurance gene 1; Lip1, Lag1/Lac1 interacting protein 1; Lcb1 and Lcb2, , long-chain base proteins 1 and 2 (respectively); MIPC, mannosyl-inositol-phosphorylceramide; $M(IP)_2C$, mannosyl-di-inositol-phosphorylceramide; Orm1 and Orm2, orosomucoid 1 and 2 (respectively); PM, plasma membrane; Sac1, suppressor of actin 1; SPOTS, serine palmitoyltransferase, Orm1/2 and Sac1; SPT, serine palmitoyltransferase; Sur2, suppressor 2 of Rvs161 and rvs167 mutations; Tsc3 and Tsc10, temperature-sensitive suppressors of Csg2 mutants 3 and 10. From: Reference [83. Mitrofanova D, Dakik P, McAuley M, Medkour Y, **Mohammad K**, Titorenko VI. Lipid metabolism and transport define the longevity of the yeast Saccharomyces cerevisiae. Front Biosci (Landmark Ed). 2018; 23:1166-1194] with modifications.

After being synthesized in the ER, dhCer or phytoCer are transported to the Golgi apparatus via two different mechanisms (Figure 1.8). One mechanism involves vesicular trafficking via the coat protein complex II-coated vesicles (Figure 1.8) [201, 202]. The other mechanism is mediated by the non-vesicular transfer of dhCer or phytoCer through the ER-Golgi membrane contact sites created by the Nvj2 protein (Figure 1.8) [201, 203]. Following dhCer and phytoCer delivery to the Golgi apparatus, these ceramides undergo a series of covalent modification reactions that yield the complex sphingolipids inositol-phosphorylceramide (IPC), mannosyl-inositol-phosphorylceramide (MIPC) and mannosyl-di-inositol-phosphorylceramide [$M(IP)_2C$] (Figure 1.8) [155, 190, 204-206].

IPC, MIPC and $M(IP)_2C$ can be sorted from the Golgi apparatus to two different cellular locations. One of these locations is the PM. The vesicular transport of IPC, MIPC and $M(IP)_2C$ from the Golgi apparatus to the PM is an essential contributor to several aspects of the PM functionality (Figure 1.8) [207, 208]. The other cellular location is the mitochondrion. The Golgi apparatus-to-mitochondria transfer mechanism of IPC, MIPC and $M(IP)_2C$ in budding yeast remains unknown [207, 208]. The hydrolysis of complex sphingolipids in mitochondria is catalyzed by the Isc1 (phosphosphingolipid phospholipase C), which is sorted to mitochondria from the ER after the exponential growth of a budding yeast culture is completed (Figure 1.8)

[209-211]. The regeneration of ceramide in the Isc1-dependent reaction is essential for maintaining mitochondrial structure and function [209-211].

1.7 The maintenance of cellular lipid homeostasis contributes to longevity assurance in chronologically aging budding yeast.

This section describes growing evidence that the preservation of lipid homeostasis plays an essential role in regulating the longevity of chronologically aging budding yeast.

As outlined above, budding yeast cells cultured in a complete, nutrient-rich medium initially containing 2% glucose as the only carbon source undergo chronological aging under so-called non-CR conditions [59]. A "radical sink" mechanism has been proposed to explain the pro-longevity role of TAG biosynthesis in these cells [212, 213]. A characteristic property of budding yeast cells not limited in calorie supply is a gradual build-up of considerable TAG quantities before the yeast culture reaches the ST phase [59]. The deposition of the *de novo* synthesized TAG in LD of these cells (Figure 1.7) causes the accumulation of many enlarged LD before culture entered into the ST phase [59]. Following such entry, the lipolytic hydrolysis of the LD-deposited TAG elicits a gradual decline in TAG concentration and LD number and size [59]. Because FFA is the major product of TAG, DAG and MAG lipolysis (Figure 1.7), the bulk quantities of FFA (including the unsaturated FFA species) become available for the ER-confined biosynthesis of phospholipids that are then incorporated into cellular membranes (Figure 1.7) [166, 167].

The other characteristic property of budding yeast cells not limited in calorie supply is an aging-associated build-up of intracellular ROS and the resulting rise in the abundance of oxidatively damaged cellular macromolecules [8, 90, 95, 213]. These oxidatively damaged cellular macromolecules include both water-soluble macromolecules (i.e., DNA, RNA and hydrophilic proteins) and membrane-associated ones (i.e., hydrophobic proteins, phospholipids, FFA and other lipid classes) [97-101, 213]. Among these macromolecules, the unsaturated species of FFA are the most vulnerable to oxidative damage [97-101, 213]. An age-related rise in the oxidative damage to water-soluble and membrane-associated macromolecules accelerates the chronological aging of WT yeast cells (and WT cells of other organisms) that are not subjected to geroprotective genetic, dietary or pharmacological interventions (Figure 1.9A) [97-101, 213].

A hypothesis proposed for the "radical sink" mechanism links TAG biosynthesis to the extent of ROS-inflicted oxidative macromolecular damage in chronologically aging yeast under

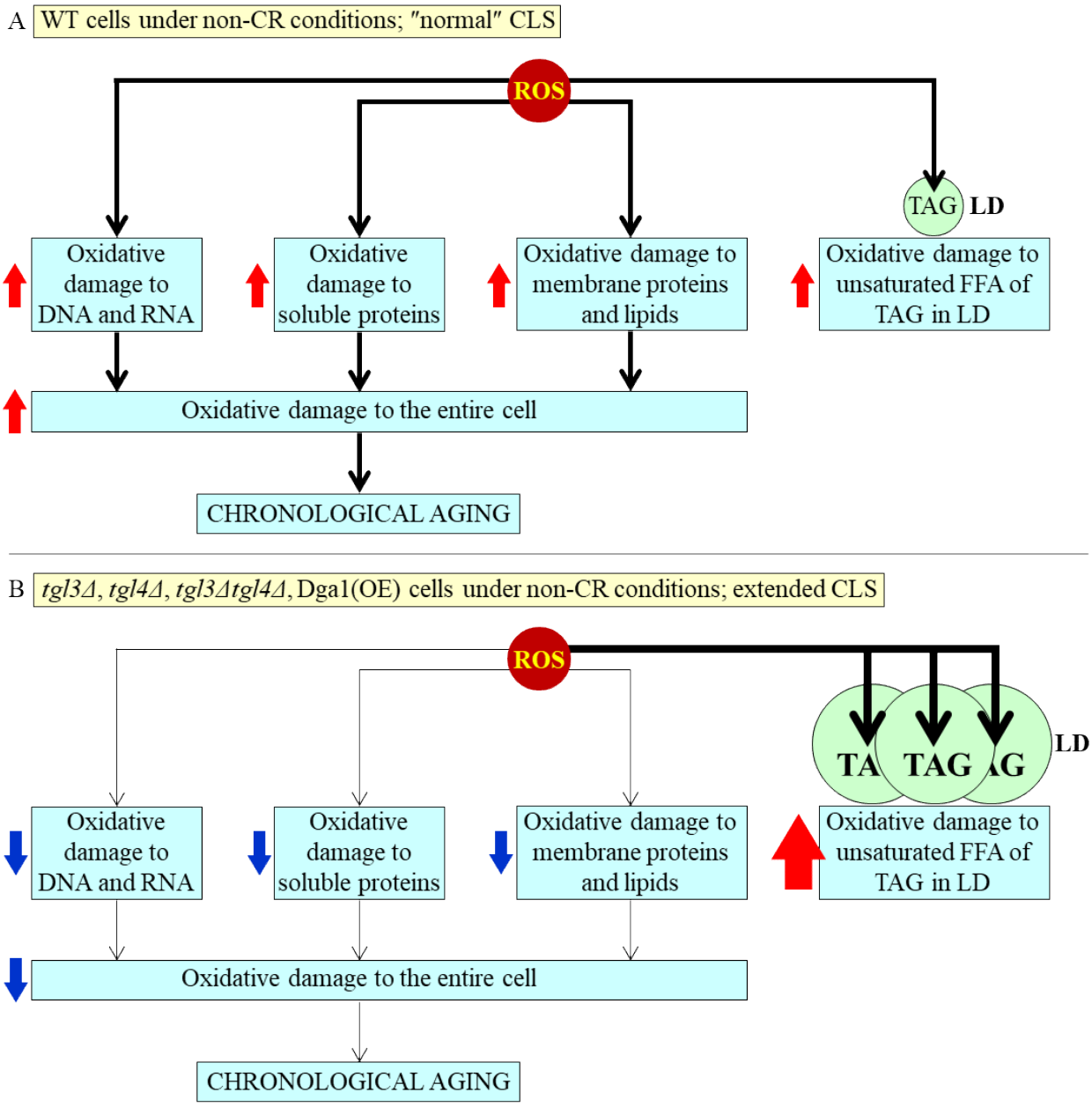

Figure 1.9. A "radical sink" mechanism links TAG biosynthesis to the extent of ROS-inflicted oxidative macromolecular damage in chronologically aging yeast not limited in calorie supply. (A) An age-related rise in the oxidative damage to water-soluble and membrane-associated macromolecules accelerates the chronological aging of WT yeast cells that are not subjected to geroprotective interventions under non-CR conditions. (B) The single-gene-deletion mutations *tgl3Δ* and *tgl4Δ*, double single-gene-deletion mutation *tgl3Δtgl4Δ*, and overexpression (OE) of the DAG acyltransferase Dga1 rise intracellular TAG and increase the CLS of budding yeast under non-CR conditions. See the text for more details. The thickness of black arrows is proportional to

the extent of the ROS-inflicted oxidative damage. Processes that are activated or suppressed are marked by the red or blue arrows (respectively) next to the boxes in which these processes are named. From: Reference [83. Mitrofanova D, Dakik P, McAuley M, Medkour Y, **Mohammad K**, Titorenko VI. Lipid metabolism and transport define the longevity of the yeast Saccharomyces cerevisiae. Front Biosci (Landmark Ed). 2018; 23:1166-1194].

CR conditions [212, 213]. This hypothesis is based on the observations that the gene-deletion mutations or gene-overexpression manipulation that increase or decrease TAG concentration alter the CLS of budding yeast not limited in calorie supply. Indeed, the single-gene-deletion mutations *tgl3Δ* and *tgl4Δ*, double single-gene-deletion mutation *tgl3Δtgl4Δ*, and overexpression of the DAG acyltransferase Dga1 rise intracellular TAG (Figure 1.7) and increase the CLS of budding yeast under non-CR conditions [212, 213]. In contrast, the double single-gene-deletion mutation *dga1Δlro1Δ* lowers intracellular TAG (Figure 1.7) and decreases the CLS of budding yeast not limited in calorie supply [212, 213].

The hypothesis of the "radical sink" mechanism posits that the genetic geroprotective interventions that raise intracellular TAG may increase the CLS of yeast because they promote the incorporation of oxidative damaged unsaturated FFA into TAG deposited in LD (Figure 1.9B) [212, 213]. According to this hypothesis, the resulting sequestration of unsaturated FFA only within the hydrophobic core of LD may decrease the extent of an aging-associated oxidative macromolecular damage in the cellular locations outside LD (Figure 1.9B) [212, 213]. The subsequent decline in oxidative damage to the entire cell may slow the chronological aging of budding yeast and extend the CLS. Critical testing of the hypothesis proposed for the "radical sink" mechanism will require assessing how the genetic geroprotective interventions that increase intracellular TAG influence the abundance of oxidatively damaged unsaturated FFA in LD and how they affect the extent of oxidative damage in the other cellular locations.

A different mechanism links longevity regulation to the metabolism of TAG, DAG and TAG-derived FFA in the ER, LD and peroxisomes of chronologically aging budding yeast (Figure 1.10) [59, 106, 107, 185, 214, 215]. Yeast cells that are not limited in calorie supply when they are cultured on 2% glucose ferment glucose to ethanol (Figure 1.10) [59]. The build-up of ethanol in yeast cultures under non-CR conditions represses the synthesis of the peroxisomal proteins Fox1, Fox2 and Fox3 (Figure 1.10) [59, 185]. Fox1, Fox2 and Fox3 catalyze peroxisomal beta-oxidation

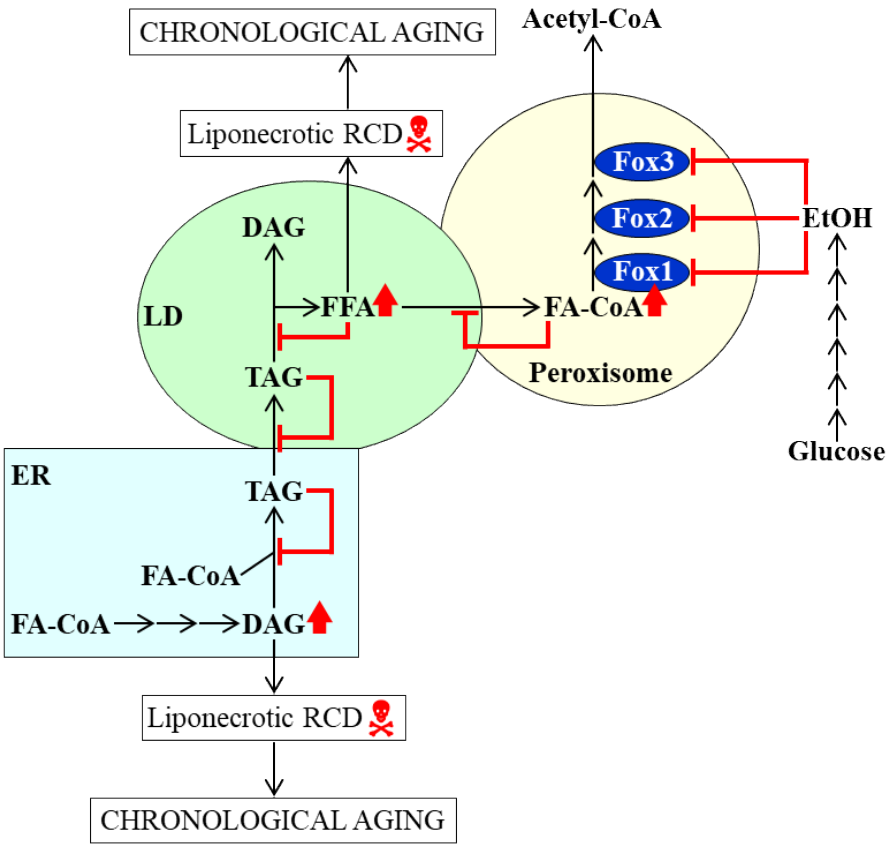

Figure 1.10. A mechanism that links chronological aging to the metabolism of TAG, DAG and TAG-derived FFA in the ER, LD and peroxisomes of budding yeast not limited in calorie supply. The build-up of ethanol in yeast cultures under non-CR conditions represses the synthesis of the peroxisomal proteins Fox1, Fox2 and Fox3. The repression of Fox1, Fox2 and Fox3 generates four consecutive negative feedback loops responsible for a distinct remodeling of lipid metabolism. The lipid metabolism remodeling under non-CR conditions causes the excessive accumulation of FFA in LD and DAG in the ER, thereby accelerating an aging-associated liponecrotic form of regulated cell death (RCD). See the text for more details. Lipid classes whose concentrations are increased in non-CR yeast are marked by red arrows next to the lipids' names. The negative feedback loops responsible for the lipid metabolism remodeling under non-CR conditions are shown as inhibition bars in red. From: Reference [83. Mitrofanova D, Dakik P, McAuley M, Medkour Y, **Mohammad K**, Titorenko VI. Lipid metabolism and transport define the longevity of the yeast Saccharomyces cerevisiae. Front Biosci (Landmark Ed). 2018; 23:1166-1194] with modifications.

of FA-CoA (Figure 1.10) [216, 217]. The ethanol-dependent repression of these enzymes' synthesis causes FA-CoA accumulation in the peroxisomes of yeast cultured under non-CR conditions (Figure 1.10) [59]. Peroxisomal FA-CoA molecules originate from FFA molecules formed in LD during TAG lipolysis (Figure 1.10). LD are known to form tight contacts with peroxisomes (Figure 1.10) [184, 185, 187]. The accumulation of FA-CoA in the peroxisomes above a threshold level inhibits the LD-to-peroxisome transport of FFA in a negative feedback manner (Figure 1.10) [59, 106, 107, 185, 214, 215]. The FFA molecules accumulate in LD and form the electron-dense arrays called "gnarls" [184, 187]. The build-up of "gnarls" suppresses TAG lipolysis in LD, thereby causing TAG accumulation there and inhibiting the ER-to-LD transport of TAG in a negative feedback fashion (Figure 1.10) [59, 106, 107, 185, 214, 215]. The resulting accumulation of TAG in the ER generates a negative feedback loop suppressing TAG synthesis from DAG in the ER (Figure 1.10) [59, 106, 107, 185, 214, 215].

The described above remodeling of TAG, DAG and FFA metabolism in remodeling of TAG, DAG and FFA metabolism elicits the excessive accumulation of FFA in LD and DAG in the ER (Figure 1.10) [59, 106, 107, 185, 214, 215]. FFA and DAG are known to accelerate the onset of an aging-associated form of regulated cell death (RCD) called liponecrosis (Figure 1.10) [106, 107]. The accelerated onset of liponecrosis shortens the longevity of chronologically aging budding yeast not limited in calorie supply (Figure 1.10).

The above pro-aging remodeling of TAG, DAG and FFA metabolism does not occur in budding yeast cultures under CR conditions on 0.2% or 0.5% glucose. In these cultures, ethanol does not accumulate in the quantities sufficient to initiate such distinct remodeling of lipid metabolism [59, 106, 107, 185, 214, 215].

Genetic and pharmacological interventions that target some steps of sphingolipid metabolism prolong the longevity of chronologically aging budding yeast.

The genetic geroprotective interventions altering sphingolipid metabolism include the single-gene-deletion mutations *ipt1Δ* and *skn1Δ* and the double single-gene-deletion mutation *ipt1Δskn1Δ* [218, 219]. All these genetic interventions extend the longevity of chronologically aging yeast and make yeast more resistant to oxidative stress [218]. Of note, Ipt1 and Skn1b are inositolphosphotransferases that catalyze the conversion of MIPC into $M(IP)_2C$ (Figure 1.8) [220, 221]. Therefore, the *ipt1Δ*, *skn1Δ* and *ipt1Δskn1Δ* mutations increase intracellular MIPC and decrease intracellular $M(IP)_2C$ [218]. It is conceivable that the complex sphingolipid MIPC

increases the resistance of budding yeast cells to oxidative stress and slows their chronological aging [218]. It is also plausible that the complex sphingolipid $M(IP)_2C$ makes budding yeast cells less resistant to oxidative stress and accelerates and accelerates their chronological aging [218]. Further studies are required to clarify this issue.

Some genetic and pharmacological geroprotectors target a different step of sphingolipid metabolism, namely the initial, SPT protein complex-dependent step of sphingolipid biosynthesis *de novo* (Figure 1.8). A tetracycline-repressible promoter cassette was used to down-regulate transcription of genes for the Lcb1 or Lcb2 subunit of the SPT complex [222]. Low doses of the SPT inhibitor myriocin were used to reduce the enzymatic activity of SPT [222]. Noteworthy, the conditions for exposing yeast cells to the above genetic or pharmacological intervention were optimized to achieve an only partial (not complete) weakening of sphingolipid biosynthesis *de novo* [222]. The exposure of budding yeast to each of these interventions decreased DHS, PHS, and IPC concentrations, made yeast more resistant to the temperature and oxidative stress, and prolonged the longevity of chronologically aging yeast [222]. The longevity-extending effects of both interventions were likely due to their abilities to weaken the activating phosphorylation of the pro-aging protein kinase Sch9 by the sphingolipid-stimulated protein kinases Pkh1 and Pkh2 (Pkb-activating kinase homolog proteins 1 and 2) [222]. Sphingolipid binding to Pkh1 and Pkh2 stimulates both these pro-aging protein kinases [190, 206, 223-225]. Therefore, it was suggested that in WT cells not exposed to geroprotectors, sphingolipids limit yeast longevity because they stimulate the pro-aging Pkh1/2-Sch9 signaling pathway [222]. This pathway is known to inhibit the pro-longevity processes of mitochondrial respiration, mitochondrial protein synthesis and genome stability maintenance [226-229]. The Pkh1/2-Sch9 signaling pathway also activates the pro-aging process of protein synthesis in the cytosol [128, 208].

In sum, the above examples provide strong evidence that the maintenance of cellular lipid homeostasis is an essential contributor to longevity assurance of chronologically aging budding yeast. The Titorenko laboratory has discovered geroprotective plant extracts that substantially extend the longevity of chronologically aging budding yeast [138, 230]. Some of these geroprotective plant extracts accelerate an aging-associated degradation of TAG deposited in LD [230]. It would be interesting to investigate how these geroprotectors of plant origin influence the intracellular concentrations of other lipid classes during the chronological aging of *S. cerevisiae*.

1.8 Some intracellular and extracellular water-soluble metabolites are essential contributors to longevity regulation in chronologically aging budding yeast.

This section focuses on emerging evidence that the intracellular and extracellular concentrations of some water-soluble metabolites play essential roles in regulating the longevity of chronologically aging *S. cerevisiae*. A common scenario for the longevity-defining action of these metabolites is the following. Proteins capable of detecting the age-related changes in the concentrations of specific water-soluble metabolites bind to these metabolites and alter their functional states [8, 32, 33, 39, 95, 108, 188, 231-238]. After undergoing the alterations in functionality, these metabolite-sensing proteins extend or shorten yeast CLS by changing the pace of certain longevity-defining cellular processes [8, 32, 33, 39, 95, 108, 188, 231-238].

The Zwf1- and Gnd1-catalyzed reactions of the cytosolic pentose phosphate pathway and the mitochondrial Ald4-, Pos5-, Mae1- and Idp1-dependent reactions produce nicotinamide adenine dinucleotide phosphate hydride (NADPH) within budding yeast cells [8, 60]. NADPH is the primary source of reducing equivalents for synthesizing amino acids, FFA and sterol lipids [60, 239]. Therefore, NADPH supports the growth and survival of *S. cerevisiae* under any laboratory or environmental conditions [60, 239]. As an electron donor for thioredoxin and glutathione reductase systems, NADPH is an essential and specific contributor to longevity assurance in chronologically aging budding yeast cells [240, 241]. The essential and specific contribution of NADPH to longevity assurance is due to the ability of the NADPH-dependent thioredoxin and glutathione reductase systems to reduce oxidative damage to the thiol-containing proteins found within the cytosol, nucleus and mitochondria of chronologically aging *S. cerevisiae* [240, 241]. This ability of both NADPH-dependent reductase systems plays an essential role in decelerating budding yeast's chronological aging (Figure 1.11A) [241].

Glucose fermentation in the cytosol of budding yeast produces several metabolites, including glycerol [60]. The intracellular and extracellular glycerol is a potent geroprotective metabolite in chronologically aging *S. cerevisiae* [32, 242]. A rise in glucose fermentation to glycerol weakens the glucose-to-ethanol and glucose-to-acetic acid types of fermentation [32, 242]. Because both ethanol and acetic acid increase the pace of chronological aging in budding yeast [32, 59], a re-direction of metabolite flow into glucose-to-glycerol fermentation has a geroprotective effect in chronologically aging *S. cerevisiae* (Figure 1.11B) [242]. Furthermore, glycerol makes budding yeast more resistant to chronic (long-term) oxidative, thermal and osmotic

stresses; the mechanism underlying the glycerol-dependent increase in stress resistance of *S. cerevisiae* remains unknown [242]. Since an enhancement of cell resistance to chronic stresses is geroprotective [6, 8], a rise in the intracellular and extracellular glycerol extends the CLS of budding yeast (Figure 1.11B) [242]. Moreover, a re-direction of metabolite flow into the glucose-to-glycerol fermentation increases intracellular nicotinamide adenine dinucleotide (NAD^+) and raises the intracellular NAD^+/NADH ratio [242]. Given that both these changes in NAD^+ and NAD^+/NADH ratio are characteristic features of a pro-longevity cellular pattern in chronologically aging budding yeast [8, 242], the re-channeling of metabolite flow into the glucose-to-glycerol fermentation prolongs yeast CLS (Figure 1.11B) [242].

The non-reducing disaccharide trehalose is synthesized from glucose [243]. Besides being a storage form of glucose for energy production [243], trehalose exhibits two specific effects on the pace of chronological aging in *S. cerevisiae* [59, 68, 79, 244-248]. Trehalose influences yeast chronological aging because this disaccharide can use its ability to interact with unfolded portions of proteins to regulate the longevity-defining process of cellular proteostasis. The effects of trehalose on cellular proteostasis and budding yeast's longevity in proliferating cells differ from those in non-proliferating cells. In chronologically "young" yeast cells that grow and divide, trehalose interacts with newly synthesized, partially unfolded proteins [59, 79, 249, 250]. This interaction of trehalose promotes cellular proteostasis and creates an anti-aging cellular pattern because it reduces the misfolding and aggregation of the newly synthesized proteins interacting with trehalose (Figure 1.11C) [59, 79, 249, 250]. In chronologically "old" yeast cells that ceased growth and division, trehalose interacts with hydrophobic side chain amino acids in the exposed domains of partially folded and unfolded proteins [59, 79, 249]. This interaction of trehalose weakens cellular proteostasis and generates a pro-aging cellular pattern since it prevents the binding of molecular chaperones to the exposed protein domains enriched in hydrophobic side chain amino acids (Figure 1.11C) [59, 79, 249].

The respiration in mitochondria and β-oxidation of fatty acids in peroxisomes of chronologically aging budding yeast generate H_2O_2 as a by-product of these processes [91, 186]. Following H_2O_2 release from mitochondria and peroxisomes, this ROS molecule may create either pro-aging or pro-longevity cellular pattern in an H_2O_2 concentration-dependent manner [14, 186, 215, 252]. If H_2O_2 concentration in chronologically aging yeast is above a toxic threshold, H_2O_2 causes oxidative damage to cellular macromolecules in different cellular locations [91, 186, 215,

252]. The H_2O_2-inflicted oxidative macromolecular damage generates a pro-aging cellular pattern and shortens the CLS of budding yeast [91, 186, 215, 252]. If H_2O_2 concentration in chronologically aging yeast is below a toxic threshold, this ROS molecule elicits a "hormetic" response because it stimulates at least two pro-longevity signaling pathways. The H_2O_2-stimulated signaling pathways create a pro-longevity cellular pattern and extend yeast CLS [6, 8, 188]. In one of these pathways, the "hormetic" concentrations of H_2O_2 promote the expression of many genes by the transcription factors Gis1, Msn2 and Msn4 (Figure 1.11D) [252-254]. Protein products of these genes have been implicated in nutrient sensing, stress response, metabolism, autophagy and cell cycle regulation [252-254]. In the other H_2O_2-stimulated signaling pathway, an H_2O_2-sensitive cascade of the protein kinases Tel1 and Rad53 inhibits the pro-aging process in which the histone demethylase Rph1 promotes transcription of sub-telomeric chromatin regions (Figure 1.11D) [255, 256].

Some intermediates of the tricarboxylic acid (TCA) cycle are used as the substrates to synthesize the amino acids aspartate, asparagine, glutamate and glutamine in mitochondria of chronologically aging budding yeast [60, 239]. After these amino acids exit mitochondria, they stimulate the protein kinase activity of the pro-aging protein complex TORC1 (Figure 1.11E) [219, 257-259]. TORC1 phosphorylates and activates or inhibits three proteins that define the pace of yeast chronological aging. The cellular targets of TORC1 include Sch9, Tap42 and Atg13 (Figure 1.11E). The TORC1-dependent phosphorylation of Sch9 activates its protein kinase activity [258, 259]. Active Sch9 stimulates the pro-aging process of protein synthesis in the cytosol because it accelerates both the assembly of cytosolic ribosomes and translation initiation of cytosolic mRNAs (Figure 1.11E) [260-263]. Furthermore, active Sch9 suppresses the anti-aging process of mitochondrial protein synthesis (Figure 1.11E) [87, 88, 258, 259]. Moreover, active Sch9 decelerates the anti-aging process of nuclear import of the protein kinase Rim15; the presence of Rim15 in the nucleus is required for the Rim15-driven activating phosphorylation of the transcription factors Gis1, Msn2 and Msn4 (Figure 1.11E) [127, 264, 265]. The TORC1-driven phosphorylation of Tap42 promotes the pro-aging process of protein synthesis in the cytosol (Figure 1.11E); Tap42 is an essential contributor to ribosome assembly and mRNA translation initiation in the cytosol [261, 266]. The TORC1-dependent phosphorylation of the autophagy-initiating protein Atg13 down-regulates the anti-aging process of autophagy because it weakens autophagosome formation in the cytosol (Figure 1.11E) [267-271]. In sum, aspartate, asparagine,

glutamate and glutamine initiate a cascade of signaling events generating a pro-aging cellular pattern.

Two mechanisms have been proposed to explain why the amino acid methionine can accelerate budding yeast's chronological aging. In one mechanism, methionine up-regulates the methylation of cytosolic tRNAs, thus reducing the abundance of non-methylated tRNAs in the cytosol (Figure 1.11F) [278]. The cytosolic non-methylated tRNAs are essential for importing the Rtg1/Rtg2/Rtg3 heterotrimeric transcription factor to the nucleus [278]. In the nucleus, the Rtg1/Rtg2/Rtg3 heterotrimer activates transcription of many genes involved in longevity assurance of chronologically aging yeast [278]. Thus, methionine contributes to establishing a pro-aging cellular pattern because it lowers non-methylated tRNAs in the cytosol of chronologically aging yeast (Figure 1.11F). In the other mechanism, methionine suppresses the pro-aging process of autophagy because it inhibits autophagosome formation in a TORC1-dependent and TORC1-independent fashion (Figure 1.11F) [279]. Of note, the methionine-dependent suppression of autophagy has been shown to coincide with a decline in vacuole acidity and acetic acid accumulation in the extracellular medium [279]. As discussed below, extracellular acetic acid accumulation accelerates chronological aging in budding yeast [32]. The relative contributions of the methionine-dependent autophagy suppression and extracellular acetic acid accumulation to the methionine-driven aging acceleration remain unknown [279-281].

Spermidine is a polyamine synthesized from the amino acids arginine and methionine in the chemical reactions taking place in mitochondria, the cytosol and peroxisomes of budding yeast [16]. Spermidine is a potent geroprotective metabolite that slows the chronological aging of *S. cerevisiae* [16, 134, 282]. This polyamine inhibits the histone acetyltransferases Iki3 and Sas3, thus suppressing histone H3 acetylation at the promoters of most genes other than the autophagy-related (ATG) ones [134]. Transcription of these non-ATG genes is down-regulated in yeast treated with spermidine [134]. The effects of spermidine on histone H3 acetylation at the promoters of the ATG genes and their transcription are different. Namely, histone H3 acetylation at these promoters and ATG gene transcription are activated in spermidine-treated yeast (Figure 1.11G) [134]. The resulting enhancement of the autophagic degradation of dysfunctional macromolecules and organelles is responsible for spermidine's geroprotective action (Figure 1.11G) [16, 134, 282].

Hydrogen sulfide (H_2S) is a gas soluble in water and cellular membranes [283]. Budding yeast can produce H_2S either via the assimilation of exogenous inorganic sulfate or via the

transsulfuration pathway of sulfur transfer from methionine to cysteine [284]. The synthesis of H_2S via the transsulfuration pathway is stimulated in budding yeast cells cultured under CR conditions on 0.5% glucose [285]. Moreover, exogenous H_2S donors act as CR-mimetics in budding yeast. They extend the CLS of yeast cells cultured under non-CR conditions on 2% glucose [285]. Therefore, it was concluded that H_2S is a metabolite responsible for the geroprotective effect of the CR diet in budding yeast [285]. It was hypothesized that H_2S slows the chronological aging of budding yeast in part because it stimulates the mitochondrial electron transport chain to protect cells from age-related stress and damage (Figure 1.11H) [285]. The other mechanism that may underlie the geroprotective action of H_2S in calorically restricted yeast is the H_2S-dependent up-regulation of transcription of the nuclear genes whose protein products protect the cell from various stresses associated with aging (Figure 1.11H) [285].

Glucose fermentation in budding yeast yields several metabolite products, including acetic acid [6, 32, 60]. The Ald6- and Ald4-catalyzed reactions in the cytosol and mitochondria (respectively) produce acetic acid in the yeast cell [8]. The accumulation of acetic acid in the extracellular medium or inside the cell accelerates the chronological aging of budding yeast [32, 231]. The acetic acid-dependent acidification of the extracellular medium or the accumulation of acetic acid inside the cell triggers apoptotic regulated cell death (RCD) [32, 33, 39, 108, 231, 232]. It was therefore proposed that the build-up of acetic acid inside or outside of chronologically "old" yeast may promote an aging-associated form of apoptotic RCD (Figure 1.11I) [32, 33, 39, 108, 231, 232]. Furthermore, it is believed that the acetic acid-dependent intracellular acidification may accelerate yeast chronological aging because it up-regulates the cAMP/PKA signaling pathway; this pathway activates several pro-aging cellular processes and suppresses several pro-longevity cellular processes (Figure 1.11I) [6, 8, 39, 231]. The other possible pro-aging effects of the acetic acid-driven intracellular acidification include a rise in intracellular ROS and ROS-inflicted oxidative macromolecular damage, as well as amplified cellular stress of inefficient DNA replication (Figure 1.11I) [6, 8, 39, 231]. Moreover, after intracellular acetic acid is transported into the nucleus, it is transformed into acetyl-CoA in the reaction catalyzed by Acs2 [233-236]. Acetyl-CoA in the nucleus elicits histone H3 hyperacetylation at the ATG gene promoters, thereby down-regulating the anti-aging process of autophagy and shortening the CLS of budding yeast (Figure 1.11I) [233-236]. Of note, none of the above effects of acetic acid on the CLS of budding yeast and longevity-defining cellular processes can be elicited by other organic acids found in

yeast cultures, exogenous hydrochloric acid or the conjugate base of acetic acid added at neutral pH [32]. Therefore, it was concluded these effects are due to both the chemical structure of acetic acid and culture medium acidification it causes [32].

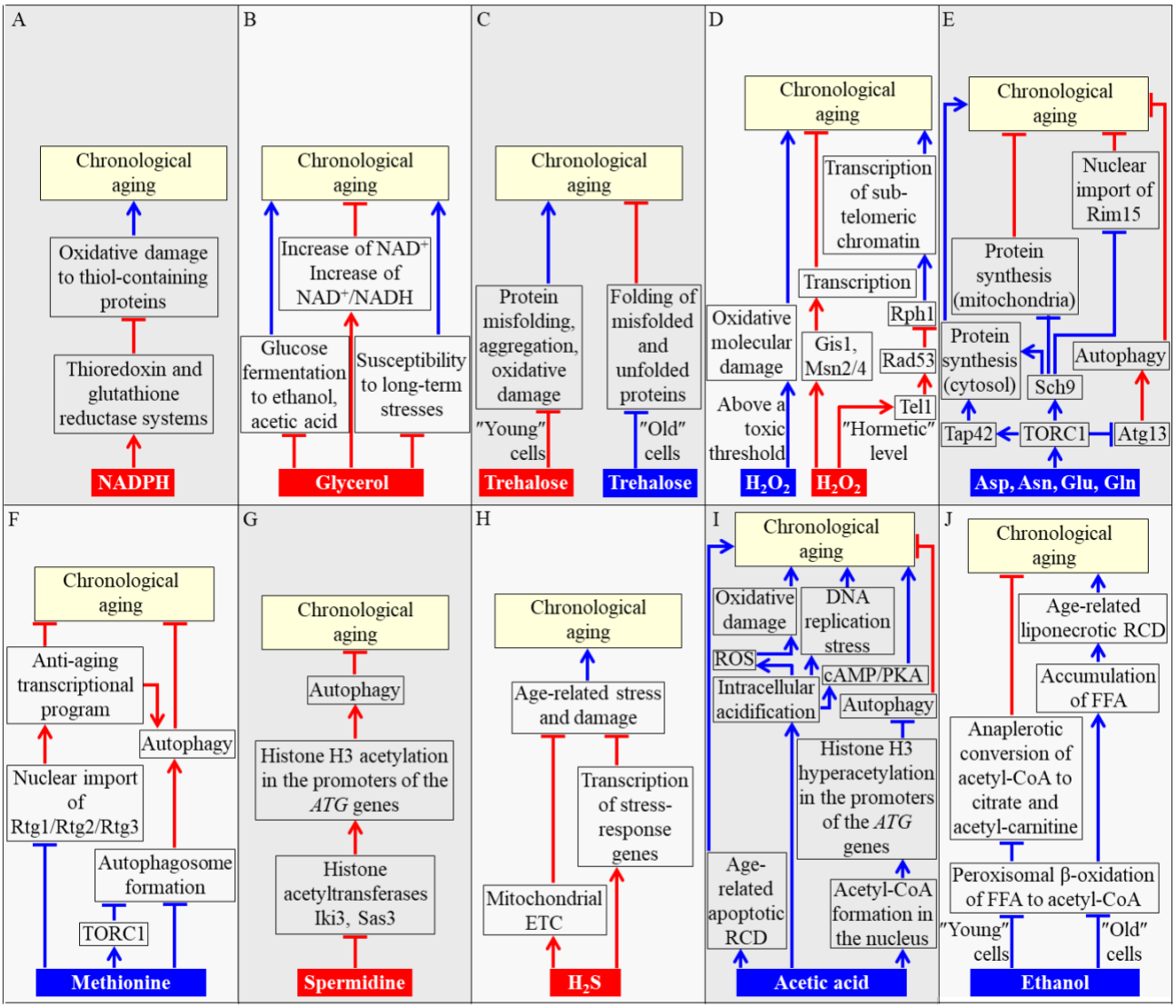

Figure 1.11. Some water-soluble metabolites are essential contributors to longevity regulation in chronologically aging budding yeast. Proteins capable of detecting the age-related changes in the concentrations of specific water-soluble metabolites bind to these metabolites and alter their functional states. After undergoing the alterations in functionality, these metabolite-sensing proteins extend or shorten yeast CLS by changing the pace of specific longevity-defining cellular processes. See the text for more details. Metabolites that slow yeast chronological aging are shown in red color. Metabolites that accelerate yeast chronological aging are shown in blue

color. Cellular processes that delay yeast chronological aging are marked by red activation arrows or inhibition bars. Cellular processes that accelerate yeast chronological aging are marked by blue activation arrows or inhibition bars. Abbreviations: Asp, aspartate; Asn, asparagine; ATG, autophagy-related genes; ETC, electron transport chain; FFA, free (non-esterified) fatty acids; DAG, diacylglycerol; Glu, glutamate; Gln, glutamine; PKA, protein kinase A; RCD, regulated cell death; ROS, reactive oxygen species. From: Reference [238. **Mohammad K**, Dakik P, Medkour Y, McAuley M, Mitrofanova D, Titorenko VI. Some Metabolites Act as Second Messengers in Yeast Chronological Aging. Int J Mol Sci. 2018; 19: 860] with modifications.

Ethanol is one of the glucose fermentation products in budding yeast [6, 8, 24, 31, 60]. The Adh1-dependent reaction in the cytosol generates ethanol in the yeast cell [6, 8, 24, 31, 60]. Ethanol accelerates the chronological aging of budding yeast [8, 59, 186, 229]. The aging-accelerating effect of ethanol is due to its ability to inhibit the β-oxidation of FFA to acetyl-CoA [59, 186]. The ethanol-dependent inhibition of this process decreases intracellular acetyl-CoA and increases intracellular FFA concentrations [59, 186]. The ethanol-inflicted decline in acetyl-CoA concentration within peroxisomes of chronologically "young" yeast slows the acetyl-CoA-to-citrate and acetyl-CoA-to-acetyl-carnitine conversion reactions that occur in these organelles (Figure 1.11J) [59, 186]. Peroxisomally produced citrate and acetyl-carnitine are used to replenish their pools in mitochondria [59, 186]. Therefore, the ethanol-dependent decrease in citrate and acetyl-carnitine availability to mitochondria of chronologically "young" yeast weakens mitochondrial functionality and creates a pro-aging cellular pattern in these cells (Figure 1.11J) [59, 186]. The ethanol-driven rise in FFA concentration within peroxisomes of chronologically "old" yeast promotes an aging-associated form of liponecrotic RCD, thereby shortening the CLS of budding yeast (Figure 1.11J) [8, 59, 106, 107, 186, 286].

Altogether, the above examples support the notion that some water-soluble metabolites play essential roles in regulating the longevity of chronologically aging budding yeast. It would be interesting to use the quantitative mass spectrometry-based metabolomics to assess how various dietary, genetic and pharmacological geroprotectors influence the entire water-soluble metabolome of *S. cerevisiae* at different stages of the chronological aging process. It would also be interesting to compare the effects of different geroprotectors on the water-soluble metabolome of chronologically aging budding yeast.

1.9 Thesis outline and contributions of colleagues.

Chapter 1 of my Thesis provides an overview of the use of budding yeast as a model organism in the research on aging, replicative and chronological modes of budding yeast's aging, mechanisms linking chronological aging to a cellular quiescence program in budding yeast, mechanisms by which some geroprotective phytochemicals extend the longevity of chronologically aging budding yeast, mechanisms underlying the delay of budding yeast's chronological aging by LCA, integration of lipid metabolism in various cellular compartments of budding yeast, contribution of cellular lipid homeostasis maintenance to the longevity regulation in budding yeast, and mechanisms through which some water-soluble metabolites define the pace of chronological aging in budding yeast. Dr. Titorenko edited the first draft of the Chapter 1 text that I wrote for my Thesis.

Chapter 2 of my Thesis outlines the materials and methods used in the studies described here. These Materials and Methods chapter includes the names and descriptions of yeast strains used, growth media and cell culturing conditions, a method for mass spectrometric identification and quantitation of cellular lipids using the direct-injection lipidomic analysis, chronological lifespan assay, statistical analyses methods, an LC-MS/MS method for the identification and quantitation of cellular lipids, a procedure for the Percoll density gradient centrifugation to separate high-density and low-density Q cells for lipid extraction, cell quenching method for extracting water-soluble metabolites, a procedure for fluorescence microscopy, extraction of water-soluble metabolites from quenched cells, a method for LC-MS/MS analysis of extracted water-soluble metabolites, and a protocol for metabolite identification and quantitation using the LC-MS/MS raw data.

Chapter 3 of my Thesis describes how the ethanol/water extract from *Salix alba's* bark, called PE21, affects budding yeast's cellular lipidome. Vicky Lutchman and Pamela Dakik performed a screen of extracts from the plants traditionally used in Chinese herbal medicines or present in the Mediterranean diet. They discovered that many of them (including PE21) delay the chronological aging of budding yeast. The geroprotective effect of PE21 exceeded those of currently known aging-delaying chemicals. Amanda Piano found that PE21 elicits several significant age-related changes in budding yeast. One of these changes is a prompt decline in the abundance of the neutral lipids TAG and ergosterol stored in LPD. Because the maintenance of

lipid homeostasis in budding yeast affects several lipid classes, I hypothesized that PE21 might alter the intracellular concentrations of other lipid classes as well. To test this hypothesis, I used tandem mass spectrometry (MS/MS) to identify and quantitate cellular lipids using a direct-injection method of lipidomic analysis.

Chapter 4 of my Thesis describes the development of novel liquid chromatography coupled to tandem mass spectrometry (LC-MS/MS method for the quantitative analysis of the entire cellular lipidome of budding yeast. The limitations of the LC-MS/MS methods presently used for his purpose are that they are not sufficiently robust, sensitive and versatile. Based on the currently employed LC-MS/MS lipidomic procedures, I developed a novel method for analyzing budding yeast's lipidome using LC-MS/MS. The technical details of the novel method are provided in sections 2.2 and 2.8 of my Thesis. In chapter 4, I described the advantageous features of the novel method. These features include the high efficiency of lipid extraction, versatility and robustness, sensitivity, ability to distinguish between isobaric and isomeric lipid species, use of alternative mobile phase additives to enhance ionization of all lipid classes, and increased efficiencies of two different types of precursor ions fragmentation processes. I compared these features of the novel LC-MS/MS lipidomics method to the corresponding features of the currently employed methods for LC-MS/MS lipidomics. Dr. Heng Jiang and Md Israil Hossain have assisted me in performing some experiments.

As I mentioned in the Introduction chapter of my Thesis, the robust geroprotective diet CR decreases TAG concentration and increases CL concentration in HD and LD cells of the WT strain throughout chronological aging. As I indicated in the Introduction chapter, a population of HD cells includes both Q and NQ cells. The percentage of NQ cells in the HD population slowly rises during chronological aging. As I alluded to in the Introduction chapter, a population of LD cells also includes both Q and NQ cells. The percentage of NQ cells in the LD population rapidly rises during chronological aging. Therefore, the first objective of the studies described in chapter 5 of my Thesis was to assess the effect of CR on the intracellular concentrations of all lipid classes (not only TAG and CL) within HD and LD cell populations of the WT strain recovered at different stages of chronological aging. To accomplish this objective, we (Emmanuel Orfanos and I) purified HD and LD cells from WT yeast taken on different days of culturing under CR or non-CR conditions; the purification of HD and LD cells was performed using Percoll density gradient centrifugation. We then employed the novel LC-MS/MS lipidomics method (see Chapter 4) to

conduct quantitative lipidomics of the recovered HD and LD cell populations. The second objective of the studies described in chapter 5 of my Thesis was to conduct a comparative analysis of how CR and two other geroprotective interventions (namely, the *tor1Δ* mutation and LCA) affect the lipidomes of HD and LD cells recovered at different stages of chronological aging. To accomplish this objective, we (Emmanuel Orfanos and I) used LC-MS/MS to identify and quantify the lipidomes of HD and LD cells in the WT and *tor1Δ* strains of budding yeast cultured under the conditions described under CR or non-CR conditions with or without LCA.

My research interests include the mechanisms through which the intracellular and extracellular water-soluble metabolites contribute to longevity regulation in chronologically aging budding yeast. A robust, versatile and sensitive LC-MS/MS method for identifying and quantitating water-soluble metabolites is required to dissect such mechanisms. Significant advances have recently been made in employing the LC-MS/MS methods of non-targeted metabolomics to analyze the water-soluble metabolomes of cells and tissues quantitatively. Yet, the presently used LC-MS/MS metabolomics methods have several limitations. Using some of the currently employed LC-MS/MS metabolomics procedures as prototypes, I developed a novel method for the quantitative analysis of budding yeast's water-soluble metabolome using LC-MS/MS. Sections 2.3, 2.4, 2.10, 2.12-2.14 provided the technical details of the novel LC-MS/MS metabolomics method. Chapter 6 of my Thesis focuses on several important advantages offered by the LC-MS/MS metabolomics method I developed.

A body of evidence indicates that metabolism is an essential contributor to the aging and longevity of eukaryotic organisms across phyla. Based on numerous findings, the existence of a metabolic "clock," "signature," "footprint" or "profile" of aging delay has been proposed. It remained unclear if different dietary, genetic and pharmacological anti-aging interventions set up a similar metabolic pattern of aging delay or each of them generates a distinct metabolic profile. In the studies described in chapter 7 of my Thesis, I used non-targeted metabolomics of chronologically aging budding yeast to clarify this issue. I show that three different geroprotectors (i.e., CR, the *tor1Δ* mutation and LCA) create distinct metabolic profiles. I identified a unique metabolic pattern established by one of these geroprotectors.

Chapter 2: Materials and Methods.

2.1 Strains, medium and culture conditions for the direct-injection lipidomic analysis of yeast treated with PE21 or remained untreated.

The wild-type (WT) strain *Saccharomyces cerevisiae* BY4742 (*MATα his3Δ1 leu2Δ0 lys2Δ0 ura3Δ0*) and single-gene-deletion mutant strains in the BY4742 genetic background (all from Thermo Scientific/Open Biosystems) were used. The yeast cells were cultured in a synthetic minimal YNB medium (0.67% (w/v) Yeast Nitrogen Base without amino acids from Fisher Scientific; #DF0919-15-3). The medium was supplemented with 2% (w/v) glucose (#D16-10; Fisher Scientific), 20 mg/l *L*-histidine (#H8125; Sigma), 30 mg/l *L*-leucine (#L8912; Sigma), 30 mg/l *L*-lysine (#L5501; Sigma) and 20 mg/l uracil (#U0750; Sigma). The yeast cells were cultured in the presence or absence of PE21 (Idunn Technologies Inc.), an ethanol/water extract from *Salix alba's* bark [230].

A final concentration of PE21 in the culturing medium was 0.1% (w/v). At this concentration, PE21 has the most significant extending effect on both the mean and maximum CLS of WT strain in a medium supplemented with 2% (w/v) glucose [230]. A 20% (w/v) stock solution of PE21 in ethanol was made immediately before adding it to the culturing medium. The yeast cells were inoculated into the medium first. A 20% (w/v) aqueous stock solution of glucose was then added to the culturing medium to have a final glucose concentration at 2% (w/v). The medium was then supplemented with a volume of the 20% (w/v) stock solution of PE21 in ethanol needed to have a final PE21 concentration in the medium at 0.1% (w/v). Ethanol was used as a vehicle for delivering PE21 to the cells; a final ethanol concentration in the culturing medium was 0.5% (v/v). The ethanol-mock treated cell cultures were supplemented with 2% (w/v) glucose and 0.5% (v/v) ethanol.

Cell culturing with rotational shaking at 200 rpm was conducted at 30^{o}C. The cells were cultured in Erlenmeyer flasks. A "flask volume/medium volume" ratio was 5:1.

2.2 Strain, medium and culture conditions used to develop the LC-MS/MS method for quantitative lipidomic analysis of yeast cells.

The WT strain *S. cerevisiae* BY4742 (*MATα his3Δ1 leu2Δ0 lys2Δ0 ura3Δ0*) from Thermo

Scientific/Open Biosystems was used. The yeast cells were cultured in the synthetic minimal YNB medium (0.67% (w/v) Yeast Nitrogen Base without amino acids from Fisher Scientific; #DF0919-15-3). The medium was supplemented with 2% (w/v) glucose (#D16-10; Fisher Scientific), 20 mg/l *L*-histidine (# H8125; Sigma), 30 mg/l *L*-leucine (#L8912; Sigma), 30 mg/l *L*-lysine (#L5501; Sigma) and 20 mg/l uracil (#U0750; Sigma).

Cell culturing with rotational shaking at 200 rpm was performed for 24 h at 30°C. The cells were cultured in Erlenmeyer flasks. A "flask volume/medium volume" ratio was 5:1.

2.3 Strain, medium and culture conditions used to develop the LC-MS/MS method for non-targeted metabolomic analysis of yeast cells.

The WT strain *S. cerevisiae* BY4742 (*MATα his3Δ1 leu2Δ0 lys2Δ0 ura3Δ0*) from Thermo Scientific/Open Biosystems was used. The yeast cells were cultured in a nutrient-rich YP medium (1% [w/v] yeast extract [#BP1422-2; Fisher Scientific] and 2% [w/v] peptone [#BP1420-2, Fisher Scientific]. The medium was supplemented with 2% (w/v) glucose (#D16-10; Fisher Scientific) as a sole source of carbon.

Cell culturing with rotational shaking at 200 rpm was carried out at 30°C. The cells were cultured in Erlenmeyer flasks. A "flask volume/medium volume" ratio was 5:1.

2.4 Yeast strains, media and growth conditions used to compare the effects of different geroprotectors on the intracellular metabolome of yeast.

The WT strain *S. cerevisiae* BY4742 (*MATα his3Δ1 leu2Δ0 lys2Δ0 ura3Δ0*) from Thermo Scientific/Open Biosystems was used. The yeast cells were cultured in a nutrient-rich YP medium (1% [w/v] yeast extract [#BP1422-2; Fisher Scientific] and 2% [w/v] peptone [#BP1420-2, Fisher Scientific]. The medium was supplemented with 2% (w/v) glucose (#D16-10; Fisher Scientific) as a sole carbon source, 0.2% (w/v) glucose as the only source of carbon, or 0.2% (w/v) glucose as a carbon source and 50 μM LCA.

The *tor1Δ* single-gene-deletion mutant strain in the BY4742 genetic background (Thermo Scientific/Open Biosystems) was also used. It was cultured in YP medium supplemented with 2% (w/v) glucose as a sole carbon source.

Cell culturing with rotational shaking at 200 rpm was performed at 30°C. The cells were cultured in Erlenmeyer flasks. A "flask volume/medium volume" ratio was 5:1.

2.5 Mass spectrometric identification and quantitation of cellular lipids using the direct-injection method of lipidomic analysis.

A cell culture aliquot was recovered on a particular day of culturing. A portion of the cell aliquot was diluted and then inspected with a hemocytometer (#3200; Hausser Scientific) to calculate cell concentration in the aliquot. The centrifugation in a Centra CL2 clinical centrifuge (5 min, 3,000 × g, room temperature [RT]) was used to pellet a total of 5×10^7 cells. A tabletop microcentrifuge was used to wash the cell pellet by centrifugation (1 min, 16,000 × g, 4°C); the cell washing was performed in ice-cold nanopure water (once) and then in ice-cold 155 mM ammonium bicarbonate (ABC) buffer, pH = 8.0 (once). After storing the pelleted cells at -80°C until lipid extraction, the cell pellet was thawed on ice. The thawed cell pellet was then resuspended in 200 µl of ice-cold nanopure water. Each sample of the resuspended cells was transferred to a 15-ml high-strength glass screw-top centrifuge tube with a Teflon-lined cap (#0556912; Fisher Scientific). A total sample volume was adjusted to 1 ml with ice-cold nanopure water. Each sample tube was supplemented with the following: 1) 20 µl of the internal standard mixture made in Chromasolv high pressure liquid chromatography (HPLC) (>99.9%) chloroform (#528730; Millipore-Sigma) [Table 2.1], 2) 800 µl of 425-600 µm acid-washed glass beads (#G8772; Sigma-Aldrich) for cell disintegration, and 3) 3 ml of a 17:1 mixture of Chromasolv HPLC (>99.9%) chloroform (#528730; Millipore-Sigma) and Chromasolv HPLC (>99.9%) methanol (#439193; Millipore-Sigma). After the sample tubes were vigorously vortexed (2 h, 4°C), they were centrifuged in a Centra CL2 clinical centrifuge (5 min, 3,000 × g, RT). A glass Pasteur pipette was used to transfer the lower organic phase to another 15-ml high-strength glass screw-top centrifuge tube with a Teflon-lined cap; it is essential to avoid the disruption of the glass bead layer and upper aqueous phase during the organic phase transfer. The remaining upper aqueous phase in the sample tube was supplemented with 1.5 ml of chloroform-methanol (2:1) mixture. The sample tubes were vigorously vortexed (2 h, 4°C) again; during the second vortexing of the sample tubes, the initially recovered lower organic phase was kept at 4°C. After the second 2-h vortexing of the sample tubes was completed, these tubes were centrifuged in a Centra CL2 clinical centrifuge (5 min, 3,000 × g, RT). A glass Pasteur pipette was used to transfer the lower organic phase from the sample tube to a tube with the corresponding initial organic phase; it is important to avoid disrupting the glass bead layer and upper aqueous phase during the second organic phase transfer as well. After

combining both lower organic phases, the nitrogen gas flow was used to evaporate the solvent. As soon as the solvent evaporation was completed, 100 µl of a chloroform-methanol (1:2) mixture was used to dissolve the remaining lipid film. The lipid solution was immediately transferred into 2-ml glass vials with Teflon screw tops. The samples were stored at -80°C for not more than a week before being analyzed by mass spectrometry (MS) on the Thermo Orbitrap Velos mass spectrometer.

After sample recovery from -80°C for MS, an equal volume of the chloroform/methanol (1:2) mixture containing 0.1% ammonium hydroxide was added to each sample. The dissolved lipids samples were directly injected into a Thermo Orbitrap Velos mass spectrometer equipped with a HESI-II ion source (Thermo Scientific, Waltham, MA, USA) at a flow rate of 5 µl/min. The resolution of lipids by MS was performed at the optimized tune settings and instrument methods, as outlined in Table 2.2 and Table 2.3 (respectively). The ProteoWizard MSConvert software (http://proteowizard.sourceforge.net/) was used to convert mass spectra to open format mzXML. The Lipid Identification Software LipidXplorer (https://wiki.mpi-cbg.de/lipidx/Main_Page) uses the mzXML file format to detect and quantitate lipids automatically. The settings provided in Table 2.4 were used to import the mzXML data files into the LipidXplorer software. The molecular Fragmentation Query Language (MFQL) files recovered from the above LipidXplorer page were used to identify lipids based on their m/z ratios and fragmentation patterns.

To quantify the recovered and identified cellular lipid classes, the peak intensities for these lipid classes were compared with those for the corresponding lipid standards. Because each lipid class present in the yeast cell had a corresponding internal lipid standard (spiked standard) of the same class, it was possible to calculate the molar percentage concentrations of all cellular lipid classes. The ratio of the signal intensity for the precursor ions of a particular cellular lipid class to that of the corresponding lipid standard was first calculated. To calculate the molar percentage concentration of a cellular lipid class, this calculated ratio was multiplied by the known concentration of the internal lipid standard (spiked standard).

Table 2.1: The composition of a mixture of the internal lipid standards (spiked standards)

Abbreviations: CL, cardiolipin; FFA, free fatty acid; PA, phosphatidic acid; PC, phosphatidylcholine; PE, phosphatidylethanolamine; PG, phosphatidylglycerol; PS, phosphatidylserine; TAG, triacylglycerol. CL, FFA, PA, PC, PE, PG and PS were purchased from Avanti Polar Lipids. TAG was purchased from Larodan.

The mode of detection	Lipid class	Lipid chain composition (Number of carbon atoms:Number of double bonds on the fatty acid chain)	Molecular weight (g/mol)	m/z (mass/ion charge)	Concentration in the mixture (mg/µl)
Negative	CL	14:0 / 14:0 / 14:0 /14:0	1274.9000	619.4157	0.10
	FFA	19:0	298.2872	297.2711	0.02
	PA	14:0 / 14:0	614.3920	591.4026	0.10
	PE	14:0 / 14:0	635.4526	634.4448	0.10
	PG	14:0 / 14:0	688.4290	665.4394	0.10
	PS	14:0 / 14:0	701.4240	678.4271	0.02
Positive	TAG	13:0 / 13:0 / 13:0	680.5955	698.6299	0.10
	PC	13:0 / 13:0	649.4683	650.4761	0.10

Table 2.2: Tune settings for the Thermo Orbitrap Velos mass spectrometer.

Abbreviation: FTMS, Fourier transform mass spectrometry.

Instrument polarity	Positive	Negative
Source voltage (kV)	3.9	4
Capillary temperature (^{o}C)	275	275
Sheath gas flow	5	5
Aux gas flow	1	1
FTMS injection time (ms)	100	500
FTMS microscans	3	1

Table 2.3: Instrument methods for data acquisition using the Thermo Orbitrap Velos mass spectrometer.

Abbreviations: FTMS, Fourier transform mass spectrometry; HCD, high-energy collisional dissociation.

Acquisition time	5 min (with a 0.25-min delay)	
Instrument polarity	Positive	Negative
MS (Segment I)		
Analyzer	FTMS	FTMS
Mass range	Normal	Normal
Resolution	100,000	100,000
Data type	Centroid	Centroid
Scan range	400-1,200	200-1,200
Data-dependent MS/MS (segments 2-10)		
Analyzer	FTMS	FTMS
Resolution	30,000	30,000
Data type	Centroid	Centroid
Activation	HCD	HCD
Activation time (ms)	0.1	0.1
Isolation width	1	1
Collision energy	35	65
Mass range	Normal	Normal
Data type	Centroid	Centroid
Scan range	-	-

Table 2.4 The settings used for lipid identification by the LipidXplorer software for data acquired under the positive and negative modes of detection.

Abbreviation: FWHM, full width at half maximum.

	Positive mode	Negative mode
Selection window (Da)	1	1
Time range (sec)	0-350	0-350

Calibration masses		
MS	0	0
MS/MS	0	0
m/z range (m/z-m/z)		
MS	200-1,400	200-1200
MS/MS	140-1,200	100-1200
Resolution (FMHW)		
MS	100,000	100,000
MS/MS	30,000	30,000
Tolerance (ppm)		
MS	10	10
MS/MS	10	10
Resolution gradient (res/(m/z))		
MS	0	-55
MS/MS	0	0
Minimum occupation (0<1)		
MS	0.5	0.5
MS/MS	0	0
MS1 offset (Da)	0	0

2.6 CLS assay.

A cell culture aliquot was recovered on a certain day of culturing yeast cells in the synthetic minimal YNB medium (0.67% (w/v) Yeast Nitrogen Base without amino acids; #DF0919-15-3; Fisher Scientific) supplemented with 2% (w/v) glucose (#D16-10; Fisher Scientific) in the presence or absence of PE21. A diluted portion of the cell culture aliquot was examined with a hemocytometer to calculate cell concentration in the aliquot. Serial dilutions of the cell aliquot were made. These serial cell dilutions were plated in duplicate onto the nutrient-rich solid YP medium (1% [w/v] yeast extract [#BP1422-2; Fisher Scientific] and 2% [w/v] peptone [#BP1420-2; Fisher Scientific] supplemented with 2% (w/v) glucose as a sole carbon source. The plates with the inoculated cells were incubated at 30^{o}C for 2 d. The number of colony-forming units (CFU) per plate for each culture was counted to calculate the number of viable cells per ml of the culture.

The following equation was used to calculate the percentage of viable cells for each culture: [Number of viable cells (CFU) per ml/Total number of cells per ml] × 100%. The percentage of viable cells in a culture that reaches the mid-logarithmic growth phase was set at 100%.

2.7 Statistical analysis.

Microsoft Excel's (2010) Analysis ToolPack-VBA was used to perform statistical analysis. Cell survival data are provided as mean ± SEM. A GraphPad Prism 7 statistics software was used to calculate the following: 1) the *p* values for comparing the means of two groups using an unpaired two-tailed *t* test, and 2) the *p* values for comparing a pair of survival curves using a logrank test.

2.8 Identification and quantitation of cellular lipids using the liquid chromatography (LC)-MS/MS method.

A cell culture aliquot was recovered on a specific day of culturing yeast cells. A portion of the cell aliquot was diluted and then assessed with a hemocytometer (#3200; Hausser Scientific) to calculate cell concentration in the aliquot. The centrifugation in a tabletop microcentrifuge (1 min, 16,000 × g, 4°C) was used to pellet a total of 5×10^7 cells within a pre-cooled at 4°C 1.5-ml Eppendorf tube. The cell pellet was resuspended in 1.5 ml of ice-cold nanopure water, the cells were washed by centrifugation in a tabletop microcentrifuge (1 min, 16,000 × g, 4°C) and the supernatant was discarded. The cell pellet was resuspended in 1.5 ml of ice-cold 155 mM ABC buffer (pH = 8.0). The cells were washed by centrifugation in a tabletop microcentrifuge (1 min, 16,000 × g, 4°C) and the supernatant was discarded. The pelleted cells were stored at -80°C until lipid extraction. Immediately before lipid extraction, the cell pellet was thawed on ice. The thawed cell pellet was resuspended in 200 µl of ice-cold nanopure water. Each sample of the resuspended cells was transferred to a 15-ml high-strength glass screw-top centrifuge tube with a Teflon-lined cap (#05-550; Pyrex). Each sample tube was supplemented with the following: 1) 25 µl of the internal standard mixture prepared in a 2:1 mixture of Chromasolv HPLC (>99.9%) chloroform (#528730; Millipore-Sigma) and Chromasolv HPLC (>99.9%) methanol (#439193; Millipore-Sigma); 2) 100 µl of 425-600 µm acid-washed glass beads (#G8772; Sigma-Aldrich) for cell disintegration, and 3) 600 µl of a 17:1 mixture of chloroform and methanol. The sample tube was vortexed (5 min RT) at a high speed to disintegrate the cells. The tube was then vortexed (1 h, RT) at a low speed to facilitate the extraction of lipids. After the second vortexing, each sample tube

was incubated for 30 min on ice to allow protein precipitation and enable aqueous and organic phases separation. The separation of the upper aqueous phase and the lower organic phase in the sample tubes was facilitated by centrifuging the tubes in a Centra CL2 clinical centrifuge (5 min, 3,000 × g, RT); all cellular lipids were present only in the lower organic phase. The lower organic phase (~400 µl) was transferred with a borosilicate glass pipette to another 15-ml high-strength glass screw-top centrifuge tube with a Teflon-lined cap. The nitrogen gas flow was used to evaporate the solvent in the lower organic phase. The remaining upper aqueous phase was supplemented with 300 µl of a 2:1 mixture of chloroform and methanol to enable the extraction of PA, PS, PI, PG and sphingolipids. After vigorously vortexing (5 min, RT) the sample tubes with the remaining upper aqueous phase and chloroform/methanol mixture, the tubes were centrifuged (5 min, 3,000 × g, RT) in a Centra CL2 clinical centrifuge. The lower organic phase (~ 200 µl) formed after such centrifugation was transferred with a borosilicate glass pipette to the lower organic phase collected at the previous step. The nitrogen gas flow was used to evaporate the solvent in the sample tubes containing the combined organic phases. After solvent evaporation, the sample tubes were stored at -80°C before being analyzed by LC-MS/MS. Each batch of the experiment was analyzed on different days.

Each sample tube with the lipid film stored at -80°C was supplemented with 500 µl of acetonitrile (ACN; Thermo Scientific)/2-propanol/nanopure water (65:35:5). After vortexing the sample tube 3 times for 10 s at RT, its content was ultrasonicated for 15 min. The tube was vortexed (3 times, 10 s, RT), and 100 µl of its content was added to a glass vial with an insert used for a wellplate. Different lipid classes were subjected to separation on an LC system equipped with a reverse-phase C18 column CSH coupled to a pre-column system (Waters). The column was maintained at 55°C, a flow rate was 0.3 ml/min, and the sample was kept in the wellplate at RT during lipid separation by LC. Two mobile phases were used for lipid separation by LC, the mobile phase A (ACN/nanopure water [60:40 (v/v)]) and mobile phase B (isopropanol/ACN [90:10 (v/v)]). The electrospray ionization (ESI) ion source was used to create parent ions. The parent ions were detected in a positive or negative mode (ESI (+) or ESI (-) mode, respectively). The mobile phases A and B were supplemented with 10 mM ammonium formate for the ESI (+) mode of parent ions detection. Ammonium acetate at the final concentration of 10 mM was added to the mobile phases A and B for detecting the parent ions in the ESI (-) mode. At both modes of parent ions detection, a sample volume was 10 µl. The following LC gradient was used to separate

different lipid classes: 1) 0–1 min: 10% of phase B, 2) 1–4 min: 60% of phase B, 3) 4–10 min: 68% of phase B, 4) 10–21 min: 93% of phase B, 5) 21–24 min: 97% of phase B, and 6) 24–33 min: 10% of phase B. During lipid separation by LC, extraction blanks were run as the first run, runs between every four samples and the last run. Also, the pooled quality control and the standard mix samples were run on the beginning, end and every 4 samples to monitor the quality of the sequence. Data normalization was performed by subtracting the background and by using the integrated peaks areas of standard metabolites. The samples sizes were normalized by the number of cells in present in each sample. Free fatty acid (FFA) lipid species are very sticky, i.e., they bind to the column very strongly, the re-equilibrium of the gradient is not enough to wash away all the FFA molecules from the column. Therefore, in order to analyze the FFA a blank sample was run after each sample. For some of the FFA molecules there are some large backgrounds peaks from the system, consumables, and solvents that interfere with the analysis, which can make the absolute quantification of these lipid species very challenging. However, the purpose of my studies was to quantify and compare the lipid concentration between different sample. Therefore, the background peaks were not as much of an issue as far as the peak shapes were good enough to be integrated.

After LC separation of cellular lipids, they were analyzed using the Thermo Orbitrap Velos mass spectrometer equipped with a HESI (heated electrospray ionization) ion source. Table 2.5 shows the settings used for lipid analysis by MS/MS. The parent ions (MS1) were detected by the Fourier transform analyzer at a resolution of 60,000 and within the mass range of 150–2,000 Da. Table 2.6 provides the settings used to detect product ions (MS2).

The identification and quantitation of cellular lipids from LC-MS raw spectra files were performed using the Lipid Search software (V4.1; Fisher Scientific). Lipid Search uses the largest lipid database that includes more than 1.5 million lipids MS1 and the predicted MS2 of their fragmentation. The identification of cellular lipids using Lipid Search was performed by analyzing MS2 peaks. MS1 peaks were used to quantify cellular lipids with the help of Lipid Search. LC-MS raw files included the full-scan records for MS1 data and data-dependent records for MS2. The search of these files was conducted for FFA, CL, phytoceramide (PHC), phytosphingosine (PHS), PC, PE, PG, phosphatidylinositol (PI), PS and TAG. The m/z tolerance values for searching LC-MS raw files were 5 ppm for MS1 and 10 ppm for MS2. Table 2.7 shows other constraints used for the search of LC-MS raw files. The freely available open-source alternatives for processing LC-MS raw files using the commercial Lipid Search software include Lipid Data

Analyzer (http://genome.tugraz.at/lda2/lda_download.shtml), MZmine 2 (http://mzmine.github.io/) and XCMS (https://bioconductor.org/packages/release/bioc/html/xcms.html).

Table 2.5. The settings used to analyze cellular lipids using the Thermo Orbitrap Velos mass spectrometer.

Abbreviation: FTMS, Fourier transform mass spectrometry; HESI, heated electrospray ionization.

FTMS - p resolution	60000
Mass range (dalton)	150-2000
Ion source type	HESI
Capillary temperature (℃)	300
Source heater temperature (℃)	300
Sheath gas flow	10
Aux gas flow	5
Positive polarity voltage (kV)	3
Negative polarity voltage (kV)	3
Source current (μA)	100

Table 2.6. The settings used to detect MS2 ions using the Fourier transform analyzer.

Abbreviation: FTMS, Fourier transform mass spectrometry.

Instrument polarity	Positive	Negative
Activation type	High-energy-induced-collision-dissociation	Collision-induced-dissociation
Minimal signal required	5000	5000
Isolation width	2	2
Normalized collision energy	55	35
Default charge state	1	2
Activation time	0.1	10
5 most intense peaks were selected for MS/MS		

Table 2.7. The constraints used to identify and quantify cellular lipids by searching the LC-MS raw files that included the full-scan records for MS1 data and data-dependent records for MS2.

Abbreviations: ESI (+), electrospray ionization positive mode; ESI (-), electrospray ionization negative mode; CER, ceramide; CL, cardiolipin; FFA, free fatty acid; PC, phosphatidylcholine; PE, phosphatidylethanolamine; PG, phosphatidylglycerol; PS, phosphatidylserine; TAG, triacylglycerol.

Identification	
Database	Orbitrap
Peak detection	Recall isotope (ON)
Search option	Product search Orbitrap
Search type	Product
Experiment type	LC-MS
Precursor tolerance	10 ppm
Product tolerance	High-energy-induced-collision-dissociation [ESI (+) mode]: 20 ppm
	Collision-induced-dissociation [ESI (-) mode]: 0.5 Daltons
Quantitation	
Execute quantitation	ON
m/z tolerance	-5.0; +5.0
Tolerance type	ppm
Filter	
Top rank filter	ON
Main node filter	Main isomer peak
m-score threshold	5
c-score threshold	2
FFA priority	ON
ID quality filter	A: Lipid class & all fatty acids are completely identified
	B: Lipid class & some fatty acids are identified

	C: Lipid class or fatty acids are identified
	D: Lipid identified by other fragment ions (H2O, etc.)
Lipid Class	
High-energy-induced-collision-dissociation [ESI (+) mode]	PC, TAG
Collision-induced-dissociation [ESI (-) mode]	CER, CL, FFA, PE, PG, PI, PS
Ions	
High-energy-induced-collision-dissociation [ESI (+) mode]	+ H; + NH4; + Na
Collision-induced-dissociation [ESI (-) mode]	- H; - 2H; C2H3O2-

2.9 Percoll density gradient centrifugation to separate high-density and low-density Q cells for lipid extraction.

2 ml of 1.5 M NaCl (#S7653; Sigma) and 16 ml of the Percoll solution (#P1644; Sigma) were mixed by pipetting in a 50-ml conical polypropylene centrifuge tube (#055398; Fisher Scientific). Each of the four polyallomer tubes for an MLS-50 rotor (Beckman Coulter) for an Optima MAX ultracentrifuge (Beckman Coulter) was filled with 4 ml of the NaCl/Percoll mixture for making four Percoll density gradients. The Optima MAX ultracentrifuge was used to create the gradients by centrifuging (15 min, 25,000 × g, 4^{o}C) the tubes. A cell culture aliquot was recovered on a particular day of culturing. A portion of the cell aliquot was diluted and then assessed with a hemocytometer (#3200; Hausser Scientific) to calculate cell concentration in the aliquot. For each of the four Percoll density gradients, a 15-ml conical polypropylene centrifuge tube (#0553912; Fisher Scientific) was supplemented with a cell culture aliquot containing a total

of 1×10^9 yeast cells. The cells were pelleted by centrifugation in a Centra CL2 clinical centrifuge (5 min, 3,000 × g, RT). The supernatant was discarded, and the cell pellet in each of the four conical polypropylene centrifuge tubes was resuspended in 500 µl of 50 mM Tris/HCl buffer (pH 7.5). After overloading the cell suspension onto each of the four preformed Percoll gradients, the gradients were subjected to centrifugation (30 min, 2,300 × g, 25°C) in the Optima MAX ultracentrifuge. A pipette was used to collect the gradient's upper and lower cell fractions and place them into the Eppendorf test tubes. After pelleting the cells by centrifugation in a tabletop ultracentrifuge (1 min, 16,000 × g, RT) and discarding the supernatant, the cells were washed twice with 50 mM Tris/HCl buffer (pH 7.5) to remove Percoll. The supernatants formed after the second wash were discarded, and the cell pellets were resuspended in 50 mM Tris/HCl buffer (pH 7.5) for lipid extraction.

2.10 Cell quenching for extracting water-soluble metabolites.

A cell culture aliquot was recovered on a particular day of culturing. A portion of the cell aliquot was diluted and then examined with a hemocytometer (#3200; Hausser Scientific) to calculate cell concentration in the aliquot. After transferring a cell culture aliquot containing 5.0×10^8 cells into a pre-cooled at -5°C 500-ml centrifuge bottle for a high-speed Beckman Coulter centrifuge, a total volume of the liquid in the bottle was adjusted to 200 ml by adding a quenching solution (60% methanol in 155 mM ABC buffer, pH = 8.0) stored at -20°C. Chromasolv HPLC (>99.9%) methanol (#439193; Millipore-Sigma) was used for making the quenching solution. The bottle was subjected to centrifugation (3 min, 11,325 × g, -5°C) in the high-speed Beckman Coulter centrifuge and gently and rapidly recovered from the centrifuge without disturbing the quenched cells pellet. The removal of the bottle's lid and the supernatant transfer were also performed quickly and tenderly, without disturbing the quenched cells pellet. After resuspending the pelleted cells in each tube in 10 ml of ice-cold ABC buffer, the cell suspension was transferred into a 15-ml high-speed glass centrifuge tube with a Teflon-lined cap (Pyrex) to extract water-soluble metabolites. A Centra CL2 clinical centrifuge was used to pellet the quenched cells (3 min, 3,000 × g, 0°C), and the supernatant was rapidly discarded. Before being used for metabolite extraction, the sample tubes with quenched cell pellets were kept on dry ice or stored at -80°C.

2.11 Fluorescence microscopy.

The established procedure was used to assess the extent of plasma membrane permeability for small molecules by staining with propidium iodide (PID; #P4170, Sigma) [287]. Phosphatidylserine externalization was examined by staining with Annexin V (#A13201; Thermo Fisher Scientific) as described previously [287]. A Leica DM6000B epifluorescence microscope equipped with a high-resolution Hamamatsu Orca ER CCD camera and a 100× objective was used for live imaging. A PerkinElmer Volocity software was used for image acquisition with 20-ms exposures. Image files were exported into the TIFF format. An ImageJ software was then used to calculate the percentage of PI- and Annexin V-positive cells.

2.12 Extraction of water-soluble metabolites from quenched cells.

Each sample tube with the pelleted quenched cells kept on dry ice or stored at -80°C was supplemented with 2 ml of chloroform kept at -20°C, 1 ml of methanol stored at -20°C, 1 ml of ice-cold nanopure water and 200 µl of 425-600 µm acid-washed glass beads (#G8772; Sigma-Aldrich). Chromasolv HPLC (>99.9%) chloroform (#528730; Millipore-Sigma) and Chromasolv HPLC (>99.9%) methanol (#439193; Millipore-Sigma) were used. Aluminum foil was used to cover the sample tube's mouth. After placing the tube in a foam tube holder kit with a retainer (Thermo Scientific), it was vortexed (30 min, 4°C) to promote metabolite extraction. To allow protein precipitation and enable aqueous and organic phase separation, the sample tube was kept for 30 min on ice. The centrifugation of the sample tube in a Centra CL2 clinical centrifuge (10 min, 3,000 × g, 4°C) was used to facilitate the efficient separation of the upper aqueous, middle and lower organic phases. The upper aqueous phase included water-soluble metabolites, the middle phase contained cell debris and proteins, and the lower organic phase was mainly composed of different lipid classes. The upper aqueous phase of a total volume of ~ 400 µl was transferred with a glass micropipette to a 1.5-ml Eppendorf tube holding 800 µl of ACN (Thermo Scientific) held at -20°C. After centrifuging the tube in a tabletop ultracentrifuge (10 min, 13,400 × g, 4°C), the upper portion of a liquid in the tube with a total volume of 800 µl was placed in an MS vial. Before a sample in this vial was analyzed by LC-MS/MS, the vial was kept at 0°C.

2.13 LC-MS/MS analysis of extracted water-soluble metabolites.

An Agilent 1100 HPLC system (Agilent Technologies) linked to an LTQ Orbitrap Velos

mass spectrometer (Thermo Fisher Scientific) was used to acquire LC-MS/MS data.

A sample of extracted water-soluble metabolites was ultrasonicated (15 min), vortexed (3 times, 10 s, RT) and then analyzed by LC-MS/MS. A ZIC-pHILIC column (Merck SeQuant; 150 × 2.1 mm, 5 µm particle size) was used to perform LC separation of the metabolites. Two mobile phases were used for metabolite separation by LC, the mobile phase A (nanopure water/ACN [95:5 (v/v)] supplemented with 20 mM ammonium acetate) and mobile phase B (ACN). A gradient program used to separate metabolites by LC is sown in Table 2.8. During metabolite separation, the ZIC-pHILIC column and the samples were held at 45°C and 4°C (respectively).

A Thermo Orbitrap Velos mass spectrometer equipped with a heated electrospray ionization ion source (Thermo Scientific) was used to carry out the MS-based analyses of the water-soluble cellular metabolites separated by LC. The MS1 ions were detected using the FTMS analyzer. The high-energy collisional dissociation (HCD) and collision-induced dissociation (CID) were used to analyze the MS2 ions. The settings used to analyze MS1 and MS2 are shown in Tables 2.9 and 2.10, respectively. At both positive and negative ionization modes of injection, a sample volume was 10 µl.

2.14 Metabolite identification and quantitation using the LC-MS/MS raw data.

A Compound Discoverer 3.1 software (Fisher Scientific) was used to identify and quantify the extracted water-soluble metabolites subjected to LC-MS/MS. The identification of water-soluble metabolites using Compound Discoverer 3.1 was performed by analyzing MS2 peaks. MS1 peaks were used to quantify water-soluble metabolites with the help of Compound Discoverer 3.1. A freely available online library of databases and spectra (https://www.mzcloud.org) was used to search for MS2 spectra of the LC-MS/MS raw data.

Time (min)	Flow rate (ml/min)	Relative concentrations (%) of mobile phases A and B	
		A	B
0.5	0.25	5	95
26	0.25	40	60
30	0.25	70	30
31	0.25	70	30
31.1	0.4	5	95
43.9	0.4	5	95
44	0.25	5	95
45	0.25	5	95

Table 2.8. A gradient program used to separate the extracted water-soluble metabolites by LC on the ZIC-pHILIC column. Mobile phase A: a 95:5 (v/v) mixture of nanopure water with ACN supplemented with 20 mM ammonium acetate. Mobile phase B: ACN.

Table 2.9. The settings used for the MS-based analysis of the MS1 ions of the water-soluble metabolites separated by LC. Abbreviations: AGC, automatic gain control; FTMS, Fourier transform mass spectrometry; HCD, higher-energy collisional dissociation; HESI, heated electrospray ionization; LTQ, linear trap quadrupole; MSn, multi-stage mass spectrometry.

Full scan mass range (dalton)	70-900
FTMS full scan resolution	6.0×10^4
FTMS HCD resolution	7500
FTMS full scan AGC target	1.0×10^6
FTMS MSn AGC target	5.0×10^4
Ion trap (LTQ) MSn AGC target	1.0×10^4
Ion source type	HESI
Capillary temperature (°C)	275
Source heater temperature (°C)	250

Sheath gas flow	10
Aux gas flow	5

Table 2.10. The settings used for the MS-based analysis of the MS2 ions of the water-soluble metabolites separated by LC. Abbreviations: CID, collision-induced dissociation; HCD, higher-energy collisional dissociation; ms, milliseconds; MS/MS, tandem mass spectrometry.

Instrument polarity	positive/negative
Activation type	CID/HCD
Minimum signal required	5000
Isolation width	2
Normalized collision energies for CID	35, 60
Normalized collision energies for HCD	35, 45, 55
Default charge state	1
Activation time for CID (ms)	10, 30
Activation time for HCD (ms)	10
Number of MS/MS events in CID	top 3, top 5, top 10
Number of MS/MS events in HCD	top 5
Number of micro scans used in both HCD and CID	1

Chapter 3: The geroprotective plant extract PE21 alters the cellular lipidome of budding yeast and slows chronological aging by delaying the onset of liponecrotic cell death.

3.1 Introduction.

The Titorenko laboratory performed a screen of a collection of extracts from the plants traditionally used in Chinese herbal medicines or present in the Mediterranean diet and discovered that several of them delayed the chronological aging of budding yeast [230]. The ethanol/water extract from *Salix alba's* bark, called PE21, was one of the aging-delaying (geroprotective) plant extract discovered [230]. The geroprotective effect of PE21 exceeds those of currently known aging-delaying chemicals [230]. The Titorenko laboratory found that PE21 elicits several significant age-related changes in budding yeast. One of these changes is a prompt decline in the abundance of the neutral lipids TAG and ergosterol stored in LD [230]. Because the maintenance of lipid homeostasis in budding yeast affects several lipid classes [83, 155-158], I hypothesized that PE21 might alter the intracellular concentrations of other lipid classes as well. To test this hypothesis, I used tandem mass spectrometry (MS/MS) to identify and quantitate cellular lipids using a direct-injection method of lipidomic analysis.

3.2 PE21 elicits substantial changes in the concentrations of different lipid classes within chronologically aging budding yeast.

It has been previously shown that the highest efficiency of chronological aging delay and CLS extension by PE21 can be observed in a WT strain of yeast cultured in a synthetic minimal YNB medium supplemented with 2% (w/v) glucose as a carbon source [230]. The geroprotective efficiency of PE21 in yeast cultured under these non-CR conditions was substantially higher than that in yeast cultured under CR conditions on 0.5% (w/v) glucose [230]. Noteworthy, the chronological aging process is accelerated in yeast under non-CR conditions, whereas this process is decelerated in yeast under CR conditions [2, 8, 55]. Therefore, it was concluded that PE21 slows yeast chronological aging by acting as a CR-mimetic [230]. CR mimetics are defined as geroprotective interventions targeting similar types of pro- and anti-aging cellular processes under

CR and non-CR conditions [288-290]. Of note, it remains to be tested whether PE21 exhibits this characteristic property of CR-mimetics.

The highest geroprotective efficiency of PE21 under non-CR conditions was observed if this plant extract was used at a final concentration of 0.1% (w/v) [230]. Ethanol was used as a vehicle, and its final concentration was 0.5% (v/v) [230]. The control samples for the ethanol-mock treatment of budding yeast were cultured in the YNB medium supplemented with 2% (w/v) glucose and 0.5% ethanol (v/v) [230].

Using a direct-injection method of the MS/MS-based lipidomic analysis, I assessed how PE21 influences the cellular lipidome of the WT strain of budding yeast. The lipidome of WT yeast cultured in the YNB medium supplemented with 2% (w/v) glucose and 0.1% (w/v) PE21 (added with the ethanol vehicle) was compared to that of WT yeast cultured under ethanol-mock treatment conditions. The viability curves of the WT yeast cultured in the presence of PE21 or in its absence have been published by the Titorenko laboratory earlier (Figure 3.1) [230]. Based on these viability curves, I conducted the lipidomic analysis of the WT yeast taken on days 1, 2, 3 and 4 of culturing with or without PE21. The cellular lipidomes of yeast cultured more than 4 days were not analyzed because less than 10% of the WT yeast cultured in the absence of PE21 remained viable on day 5 of culturing (Figure 3.1) [230].

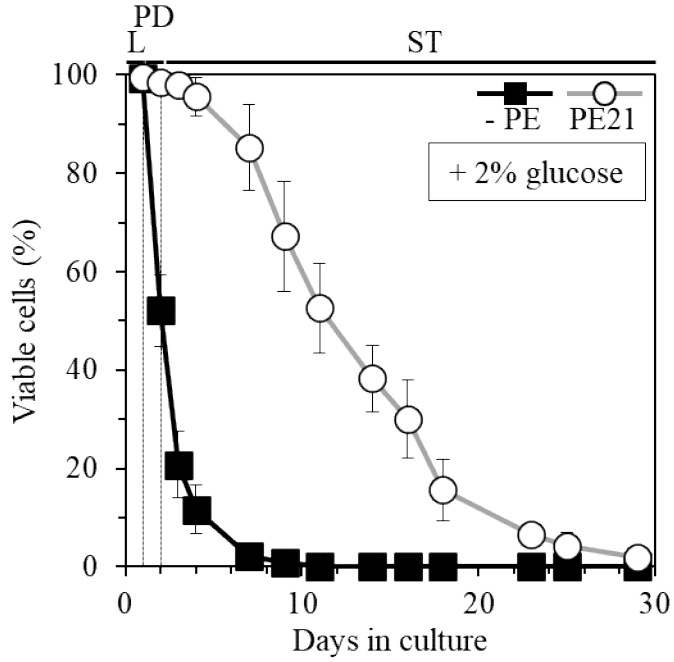

Figure 3.1. PE21 is a CR-mimetic that prolongs the longevity of chronologically aging

budding yeast cultured under non-CR conditions. Culturing of WT yeast was conducted in the synthetic minimal YNB medium supplemented with 2% (w/v) glucose as a carbon source, in the presence of 0.1% (w/v) PE21 or its absence. Survival curves of chronologically aging WT yeast cultured with or without PE21 are presented. Data are provided as means ± SEM (n = 21). Abbreviations: Logarithmic (L), post-diauxic (PD) or stationary (ST) phase of culturing.
From: Reference [230. Lutchman V, Medkour Y, Samson E, Arlia-Ciommo A, Dakik P, Cortes B, Feldman R, Mohtashami S, McAuley M, Chancharoen M, Rukundo B, Simard É, Titorenko VI. Discovery of plant extracts that greatly delay yeast chronological aging and have different effects on longevity-defining cellular processes. Oncotarget. 2016; 7:16542-16566].

My MS/MS-based lipidomic analysis revealed that PE21 alters the intracellular concentrations of all lipid classes on various days of the chronological aging process. The intracellular concentration of every lipid class was calculated in mol% to reflect its relative abundance on days 1, 2, 3 and 4 of culturing.

I found that PE21 substantially decreases the intracellular concentrations of triacylglycerols (TAG) and free fatty acids (FFA) in WT yeast taken on days 2, 3 and 4 of culturing (Figures 3.2A and 3.2B). On day 2 of culturing, WT yeast cells are in the PD growth phase (Figure 3.1). WT yeast cells taken on days 3 and 4 of culturing enter the ST phase of culturing (Figure 3.1). As discussed in the Introduction chapter of my Thesis, TAG is synthesized in the endoplasmic reticulum (ER), is transferred to and accumulated in the lipid droplets (LDP), and can be used as a source for the formation of FFA (Figure 1.7).

The effect of PE21 on the intracellular concentrations of the phospholipids phosphatidic acid (PA), phosphatidylserine (PS), phosphatidylethanolamine (PE), phosphatidylcholine (PC) and phosphatidylinositol (PI) was quite different. As I mentioned in the Introduction chapter of the Thesis, all these lipid classes are synthesized in the ER (Figure 1.7). I found that PE21 considerably increases the intracellular concentrations of these phospholipids. However, the age-related dynamics of such effect of PE21 on the ER-derived phospholipids were different for different phospholipid classes. The intracellular concentrations of PA (Figure 3.2C), PS (Figure 3.2D) and PI (Figure 3.2G) were increased during the PD phase (on day 2) and ST phase (on days 3 and 4) of culturing in the YNB medium with PE21. PE21 increased the intracellular concentration of PE on all four days of culturing, including day 1 (i.e., during the L growth phase).

The statistically significant effect of PE21 on the intracellular concentration of PC was observed only on day 4, during the ST phase of culturing.

PE21 substantially decreased the intracellular concentrations of cardiolipin (CL) on all four days of culturing (Figure 3.2H). As outlined in the Introduction chapter of my Thesis, CL is synthesized and remains in the inner mitochondrial membrane (IMM) (Figure 1.5).

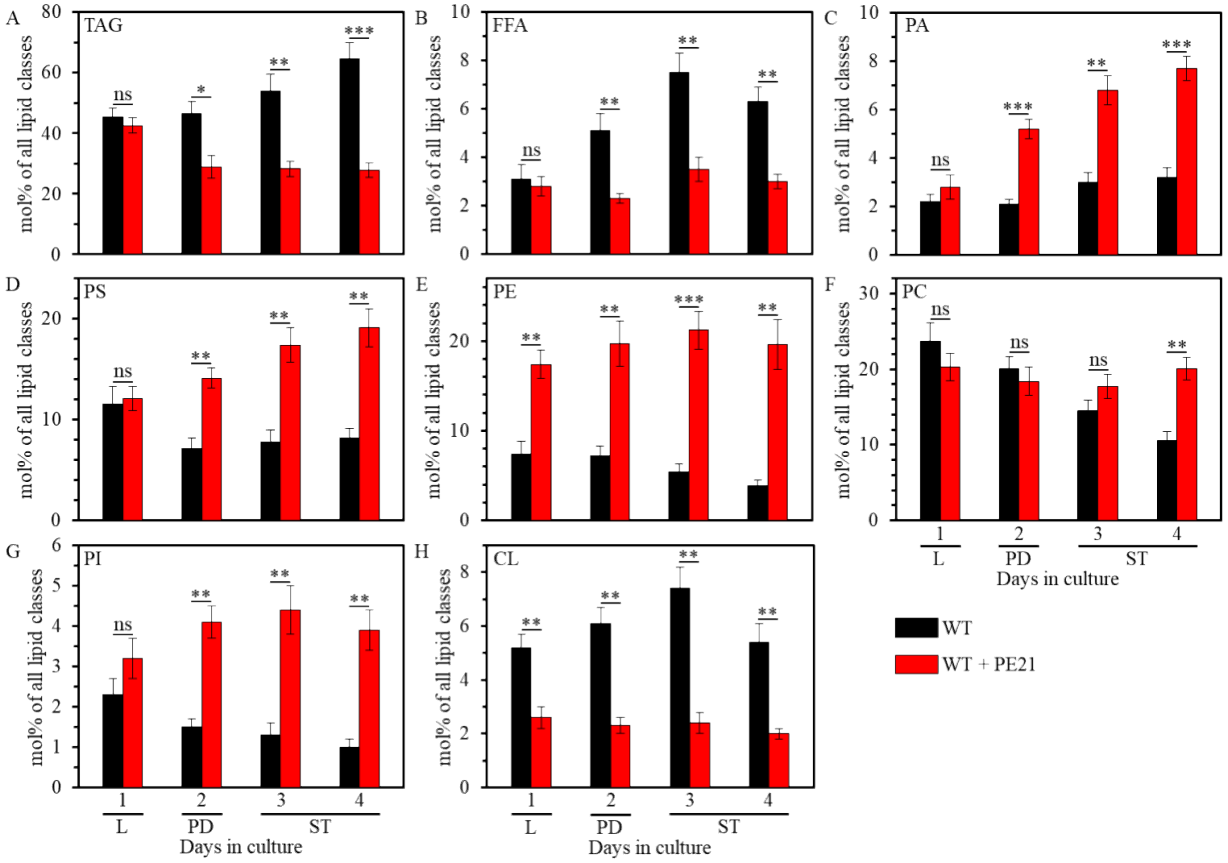

Figure 3.2. PE21 changes the intracellular concentrations of all lipid classes on various days of chronological aging. WT yeast cells were cultured in the synthetic minimal YNB medium supplemented with 2% (w/v) glucose as a carbon source, in the presence of 0.1% (w/v) PE21 or its absence. Ethanol was used as a vehicle, and its final concentration was 0.5% (v/v) both in control samples and in samples with PE21. Cells taken on days 1, 2, 3 and 4 of culturing with or without PE21 were subjected to an MS/MS-based direct-injection method of the lipidomic analysis. The intracellular concentrations of different lipid classes were calculated in mol% to reflect their relative abundance on days 1, 2, 3 and 4 of culturing. Data are shown as means ± SEM (n = 4; *$p < 0.05$; **$p < 0.01$; ***$p < 0.001$; ns, not significant). Abbreviations: Logarithmic (L), post-diauxic (PD) or stationary (ST) growth phase.

Altogether, the above data provide evidence that PE21 alters the intracellular concentrations of all lipid classes in chronologically aging budding yeast.

3.3 A hypothetical model of how PE21 reorganizes lipid metabolism and transport in budding yeast.

As described in the Introduction chapter of my Thesis, the metabolism and interorganellar transport of various lipid classes are well known (see section 1.6). Based on this knowledge and considering the data presented in section 3.2, we proposed a hypothetical model of how PE21 reorganizes lipid metabolism and transport in budding yeast (Figure 3.3). The model posits that PE21 promotes the incorporation of FFA into PA; this causes a decline in the intracellular concentration of FFA and elicits a rise in the intracellular concentration of PA (Figure 3.3).

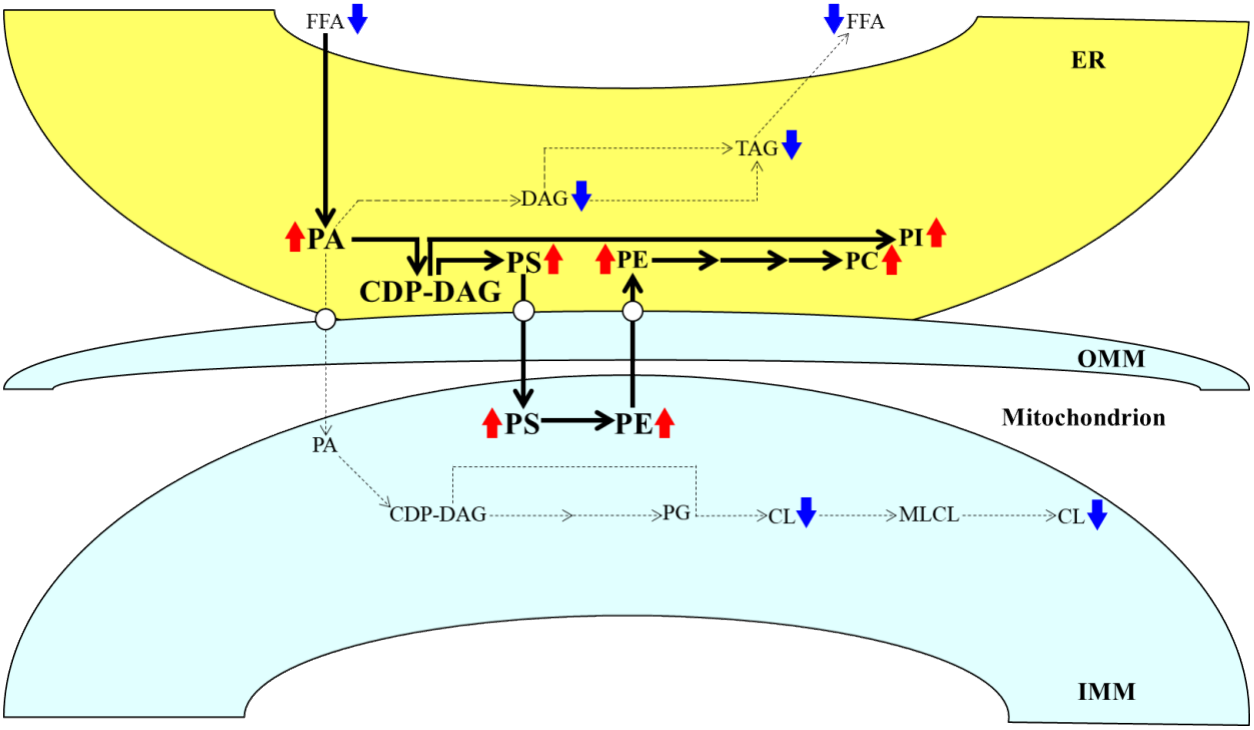

Figure 3.3. A hypothetical model posits that the observed changes in lipid concentrations within PE21-treated budding yeast are due to a specific reorganization of lipid metabolism and transport. The model predicts that PE21 alters the lipidome of budding yeast because it influences how efficiently FFA and PA are incorporated into other classes of lipids in the ER and mitochondria. Red and blue arrows next to the names of lipid classes signify those whose concentrations are increased or decreased (respectively) in response to the treatment of budding

yeast with PE21. The efficiency of FFA and PA incorporation into other lipid classes is proportional to the thickness of black arrows. See the text for more details. Abbreviations: CL, cardiolipin; CDP, cytidine diphosphate; DAG, diacylglycerol; ER, the endoplasmic reticulum; FFA, free fatty acids; IMM, inner mitochondrial membrane; MLCL, monolysocardiolipin; OMM, outer mitochondrial membrane; PA, phosphatidic acid; PC, phosphatidylcholine; PE, phosphatidylethanolamine; PG, phosphatidylglycerol; PI, phosphatidylinositol; PS, phosphatidylserine; TAG, triacylglycerol.

According to the proposed model, PE21 weakens TAG synthesis from PA in the ER; this decreases TAG concentration, lowers the concentration of FFA formed via lipolytic hydrolysis of TAG and further increases the intracellular concentration of PA (Figure 3.3). The model predicts that PE21 stimulates the incorporation of PA into the phospholipids synthesized in the ER and mitochondria; this raises the concentrations of PS, PE, PC and PI (Figure 3.3). The model further posits that PE21 attenuates the ER-to-mitochondria transport of PA; this causes a decline in the concentration of CL synthesized from PA in a series of reactions confined to the IMM (Figure 3.3).

3.4 A hypothesis on three mechanisms by which the PE21-dependent changes in the cellular lipidome might slow the chronological aging of budding yeast.

As discussed in section 3.2 of this chapter, PE21 causes substantial changes in the concentrations of different lipid classes within chronologically aging budding yeast. We explained these findings by proposing a hypothetical model of how PE21 reorganizes lipid metabolism and transport in budding yeast (see section 3.3 of this chapter). It needs to be underscored that the Titorenko laboratory has previously shown that PE21 elicits specific changes to several longevity-defining cellular processes in budding yeast [230]. These PE21-dependent changes include a rise in mitochondrial respiration, increased mitochondrial membrane potential, the altered age-related chronology of changes in cellular reactive oxygen species (ROS), lessened oxidative damage to all classes of biological macromolecules, and reduced cell susceptibility to thermal and oxidative stresses [230]. Considering all of the above, we propose three mechanisms through which the PE21-driven changes in the cellular lipidome might delay the chronological aging of budding yeast.

In the first proposed mechanism, a substantial PE21-dependent decline in intracellular FFA

is an essential contributor to the delay of yeast chronological aging by this geroprotective plant extract. We hypothesize that PE21 might slow chronological aging because it weakens a form of cell death induced by FFA concentrations exceeding a toxic threshold and/or postpones the age-related onset of this cell death mode (Figure 3.4, mechanism 1). The MS/MS-based lipidomic analysis showed that PE21 decreases intracellular FFA (Figure 3.2B). We hypothesized that the PE21-dependent decline in the intracellular FFA might be due to the ability of PE21 to intensify the incorporation of FFA into PA (Figure 3.3). The other possible contributing factor to the PE21-driven decline in the intracellular FFA is the proposed ability of PE21 to weaken TAG synthesis from PA in the ER, thus decreasing TAG concentration (Figure 3.2A) and lowering the concentration of FFA formed via lipolytic hydrolysis of TAG (Figure 3.3). It needs to be underlined that the addition of excessive quantities of FFA to budding yeast cells triggers an age-related form of regulated cell death called "liponecrosis" [83, 107, 139, 188, 286, 291-294]. After adding excessive quantities of FFA to budding yeast cells, the exogenously added form of FFA is incorporated into phospholipids and TAG [83, 107, 139, 188, 286, 291-294]. It elicits a specific reorganization of lipid metabolism and interorganellar transport [83, 107, 139, 188, 286, 291-294]. Some patterns of the FFA-dependent reorganization of lipid metabolism and interorganellar transport commit budding yeast to liponecrotic regulated cell death (RCD) or execute liponecrosis [83, 107, 139, 188, 286, 291-294]. These patterns include increased permeability of the plasma membrane (PM) to low-molecular-weight molecules, a lowered functionality of mitochondria, mitochondrial ROS overproduction, oxidative damage to the membranes surrounding many organelles and the resulting activation of the massive autophagic clearance of these organelles, oxidative damage to many proteins and the ensuing accumulation of their cytosolic aggregates [83, 107, 139, 188, 286, 291-294]. Of note, there is no evidence that genomic instability is increased in budding yeast committed to FFA-dependent liponecrotic RCD. It needs to be emphasized that PE21 affects some patterns of the FFA-driven reorganization of lipid metabolism and interorganellar transport [230]. Specifically, PE21 decelerates an aging-associated decrease in the functionality of mitochondria, alters the age-related chronology of changes in cellular ROS, and lowers the abundance of oxidatively damaged proteins [230].

In lieu of all the above, we propose that the first mechanism through which the PE21-driven changes in the cellular lipidome might delay the chronological aging of budding yeast is linked to the PE21-dependent decline in cellular FFA below the toxic threshold. This FFA decline weakens

liponecrotic RCD and/or delays the age-related onset of liponecrosis, thus increasing the probability of cell survival during the entire process of chronological aging (Figure 3.4, mechanism 1).

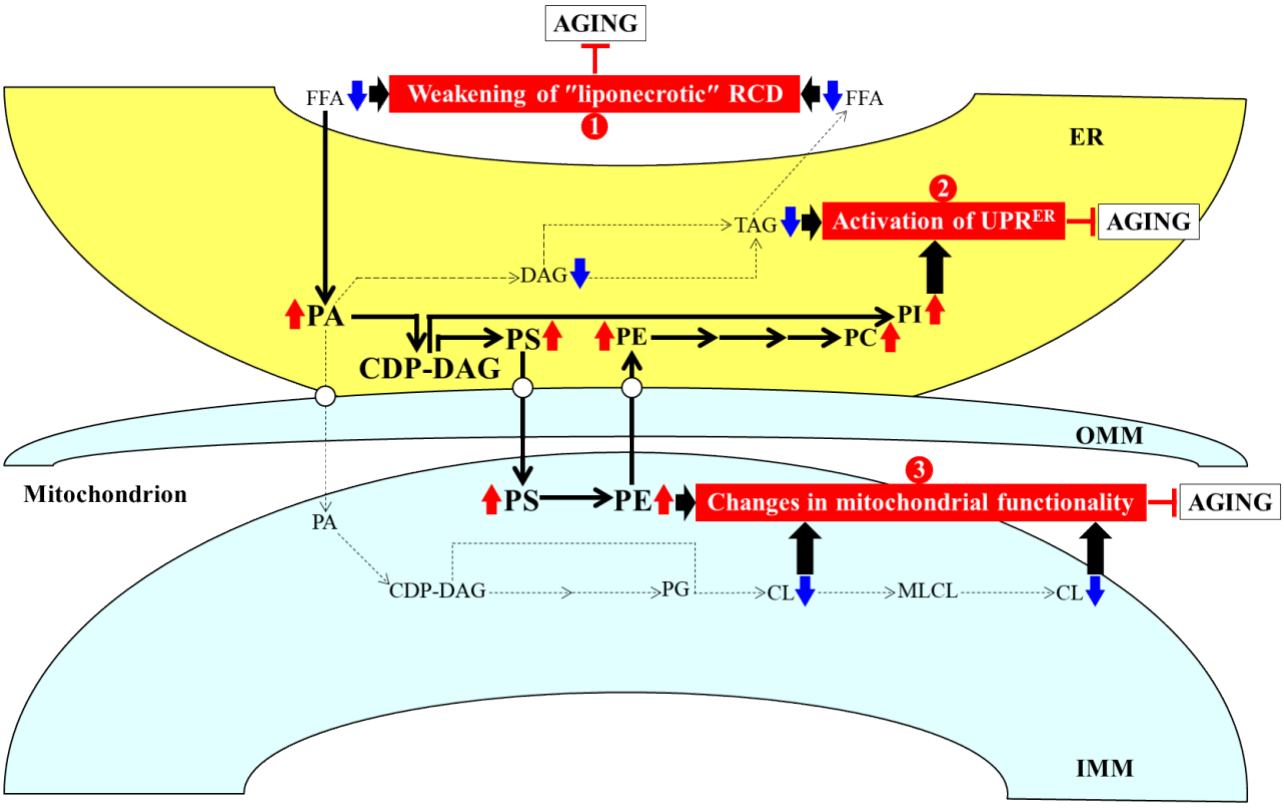

Figure 3.4. Three mechanisms by which the PE21-driven changes in the cellular lipidome might delay the chronological aging of budding yeast. Red and blue arrows next to the names of lipid classes signify those whose concentrations are increased or decreased (respectively) in response to the treatment of budding yeast with PE21. The efficiency of FFA and PA incorporation into other lipid classes is proportional to the thickness of black arrows. The proposed mechanisms are numbered. See the text for more details. Abbreviations: CDP, cytidine diphosphate; CL, cardiolipin; DAG, diacylglycerol; ER, the endoplasmic reticulum; FFA, free fatty acids; IMM, inner mitochondrial membrane; MLCL, monolysocardiolipin; OMM, outer mitochondrial membrane; PA, phosphatidic acid; PC, phosphatidylcholine; PE, phosphatidylethanolamine; PG, phosphatidylglycerol; PI, phosphatidylinositol; PS, phosphatidylserine; TAG, triacylglycerol; UPR^{ER}, the unfolded protein response in the ER.

In the second proposed mechanism, a significant PE21-dependent rise in the concentrations of ER-generated phospholipids (Figures 3.2C, 3.2D, 3.2E, 3.2F and 3.2G) and a substantial PE21-driven decline in the concentration of ER-produced TAG (Figure 3.2A) might slow chronological aging because both these alterations in the ER lipid homeostasis activate the unfolded protein response in the ER (UPR^{ER}) (Figure 3.4, mechanism 2). The activation of the UPR^{ER} in response to alterations in lipid homeostasis within the ER is a well-documented phenomenon in budding yeast and other organisms [295-318]. It mimics the activation of the UPR^{ER} in response to alterations in the homeostasis of proteins (proteostasis) within the ER [318-325]. If the UPR^{ER} system is activated (in response to the disturbances either in lipid or protein homeostasis within the ER), it enables to restore and sustain the homeostasis of both these types of macromolecules in this organette [295-325]. Once the UPR^{ER} system is activated, it restores and sustains lipid and protein homeostasis in the ER because this quality control system decreases the rate of protein synthesis on the ER-attached ribosomes, promotes *N*-linked protein glycosylation in the ER, stimulates a refolding of the ER proteins whose conformation was altered due to oxidative and/or thermal damage, assists in the ER-associated proteasomal or autophagic degradation of unfolded or misfolded proteins, activates the outward vesicular traffic for removing the improperly folded proteins from the ER, and alters the rates of lipid synthesis in the ER membrane [315, 319-325]. Because the UPR^{ER} system contributes to these essential quality control processes in the ER, it plays vital roles in regulating protein and lipid homeostasis within the entire cell, decreasing the pace of cellular and organismal aging and delaying the onset of the disorders of old age [299, 300, 302, 306, 309, 313-315, 317, 320, 324-341]. Noteworthy, PE21 influences some of the processes controlled by the UPR^{ER} system. Specifically, PE21 reduces oxidative damage to cellular lipids and proteins and decreases cell susceptibility to oxidative stress [230].

Altogether, the above data indicate that the second mechanism by which the PE21-dependent changes in the cellular lipidome might slow the chronological aging of budding yeast is due to the PE21-driven rise in the concentrations of ER-generated phospholipids and a PE21-dependent decline in the concentration of ER-produced TAG. These disturbances of the lipid homeostasis in the ER activate the pro-longevity process of UPR^{ER} (Figure 3.4, mechanism 2).

In the third proposed mechanism, PE21 might delay chronological aging because it alters the mitochondrial membrane lipidome (Figure 3.4, mechanism 3). The PE21-dependent changes in the mitochondrial membrane lipid composition include a rise in the concentration of the ER-to-

mitochondria transported lipid PS (Figure 3.2D), an increase in the concentration of the mitochondria-synthesized lipid PE (Figure 3.2E) and a decline in the concentration of CL (Figure 3.2H), a lipid synthesized in the IMM [83-86]. The mitochondrial membrane lipidome is known as an essential contributor to the functional state of mitochondria [83, 95, 142, 146-148, 153, 154, 343, 344], which plays an essential role in defining the pace of aging in chronologically aging budding yeast and evolutionarily diverse eukaryotic organisms [83, 95, 142, 146-148, 153, 154, 342-346]. It needs to be underscored that PE21 affects several patterns of the functional state of mitochondria. The effects of PE21 on mitochondrial functionality include a rise in mitochondrial respiration, increased mitochondrial membrane potential and alterations in the age-related chronology of mitochondria-generated ROS [230].

In sum, the above data support the view that the third mechanism through which the PE21-dependent alterations in the cellular lipidome might delay the chronological aging of budding yeast is due to the ability of PE21 to change the mitochondrial membrane lipidome. The PE21-induced changes in the composition of mitochondrial membrane lipids create a pro-longevity pattern of mitochondrial functionality (Figure 3.4, mechanism 3).

3.5 The experimental testing of a hypothesis about the first mechanism by which a PE21-dependent reorganization of the cellular lipidome slows budding yeast's chronological aging.

As discussed in section 3.4, we hypothesized that the first mechanism through which the PE21-driven changes in the cellular lipidome might delay the chronological aging of budding yeast is linked to the PE21-dependent decline in cellular FFA below the toxic threshold. In our hypothesis, this FFA decline weakens liponecrotic RCD and/or delays the age-related onset of liponecrosis, thus increasing the probability of cell survival during the entire process of chronological aging (Figure 3.4, mechanism 1). To test this hypothesis, we performed experiments discussed in section 3.5 of my Thesis.

The above hypothesis envisions that the mutations eliciting a rise in cellular FFA will lower the chronological aging-delaying and longevity-extending abilities of PE21 (Figure 3.4). Four single-gene-deletion mutations were selected for this type of analysis. They included the *faa1Δ*, *faa4Δ*, *ale1Δ* and *slc1Δ* mutations. These mutations eliminate the redundant enzymes needed either for FFA incorporation into FA-CoA in LD (i.e., *faa1Δ*, *faa4Δ*) or for FA-CoA incorporation into PA in the ER (i.e., *ale1Δ*, *slc1Δ*) [83, 186, 347, 348]. Each of these mutations has been shown to raise

intracellular FFA in budding yeast cultured in the nutrient-rich medium containing 1% yeast extract, 2% peptone and 2% glucose (YEPD) [169, 176, 177, 349, 350]. Yet, it was not tested if the *faa1Δ*, *faa4Δ*, *ale1Δ* and *slc1Δ* mutations similarly affect FFA concentrations in budding yeast cultured in a medium we used here, i.e., a synthetic minimal medium containing 0.67% yeast nitrogen base and 2% glucose. Therefore, we assessed the effects of *faa1Δ*, *faa4Δ*, *ale1Δ* and *slc1Δ* on both the longevity-extending efficiency of PE21 and on its ability to affect intracellular FFA in budding yeast cultured in the above synthetic minimal medium.

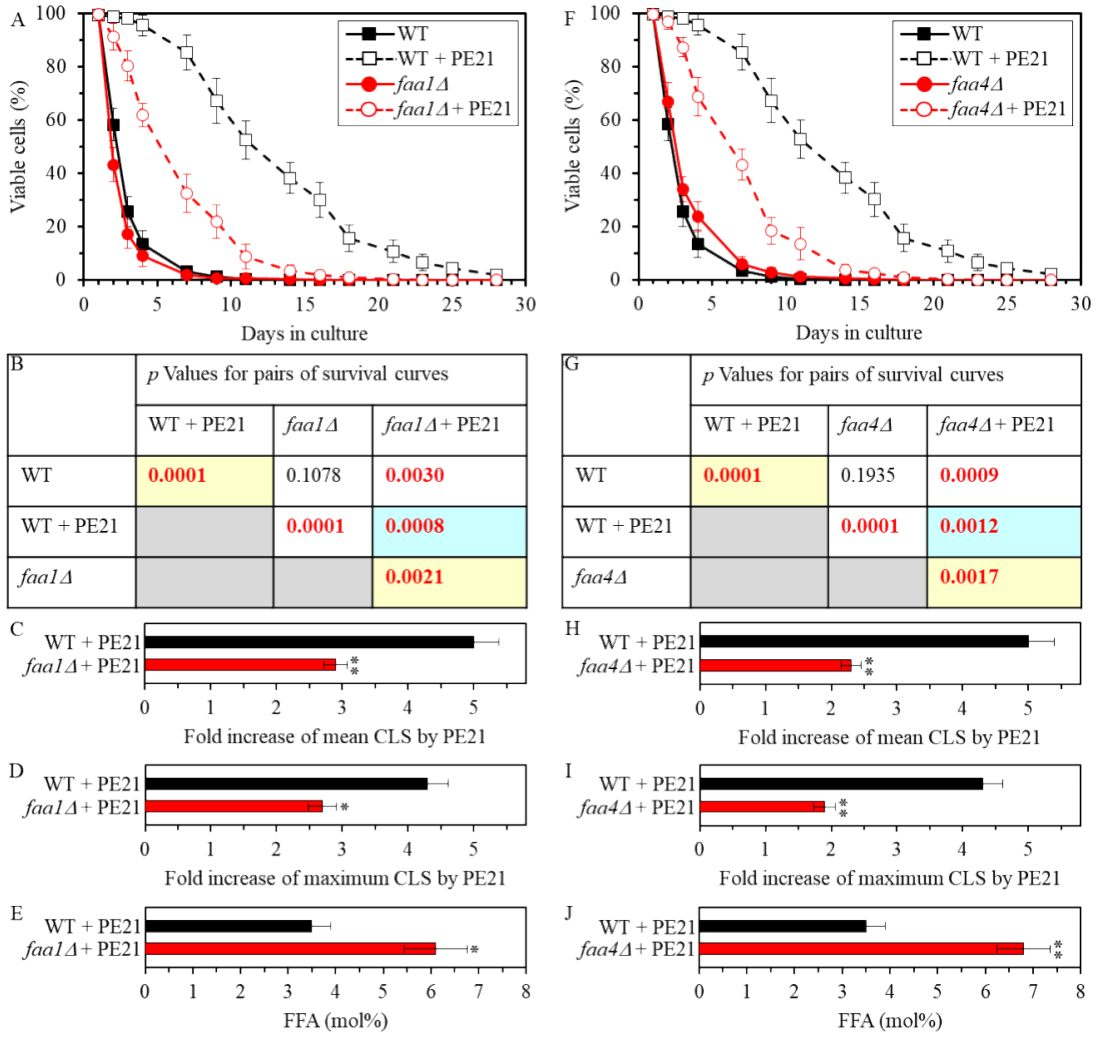

Figure 3.5. The faa1Δ and faa4Δ mutations rise intracellular FFA and reduce the longevity-extending efficiency of PE21. WT strain and mutant strains (both in the WT genetic background) were cultured in the synthetic minimal YNB medium supplemented with 2% glucose in the presence or absence of 0.1% PE21. (A, F) Survival curves of the WT and *faa1Δ* (A) or WT and

faa4Δ (F) strains are displayed as means ± SEM (n = 3). (B, G) The values of *p* for the WT and *faa1Δ* (B) or WT and *faa4Δ* (G) survival curves pairs presented in (A) or (F), respectively. The logrank test for comparing a pair of survival curves was performed as explained in the Materials and Methods chapter. PE21 statistically significantly extends the CLS of WT (B and G), *faa1Δ* (B) and *faa4Δ* (G); the *p* values for the corresponding pairs of survival curves are shown on yellow color background. PE21 extends the CLS of *faa1Δ* (B) and *faa4Δ* (G) to a lower extent than that of WT (B and G); the *p* values for the corresponding pairs of survival curves are shown on blue color background. (C, D, H, I) The fold of the PE21-dependent extension of the mean CLS (C, H) or maximum CLS (D, I) for WT and *faa1Δ* (C, D) or WT and *faa4Δ* (H, I); the fold extension values were calculated from the survival curves in (A) and (F) and are displayed as means ± SEM (n = 3; *$p < 0.05$; **$p < 0.01$). (E, J) The maximum concentrations of FFA in WT and *faa1Δ* (E) or WT and *faa4Δ* (J) cells are shown in mol% as means ± SEM (n = 4; *$p < 0.05$; **$p < 0.01$); these FFA concentrations were detected in WT and mutant cells on day 3 of culturing in the presence of PE21.

Our assessment has revealed that the *faa1Δ* and *faa4Δ* mutations decrease the longevity-extending efficiency of PE21 (Figures 3.5A, 3.5B, 3.5F and 3.5G), lower the fold increase by PE21 for both the mean and maximum CLS (Figures 3.5C, 3.5D, 3.5H and 3.5I), and raise intracellular FFA (Figures 3.5E and 3.5J). The effects of the *ale1Δ* and *slc1Δ* mutations on the longevity-extending efficiency of PE21 (Figures 3.6A, 3.6B, 3.6F and 3.6G), the fold increase by PE21 for both the mean and maximum CLS (Figures 3.6C, 3.6D, 3.6H and 3.6I), and intracellular FFA (Figures 3.6E and 3.6J) were qualitatively similar (but not quantitively identical) to the ones observed for *faa1Δ* and *faa4Δ*. Of note, the quantitative effects on the PE21-dependent fold increase of the mean and maximum CLS and the PE21-driven rise of intracellular FFA were different for *faa1Δ*, *faa4Δ*, *ale1Δ* and *slc1Δ* (Figures 3.5C, 3.5D, 3.5H, 3.5I, 3.6C, 3.6D, 3.6H and 3.6I). The above data confirm our prediction that the mutations that increase cellular FFA cause a decline in the chronological aging-delaying and longevity-extending abilities of PE21.

The proposed hypothesis about the first mechanism by which a PE21-dependent reorganization of the cellular lipidome slows budding yeast's chronological aging also predicts that the mutations causing a decline in cellular FFA will increase the chronological aging-delaying

and longevity-extending abilities of PE21 (Figure 3.4). We selected four single-gene-deletion mutations to test this prediction. These mutations are *tgl1Δ*, *tgl3Δ*, *tgl4Δ* and *tgl5Δ*. Each of them eliminates a redundant enzyme involved in the lipolytic hydrolysis of TAG yielding FFA in LD [83, 179, 187, 351-356]. *tgl1Δ*, *tgl3Δ*, *tgl4Δ* and *tgl5Δ* are known to decrease intracellular FFA in budding yeast cultured in the nutrient-rich medium supplemented with 1% yeast extract, 2% peptone and 2% glucose [104, 351-353, 356, 357]. However, whether *tgl1Δ*, *tgl3Δ*, *tgl4Δ* and *tgl5Δ* lower intracellular FFA in budding yeast cultured in a synthetic minimal medium supplemented with 0.67% yeast nitrogen base and 2% glucose was unknown. We, therefore, examined how each of these mutations influences the efficiency of longevity extension by PE21 and how it affects intracellular FFA when budding yeast cells were cultured in the above synthetic minimal medium.

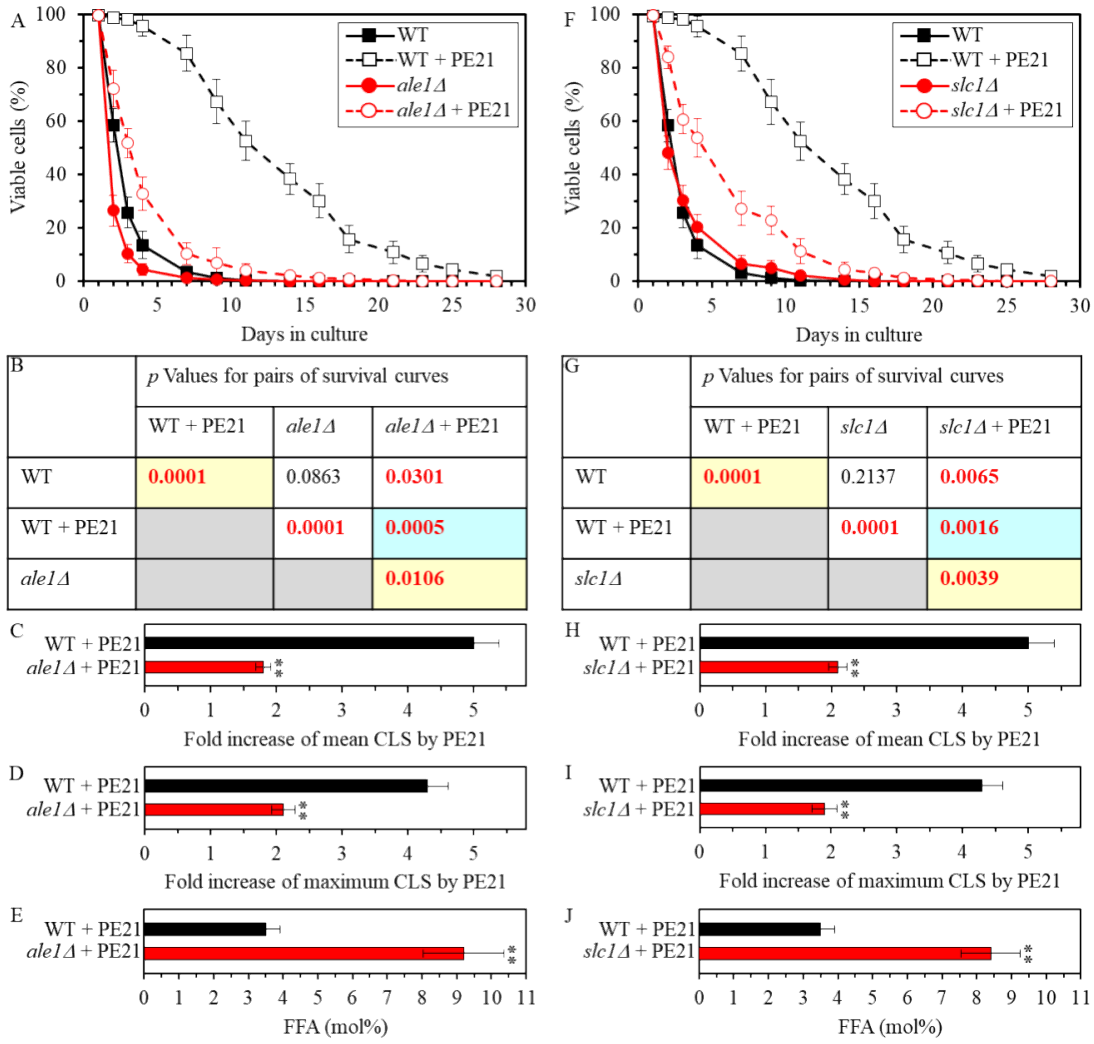

Figure 3.6. The ale1Δ and slc1Δ mutations increase intracellular FFA and weaken the ability of PE21 to prolong the longevity of chronologically aging buffing yeast. WT and mutant strains

in the same genetic background were cultured in the synthetic minimal YNB medium supplemented with 2% glucose in the presence or absence of 0.1% PE21. (A, F) Survival curves of the WT and *ale1Δ* (A) or WT and *slc1Δ* (F) strains are shown as means ± SEM (n = 3). (B, G) *p* Values for the survival curves pairs of the WT and *ale1Δ* (B) or WT and *slc1Δ* (G) strains; survival curves pairs presented in (A) or (F), respectively, were compared. The logrank test for comparing a pair of survival curves was conducted as described in the Materials and Methods chapter. PE21 statistically significantly prolongs the CLS of WT (B and G), *ale1Δ* (B) and *slc1Δ* (G); the *p* values for the corresponding pairs of survival curves are displayed on yellow color background. PE21 prolongs the CLS of *ale1Δ* (B) and *slc1Δ* (G) to a lesser degree than that of WT (B and G); the *p* values for the corresponding pairs of survival curves are displayed on blue color background. (C, D, H, I) The fold of the PE21-dependent increase of the mean CLS (C, H) or maximum CLS (D, I) for WT and *ale1Δ* (C, D) or WT and *slc1Δ* (H, I); the fold increase values were calculated from the survival curves in (A) and (F) and are presented as means ± SEM (n = 3; $^{**}p < 0.01$). (E, J) The maximum concentrations of FFA in WT and *ale1Δ* (E) or WT and *slc1Δ* (J) cells are provided in mol% as means ± SEM (n = 4; $^{**}p < 0.01$); these FFA concentrations were detected in WT and mutant cells on day 3 of culturing in the presence of PE21.

We found that the *tgl1Δ* and *tgl3Δ* mutations enhance the ability of PE21 to prolong the longevity of chronologically aging budding yeast (Figures 3.7A, 3.7B, 3.7F and 3.7G), amplify the fold increase by PE21 for both the mean and maximum CLS (Figures 3.7C, 3.7D, 3.7H and 3.7I), and lower intracellular FFA (Figures 3.7E and 3.7J). The *tgl4Δ* and *tgl5Δ* mutations exhibited qualitatively similar (but not quantitively identical) effects on the PE21-dependent longevity extension of chronologically aging yeast (Figures 3.8A, 3.8B, 3.8F and 3.8G), fold increase for both the mean and maximum CLS (Figures 3.8C, 3.8D, 3.8H and 3.8I), and decline in intracellular FFA (Figures 3.8E and 3.8J). It needs to be underscored that the *tgl1Δ*, *tgl3Δ*, *tgl4Δ* and *tgl5Δ* mutations had different quantitative effects on the PE21-dependent fold increase of the mean and maximum CLS and the PE21-driven decline in intracellular FFA (Figures 3.7C, 3.7D, 3.7H, 3.7I, 3.8C, 3.8D, 3.8H and 3.8I). The data presented in Figures 3.7 and 3.8) support our expectation that the single-gene mutations eliciting a decline in cellular FFA enhance the chronological aging-delaying and longevity-extending abilities of PE21. In the future, it would be interesting to test effects of double mutations in the *TGL* genes on cellular FFA and the ability of

PE21 to extend longevity.

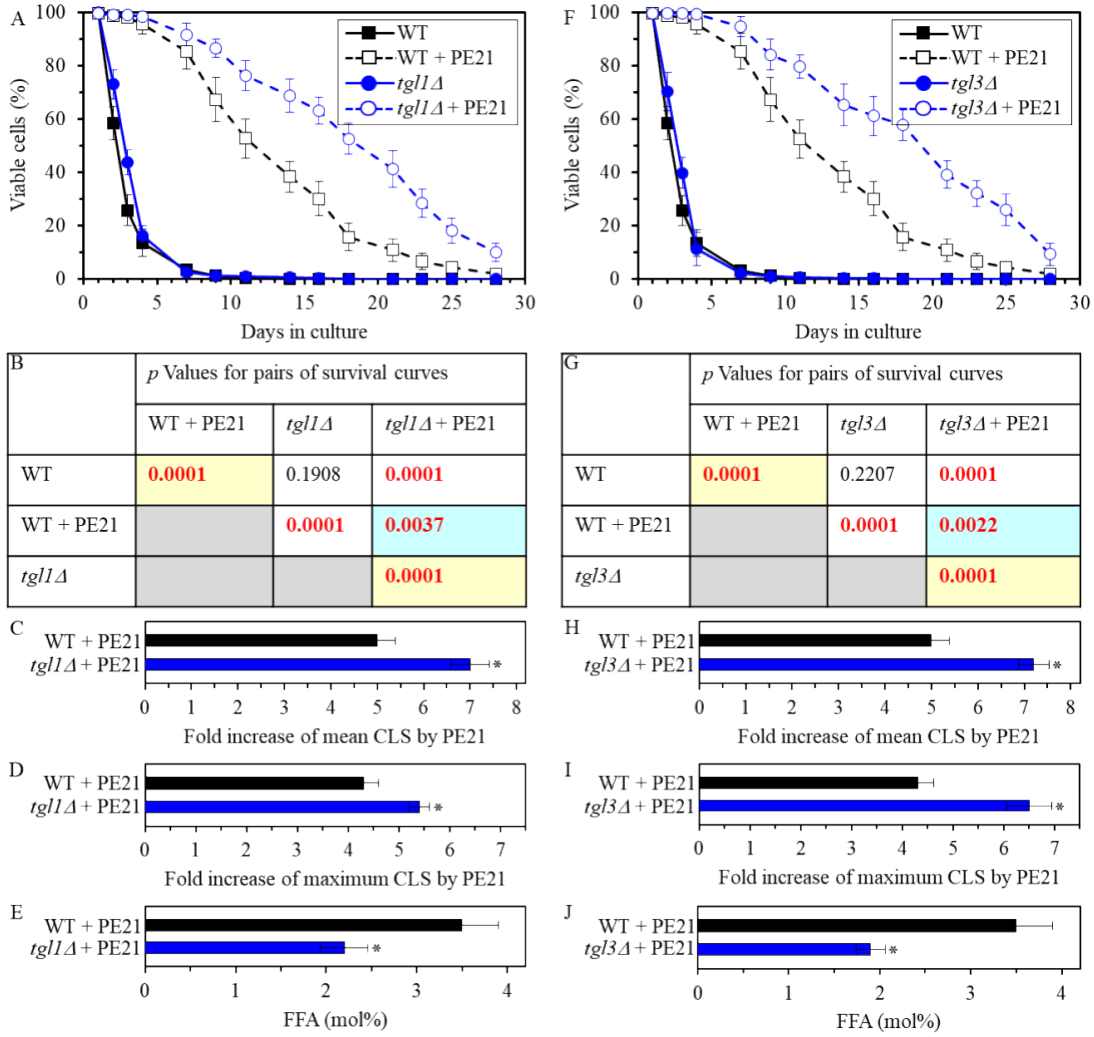

Figure 3.7. The tgl1Δ and tgl3Δ mutations decrease intracellular FFA and enhance the ability of PE21 to prolong the longevity of chronologically aging budding yeast. WT strain and mutant strains (both in the WT genetic background) were cultured in the synthetic minimal YNB medium supplemented with 2% glucose in the presence or absence of 0.1% PE21. (A, F) Survival curves of the WT and *tgl1Δ* (A) or WT and *tgl3Δ* (F) strains are displayed as means ± SEM (n = 3). (B, G) The values of *p* for the WT and *tgl1Δ* (B) or WT and *tgl3Δ* (G) survival curves pairs presented in (A) or (F), respectively. The logrank test for comparing a pair of survival curves was performed as explained in the Materials and Methods chapter. PE21 statistically significantly extends the CLS

of WT (B and G), *tgl1Δ* (B) and *tgl3Δ* (G); the *p* values for the corresponding pairs of survival curves are shown on yellow color background. PE21 extends the CLS of *tgl1Δ* (B) and *tgl3Δ* (G) to a greater extent than that of WT (B and G); the *p* values for the corresponding pairs of survival curves are shown on blue color background. (C, D, H, I) The fold of the PE21-dependent extension of the mean CLS (C, H) or maximum CLS (D, I) for WT and *tgl1Δ* (C, D) or WT and *tgl3Δ* (H, I); the fold extension values were calculated from the survival curves in (A) and (F) and are displayed as means ± SEM (n = 3; **p* < 0.05). (E, J) The maximum concentrations of FFA in WT and *faa1Δ* (E) or WT and *faa4Δ* (J) cells are shown in mol% as means ± SEM (n = 4; **p* < 0.05); these FFA concentrations were detected in WT and mutant cells on day 3 of culturing in the presence of PE21.

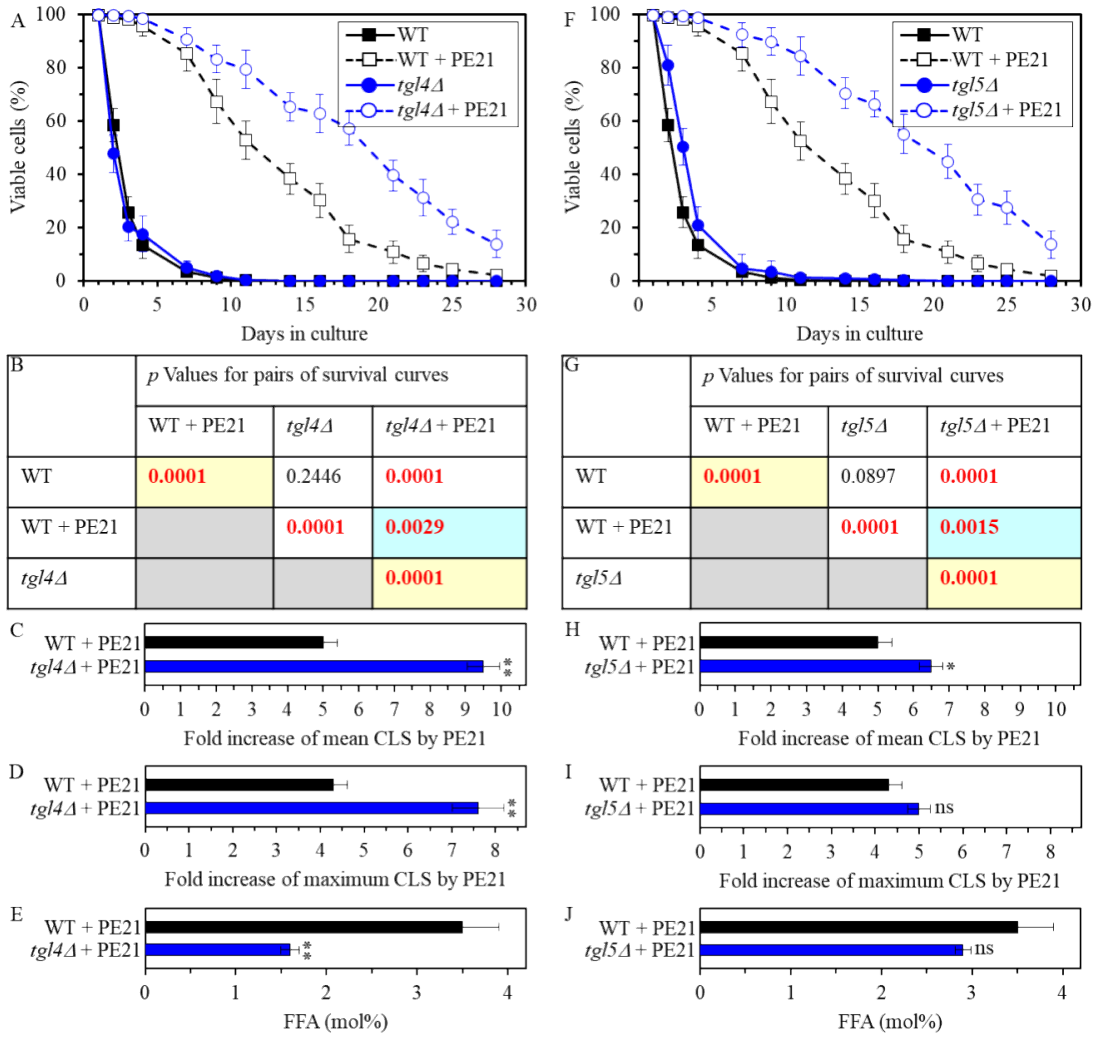

Figure 3.8. The tgl4Δ and tgl5Δ mutations decrease intracellular FFA and enhance the ability

of PE21 to prolong the longevity of chronologically aging buffing yeast. WT and mutant strains in the same genetic background were cultured in the synthetic minimal YNB medium supplemented with 2% glucose in the presence or absence of 0.1% PE21. (A, F) Survival curves of the WT and *tgl4Δ* (A) or WT and *tgl5Δ* (F) strains are shown as means ± SEM (n = 3). (B, G) *p* Values for the survival curves pairs of the WT and *tgl4Δ* (B) or WT and *tgl5Δ* (G) strains; survival curves pairs presented in (A) or (F), respectively, were compared. The logrank test for comparing a pair of survival curves was conducted as described in the Materials and Methods chapter. PE21 statistically significantly prolongs the CLS of WT (B and G), *tgl4Δ* (B) and *tgl5Δ* (G); the *p* values for the corresponding pairs of survival curves are displayed on yellow color background. PE21 prolongs the CLS of *tgl4Δ* (B) and *tgl5Δ* (G) to a greater extent than that of WT (B and G); the *p* values for the corresponding pairs of survival curves are displayed on blue color background. (C, D, H, I) The fold of the PE21-dependent increase of the mean CLS (C, H) or maximum CLS (D, I) for WT and *tgl4Δ* (C, D) or WT and *tgl5Δ* (H, I); the fold increase values were calculated from the survival curves in (A) and (F) and are presented as means ± SEM (n = 3; $^{**}p < 0.01$). (E, J) The maximum concentrations of FFA in WT and *tgl4Δ* (E) or WT and *tgl5Δ* (J) cells are provided in mol% as means ± SEM (n = 4; $^{**}p < 0.01$); these FFA concentrations were detected in WT and mutant cells on day 3 of culturing in the presence of PE21.

Figures 3.5 to 3.8 provide data for two pairwise combinations of the variables observed in the WT, *faa1Δ*, *faa4Δ*, *ale1Δ*, *slc1Δ*, *tgl1Δ*, *tgl3Δ*, *tgl4Δ* and *tgl5Δ* strains. One pairwise combination of the variables included the PE21-dependent fold increase of the mean CLS for a particular strain and the highest FFA concentrations in the cells of this strain cultured with PE21. The other pairwise combination of the variables included the PE21-dependent fold increase of the maximum CLS for a particular strain and the highest FFA concentrations in the cells of this strain cultured with PE21. Of note, the highest intracellular FFA concentrations in the WT and all mutant strains were detected on day 3 of culturing in the presence of PE21. To assess the correlation between the variables within each of these two pairwise combinations, we calculated the Pearson's correlation coefficient (*r*) value for each pair of variables. We found that the Pearson's *r* value is less than -0.9 for each pair of compared variables (Figure 3.9). This Pearson's *r* value is indicative of a very strong negative correlation between the two compared variables [358]. We, therefore, concluded that the PE21-dependent fold increase of the mean or maximum CLS is inversely

proportional to the intracellular concentration of FFA. These findings confirm our hypothesis about the first mechanism through which a PE21-dependent reorganization of the cellular lipidome slows budding yeast's chronological aging. Indeed, these findings provide evidence that a PE21-dependent decline in intracellular FFA is an essential contributor to the delay of yeast chronological aging by this geroprotective plant extract.

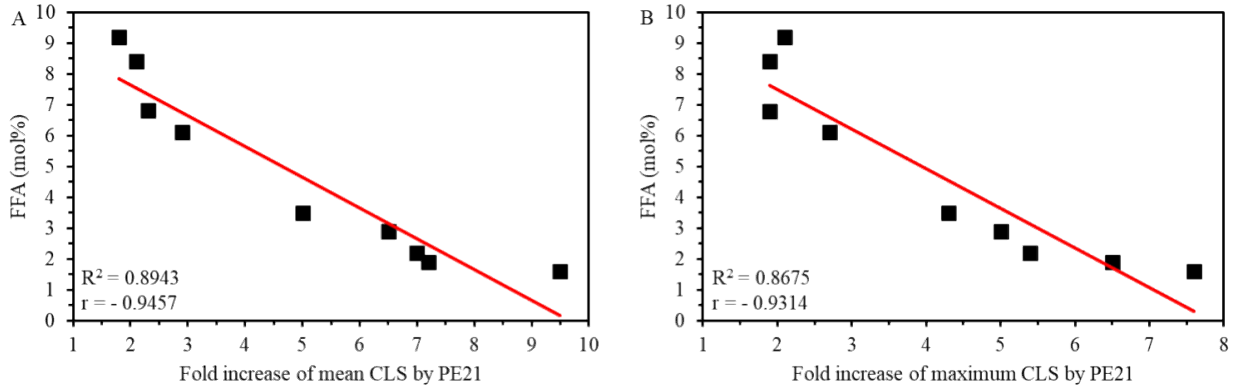

C

Genetic background	Fold increase of mean CLS by PE21	Fold increase of maximum CLS by PE21	FFA concentration (mol%)
tgl4Δ	9.5 ± 0.5	7.6 ± 0.6	1.6 ± 0.1
tgl3Δ	7.2 ± 0.3	6.5 ± 0.4	1.9 ± 0.2
tgl1Δ	7.0 ± 0.4	5.4 ± 0.2	2.2 ± 0.3
tgl5Δ	6.5 ± 0.3	5.0 ± 0.2	2.9 ± 0.1
WT	5.0 ± 0.4	4.3 ± 0.3	3.5 ± 0.4
faa1Δ	2.9 ± 0.2	2.7 ± 0.2	6.1 ± 0.7
faa4Δ	2.3 ± 0.2	1.9 ± 0.1	6.8 ± 0.6
slc1Δ	2.1 ± 0.1	1.9 ± 0.2	8.4 ± 0.9
ale1Δ	1.8 ± 0.1	2.1 ± 0.2	9.2 ± 1.2

Figure 3.9. The PE21-dependent fold increase of the mean or maximum CLS is inversely proportional to the intracellular concentration of FFA. WT and *faa1Δ*, *faa4Δ*, *ale1Δ*, *slc1Δ*, *tgl1Δ*, *tgl3Δ*, *tgl4Δ* and *tgl5Δ* mutant strains in the same genetic background were cultured in the synthetic minimal YNB medium supplemented with 2% glucose in the presence of 0.1% PE21. The PE21-dependent fold increase of the mean or maximum CLS for the WT, *faa1Δ*, *faa4Δ*, *ale1Δ*, *slc1Δ*, *tgl1Δ*, *tgl3Δ*, *tgl4Δ* and *tgl5Δ* strains was calculated using the cell survival curves presented in Figures 3.5A, 3.5F, 3.6A, 3.6F, 3.7A, 3.7F, 3.8A and 3.8F. The values of the PE21-dependent fold increase of the mean or maximum CLS for these strains are shown in Figures 3.5C, 3.5D,

3.5H, 3.5I, 3.6C, 3.6D, 3.6H, 3.6I, 3.7C, 3.7D, 3.7H, 3.7I, 3.8C, 3.8D, 3.8H and 3.8I. (A, B) The comparison plots for the values of the PE21-dependent fold increase of the mean (A) or maximum (B) CLS and the highest intracellular concentrations of FFA. Data for the WT, *faa1Δ*, *faa4Δ*, *ale1Δ*, *slc1Δ*, *tgl1Δ*, *tgl3Δ*, *tgl4Δ* and *tgl5Δ* strains are provided in (A) and (B). The panels (A) and (B) show linear trendlines; the R-squared values are provided as evidence that each of these trendlines is a good fit for the data. The panels (A) and (B) also provide the values of the Pearson's correlation coefficient (*r*) for each pair of variables; these values prove the existence of a very strong negative correlation between the two compared variables. (C) Genetic backgrounds of the strains, the values of the PE21-dependent fold increase for the mean or maximum CLS for a particular strain, and the values of the highest FFA concentration detected in a particular strain are provided (As noted above, the highest intracellular FFA concentrations in the WT and all mutant strains were detected on day 3 of culturing in the presence of PE21). The values of the PE21-dependent fold increase for the mean or maximum CLS, and the values of the highest FFA concentrations provided in (C) were used to generate the comparison plots in (A) and (B). Data are shown as means ± SEM (n = 4). Abbreviation: FFA, free fatty acids.

In our hypothesis about the first mechanism through which a PE21-dependent reorganization of the cellular lipidome slows budding yeast's chronological aging, the PE21-driven decline in intracellular FFA weakens liponecrotic RCD and/or delays the age-related onset of liponecrosis, thus increasing the probability of cell survival during the entire process of chronological aging (Figure 3.4, mechanism 1). To test this aspect of our hypothesis, we assessed how the *faa1Δ*, *faa4Δ*, *ale1Δ*, *slc1Δ*, *tgl1Δ*, *tgl3Δ*, *tgl4Δ* and *tgl5Δ* mutations influence the percentage of yeast cells undergoing necrotic RCD within a yeast culture permanently exposed to 0.1% PE21. One of the hallmarks of the necrotic mode of RCD in budding yeast is the loss of plasma membrane (PM) integrity due to PM damage [104, 107, 134, 286, 291-294]. The percentage of cells that had lost PM integrity can be examined using fluorescence microscopy of yeast treated with propidium iodide (PID), a membrane impermeant fluorescent dye [104, 291]. Only the cells whose PM is damaged because they undergo necrotic RCD exhibit PI-positive staining [104, 291].

We found that the *faa1Δ*, *faa4Δ*, *ale1Δ*, *slc1Δ* mutations accelerate necrotic RCD in yeast cell cultures containing 0.1% PE21 (Figures 3.10A-3.10D and 3.10J); indeed, the percentage of PI-positive cells in PE21-treated *faa1Δ*, *faa4Δ*, *ale1Δ*, *slc1Δ* cell populations exceeded that in

PE21-treated WT cell populations once these cell populations enter day 3 of culturing (Figures 3.10A-3.10D and 3.10J). In contrast, the *tgl1Δ*, *tgl3Δ*, *tgl4Δ* and *tgl5Δ* mutations decelerated necrotic RCD in yeast cell cultures supplemented with 0.1% PE21 (Figures 3.10E-3.10H and 3.10J); in fact, the percentage of PI-positive cells in PE21-treated WT cell populations surpassed that in PE21-treated *tgl1Δ, tgl3Δ, tgl4Δ* and *tgl5Δ* cell populations once these cell populations enter day 3 of culturing (Figures 3.10E-3.10H and 3.10J).

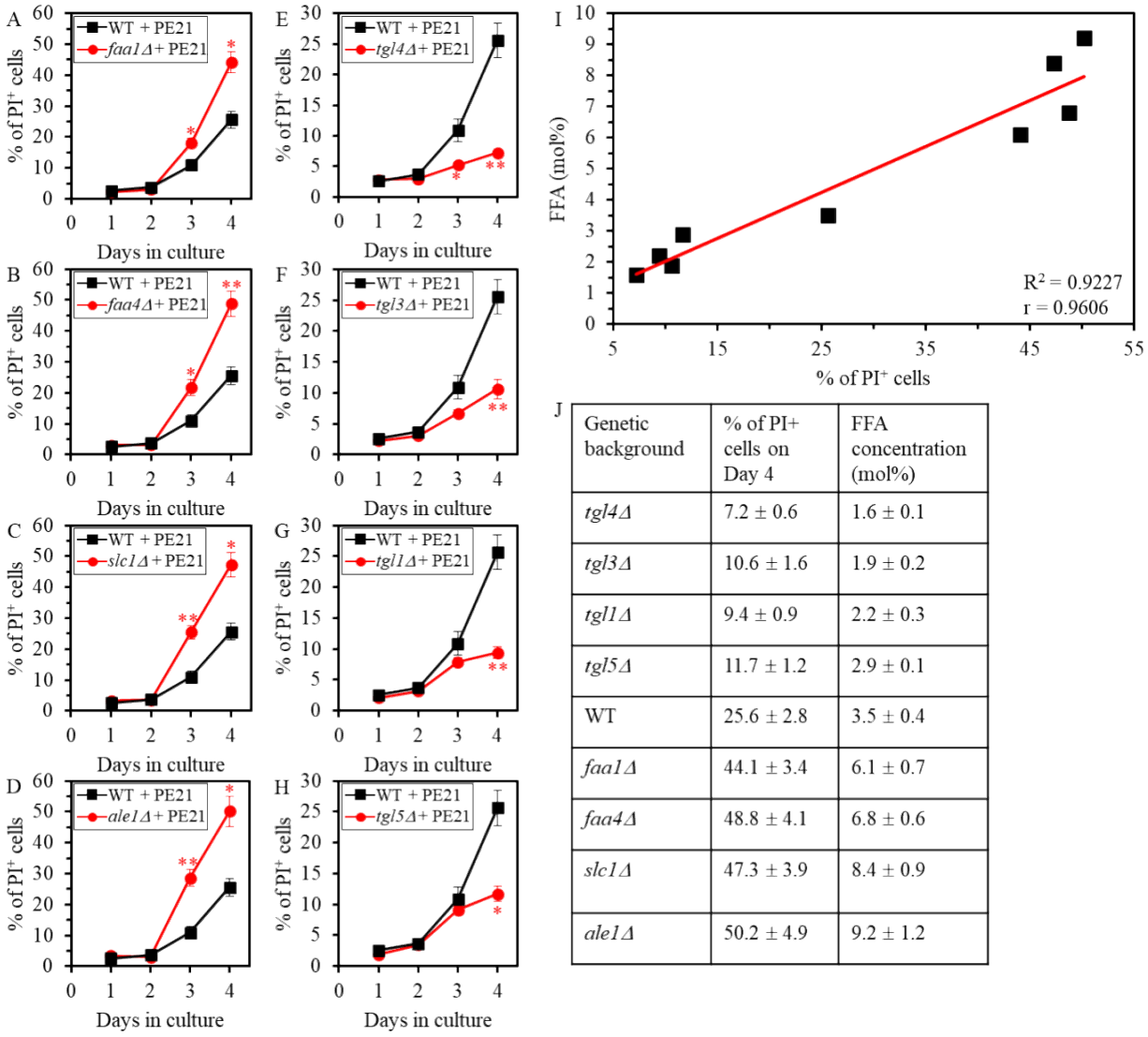

J

Genetic background	% of PI+ cells on Day 4	FFA concentration (mol%)
tgl4Δ	7.2 ± 0.6	1.6 ± 0.1
tgl3Δ	10.6 ± 1.6	1.9 ± 0.2
tgl1Δ	9.4 ± 0.9	2.2 ± 0.3
tgl5Δ	11.7 ± 1.2	2.9 ± 0.1
WT	25.6 ± 2.8	3.5 ± 0.4
faa1Δ	44.1 ± 3.4	6.1 ± 0.7
faa4Δ	48.8 ± 4.1	6.8 ± 0.6
slc1Δ	47.3 ± 3.9	8.4 ± 0.9
ale1Δ	50.2 ± 4.9	9.2 ± 1.2

Figure 3.10. The percentage of PID-positive necrotic cells is directly proportional to the intracellular concentration of FFA. WT and *faa1Δ*, *faa4Δ*, *ale1Δ*, *slc1Δ*, *tgl1Δ*, *tgl3Δ*, *tgl4Δ* and *tgl5Δ* mutant strains in the same genetic background were cultured in the synthetic minimal YNB medium supplemented with 2% glucose in the presence of 0.1% PE21. (A-H) After culture aliquots

were recovered on days 1, 2, 3 and 4, the cells were subjected to propidium iodide (PID) staining and analyzed by fluorescence microscopy. Only the cells with damaged plasma membrane because they undergo necrotic RCD exhibited PI-positive staining. The values of the percentage of PI-positive cells on different days of culturing are presented as means ± SEM (n = 3; *p < 0.05; **p < 0.01). (I) The correlation plot between the maximum percentage of PI-positive necrotic cells and the highest intracellular FFA concentration for WT and mutant cells exhibiting different values of these two compared variables. The maximum percentage of cells exhibiting PI-positive necrotic staining was detected on day 4 of culturing for all strains used. The highest concentration of FFA in cells of all these stains was observed on day 3 of culturing. The correlation plot shows a linear trendline; the R-squared value is provided as evidence that the trendline is a good fit for the data. The correlation plot also displays the value of the Pearson's correlation coefficient (*r*) for the pair of variables; this value proves the existence of a very strong positive correlation between the two compared variables. (J) Genetic backgrounds of the strains, the values of the maximum percentage of PI-positive necrotic cells for a particular strain and the values of the highest intracellular FFA concentration detected in a particular strain are provided. The values of the maximum percentage of PI-positive necrotic cells and the values of the highest intracellular FFA concentration provided in (J) were used to generate the correlation plot in (I). The values in (J) are displayed as means ± SEM (n = 3). Abbreviation: FFA, free fatty acids.

Of note, the maximum percentage of cells exhibiting PI-positive staining (and, thus, undergoing necrotic RCD) was detected on day 4 of culturing WT, *faa1Δ, faa4Δ, ale1Δ, slc1Δ, tgl1Δ, tgl3Δ, tgl4Δ and tgl5Δ* cells in the presence of 0.1% PE21 (Figures 3.10A-3.10H and 3.10J). The highest concentration of FFA in cells of all these stains was observed on day 3 of culturing in the presence of 0.1% PE21 (Figures 3.10J). To assess the correlation between the maximum percentage of PI-positive (i.e., necrotic) cells and the highest intracellular FFA concentration, we calculated Pearson's *r* value for this pair of compared variables. We found that this Pearson's *r* value is more than 0.9 (Figure 3.10I). This Pearson's *r* value proves the existence of a very strong positive correlation between the two compared variables [358]. Thus, the maximum percentage of PI-positive (i.e., necrotic) cells is directly proportional to intracellular FFA concentration. This observation further supports our hypothesis about the first mechanism by which a PE21-dependent reorganization of the cellular lipidome delays chronological aging. It demonstrates that the PE21-

dependent decline in intracellular FFA weakens a necrotic mode of RCD.

A 2-h exposure of budding yeast cells to 0.1 mM palmitoleic acid (POA), a monounsaturated form of FFA containing 16 carbon atoms, triggers liponecrotic RCD [107, 139, 291, 292]. As the further test of our hypothesis about the first mechanism through which a PE21-dependent reorganization of the cellular lipidome slows budding yeast's chronological aging, we assessed how the *faa1Δ*, *faa4Δ*, *ale1Δ*, *slc1Δ*, *tgl1Δ*, *tgl3Δ*, *tgl4Δ* and *tgl5Δ* mutations influence yeast susceptibility to the POA-induced liponecrosis within a yeast culture permanently exposed to 0.1% PE21. A decline in clonogenic survival (i.e., the ability to form a colony on the surface of a nutrient-rich solid medium) of yeast exposed to POA for 2 h was used to examine the extent of liponecrotic RCD.

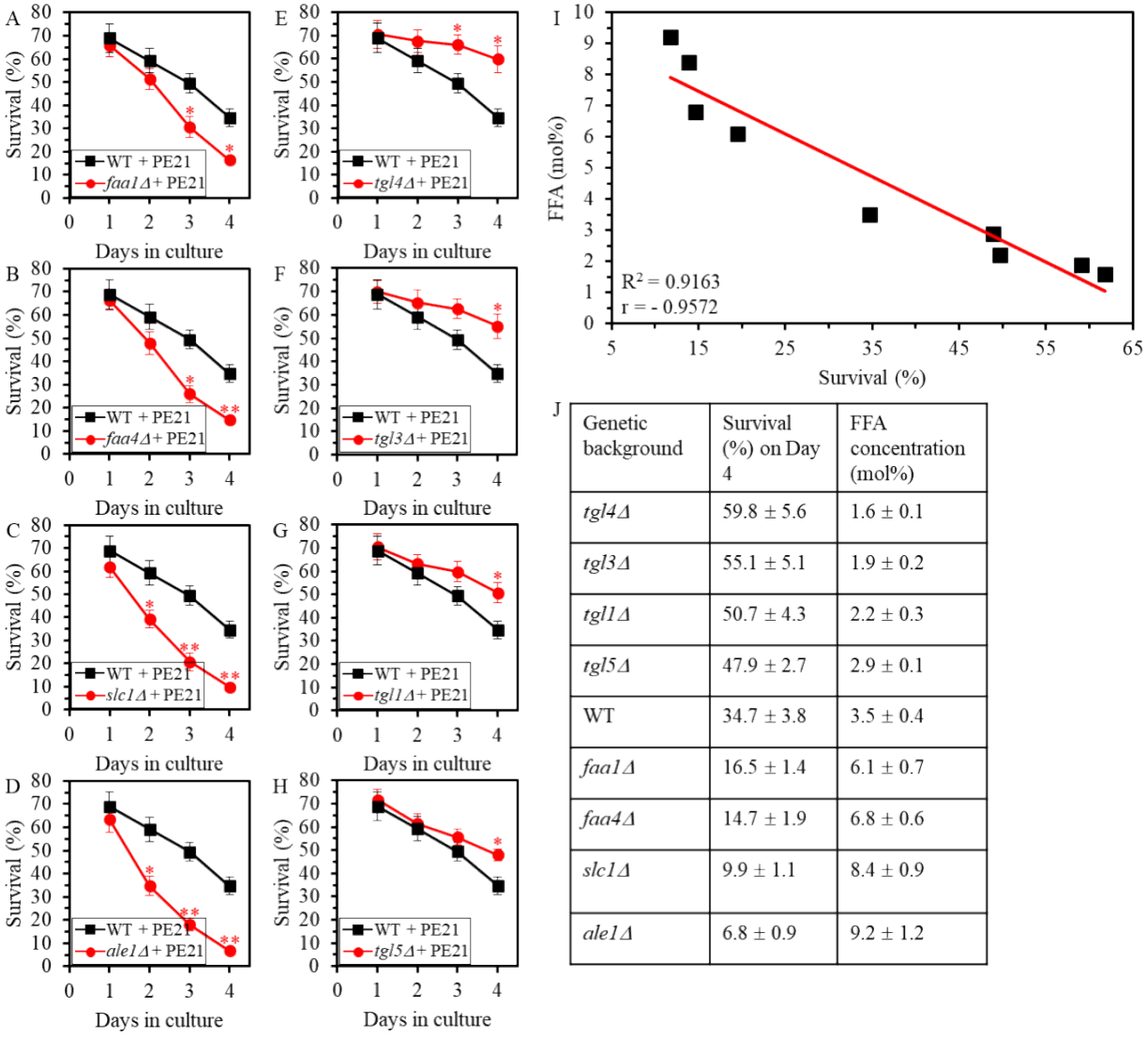

J

Genetic background	Survival (%) on Day 4	FFA concentration (mol%)
tgl4Δ	59.8 ± 5.6	1.6 ± 0.1
tgl3Δ	55.1 ± 5.1	1.9 ± 0.2
tgl1Δ	50.7 ± 4.3	2.2 ± 0.3
tgl5Δ	47.9 ± 2.7	2.9 ± 0.1
WT	34.7 ± 3.8	3.5 ± 0.4
faa1Δ	16.5 ± 1.4	6.1 ± 0.7
faa4Δ	14.7 ± 1.9	6.8 ± 0.6
slc1Δ	9.9 ± 1.1	8.4 ± 0.9
ale1Δ	6.8 ± 0.9	9.2 ± 1.2

Figure 3.11. Cell susceptibility to the POA-induced liponecrotic RCD is directly proportional to the intracellular concentration of FFA. WT and *faa1Δ*, *faa4Δ*, *ale1Δ*, *slc1Δ*, *tgl1Δ*, *tgl3Δ*, *tgl4Δ* and *tgl5Δ* mutant strains in the same genetic background were cultured in the synthetic minimal YNB medium supplemented with 2% glucose and 0.1% PE21. (A-H) Culture aliquots were taken on days 1, 2, 3 and 4 of culturing. Each aliquot was treated with 0.1 mM palmitoleic acid (POA) for 2 h. A decrease in clonogenic survival (i.e., the ability to form a colony on the surface of a nutrient-rich solid medium) of yeast treated with POA for 2 h was used to assess the extent of liponecrotic RCD. The values of the minimum percentage of clonogenic survival for POA-treated cells (in %) on different days of culturing are presented as means ± SEM (n = 3; *p < 0.05; **p < 0.01). (I) The correlation plot between the minimum clonogenic survival of POA-treated cells and the highest intracellular FFA concentration observed in WT and mutant cells exhibiting different values of these two compared variables. The minimum percentage of clonogenic survival of POA-treated cells was observed on day 4 of culturing WT, *faa1Δ, faa4Δ, ale1Δ, slc1Δ, tgl1Δ, tgl3Δ, tgl4Δ* and *tgl5Δ* cells in the presence of 0.1% PE21. The highest concentration of FFA in cells of all these stains was observed on day 3 of cell culturing with 0.1% PE21. The correlation plot shows a linear trendline. The trendline is a good fit for the data, as evident from the R-squared value provided on the correlation plot. The plot also shows the value of the Pearson's correlation coefficient (*r*) for the pair of variables; this value proves the existence of a very strong negative correlation between cell resistance to the POA-induced liponecrotic RCD and intracellular FFA concentration. (J) Genetic backgrounds of the strains, the values of the minimum percentage of clonogenic survival of POA-treated cells for a particular strain and the values of the highest intracellular FFA concentration detected in a particular strain are shown. The values of the minimum percentage of clonogenic survival of POA-treated cells and the values of the highest intracellular FFA concentration shown in (J) were used to create the correlation plot in (I). The values in (J) are provided as means ± SEM (n = 3). Abbreviation: FFA, free fatty acids.

We found that the *faa1Δ*, *faa4Δ*, *ale1Δ*, *slc1Δ* mutations make PE21-exposed yeast more susceptible to the POA-induced liponecrotic RCD (Figures 3.11A-3.11D and 3.11J); indeed, the percentage of PE21-exposed WT cells that survive a 2-h treatment with POA exceeded that of PE21-exposed *faa1Δ*, *faa4Δ*, *ale1Δ*, *slc1Δ* cells treated with POA for 2 h once the WT and mutant cell populations enter day 2 of culturing (Figures 3.11A-3.11D and 3.11J). In contrast, the *tgl1Δ*,

tgl3Δ, *tgl4Δ* and *tgl5Δ* mutations make PE21-exposed yeast more resistant to the POA-induced liponecrotic RCD (Figures 3.11E-3.11H and 3.11J); in fact, the percentage of PE21-exposed *tgl1Δ*, *tgl3Δ*, *tgl4Δ* and *tgl5Δ* cells that survive a 2-h treatment with POA surpassed that of PE21-exposed WT cells treated with POA for 2 once the WT and mutant cell populations enter day 3 of culturing (Figures 3.11E-3.11H and 3.11J).

Noteworthy, we found that the minimum percentage of clonogenic survival of POA-treated cells was observed on day 4 of culturing WT, *faa1Δ, faa4Δ, ale1Δ, slc1Δ, tgl1Δ, tgl3Δ, tgl4Δ* and *tgl5Δ* cells in the presence of 0.1% PE21 (Figures 3.11A-3.11H and 3.11J). We also found that the highest concentration of FFA in cells of all these stains was observed on day 3 of cell culturing with 0.1% PE21 (Figure 3.11J). We examined the correlation between the minimum percentage of clonogenic survival of POA-treated cells and the highest intracellular FFA concentration by calculating Pearson's *r* value for this pair of compared variables. We discovered that this Pearson's *r* value is less than - 0.9 (Figure 3.11I). Thus, there is a very strong negative correlation [358] between cell resistance to the POA-induced liponecrotic RCD and intracellular FFA concentration. This observation further supports our hypothesis about the first mechanism through which a PE21-dependent reorganization of the cellular lipidome delays chronological aging. Indeed, it shows that the PE21-dependent decrease in intracellular FFA slows an age-related form of liponecrotic RCD.

In sum, findings presented in this section of my Thesis confirm our hypothesis on the first mechanism that underlies a delay of chronological aging in budding yeast cultured with PE21. In this mechanism, the PE21-dependent decrease in cellular FFA below the toxic threshold weakens liponecrotic RCD to increase the probability of cell survival during the entire process of chronological aging (Figure 3.4, mechanism 1).

3.6 The two other mechanism through which a PE21-dependent reorganization of the cellular lipidome slows the chronological aging of budding yeast.

The other students in the Titorenko laboratory have confirmed the existence of the second and third mechanisms predicted by our hypothesis. They provided evidence that the PE21-dependent increase in the concentrations of ER-generated phospholipids activates the pro-longevity process of UPR^{ER} (Figure 3.4, mechanism 2). They also demonstrated that the PE21-dependent changes in the composition of mitochondrial membrane lipids generate a pro-longevity pattern of mitochondrial functionality (Figure 3.4, mechanism 3). Our paper on the three

mechanisms by which a PE21-dependent reorganization of the cellular lipidome delays budding yeast's chronological aging has been published (see reference [359]).

Chapter 4: Developing a method for the quantitative analysis of budding yeast's lipidome using liquid chromatography coupled with tandem mass spectrometry (LC-MS/MS).

4.1 Introduction.

In the studies described in Chapter 3 of my Thesis, I employed MS/MS to identify and quantitate cellular lipids using a direct-injection method of lipidomic analysis. Soon after these studies were completed and the results were published, the changes were implemented at the Centre for Biological Applications of Mass Spectrometry (CBAMS). According to the new standard operating procedure (SOP), no direct injections of extracted biological molecules were permitted. The new SOP instructs that the direct-injection method of lipidomic analysis results in ion detectors' contamination and exponential deterioration, causing a decline in the sensitivity. According to the new SOP, the mass spectrometric analysis of the molecules extracted from biological samples must be preceded by and coupled with a separation of these molecules by liquid chromatography. The limitations of the presently used LC-MS/MS methods for the quantitative analysis of the cellular lipidome are that these methods are not sufficiently robust, sensitive and versatile. Based on the currently employed LC-MS/MS lipidomic procedures, I developed a novel method for the quantitative analysis of budding yeast's lipidome using LC-MS/MS. The technical details of the novel method are provided in sections 2.2 and 2.8 of my Thesis. Here, I describe the advantageous features of the novel method. These features include the high efficiency of lipid extraction, versatility and robustness, sensitivity, ability to distinguish between isobaric and isomeric lipid species, use of alternative mobile phase additives to enhance ionization of all lipid classes, and increased efficiencies of two different types of precursor ions fragmentation processes. I compare these features of the novel LC-MS/MS lipidomics method to the corresponding features of the presently used methods for LC-MS/MS lipidomics.

4.2 An overview of the use of LC-MS/MS for the identification and quantitation of cellular lipids.

As described in sections 1.5-1.7 of my Thesis, various cellular lipids are essential

contributors to longevity assurance in chronologically aging budding yeast. The maintenance of cellular lipid homeostasis is also required for proper functioning of many other complex processes taking place in eukaryotic cells. Among these processes are the appropriate assembly and functionality of biological membranes, bidirectional movement of the small-molecular-weight molecules and proteins across biological membranes, cellular signaling, cellular energy homeostasis, exocytic and endocytic pathways of vesicular protein transport, apoptotic and necrotic forms of regulated cell death, and others [85, 106, 347, 356, 360-365]. To understand mechanisms through which cellular lipid homeostasis contributes to the above cellular processes, a robust and sensitive analytical method for assessing the structural diversity of various lipid classes is required [360-362, 366-370]. For a long time, the structural diversity of lipid molecules was an essential factor that limited their separation from other molecules, correct identification and quantitative assessment in a biological sample [1-3]. For decades, high-pressure liquid chromatography (HPLC) and thin-layer chromatography (TLC) were the analytical methods used to separate, identify and quantitate various lipid classes. However, both these methods exhibit insufficient resolution and sensitivity for the quantitative assessment of complex mixtures of different lipid classes.

The accurate quantitative lipidomics of complex lipid mixtures became possible only with the advent of MS as an analytical tool that can distinguish the individual lipid species [371]. The MS-based lipidomics distinguishes different lipid species by comparing their fatty acid moieties with a precision of only one double bond difference [371]. Several types of mass spectrometers are presently used for lipid identification and quantitation. They include triple quadrupole, quadrupole flight time (TOF), LTQ orbitrap, and ion trap and magnetic sector [360-362, 366-370, 372]. The three main components of all these mass spectrometers include an ion source, a mass analyzer and an ion detector [360-362, 366-370, 372].

Data analysis by a mass spectrometer begins with an appropriate method for lipid ionization and subsequent accurate annotation of the lipid molecules present in the sample [360-362, 366-370]. Due to the significant fragmentation of lipid molecules by the ion source, the use of a mass spectrometer to analyze lipids was limited. Then a soft lipid ionization approach of electrospray ionization (ESI) was introduced [373]. ESI causes almost no fragmentation of the parent lipid ion [373]. Thus, all lipid species can be detected as molecular ions when ESI is used to ionize lipids [373]. The ability of ESI to create only the molecular ions of all lipid species is a

mandatory requirement for the structural analysis of lipids [373]. In ESI, the sample flows at a slow flow rate through an extremely narrow capillary tube during ionization [373]. A significant voltage difference at the end of the capillary tube vaporizes the sample into low-charged droplets present along with the mobile phase [373]. During the ESI of lipid molecules, lipid ions are formed by adding a proton or any other cation, multiple charge cation, or proton removal [374].

Even although integration of ESI and mass spectrometry significantly advanced the field of lipidomics, only the introduction of MS/MS and its combination with ESI revolutionized this research field [375, 376]. The MS/MS technology enables an extra step by causing a collision of molecular ions with a neutral atom or molecule between the two mass analyzers [375, 376]. In the collision chamber, the fragmentation of molecular ions is referred to as collision-mediated dissociation (CID) [374]. In MS/MS, the first mass analyzer selects a precursor or molecular ion [375, 376]. It allows assigning a mass spectrometric peak to a particular lipid species [375, 376]. Then the precursor or molecular ion is moved to the collision chamber, where it dissociates into several smaller fragments [374]. Because each lipid species has a particular fragmentation pattern [371], examining the precursor ion and the collision-generated fragments allows one to identify this lipid species. Computer software, such as Lipid Search or any other MS/MS-compatible software, performs the task of identifying lipids by putting the fragments back together.

Ion suppression and isobaric and isomeric molecular species are the common causes of misidentifying the molecules during MS analysis [377]. Ion suppression yields a less precise, inaccurate and insensitive signal from the detector due to inefficient ionization caused by contamination in the sample [377]. Isobaric molecular species are multiple ions with the same molecular weights but different masses, while isomeric species represent multiple ions with the same masses [377]. To avoid the incorrect identification and quantification of the molecules following MS analysis, it is a common practice in lipidomics to couple MS to HPLC for improving the qualitative and quantitative analysis of the analytes by increasing specificity and sensitivity of the MS [377].

The accuracy of MS in identifying and quantifying the isomeric and isobaric lipid species can be improved if these species are separated by HPLC before being analyzed by MS [377]. It needs to be emphasized that MS cannot correctly identify the isomeric lipid species with the same m/z value if they are not separated by HPLC before MS [377]. HPLC also improves the ability of MS to identify and quantify lipid species of low abundance because it lowers the effects of ion

suppression [377]. Various HPLC types are presently used for analyzing lipid samples; the choice of a particular HPLC type is based on its specificity toward a particular target lipid molecule. If the objective is to evaluate the entire cellular lipidome, a reverse phase HPLC column (RP-HPLC) is the column of choice. The RP-HPLC column has a stationary hydrophobic phase and separates lipid species based on their hydrophobicity. Therefore, the classes of hydrophilic lipids cannot be separated well by the RP-HPLC columns. Moreover, hydrophilic lipid classes are eluted from the RP-HPLC columns before the classes of hydrophobic lipids. In the novel LC-MS/MS method for the quantitative analysis of budding yeast's lipidome discussed here, I used a particular RP-HPLC column type called charged-surface-hybrid (CSH). A CSH column has a mildly charged surface bonded to the hydrophobic moieties of C18 [374]. It separates molecules based on both hydrophilic and hydrophobic characteristics [374]. Thus, a CSH column separates lipid species based on their polar head groups and hydrophobic fatty acid moieties. Therefore, a CSH column has a very high-resolution capacity and can separate the members of the same lipid class if they differ by a single double bond [374].

4.3 A comparison of three commonly used methods for lipid extraction.

To select the most efficient method for extracting lipids from budding yeast cells, I have compared the efficiencies of three commonly used lipid extraction methods. These methods include methyl-tert-butyl-ether (MTBE), dichloromethane/methanol and a modified version of chloroform/methanol extraction (i.e., a 17:1 chloroform/methanol and 2:1 chloroform/methanol extraction method). I compared the efficiencies of extracting commercial lipid standards from budding yeast cells spiked with these lipid standards. I found that the modified version of chloroform/methanol extraction is the optimal method for extracting the highest amounts of all lipid classes from budding yeast cells (Table 4.1).

Table 4.1: The efficiency of the modified chloroform/methanol method (i.e., a 17:1 chloroform/methanol and 2:1 chloroform/methanol method) for extracting commercial lipid standards from budding yeast cells spiked with these lipid standards. A reverse-phase column (RP-HPLC) was used to separate lipids before the MS/MS analysis. The electrospray ionization (ESI) source was used for lipid ionization. The average values of 3 technical replicates are shown. These values represent the percentage recovery of lipid standards after the extraction from cells

spiked with these lipid standards compare to the same concentration of lipids spiked directly in the MS injection solvent. The highest values for the three compared lipid extraction methods are displayed in red. Other abbreviations: AmF ammonium formate, AmAc ammonium acetate.

Lipid Standard	ESI mode	AmF	AmAc
Phytoceramide	-	64.3	77.2
Cardiolipin	-	63.4	70.4
Free Fatty Acid	-	67.0	67.9
Phosphatidylethanolamine	-	85.2	85.5
Phosphatidylglycerol	-	55.6	68.3
Phosphatidylinositol	-	68.9	74.2
Phosphatidylserine	-	64.1	77.2
Phosphatidylcholine	+	81.3	62.3
Phosphatidylsphingosine	+	77.5	70.2
Triacylglycerol	+	80.3	78.2

Table 4.2: The efficiency of the MTBE method for extracting commercial lipid standards from budding yeast cells spiked with these lipid standards. An RP-HPLC column was used to separate lipids before the MS/MS analysis. The ESI source was used for lipid ionization. The average values of 3 technical replicates are shown. These values represent the percentage recovery of lipid standards after the extraction from cells spiked with these lipid standards compare to the same concentration of lipids spiked directly in the MS injection solvent. Abbreviations: AmF ammonium formate, AmAc ammonium acetate.

Lipid Standard	ESI mode	AmF	AmAc
Phytoceramide	-	48.1	57.4
Cardiolipin	-	47.3	52.4
Free Fatty Acid	-	50.1	50.5
Phosphatidylethanolamine	-	63.7	63.6
Phosphatidylglycerol	-	41.6	50.8
Phosphatidylinositol	-	0	0
Phosphatidylserine	-	0	0

Phosphatidylcholine	+	60.7	46.4
Phosphatidylsphingosine	+	57.9	52.3
Triacylglycerol	+	60.0	58.2

Table 4.3: The efficiency of 17:1 dichloromethane/methanol and 2:1 dichloromethane/methanol extraction method for extracting commercial lipid standards from budding yeast cells spiked with these lipid standards. An RP-HPLC column was used to separate lipids before the MS/MS analysis. The ESI source was used for lipid ionization. The average values of 3 technical replicates are shown. These values represent the percentage recovery of lipid standards after the extraction from cells spiked with these lipid standards compare to the same concentration of lipids spiked directly in the MS injection solvent. Abbreviations: AmF ammonium formate, AmAc ammonium acetate.

Lipid Standard	**ESI mode**	**AmF**	**AmAc**
Phytoceramide	-	59.9	71.2
Cardiolipin	-	59.0	64.9
Free Fatty Acid	-	62.4	62.6
Phosphatidylethanolamine	-	79.3	78.8
Phosphatidylglycerol	-	51.8	62.9
Phosphatidylinositol	-	64.2	68.4
Phosphatidylserine	-	59.6	71.2
Phosphatidylcholine	+	75.7	57.5
Phosphatidylsphingosine	+	72.1	64.8
Triacylglycerol	+	74.8	72.1

4.4 The versatility and robustness of the novel LC-MS/MS method.

The described method for the quantitative analysis of budding yeast's lipidome is versatile and robust. It allows using a single type of HPLC column to identify and quantitate 179 lipid species that belong to 18 lipid classes (Table 4.4). These lipid classes include cardiolipin (CL), free (unesterified) fatty acids (FFA), diacylglycerol (DAG), lysophosphatidic acid (LPA), lysophosphatidylcholine (LPC), lysophosphatidylethanolamine (LPE), lysophosphatidylglycerol (LPG), lysophosphatidylinositol (LPI), lysophosphatidylserine (LPS), phosphatidic acid (PA),

phosphatidylcholine (PC), phosphatidylethanolamine (PE), phosphatidylglycerol (PG), phytoceramide (PHC), phytosphingosine (PHS), PI, phosphatidylinositol, phosphatidylserine (PS), triacylglycerol (TAG). These lipid classes exhibit a wide range of structural, physical and chemical properties. All 179 lipid species were extracted from budding yeast cells using a single extraction method (i.e., the modified chloroform/methanol method), which was the optimal one for extracting the highest amounts of all these lipid species. A single type of RP-HPLC column called CSH C18 was used to separate all these lipid species.

Table 4.4: The novel LC-MS/MS method can identify and quantify 179 lipid species that belong to 18 lipid classes. The names of lipid standards are displayed in red colour and end with "std." Abbreviations: CL, cardiolipin; FFA, free (unesterified) fatty acids; DAG, diacylglycerol; free (unesterified) fatty acids; LPA, lysophosphatidic acid; LPC, lysophosphatidylcholine; LPE, lyso-phosphatidylethanolamine; LPG, lysophosphatidylglycerol; LPI, lyso-phosphatidylinositol; LPS, lyso-phosphatidylserine; M, molecular ion (neutral); PA, phosphatidic acid; PC, phosphatidylcholine; PE, phosphatidylethanolamine; PG, phosphatidylglycerol; PHC, phytoceramide; PHS, phytosphingosine; PI, phosphatidylinositol; PS, phosphatidylserine; RTT, retention time; TAG, triacylglycerol. Most of the lipid standards used in this table are deuterated (labelled).

Component Name	RT	Adduct	m/z with adduct	Component Name	RT	Adduct	m/z with adduct
PHC_32:0	15.5	M+H	512.50372	PG_31:1_std	13.4	M+NH4	724.51231
PHC_32:1	15.1	M+H	510.48807	PG_32:0	14.4	M+NH4	740.54361
PHC_34:0	16.1	M+H	540.53502	PG_32:1	13.8	M+NH4	738.52796
PHC_34:1	15.3	M+H	538.51937	PG_38:2	15.3	M+NH4	820.60621
PHC_34:2	15.5	M+H	536.50372	PG_40:0	21.3	M+NH4	852.66881
PHC_34:2_std	14.7	M+H	543.55850	PHS_30:0	12.5	M+H	649.52790
PHC_36:0	17.0	M+H	568.56632	PHS_30:1_std	11.9	M+H	647.51225
PHC_36:1	16.9	M+H	566.55067	PHS_32:0	14.4	M+H	677.55920
PHC_36:2	16.3	M+H	564.53502	PHS_32:1	13.3	M+H	675.54355
PHC_36:2_std	15.5	M+H	571.58980	PHS_38:0	18.6	M+H	761.65310
PHC_38:0	17.9	M+H	596.59762	PHS_40:0	21.6	M+H	789.68440
PHC_38:1	17.1	M+H	594.58197	PHS_40:1	20.7	M+H	787.66875
PHC_38:2_std	16.2	M+H	599.62110	PHS_44:0	22.6	M+H	845.74700
PHC_40:1	18.0	M+H	622.61327	PHS_44:1	22.2	M+H	843.73135
PHC_40:2	16.5	M+H	620.59762	PHS_44:2	21.7	M+H	841.71570
PHC_40:2_std	16.9	M+H	627.65240	PHS_48:0	23.1	M+H	901.80960
PHC_42:1	18.6	M+H	650.64457	PHS_48:1	22.9	M+H	899.79395
PHC_42:2	17.3	M+H	648.62892	PHS_48:2	22.7	M+H	897.77830

PHC_42:2_std	17.7	M+H	655.68370	TAG_48:0	22.4	M+NH4	824.77016
PHC_44:0	19.8	M+H	680.69152	TAG_48:1	22.0	M+NH4	822.75451
PHC_44:1	19.5	M+H	678.67587	TAG_48:2	21.2	M+NH4	820.73886
PHC_44:2	18.1	M+H	676.66022	TAG_48:3	20.4	M+NH4	818.72321
PHC_46:0	20.7	M+H	708.72282	TAG_51:0_std	22.9	M+NH4	866.81711
PHC_46:1	19.8	M+H	706.70717	TAG_51:1	22.7	M+NH4	864.80146
PHC_46:2	18.9	M+H	704.69152	TAG_51:2	22.3	M+NH4	862.78581
PHC_48:0	21.6	M+H	736.75412	TAG_51:3	21.7	M+NH4	860.77016
PHC_48:1	21.4	M+H	734.73847	TAG_54:0	23.3	M+NH4	908.86406
PHC_48:2	19.8	M+H	732.72282	TAG_54:1	23.1	M+NH4	906.84841
DAG_32:0	16.7	M+Na	591.49589	TAG_54:2	22.8	M+NH4	904.83276
DAG_32:1	16.1	M+Na	589.48024	TAG_54:3	22.5	M+NH4	902.81711
DAG_32:2	15.4	M+Na	587.46459	TAG_60:0	23.8	M+NH4	992.95796
DAG_34:0_std	17.5	M+Na	619.52719	TAG_60:1	23.6	M+NH4	990.94231
DAG_34:1	16.8	M+Na	617.51154	TAG_60:2	23.5	M+NH4	988.92666
DAG_34:2	16.1	M+Na	615.49589	TAG_60:3	23.3	M+NH4	986.91101
DAG_36:0	18.3	M+Na	647.55849	CL_56:0	13.1	M-2H	621.43189
DAG_36:1	17.6	M+Na	645.54284	CL_56:1	11.3	M-2H	620.42406
DAG_36:2	16.8	M+Na	643.52719	CL_56:2	10.9	M-2H	619.41624
DAG_38:0	19.2	M+Na	675.58979	CL_56:3	10.6	M-2H	618.40841
DAG_38:1	18.4	M+Na	673.57414	CL_57:2	16.3	M-2H	624.40841
LPA_17:1_std	1.0	M+NH4	440.27716	CL_57:3	16.0	M-2H	623.40059
LPA_18:1	3.0	M+NH4	454.29281	CL_57:4_std	15.9	M-2H	622.39276
LPA_20:1	3.5	M+NH4	482.32411	CL_60:0	14.1	M-2H	649.46318
LPA_22:1	4.5	M+NH4	510.35541	CL_60:1	12.9	M-2H	648.45536
LPC_16:0	3.2	M+H	496.33976	CL_60:2	11.7	M-2H	647.44753
LPC_16:1	2.0	M+H	494.32411	CL_61:0	19.8	M-2H	654.45536
LPC_17:0	4.5	M+H	510.35541	CL_61:1_std	18.6	M-2H	653.44753
LPC_17:1_std	2.7	M+H	508.33976	CL_64:0	14.3	M-2H	675.47883
LPC_18:0	6.3	M+H	524.37106	CL_80:3	22.8	M-2H	784.58056
LPC_18:1	3.8	M+H	522.35541	CL_80:4	22.4	M-2H	783.57273
LPC_20:0	9.5	M+H	552.40236	CL_86:4_std	22.9	M-2H	825.61968
LPC_20:1	7.0	M+H	550.38671	LPE_16:0	2.8	M-H	452.27826
LPC_22:0	11.7	M+H	580.43366	LPE_16:1	1.8	M-H	450.26261
LPC_24:0	15.3	M+H	608.46496	LPE_17:0	3.8	M-H	466.29391
LPS_17:0	3.1	M+H	512.29829	LPE_17:1_std	2.4	M-H	464.27826
LPS_17:1_std	1.6	M+H	510.28264	LPE_18:0	5.4	M-H	480.30956
LPS_18:1	2.2	M+H	524.29829	LPE_18:1	3.3	M-H	478.29391
LPS_22:1	4.3	M+H	580.36089	LPE_20:0	5.6	M-H	508.34086
PA_28:1	9.2	M+NH4	608.42858	LPG_17:0	2.5	M-H	497.28849
PA_28:2	8.2	M+NH4	606.41293	LPG_17:1_std	1.6	M-H	495.27284
PA_31:1_std	12.5	M+NH4	650.47553	LPI_16:0	1.5	M-H	571.28889
PA_32:1	13.1	M+NH4	664.49118	LPI_16:1	1.0	M-H	569.27324
PA_32:2	12.1	M+NH4	662.47553	LPI_17:0	1.9	M-H	585.30454
PA_36:0	15.8	M+NH4	722.56943	LPI_17:1_std	1.2	M-H	583.28889
PA_36:1	14.8	M+NH4	720.55378	LPI_18:0	2.6	M-H	599.32019
PA_36:2	14.2	M+NH4	718.53813	LPI_18:1	1.6	M-H	597.30454
PA_38:0	15.7	M+NH4	750.60073	FFA_16:0	7.0	M-H	255.23185

PA_38:1	15.7	M+NH4	748.58508	FFA_18:0	9.9	M-H	283.26315
PA_38:2	15.1	M+NH4	746.56943	FFA_18:1	7.8	M-H	281.24750
PA_40:1	16.4	M+NH4	776.61638	FFA_18:1_std	7.7	M-H	290.31793
PA_40:2	15.7	M+NH4	774.60073	FFA_22:0	13.5	M-H	339.32575
PA_44:2	17.1	M+NH4	830.66333	FFA_22:1	12.2	M-H	337.31010
PC_28:0	14.1	M+NH4	694.52555	FFA_24:0	14.7	M-H	367.35705
PC_28:1	13.0	M+NH4	692.50990	FFA_24:1	13.6	M-H	365.34140
PC_31:1_std	14.6	M+NH4	734.55685	PI_28:0	11.6	M-H	753.45595
PC_32:0	15.7	M+NH4	750.58815	PI_31:1_std	12.5	M-H	793.48725
PC_32:1	15.1	M+NH4	748.57250	PI_32:0	13.6	M-H	809.51855
PC_32:2	14.3	M+NH4	746.55685	PI_32:1	13.0	M-H	807.50290
PE_28:0	13.8	M+H	636.46098	PI_32:2	12.1	M-H	805.48725
PE_28:1	12.8	M+H	634.44533	PI_36:1	14.6	M-H	863.56550
PE_28:2	11.8	M+H	632.42968	PI_36:2	14.0	M-H	861.54985
PE_31:1_std	14.4	M+H	676.49228	PS_31:1_std	12.6	M-H	718.46646
PE_32:1	14.8	M+H	690.50793	PS_32:1	13.1	M-H	732.48211
PE_32:2	14.0	M+H	688.49228	PS_36:0	14.5	M-H	790.56036
PE_36:0	15.7	M+H	748.58618	PS_36:1	13.7	M-H	788.54471
PE_36:1	15.1	M+H	746.57053	PS_36:2	13.0	M-H	786.52906
PE_36:2	14.3	M+H	744.55488	PS_40:0	16.0	M-H	846.62296
PE_38:0	16.4	M+H	776.61748	PS_40:1	15.3	M-H	844.60731
PE_38:1	15.7	M+H	774.60183	PS_40:2	14.8	M-H	842.59166
PE_38:2	15.1	M+H	772.58618				
PE_40:1	16.6	M+H	802.63313				

4.5 The high sensitivity of the novel LC-MS/MS method.

The described method is sensitive. The lowest lipid concentration that can be detected by this method is 0.165 pmol/µl (see data for phytoceramide in Table 4.5). Of note, the sensitivity of the method varies for different lipid species (Table 4.5).

Table 4.5: The lowest concentrations of different lipid species that can be detected by the novel LC-MS/MS method. The MS peak areas for the internal standards of 10 major lipid classes were used to calculate their concentrations. These peak areas and lipid concentrations are shown in bold. The minimum detectable MS peak areas were used to calculate the lowest detectable concentration for each lipid class. The mean values of two independent experiments, each performed in three technical replicates, are provided.

Detection mode	Lipid class	Hydrophobic tail composition	Calculated m/z value	Lipid standard, MS peak	Lipid standard, concentration (pmol/µl)	Minimum MS peak detected	Lowest concentration detected (pmol/µl)
Negative	Phytoceramide	18:1_17:0	550.5204675	**3.36E+07**	**2.26E+02**	2.46E+04	1.65E-01

Negative	Cardiolipin	14:0_14:0_14:0_14:0	1239.839755	**2.18E+07**	**1.96E+02**	4.16E+04	3.74E-01
Negative	Free fatty acid	19:0	297.2799035	**6.71E+07**	**8.37E+02**	6.64E+04	8.28E-01
Negative	Phosphatidylethanolamine	15:0_15:0	662.4766305	**3.30E+07**	**3.77E+02**	6.04E+04	6.90E-01
Negative	Phosphatidylglycerol	15:0_15:0	693.4712115	**6.89E+07**	**3.49E+02**	2.24E+05	1.13E+00
Negative	Phosphatidylinositol	17:0_20:4	871.5342065	**2.94E+05**	**3.00E+00**	4.68E+04	4.78E-01
Negative	Phosphatidylserine	17:0_17:0	762.5290605	**1.98E+06**	**3.18E+02**	2.94E+04	4.72E+00
Positive	Phosphatidylcholine	13:0_13:0	650.4755335	**2.13E+08**	**3.85E+02**	1.09E+05	1.97E-01
Positive	Phytosphingosine	16:1	272.2584055	**1.26E+06**	**2.25E+02**	3.11E+05	5.55E+01
Positive	Triacylglycerol	28:1_10:1_10:1	818.7232155	**1.27E+08**	**3.67E+02**	1.07E+07	3.09E+01

4.6 The novel LC-MS/MS method can identify and quantify various isobaric and isomeric lipid species.

The described method can distinguish between isobaric or isomeric forms of lipid species that belong to several lipid classes. The nominal masses of isobaric lipid forms have the same nominal masses; however, their exact masses are different [378]. For example, the nominal masses of PHC (16:0_26:0) and PC (16:0_10:0) are the same, specifically 650 Daltons. The novel LC-MS/MS method can make a distinction between them and determine their exact masses as 650.6457 and 650.4755, respectively.

The exact masses of isomeric lipid forms are the same because their molecular formulas are the same; however, their physical structures are different [378]. For instance, the physical structures of PC (18:0_18:1; a hydrophobic tail attachment of a fatty acid containing 18 carbon atoms without double bonds and a fatty acid containing 18 carbon atoms with a double bond) and PC (20:0_16:1) are different despite their molecular formulas (C44H87N1O8P1) and exact masses (788.6163) of PC are identical. The novel LC-MS/MS method can identify PC (18:0_18:1) and PC (20:0_16:1) as two different lipid species. The novel LC-MS/MS method can also distinguish between PE (16:0_16:0) and PE (14:0_18:0), whose physical structures differ, but the molecular formulas (C37H75N1O8P1) and exact masses (692.5224) are the same.

Another example is the two isomeric forms of PS (34:0) with the same m/z value (M-H) of 762.5294. The novel LC-MS/MS method shows that these isomeric forms of PS (34:0) exhibit different retention times (7.65 min and 8.49 min) during chromatography separation on the RP-HPLC column CSH C18 used in this method (Figure 4.1). The novel LC-MS/MS method also identifies the differences in the MS1 and MS2 spectra of the two isomeric forms of PS (34:0)

(Figures 4.2 and 4.3, respectively).

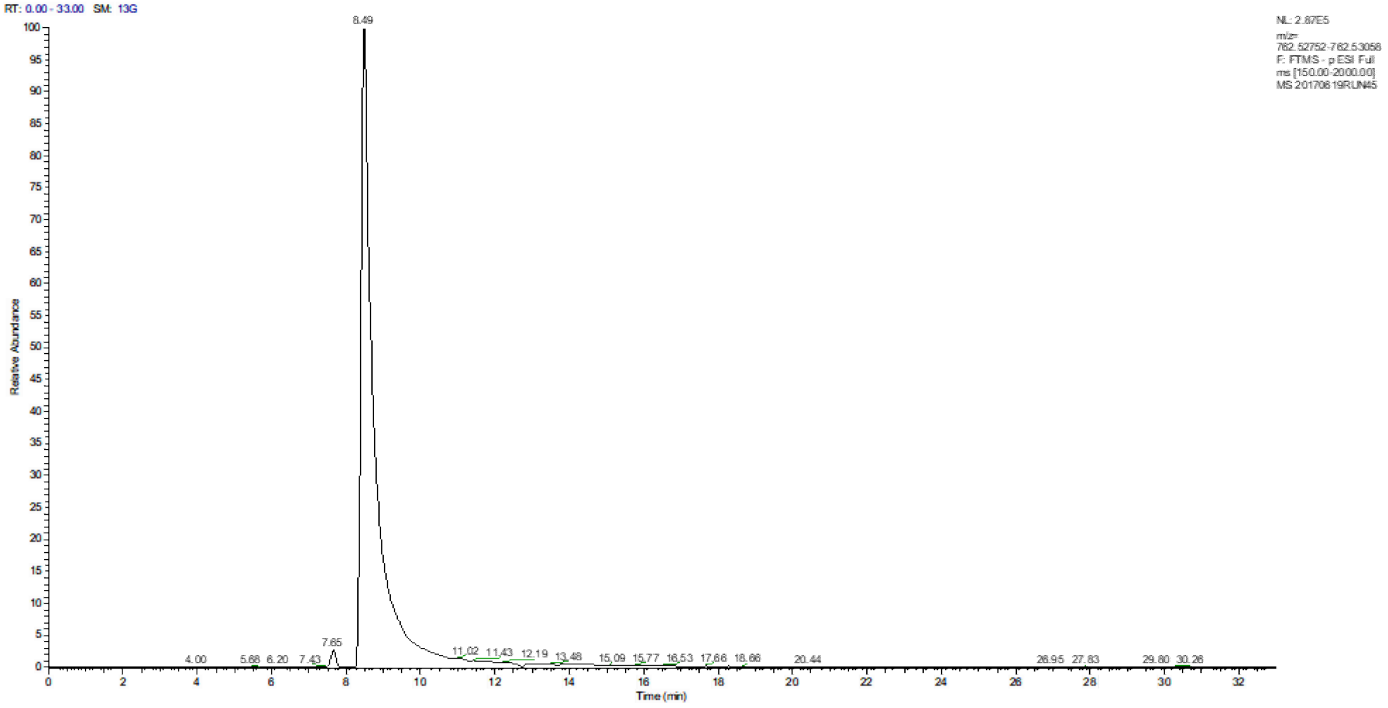

Figure 4.1. The two isomeric forms of PS (34:0) have different retention times (7.65 min and 8.49 min) during chromatography separation on the RP-HPLC column CSH C18 used in the novel LC-MS/MS method.

A

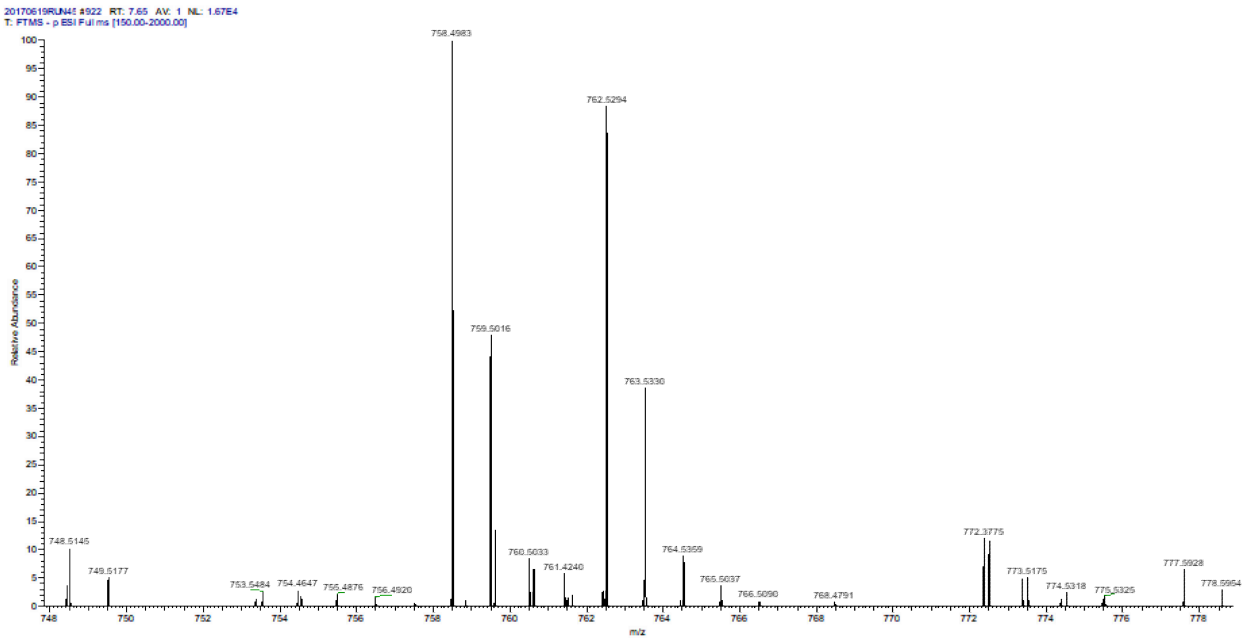

B

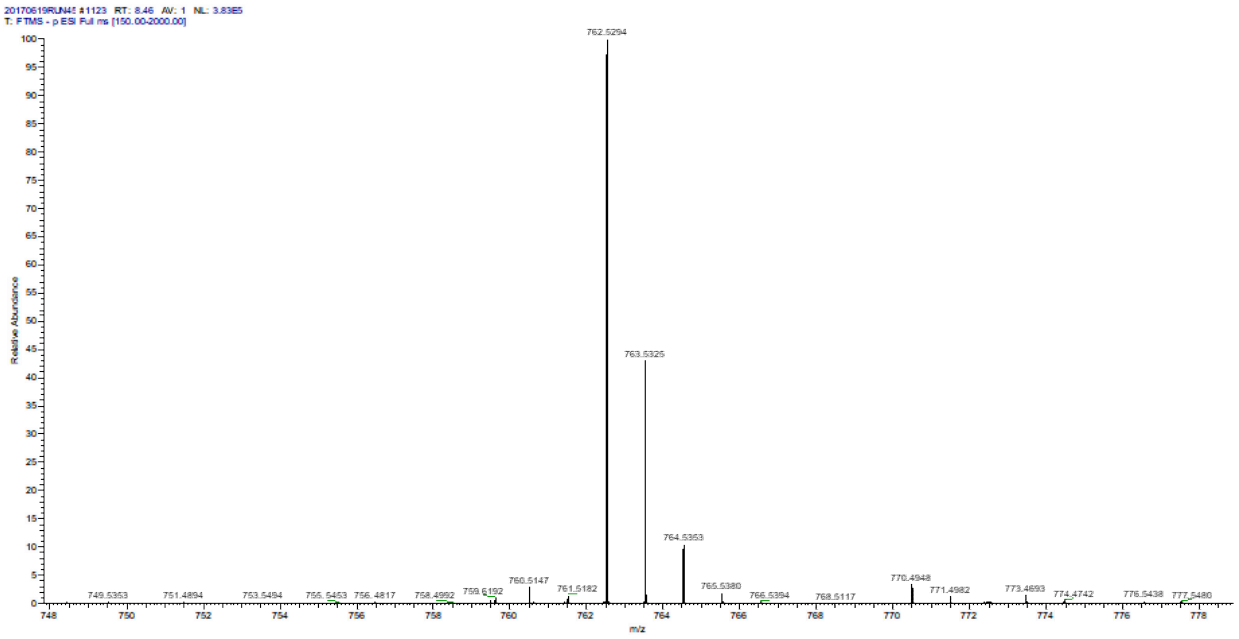

Figure 4.2. The two isomeric forms of PS (34:0) have different spectra of precursor ions (MS1). The MS1 spectrum of a PS (34:0) isomeric form that has the m/z value (M-H) of 762.5294 and the retention chromatography time of 7.65 min (**A**) or 8.49 min (**B**).

A

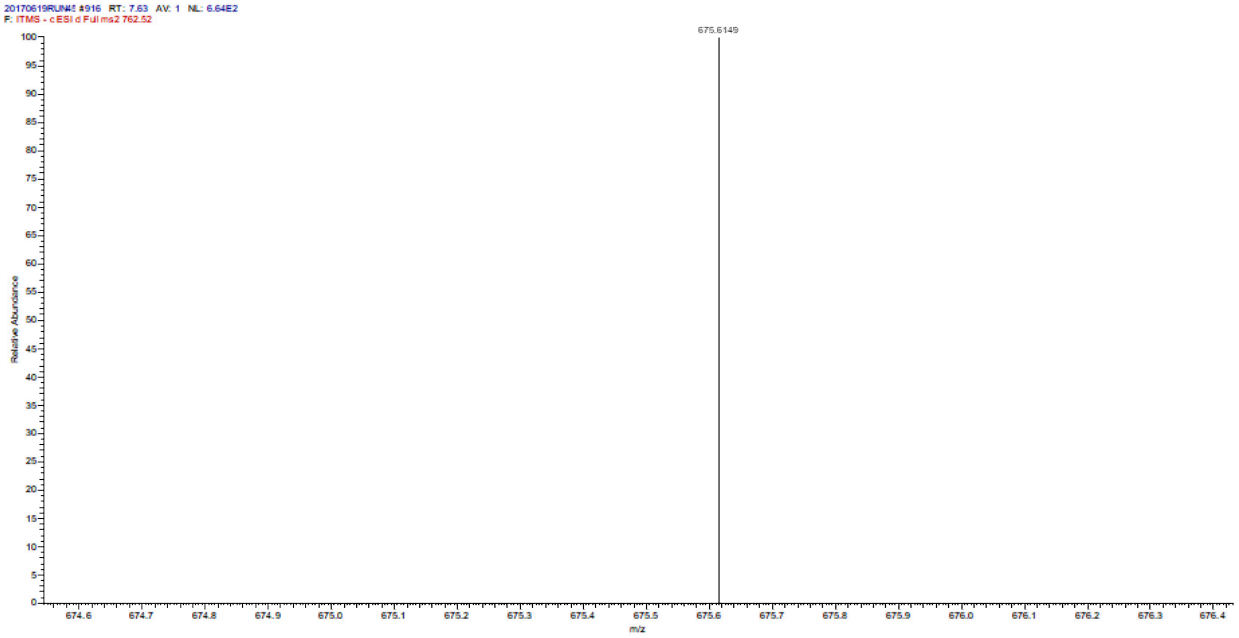

B

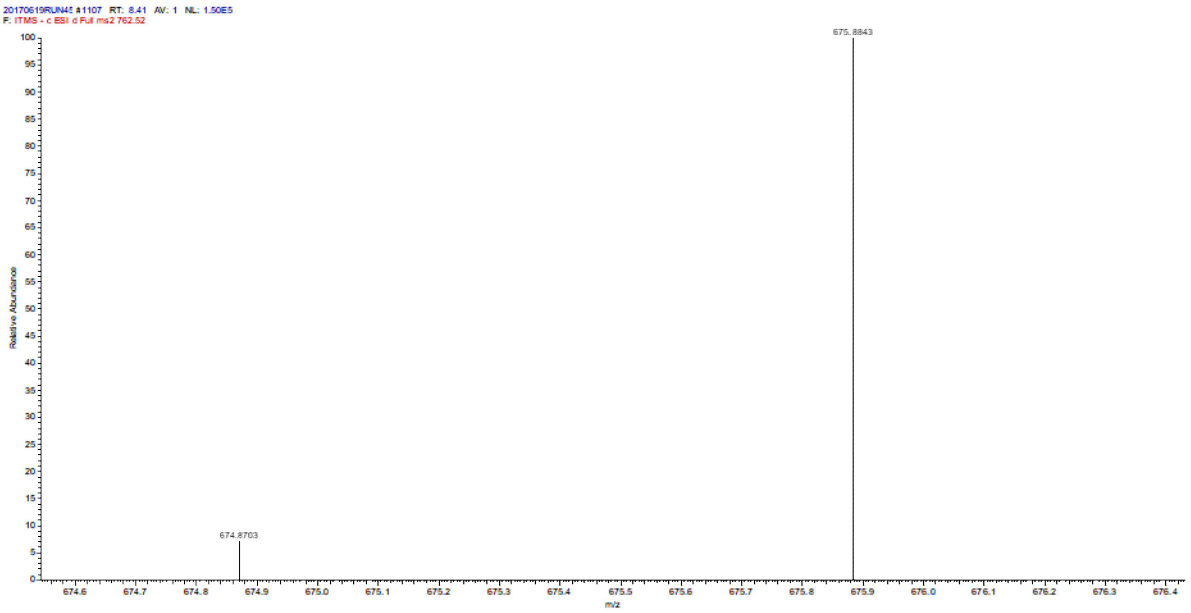

Figure 4.3. The two isomeric forms of PS (34:0) have different spectra of product ions (MS2). The MS2 spectrum of a PS (34:0) isomeric form that has the m/z value (M-H) of 762.5294 and the retention chromatography time of 7.65 min (**A**) or 8.49 min (**B**).

4.7 The novel LC-MS/MS method can use the alternative mobile phase additives for the ESI MS to enhance ionization of all lipid classes.

The described method improves the identification and quantitation of cellular lipids because it can increase ionization efficiency for all lipid classes (Table 4.6). The increase in the ionization efficiency is due to the employment of alternative mobile phase additives for the ESI MS. Ammonium formate, ammonium formate with formic acid, ammonium acetate, ammonium acetate with acetic acid, and ammonium acetate with formic acid are the mobile phase additives that the novel method can use for enhancing lipid ionization in the ESI (-) or ESI (+) mode (Table 4.6). Of note, different mobile phase additives exhibit the highest ionization efficiencies for different lipid classes (Table 4.6). Besides, both the HILIC column and reverse-phase LC column are compatible with each of the above mobile phase additives.

Table 4.6: In the novel LC-MS/MS method, different mobile phase additives can improve the ionization efficiencies for different lipid classes. Reverse-phase liquid chromatography was

used to separate commercial standards of various lipid classes. Different mobile phase additives were used for the ESI MS in the ESI (-) or ESI (+) mode of lipid ionization. The MS peak area was used to calculate the percentage of ionization for each lipid class. Data are provided as the mean values of three technical replicates. The highest value of ionization efficiency for a particular lipid class by a specific mobile phase additive is shown in red. Abbreviations: AmF, ammonium formate; AmF/FA, ammonium formate with formic acid; AmAc, ammonium acetate; AmAc/AA, ammonium acetate with acetic acid; AmAc/FA, ammonium acetate with formic acid; CL, cardiolipin; FFA, free (unesterified) fatty acid; PC, phosphatidylcholine; PE, phosphatidylethanolamine; PG, phosphatidylglycerol; PHC, phytoceramide; PHS, phytosphingosine; PI, phosphatidylinositol; PS, phosphatidylserine; TAG, triacylglycerol.

Lipid standard	**ESI mode**	**AmF**	**AmF/FA**	**AmAc**	**AmAc/AA**	**AmAc/FA**
PHC	-	74	75.2	85.8	77	74.8
CL	-	72.9	75.1	78.3	68.4	74
FFA	-	77.1	77.2	75.5	84	72.9
PE	-	98	96	95	91.5	86
PG	-	64	45.1	75.9	60.5	55
PI	-	79.3	76	82.5	80.3	77
PS	-	73.7	61.6	85.8	81.4	73.7
PC	+	93.5	86.9	69.3	60.5	62.7
PHS	+	89.1	79.2	78.1	73.7	69.3
TAG	+	92.4	88	86.9	80.3	84.7

4.8 The novel LC-MS/MS method makes precursor ions fragmentation more efficient to increase the coverage of the lipid species.

The described method can use two procedures to fragment precursor ions (MS1) of lipids into product ions (MS2). These procedures are known as high-energy collisional dissociation (HCD) and collision-induced dissociation (CID) [379]. The CID procedure enhances the MS1-to-MS2 ion fragmentation for PHC, CL, FFA, PE, PG, PI and PS if used in combination with the ammonium acetate mobile phase additive for the ESI (-) mode of MS (Table 4.7). The HCD

procedure promotes the MS1-to-MS2 ion fragmentation for PC, PHS and TAG if employed in combination with the ammonium formate mobile phase additive for the ESI (+) mode of MS (Table 4.8).

Table 4.7: The efficiencies of the MS1-to-MS2 ion fragmentation for different lipid classes using the CID procedure. Reverse-phase liquid chromatography was used to separate commercial standards of various lipid classes. An ammonium formate (AmF) or ammonium acetate (AmAc) mobile phase additive was used for the ESI MS in the ESI (-) or ESI (+) mode of lipid ionization. The MS2 peak area was used to calculate the percentage of MS1-to-MS2 ion fragmentation for each lipid class. Data are provided as the mean values of three technical replicates. The highest value of the MS1-to-MS2 ion fragmentation efficiency for a particular lipid class in the presence of a specific mobile phase additive is shown in red. Other abbreviations: CL, cardiolipin; FFA, free (unesterified) fatty acid; PC, phosphatidylcholine; PE, phosphatidylethanolamine; PG, phosphatidylglycerol; PHC, phytoceramide; PHS, phytosphingosine; PI, phosphatidylinositol; PS, phosphatidylserine; TAG, triacylglycerol.

Lipid standard	**ESI mode**	**AmF**	**AmAc**
PHC	-	75	83.8
CL	-	70.9	79.3
FFA	-	76.1	74.5
PE	-	98	95
PG	-	64	75.9
PI	-	79.3	82.5
PS	-	71.5	84.8
PC	+	52.3	60.5
PHS	+	78.4	75.2
TAG	+	65.7	69.7

Table 4.8: The efficiencies of the MS1-to-MS2 ion fragmentation for different lipid classes using the HCD procedure. Reverse-phase liquid chromatography was used to separate commercial standards of various lipid classes. An ammonium formate (AmF) or ammonium acetate (AmAc) mobile phase additive was used for the ESI MS in the ESI (-) or ESI (+) mode of lipid ionization. The MS2 peak area was used to calculate the percentage of MS1-to-MS2 ion fragmentation for each lipid class. Data are provided as the mean values of three technical replicates. The highest value of the MS1-to-MS2 ion fragmentation efficiency for a particular lipid class in the presence of a specific mobile phase additive is shown in red. Other abbreviations: CL, cardiolipin; FFA, free (unesterified) fatty acid; PC, phosphatidylcholine; PE, phosphatidylethanolamine; PG, phosphatidylglycerol; PHC, phytoceramide; PHS, phytosphingosine; PI, phosphatidylinositol; PS, phosphatidylserine; TAG, triacylglycerol.

Lipid standard	ESI mode	AmF	AmAc
PHC	-	68.4	65.4
CL	-	74.3	75.2
FFA	-	84.2	81.2
PE	-	85.1	73.1
PG	-	68.4	67.1
PI	-	58.7	55.8
PS	-	67.4	68.5
PC	+	92.5	65.3
PHS	+	87.1	75.1
TAG	+	91.4	84.9

4.9 A summary of the advantages offered by the novel LC-MS/MS lipidomics method and its comparison with presently used methods.

The described method provides several advantages over the other methods currently employed in LC-MS/MS lipidomics. These advantages are outlined below.

The novel method employs the most efficient procedure for extracting lipids from budding yeast cells, namely a modified chloroform/methanol extraction version. This procedure

uses a 17:1 chloroform/methanol and 2:1 chloroform/methanol mixture to extract cellular lipids [380]. It significantly improves the efficiency of lipid recovery for all classes of lipids, as compared to the commonly used MTBE [381] and dichloromethane/methanol [382] procedures of extracting cellular lipids (compare Figures 4.1, 4.2 and 4.3).

The novel method is versatile and robust. It allows to identify and quantitate 179 lipid species that belong to 18 lipid classes and differ significantly in their structural, physical and chemical properties. These numbers are close to the numbers of lipid species and classes identifiable and quantifiable with the help of a direct-injection method of lipidomic analysis [383], a method banned by the CBAMS to avoid the contamination of ion detectors and their exponential deterioration causing sensitivity decline. Another aspect of the novel method's versatility is that it uses a single lipid extraction method and a single type of HPLC column to identify and quantify all 179 chemically diverse lipid species. Other LC-MS/MS lipidomics methods use a two-dimensional LC setup that includes a normal-phase column in the first dimension and a reversed-phase column in the second dimension [384].

The novel method is sensitive, with the lower limit of detection at 0.165 pmol/μl for PHC. This lower detection limit is close to the best LC-MS/MS lipidomics methods in biological systems [385].

The novel method can distinguish between isobaric and isomeric lipid species that belong to several lipid classes. The ability to differentiate isobaric and isomeric lipid species is essential for understanding the biological roles of lipids and mechanisms through which lipids regulate cellular processes [386].

The novel method can use the alternative mobile phase additives for the ESI MS to enhance the ionization efficiency of all lipid classes in both ESI modes. The enhancement of lipid ionization is essential for improving the efficiency of lipid identification and quantitation by LC-MS/MS [387].

The novel method increases the efficiency of the MS1-to-MS2 ion fragmentation using both the CID and HCD ion fragmentation procedures for all lipid classes. A rise in the MS1-to-MS2 ion fragmentation efficiency is an essential contributing factor to improving lipid profiling in biological samples [388].

Chapter 5: Caloric restriction reorganizes the lipidome of quiescent and nonquiescent yeast cells differently than two other geroprotectors.

5.1 Introduction.

As I mentioned in the Introduction chapter of my Thesis, the robust geroprotective diet CR decreases TAG concentration and increases CL concentration in HD and LD cells of the WT strain throughout chronological aging [68, 70]. As I indicated in the Introduction chapter, a population of HD cells includes both Q and NQ cells. The percentage of NQ cells in the HD population slowly rises during chronological aging [68, 70]. As I alluded to in the Introduction chapter, a population of LD cells also includes both Q and NQ cells. The percentage of NQ cells in the LD population rapidly rises during chronological aging [68, 70].

Therefore, the first objective of the studies described here was to assess the effect of CR on the intracellular concentrations of all lipid classes (not only TAG and CL) within HD and LD cell populations of the WT strain recovered at different stages of chronological aging. To accomplish this objective, we purified HD and LD cells from WT yeast taken on different days of culturing under CR or non-CR conditions; the purification of HD and LD cells was complete [68] and performed using Percoll density gradient centrifugation [68]. As noted earlier, the HD cell population on day 1 of culturing includes mainly Q cells [68, 70]. As also mentioned earlier, the Q cells in the HD population are comparatively slowly converted into NQ cells [68, 70]. On day 1 of culturing, the LD cell population also contains Q cells primarily [68, 70]. The Q-to-NQ cell conversion within the LD cell population is a comparatively fast process [68, 70]. We then employed the novel LC-MS/MS lipidomics method (see Chapter 4) to conduct quantitative lipidomics of the recovered HD and LD cell populations. Because our study was the first attempt to examine the age-related changes in the lipidomes of Q and NQ cells at various phases of chronological aging, we did not know if these changes are observed only at specific stages of aging or they are permanent.

The second objective of the studies described here was to conduct a comparative analysis of how CR and two other geroprotective interventions (namely, the *tor1Δ* mutation and LCA) affect the lipidomes of HD and LD cells recovered at different stages of chronological aging. CR, *tor1Δ* and LCA are potent geroprotective interventions that considerably extend the longevity of

chronologically aging budding yeast (Figure 5.1). We selected these three geroprotectors for the comparative study of their effects on the lipidomes of HD and LD cells for several reasons. One reason was that the ways of administering these geroprotective interventions to slow aging and prolong longevity are different; CR is a robust aging-delaying diet, *tor1Δ* is a single-gene mutation that slows aging and LCA is a potent anti-aging chemical compound. The other equally important reason for selecting CR, *tor1Δ* and LCA for these studies was that their targeting specificities in budding yeast are different. The geroprotective targets of CR include the metabolism of carbohydrates and lipids, organellar protein import, mitochondrial structure and function, protein translation, quality control of proteins and organelles, stress resistance, and resistance to age-related apoptosis and necrosis [6, 8]. The *tor1Δ* mutation impairs the abilities of the major pro-

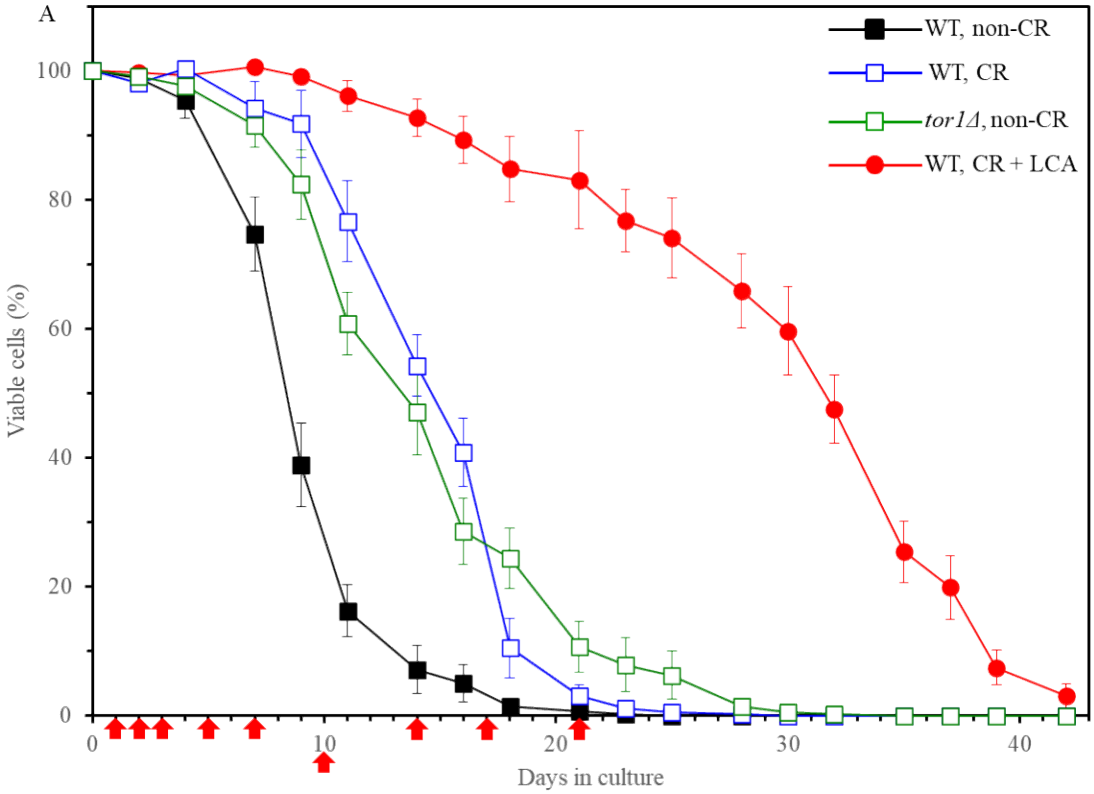

Figure 5.1: CR, the *tor1Δ* mutation and LCA extend the longevity of chronologically aging budding yeast. WT cells cultured in the nutrient-rich YP medium initially containing 0.2% (w/v) glucose were used to examine how CR influences yeast longevity; in these experiments, a control non-CR culture was the culture of WT cells in the same medium but initially containing 2% (w/v) glucose. Cells carrying a single-gene-deletion mutation *tor1Δ* and cultured in the YP medium initially containing 2% (w/v) glucose were used to assess how the *tor1Δ* mutation affects yeast

longevity; in these experiments, a control culture was the WT culture in the same genetic background and the same medium. WT cells cultured in the YP medium initially containing 0.2% (w/v) glucose and 50 μM LCA were used to examine how LCA influences yeast longevity; in these experiments, a control culture was the WT culture in the same medium with 0.2% (w/v) glucose but without LCA. Survival curves are presented as means ± SEM (n = 3). According to the logrank test, all three geroprotective interventions exhibited a statistically significant longevity extension ($p < 0.05$). Cell aliquots for the LC-MS/MS lipidomic analysis were recovered at the time points marked by red arrows.

aging regulator TORC1 to promote protein translation, inhibit the autophagy-based quality control mechanisms and suppress stress resistance [6, 8]. As described in the Introduction chapter, LCA's primary targets are processes implicated in mitochondrial lipid metabolism, protein translation and signaling [90, 142, 147]. Yet another reason why we selected CR, *tor1Δ* and LCA for this comparative study was that the extent of longevity extension by LCA under CR-conditions of cell culturing (but not when cells were cultured under non-CR conditions) substantially exceed those by CR or *tor1Δ* (Figure 5.1). Therefore, we thought that the effect of LCA on the lipidomes of HD and LD cells might differ from those of CR and/or the *tor1Δ* mutation.

In studies described here, we used LC-MS/MS to identify and quantify the lipidomes of HD and LD cells in the WT and *tor1Δ* strains of budding yeast cultured under the conditions described in the legend for Figure 5.1. Cell aliquots for the LC-MS/MS lipidomic analysis were recovered at the time points marked by red arrows on this figure.

5.2 TAG concentration in HD and LD cells is substantially decreased by CR on most days of the chronological lifespan, while neither tor1Δ nor LCA has a similar long-term effect.

As I mentioned earlier, CR lowers TAG concentration in HD and LD cells of the WT strain throughout chronological aging [68, 70]. This CR-dependent, long-lasting decline in TAG concentration was observed using the direct-injection method of MS/MS lipidomics, which is now prohibited from using at the CBAMS. Therefore, we used the novel LC-MS/MS lipidomics method to assess how CR influences TAG concentrations in HD and LD cells on different days of culturing. The use of the novel LC-MS/MS lipidomics method has confirmed the early observation that CR decreases TAG concentration on most days of cell culturing other than day 1 (Figures

5.2A and 5.2B).

In contrast, *tor1Δ* and LCA did not cause significant age-related changes in TAG concentrations within LD cells (Figures 5.3A and 5.4A, respectively). *tor1Δ* and LCA promoted only temporary age-related changes in TAG concentrations within HD cells (Figures 5.3B and 5.4B, respectively). Specifically, TAG concentrations in HD cells were increased by *tor1Δ* between days 5 and 10 of cell culturing (Figures 5.3B). In cells treated with LCA, TAG concentrations in HD cells were decreased between days 10 and 17 of cell culturing (Figure 5.4B). The significance of temporary changes in TAG within HD cells of the *tor1Δ* mutant or within HD cells of the culture treated with LCA remains to be determined.

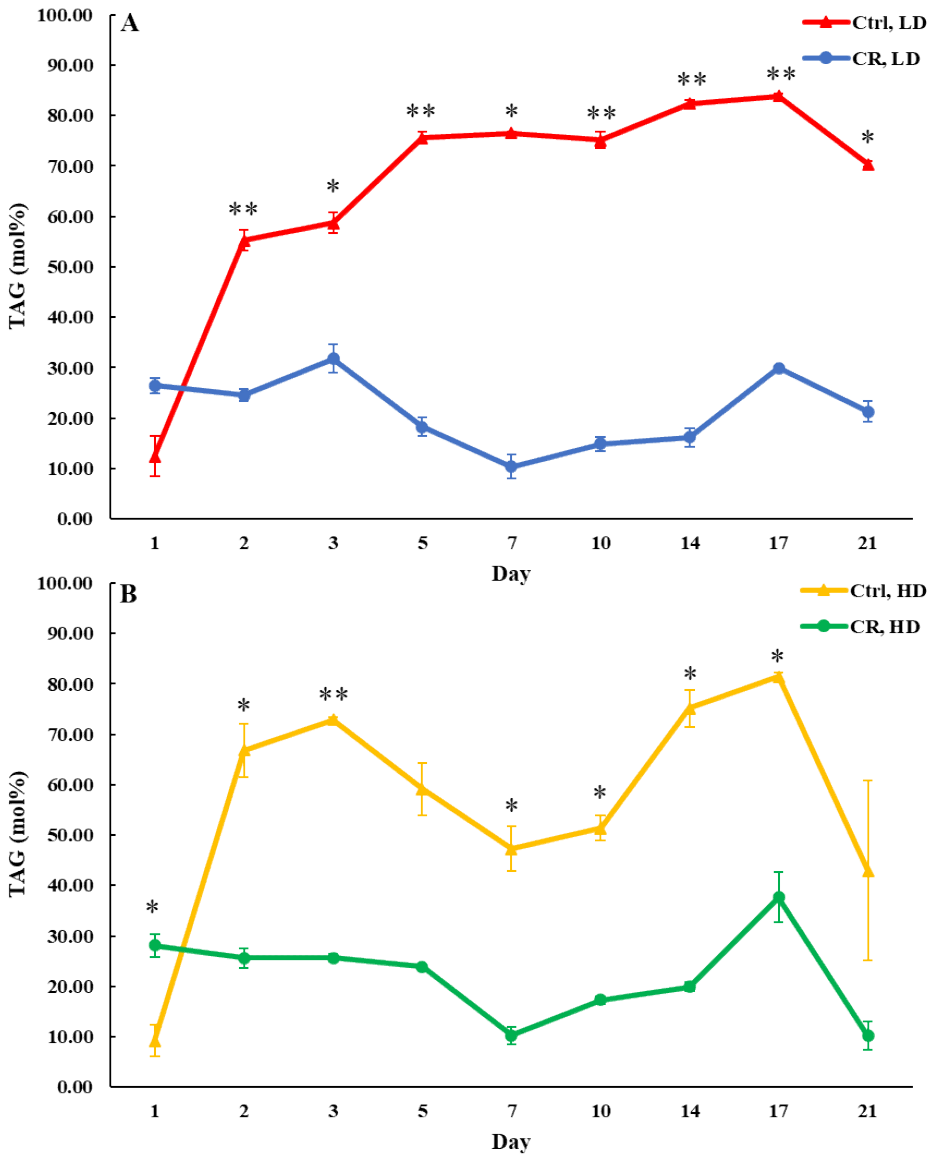

Figure 5.2: The concentration of TAG in HD and LD cells of WT is considerably lowered by CR on most days of culturing other than day 1. WT cells were cultured in YP medium supplemented with 0.2% glucose (CR conditions) or 2% glucose (control non-CR conditions). Cell aliquots were taken on different days of culturing. The Percoll density gradient centrifugation was used to purify HD and LD cells from these cell aliquots. LC-MS/MS was used to assess TAG concentrations in these cells. Data are shown as means ± SD (n = 2; *$p < 0.05$; **$p < 0.01$).

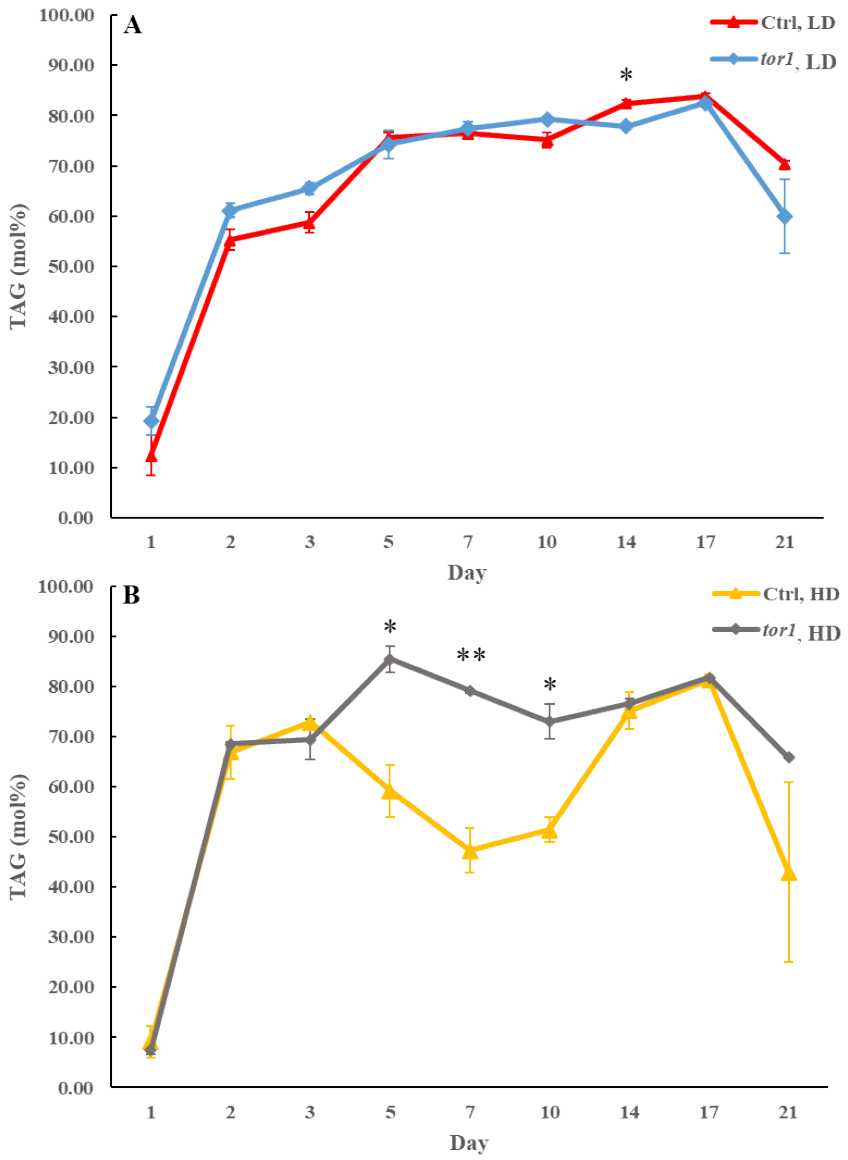

Figure 5.3: The concentration of TAG in HD cells between days 5 and 10 of cell culturing is increased by the *tor1Δ* mutation. WT and *tor1Δ* cells were cultured in the YP medium supplemented with 2% glucose (non-CR conditions). Cell aliquots were taken on different days of culturing. The Percoll density gradient centrifugation was used to purify HD and LD cells from these cell aliquots. LC-MS/MS was used to assess TAG concentrations in these cells. Data are shown as means ± SD (n = 2; *$p < 0.05$; **$p < 0.01$).

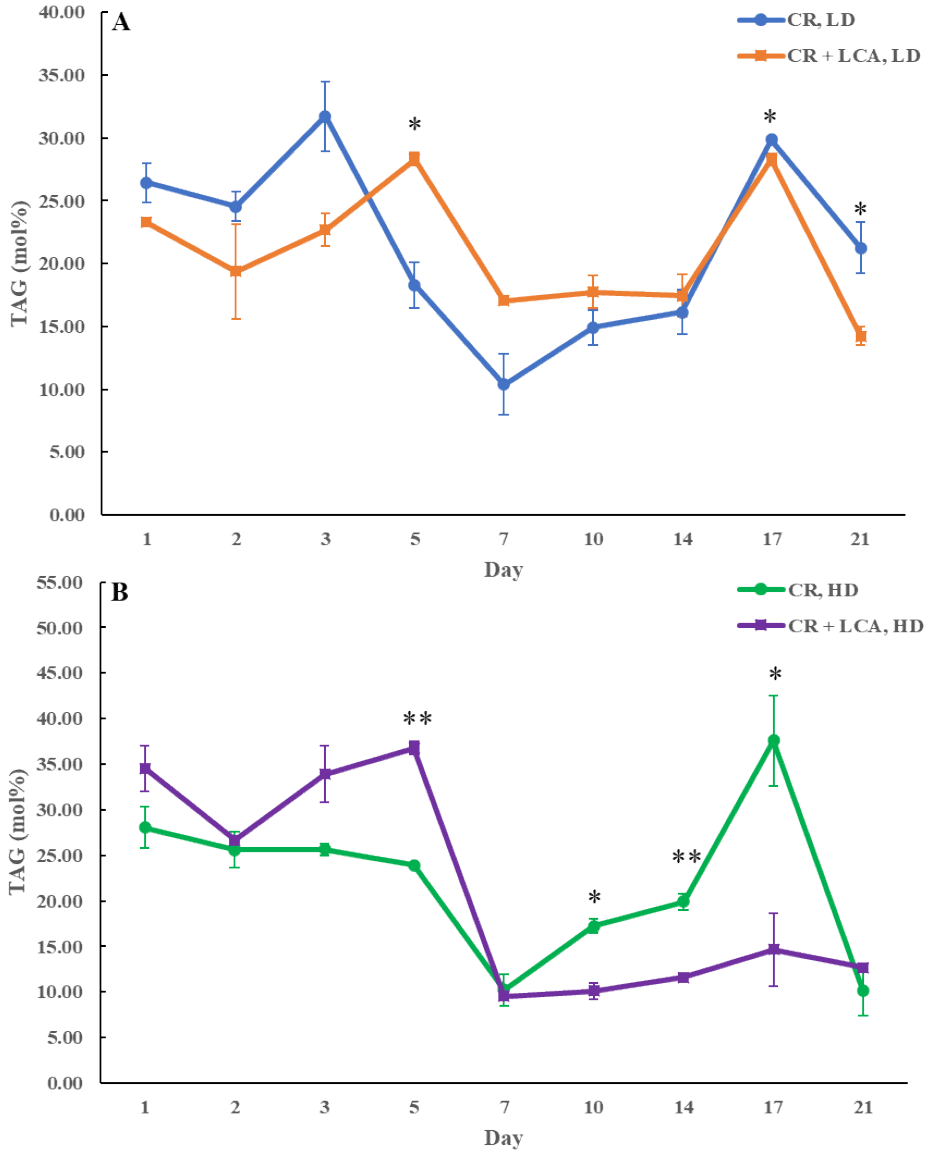

Figure 5.4: The concentration of TAG in HD cells between days 10 and 17 of cell culturing is decreased by 50 µM LCA. WT cells were cultured in YP medium supplemented with 0.2% glucose (CR conditions) in the presence of 50 µM LCA or its absence. Cell aliquots were taken on different days of culturing. The Percoll density gradient centrifugation was used to purify HD and LD cells from these cell aliquots. LC-MS/MS was used to assess TAG concentrations in these cells. Data are shown as means ± SD (n = 2; *$p < 0.05$; **$p < 0.01$).

In sum, findings presented in section 5.2 indicate that CR substantially lowers TAG concentration in both HD and LD cells on most days of cell culturing other than day 1. Unlike CR, neither *tor1Δ* nor LCA significantly affects TAG concentration within LD cells throughout the chronological lifespan of budding yeast. Furthermore, the increasing effect of *tor1Δ* and decreasing effect of LCA on TAG concentrations in HD cells were temporary and much less pronounced than that of CR.

5.3 FFA concentration in HD and LD cells is considerably increased by CR on most days of the chronological lifespan, whereas neither *tor1Δ* nor LCA exhibit a similar long-term effect.

We thought that one explanation for the observed decline in TAG concentration within HD and LD cells cultured under CR conditions is that CR might promote the lipolytic hydrolysis of TAG in lipid droplets (LDP) (Figure 1.7). If the efficiency of free fatty acids (FFA) oxidation in peroxisomes is not altered by CR, the promotion of TAG lipolysis under CR conditions will increase the intracellular concentration of FFA in yeast under CR conditions (Figure 1.7). We found that CR substantially increases FFA concentrations in HD and LD cells limited in calorie supply after day 2 of culturing (Figures 5.5A and 5.5B). We concluded that CR promotes the lipolytic hydrolysis of TAG in LDP but does not alter peroxisomal FFA oxidation. Considering the extending effect of CR on longevity, it is likely that FFA concentration under CR conditions of cell culturing does not exceed a toxic threshold.

On the contrary, *tor1Δ* did not cause significant age-related changes in FFA concentrations within LD cells (Figure 5.6A). Besides, the increasing effect of LCA on FFA concentration within LD cells was much less pronounced than the one under CR conditions (Figure 5.7A). In HD cells, *tor1Δ* caused a decline in FFA concentration between days 5 and 10 of cell culturing (Figure 5.6B) and LCA increased FFA (to a lesser extent than CR) only between days 10 and 17 of cell culturing (Figure 5.7B). The importance of temporary and low-intensity changes in FFA within HD cells of the *tor1Δ* mutant or HD cells of the culture treated with LCA remains unclear.

Altogether, findings reported in section 5.3 provide evidence that CR considerably rises FFA concentrations in HD and LD cells after day 2 of culturing. The effects of *tor1Δ* and LCA on FFA concentrations in these cells are much less dramatic (or insignificant, as in the case of LD cells of *tor1Δ*) or only temporary.

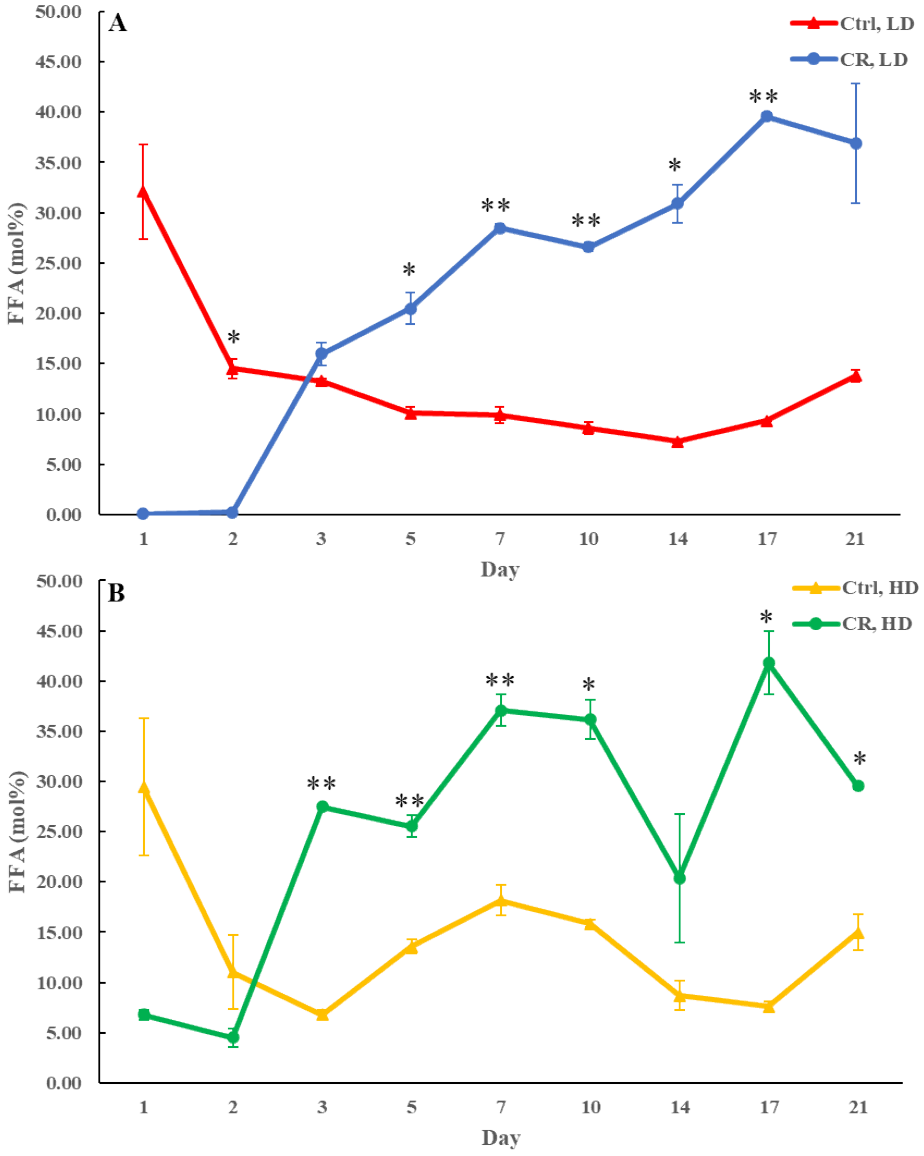

Figure 5.5: The concentration of FFA in HD and LD cells of WT is considerably increased by CR after day 2 of culturing. WT cells were cultured in the YP medium supplemented with 0.2% glucose (CR conditions) or 2% glucose (control non-CR conditions). Cell aliquots were taken on different days of culturing. The Percoll density gradient centrifugation was used to purify HD and LD cells from these cell aliquots. LC-MS/MS was used to assess FFA concentrations in these cells. Data are shown as means ± SD (n = 2; *$p < 0.05$; **$p < 0.01$).

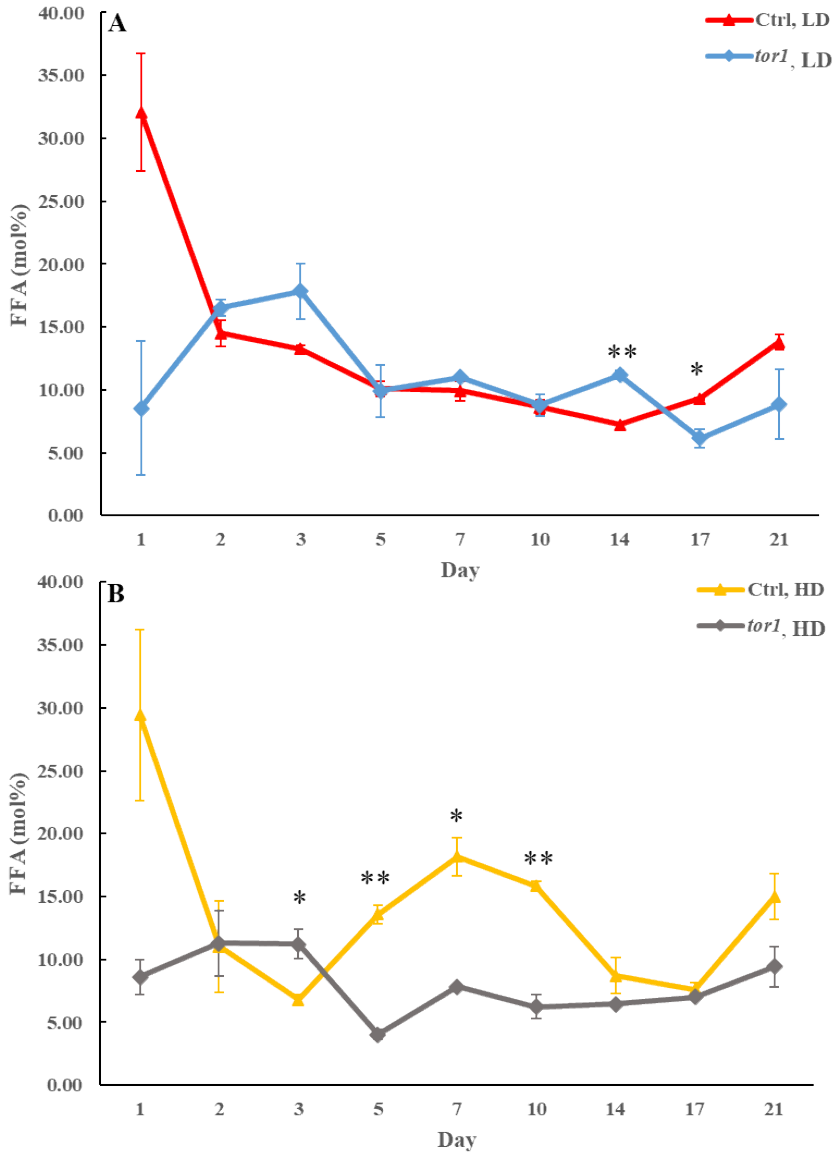

Figure 5.6: In HD cells, *tor1Δ* causes a decline in FFA concentration between days 5 and 10 of cell culturing. WT and *tor1Δ* cells were cultured in the YP medium supplemented with 2% glucose (non-CR conditions). Cell aliquots were taken on different days of culturing. The Percoll density gradient centrifugation was used to purify HD and LD cells from these cell aliquots. LC-MS/MS was used to assess FFA concentrations in these cells. Data are shown as means ± SD (n = 2; *$p < 0.05$; **$p < 0.01$).

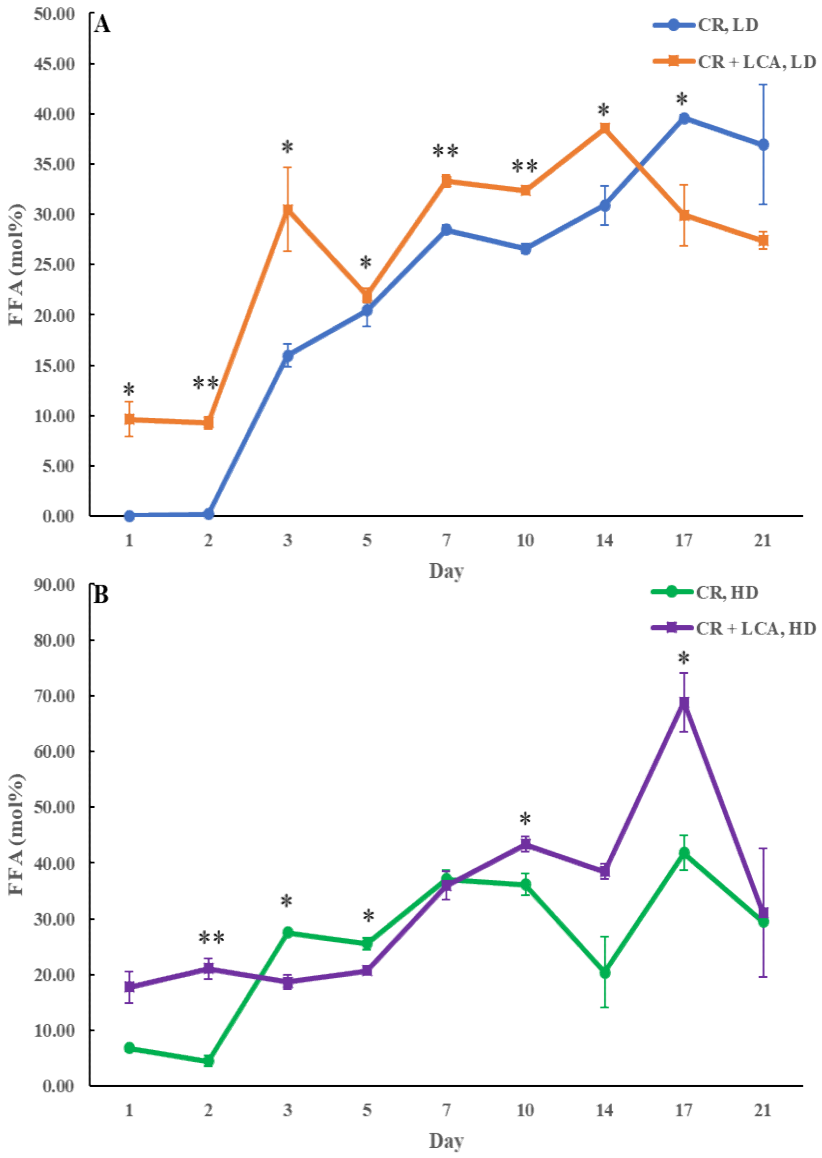

Figure 5.7: The effects of 50 µM LCA on FFA concentrations in HD and LD cells under CR are much less dramatic (than under CR without LCA) and only temporary. WT cells were cultured in YP medium supplemented with 0.2% glucose (CR conditions) in the presence of 50 µM LCA or its absence. Cell aliquots were taken on different days of culturing. The Percoll density gradient centrifugation was used to purify HD and LD cells from these cell aliquots. LC-MS/MS was used to assess FFA concentrations in these cells. Data are shown as means ± SD (n = 2; *p < 0.05; **p < 0.01).

5.4 DAG concentration in HD and LD cells is not significantly and not for a long time affected

by CR, *tor1Δ* or LCA.

We thought that the observed decline in TAG concentration within HD and LD cells cultured under CR conditions might also be explained by a decline in TAG synthesis from DAG within the ER (Figure 1.7). We found that CR does not exhibit any significant and long-lasting effect on DAG concentration within HD and LD cells throughout the chronological lifespan of budding yeast (Figure 5.8). This observation strongly supports the view that a decline in TAG concentration within HD and LD cells under CR conditions was not due to a suppression of TAG synthesis from DAG within the ER. Akin to the lack of any effect of CR on DAG concentration within HD and LD cells, the concentration of DAG in these cells was not influenced by *tor1Δ* or LCA (Figures 5.9 and 5.10, respectively).

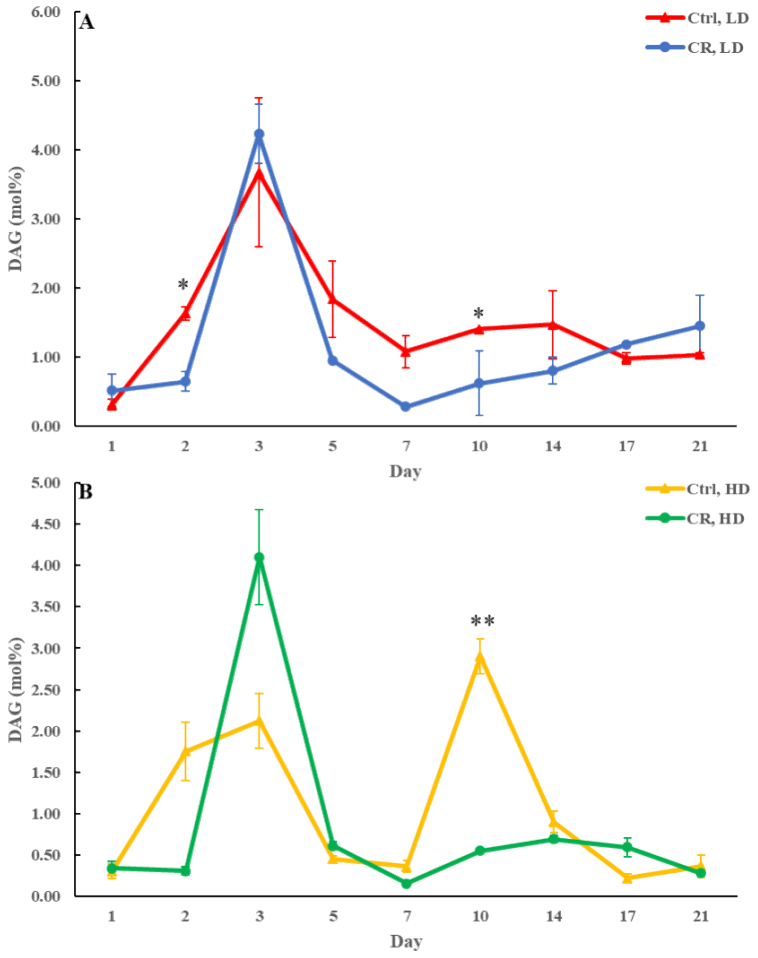

Figure 5.8: CR does not affect significantly and for a long time DAG concentration within HD and LD cells throughout the chronological lifespan of budding yeast. WT cells were cultured in the YP medium supplemented with 0.2% glucose (CR conditions) or 2% glucose

(control non-CR conditions). Cell aliquots were taken on different days of culturing. The Percoll density gradient centrifugation was used to purify HD and LD cells from these cell aliquots. LC-MS/MS was used to assess DAG concentrations in these cells. Data are shown as means ± SD (n = 2; *$p < 0.05$; **$p < 0.01$).

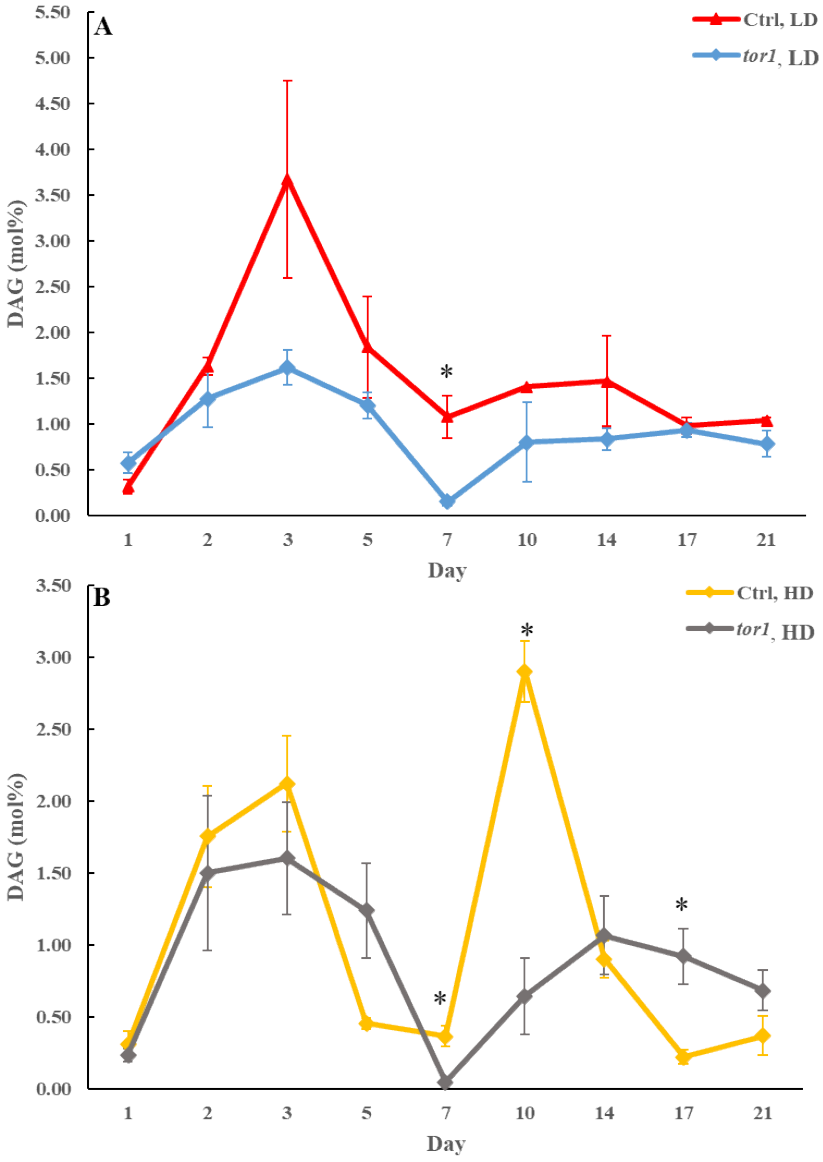

Figure 5.9: *tor1Δ* does not affect significantly and for a long time DAG concentration within HD and LD cells throughout the chronological lifespan of budding yeast. WT and *tor1Δ* cells were cultured in the YP medium supplemented with 2% glucose (non-CR conditions). Cell aliquots were taken on different days of culturing. The Percoll density gradient centrifugation was

used to purify HD and LD cells from these cell aliquots. LC-MS/MS was used to assess DAG concentrations in these cells. Data are shown as means ± SD (n = 2; *$p < 0.05$).

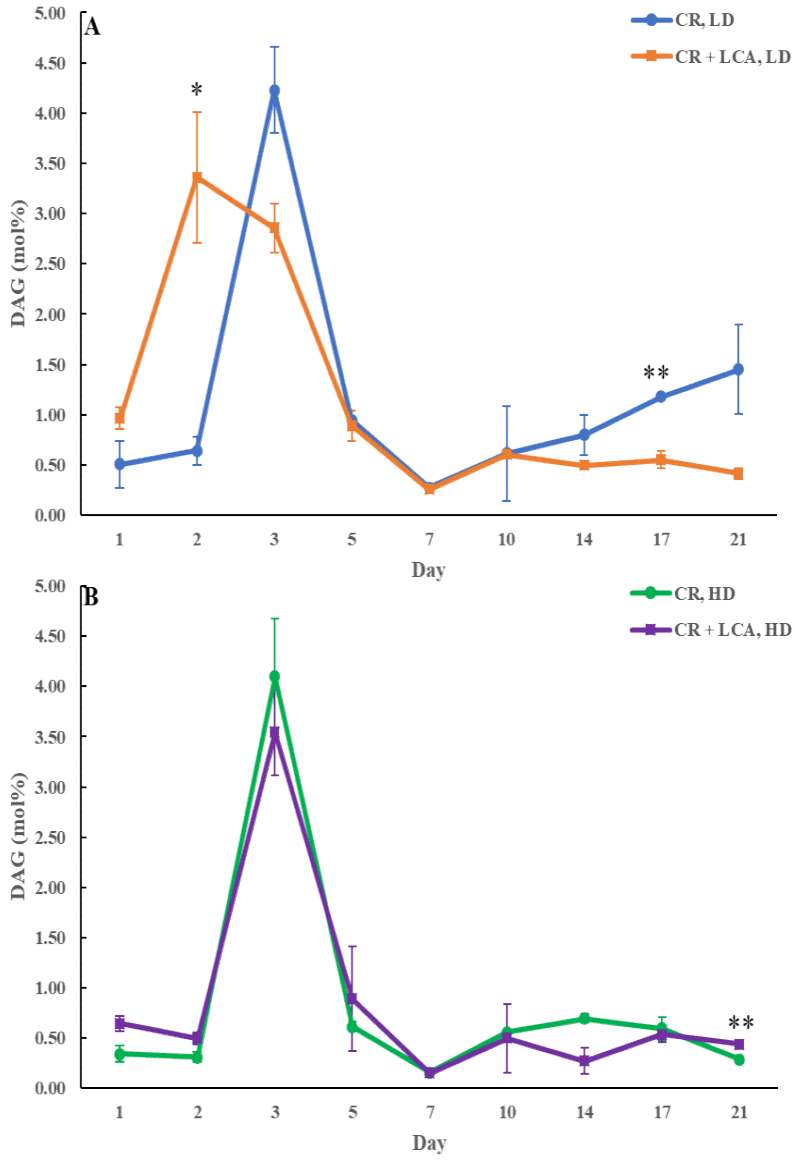

Figure 5.10: LCA does not affect significantly and for a long time DAG concentration within HD and LD cells throughout the chronological lifespan of budding yeast. WT cells were cultured in YP medium supplemented with 0.2% glucose (CR conditions) in the presence of 50 µM LCA or its absence. Cell aliquots were taken on different days of culturing. The Percoll density gradient centrifugation was used to purify HD and LD cells from these cell aliquots. LC-MS/MS was used to assess DAG concentrations in these cells. Data are shown as means ± SD (n = 2; *$p <$

0.05; **$p < 0.01$).

5.5 Ceramide (CER) concentration in LD cells is significantly increased by CR but not by *tor1Δ* or LCA.

We then used LC-MS/MS to identify cellular lipids that accumulate in excessive amounts within HD and LD cells because the synthesis of these lipids involves incorporating the excess of FFA present within HD and LD cells.

One lipid class whose formation requires FFA incorporation is CER, which is synthesized in the ER from serine and fatty acyl-CoA esters of palmitic acid [190, 191]. We found that CER concentration in LD cells limited in calorie supply is significantly increased throughout the chronological lifespan (Figure 5.11A). CER concentration in HD cells under CR conditions was also increased; however, this increase was statistically insignificant (Figure 5.11B). Unlike the effects of CR on CER concentration, *tor1Δ* caused a decline in the concentration of this lipid class in HD cells on some days of culturing (Figure 5.12B). LCA decreased CER concentration in LD cells throughout the chronological lifespan (Figure 5.13A). Of note, because CR extended the longevity of budding yeast, it is unlikely that CER concentration in yeast cells under CR conditions exceeded the toxic threshold. Furthermore, it remains unclear whether the observed low concentrations of CER play any regulatory role under the conditions of cell culturing tested in these experiments.

5.6 The concentration of complex sphingolipids (SPH) in HD and LD cells is not significantly altered by CR, *tor1Δ* or LCA throughout the chronological lifespan.

After being formed in the ER from serine and fatty acyl-CoA esters of palmitic acid, CER is converted into SPH [190, 191]. We found that SPH concentration does not undergo significant changes throughout the chronological lifespan of HD or LD cells placed on the CR diet, carrying the *tor1Δ* mutation or treated with LCA (Figures 5.14, 5.15 and 5.16, respectively). Of note, because CR extended the longevity of budding yeast, it is unlikely that SPH concentration in yeast cells under CR conditions exceeded the toxic threshold. Moreover, further studies are needed to clarify whether the observed low concentrations of SPH perform any essential regulatory role under the conditions of cell culturing assessed in these experiments.

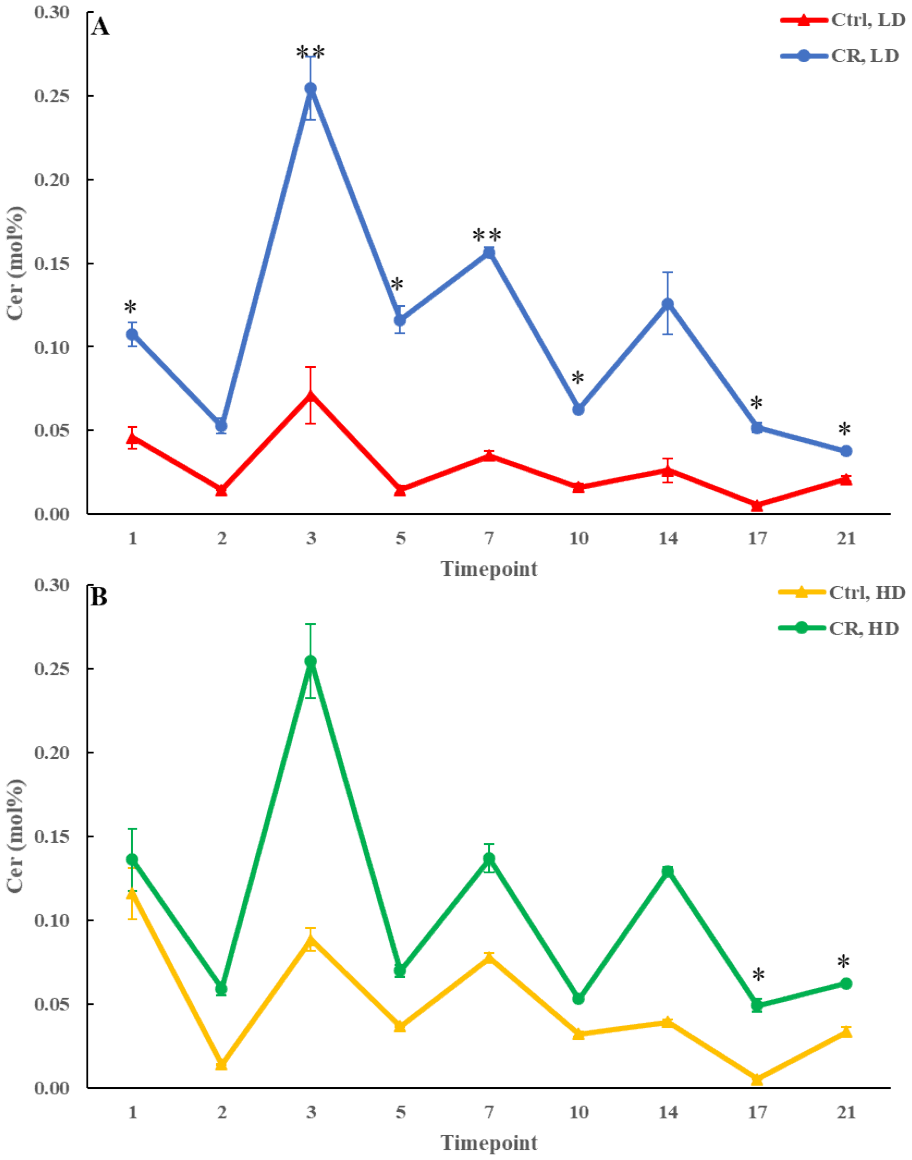

Figure 5.11: CER concentration in the LD cells cultured under CR conditions significantly increases throughout the chronological lifespan. WT cells were cultured in the YP medium supplemented with 0.2% glucose (CR conditions) or 2% glucose (control non-CR conditions). Cell aliquots were taken on different days of culturing. The Percoll density gradient centrifugation was used to purify HD and LD cells from these cell aliquots. LC-MS/MS was used to assess CER concentrations in these cells. Data are shown as means ± SD (n = 2; *$p < 0.05$; **$p < 0.01$).

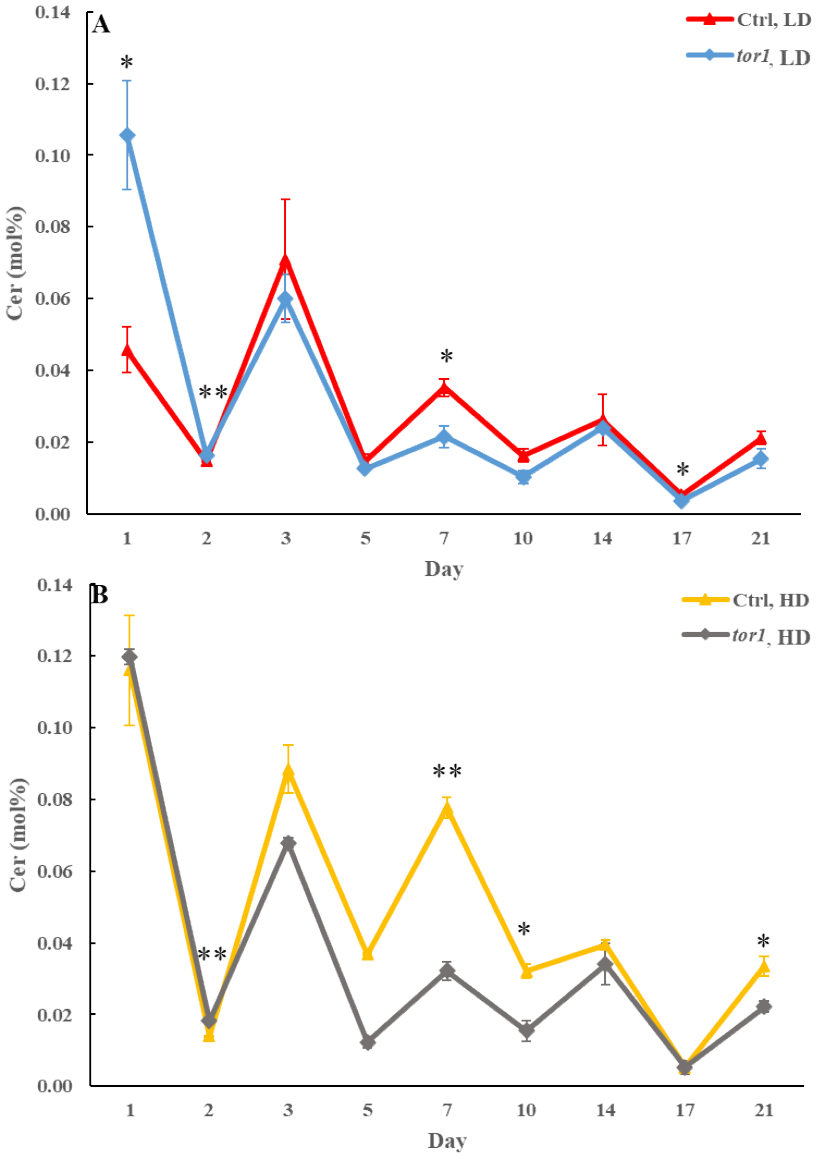

Figure 5.12: *tor1Δ* causes a decline in CER concentration in HD cells on some days of culturing. WT and *tor1Δ* cells were cultured in the YP medium supplemented with 2% glucose (non-CR conditions). Cell aliquots were taken on different days of culturing. The Percoll density gradient centrifugation was used to purify HD and LD cells from these cell aliquots. LC-MS/MS

was used to assess CER concentrations in these cells. Data are shown as means ± SD (n = 2; *p < 0.05; **p < 0.01).

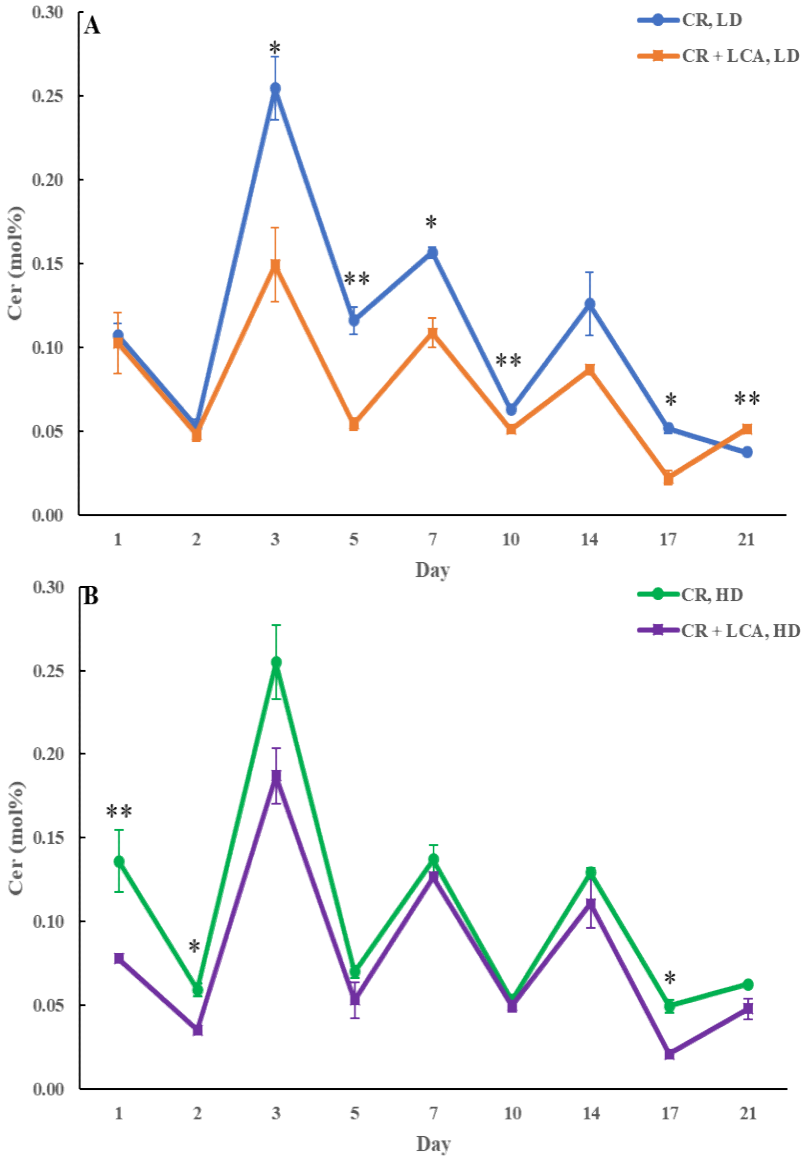

Figure 5.13: LCA decreases CER concentration in LD cells throughout the chronological lifespan. WT cells were cultured in YP medium supplemented with 0.2% glucose (CR conditions) in the presence of 50 µM LCA or its absence. Cell aliquots were taken on different days of culturing. The Percoll density gradient centrifugation was used to purify HD and LD cells from these cell aliquots. LC-MS/MS was used to assess CER concentrations in these cells. Data are

shown as means ± SD (n = 2; *$p < 0.05$; **$p < 0.01$).

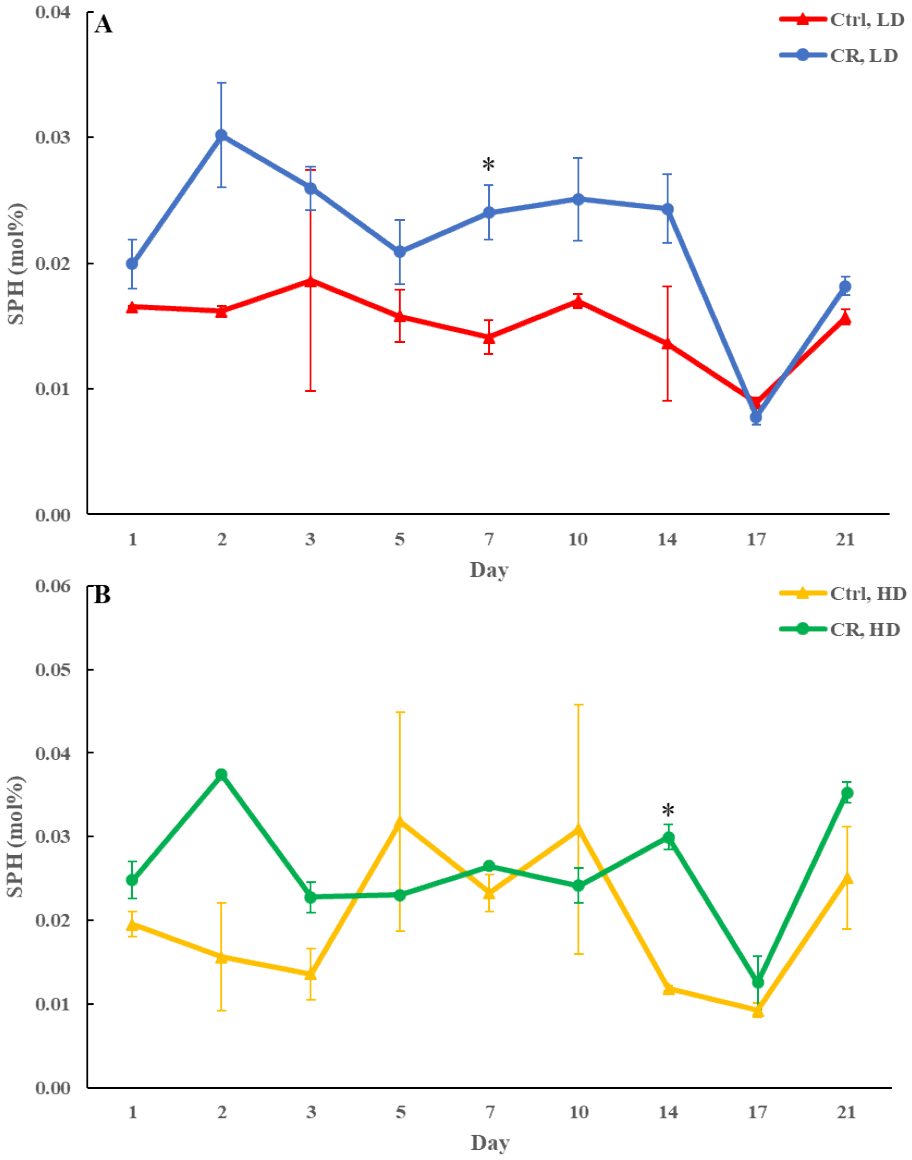

Figure 5.14: SPH concentration does not change significantly throughout the chronological lifespan of the HD or LD cells placed on the CR diet. WT cells were cultured in the YP medium supplemented with 0.2% glucose (CR conditions) or 2% glucose (control non-CR conditions). Cell aliquots were taken on different days of culturing. The Percoll density gradient centrifugation was used to purify HD and LD cells from these cell aliquots. LC-MS/MS was used to measure SPH concentrations in these cells. Data are shown as means ± SD (n = 2; *$p < 0.05$).

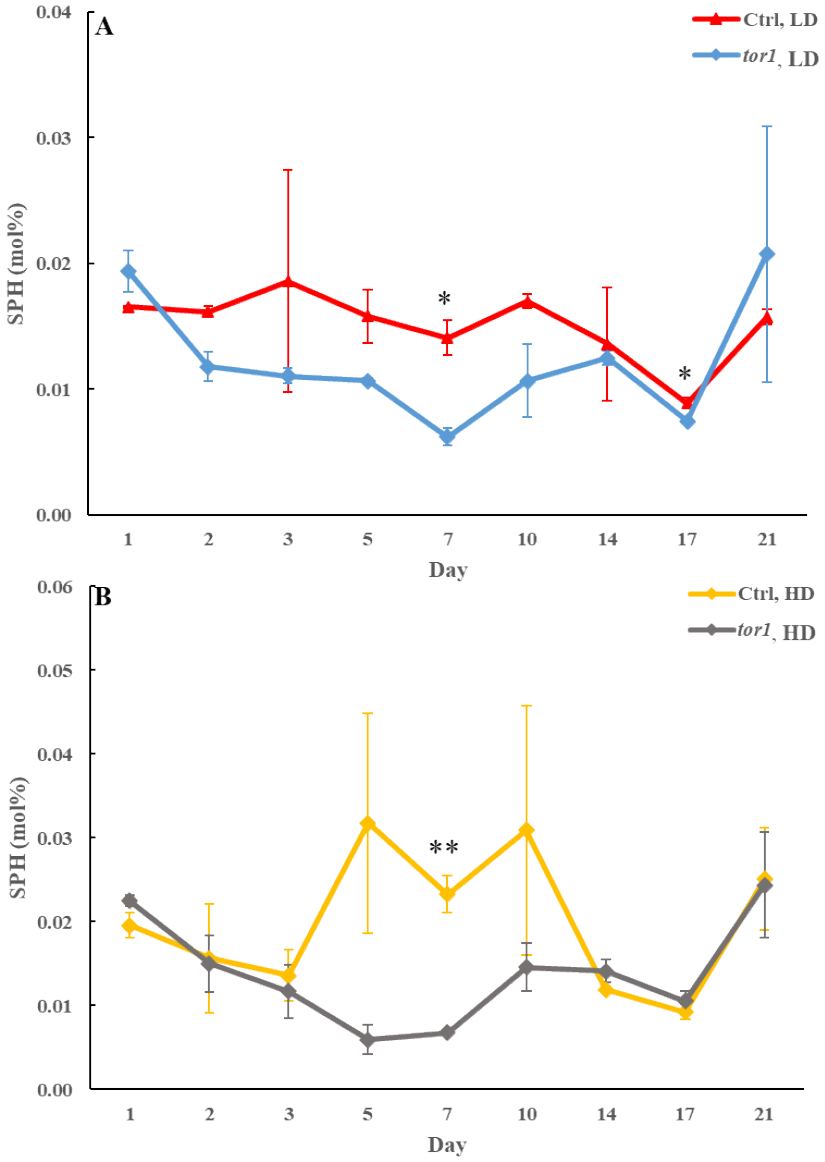

Figure 5.15: SPH concentration does not change significantly throughout the chronological lifespan of the HD or LD cells carrying the *tor1Δ* mutation. WT and *tor1Δ* cells were cultured in the YP medium supplemented with 2% glucose (non-CR conditions). Cell aliquots were taken on different days of culturing. The Percoll density gradient centrifugation was used to purify HD and LD cells from these cell aliquots. LC-MS/MS was used to measure SPH concentrations in these cells. Data are shown as means ± SD (n = 2; *$p < 0.05$; **$p < 0.01$).

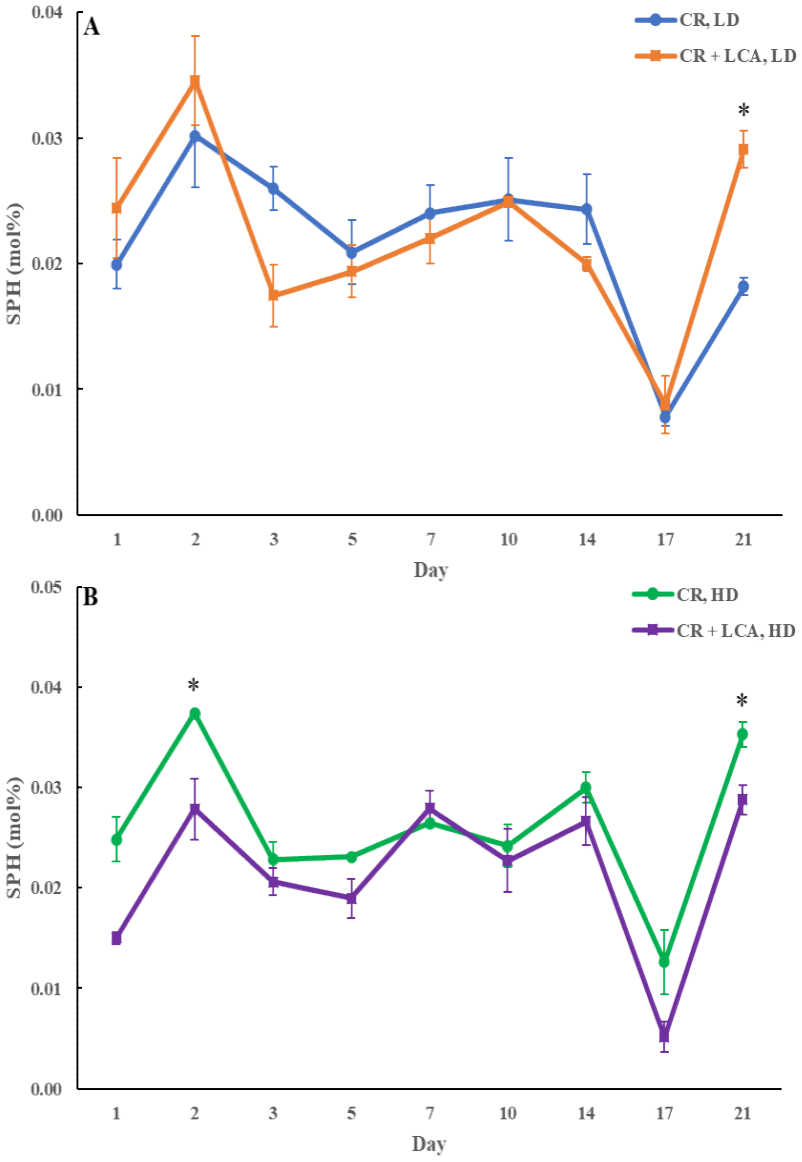

Figure 5.16: SPH concentration does not change significantly throughout the chronological lifespan of the HD or LD cells treated with LCA. WT cells were cultured in YP medium supplemented with 0.2% glucose (CR conditions) in the presence of 50 µM LCA or its absence. Cell aliquots were taken on different days of culturing. The Percoll density gradient centrifugation was used to purify HD and LD cells from these cell aliquots. LC-MS/MS was used to measure

SPH concentrations in these cells. Data are shown as means ± SD (n = 2; *$p < 0.05$).

5.7 The concentrations of all ER- and mitochondria-synthesized phospholipids are significantly increased in the HD and LD cells placed on CR diet but not in the HD or LD cells carrying the *tor1Δ* mutation or treated with LCA.

Phospholipids in yeast cells are generated in the ER, mitochondria and LD (Figure 1.7) [156, 158, 354]. The major forms of phospholipids are the ER-synthesized LPA, PA, PI, PS and PC and mitochondria-formed PE, PG and CL (Figure 1.7) [156, 158, 354]. The minor forms of phospholipids are LPI, LPS, LPE, LPC and LPG [156, 158, 354]. The broad-specificity lysophospholipid acyltransferase Ale1 in the ER, LPC acyltransferase Taz1 in mitochondria, and LPI acyltransferase Psi1 in LD and mitochondria have been implicated in the synthesis of these secondary phospholipids (Figure 1.7) [156, 158, 354].

We found that the concentrations of all these phospholipids in the HD and LD cells placed on the CR diet are increased throughout the chronological lifespan. This chapter of my Thesis shows the data on how CR influences age-related changes in the concentrations of LPA (Figure 5.17), PA (Figure 5.18), PI (Figure 5.19), PS (Figure 5.20), PE (Figure 5.21), PC (Figure 5.22), LPI (Figure 5.23), LPS (Figure 5.24), LPE (Figure 5.25), LPC (Figure 5.26), PG (Figure 5.27), CL (Figure 5.28) and LPG (Figure 5.29) in HD and LD cells. It needs to be emphasized that the concentrations of many of these phospholipids within the Q and NQ cells of a short-lived LD population were higher than those within the Q and NQ cells of a long-lived HD population. Moreover, it remains to be determined whether the observed low concentrations of LPI (Figure 5.23) perform any regulatory role under the conditions of cell culturing tested in these experiments.

We also noted that no significant and continuing changes in the concentrations of all these phospholipids are observed within the HD and LD cell populations carrying the *tor1Δ* mutation or treated with LCA. These data are presented in the Appendix chapter LPA (Figures 10.1 and 10.2), PA (Figures 10.3 and 10.4), PI (Figures 10.5 and 10.6), PS (Figures 10.7 and 10.8), PE (Figures 10.9 and 10.10), PC (Figures 10.11 and 10.12), LPI (Figures 10.13 and 10.14), LPS (Figures 10.15 and 10.16), LPE (Figures 10.17 and 10.18), LPC (Figures 10.19 and 10.20), PG (Figures 10.21 and 10.22), CL (Figures 10.23 and 10.24) and LPG (Figures 10.25 and 10.26).

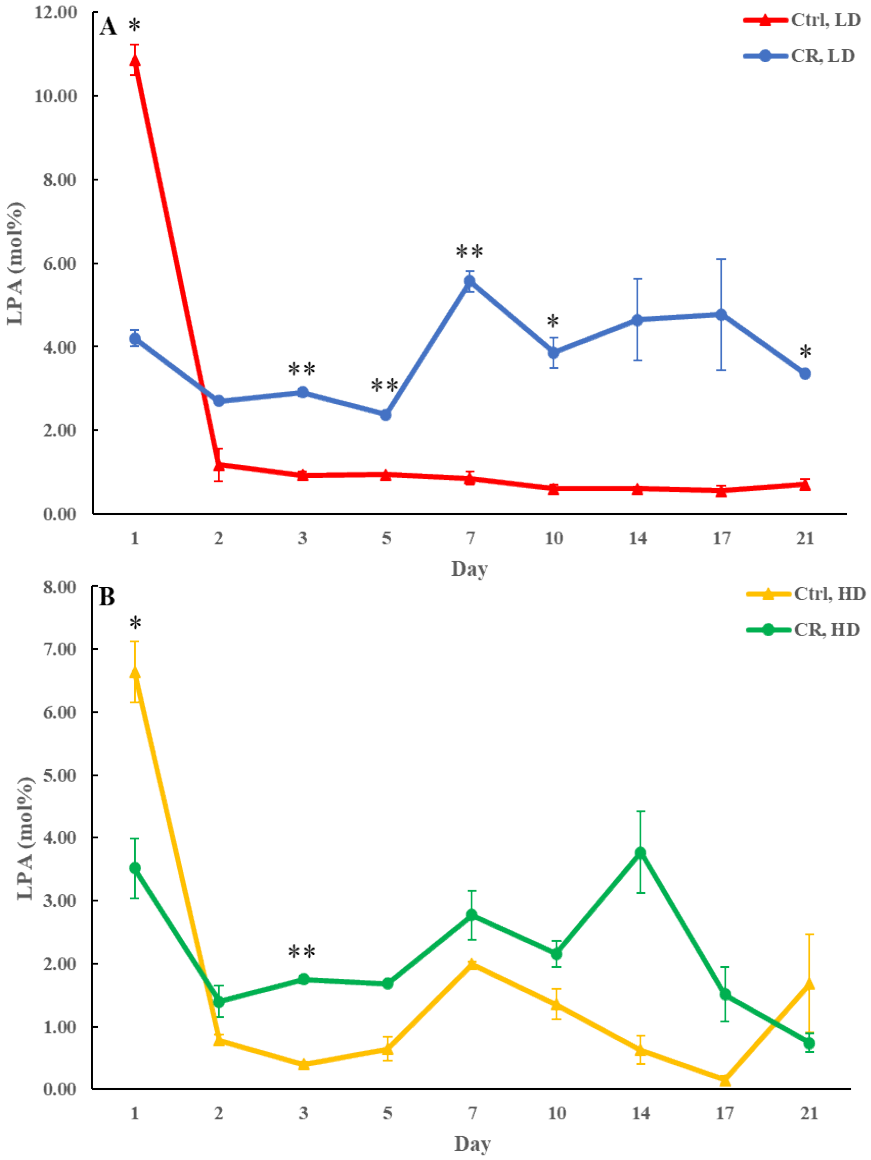

Figure 5.17: LPA concentration in the LD cells (and to a lesser extent in HD cells) placed on the CR diet is increased throughout most of the chronological lifespan. WT cells were cultured in the YP medium supplemented with 0.2% glucose (CR conditions) or 2% glucose (control non-CR conditions). Cell aliquots were taken on different days of culturing. The Percoll density gradient centrifugation was used to purify HD and LD cells from these cell aliquots. LC-MS/MS was used to measure LPA concentrations in these cells. Data are shown as means ± SD (n = 2; *$p < 0.05$; **$p < 0.01$).

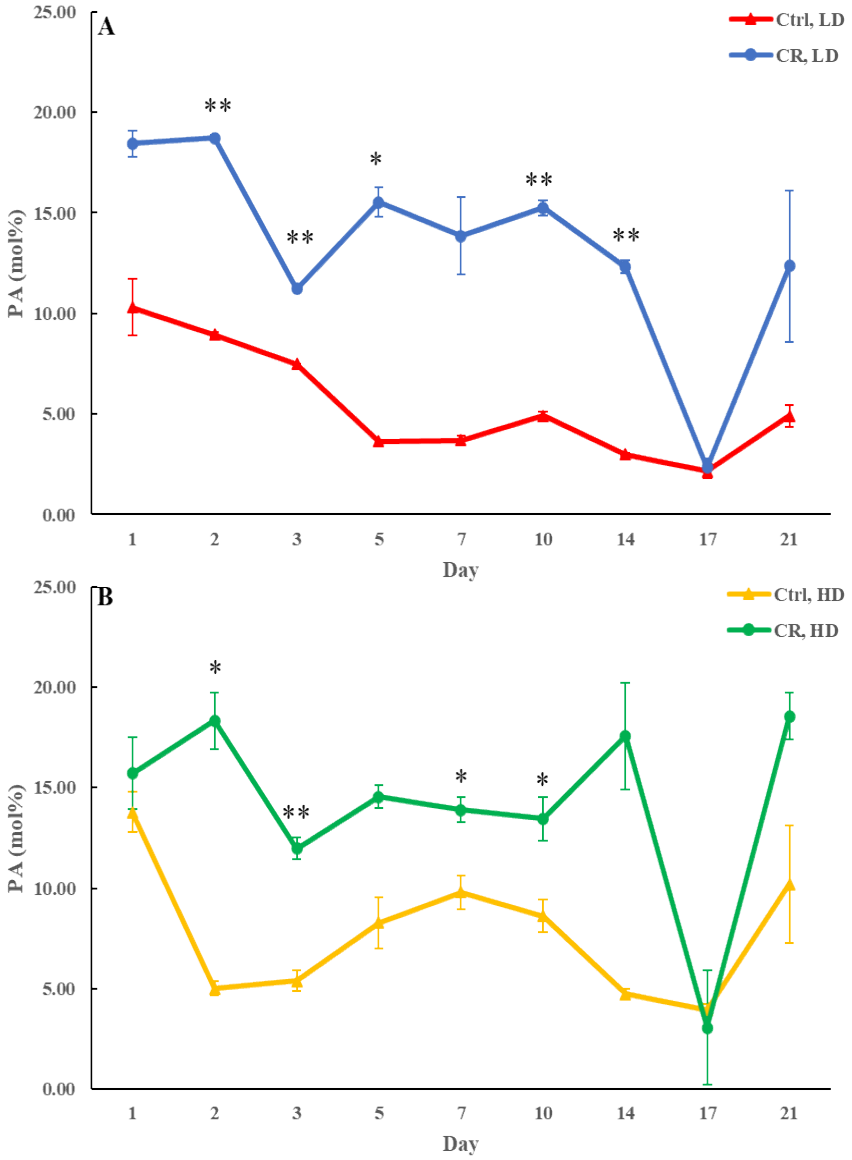

Figure 5.18: PA concentration in the HD and LD cells placed on the CR diet is increased throughout most of the chronological lifespan. WT cells were cultured in the YP medium supplemented with 0.2% glucose (CR conditions) or 2% glucose (control non-CR conditions). Cell aliquots were taken on different days of culturing. The Percoll density gradient centrifugation was used to purify HD and LD cells from these cell aliquots. LC-MS/MS was used to measure PA concentrations in these cells. Data are shown as means ± SD (n = 2; *$p < 0.05$; **$p < 0.01$).

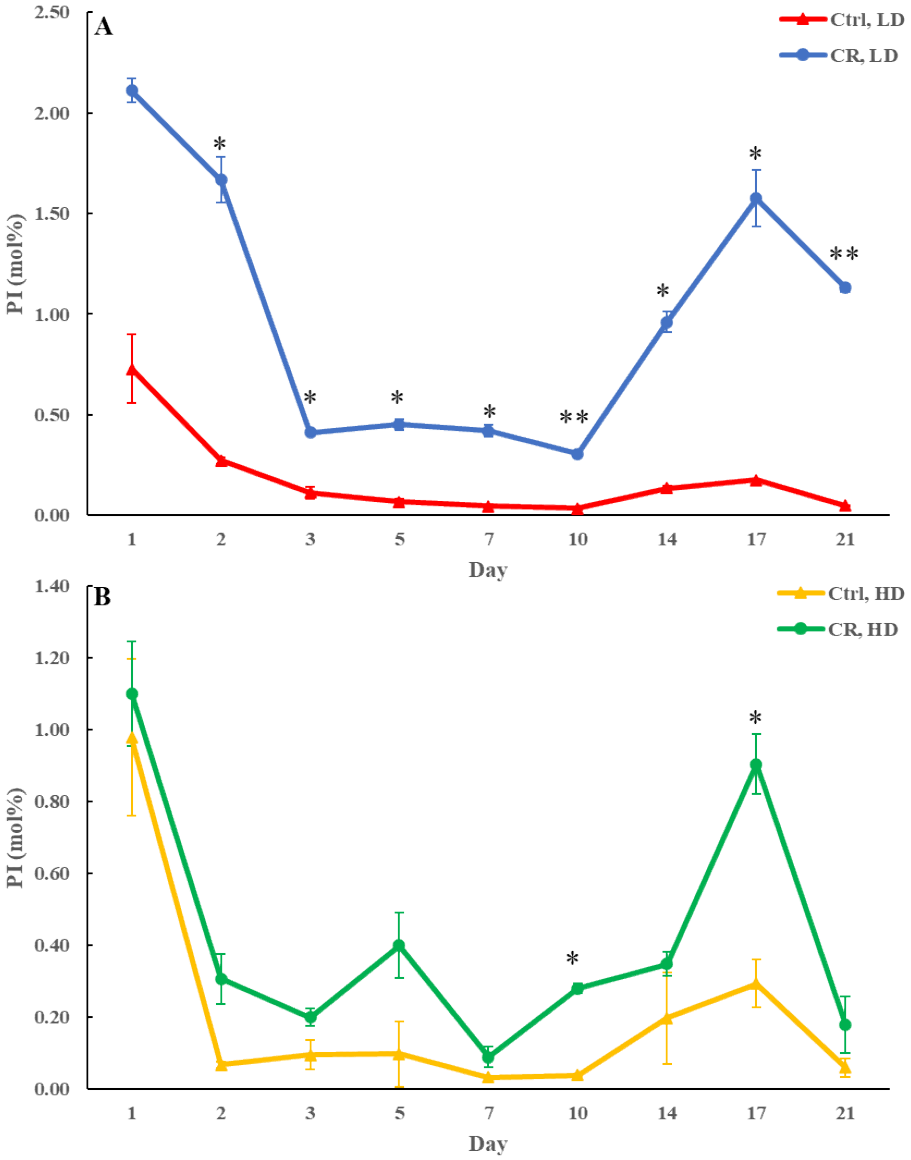

Figure 5.19: PI concentration in the LD cells (and to a lesser extent in HD cells) placed on the CR diet is increased throughout the chronological lifespan. WT cells were cultured in the YP medium supplemented with 0.2% glucose (CR conditions) or 2% glucose (control non-CR conditions). Cell aliquots were taken on different days of culturing. The Percoll density gradient centrifugation was used to purify HD and LD cells from these cell aliquots. LC-MS/MS was used to measure PI concentrations in these cells. Data are shown as means ± SD (n = 2; *$p < 0.05$; **$p < 0.01$).

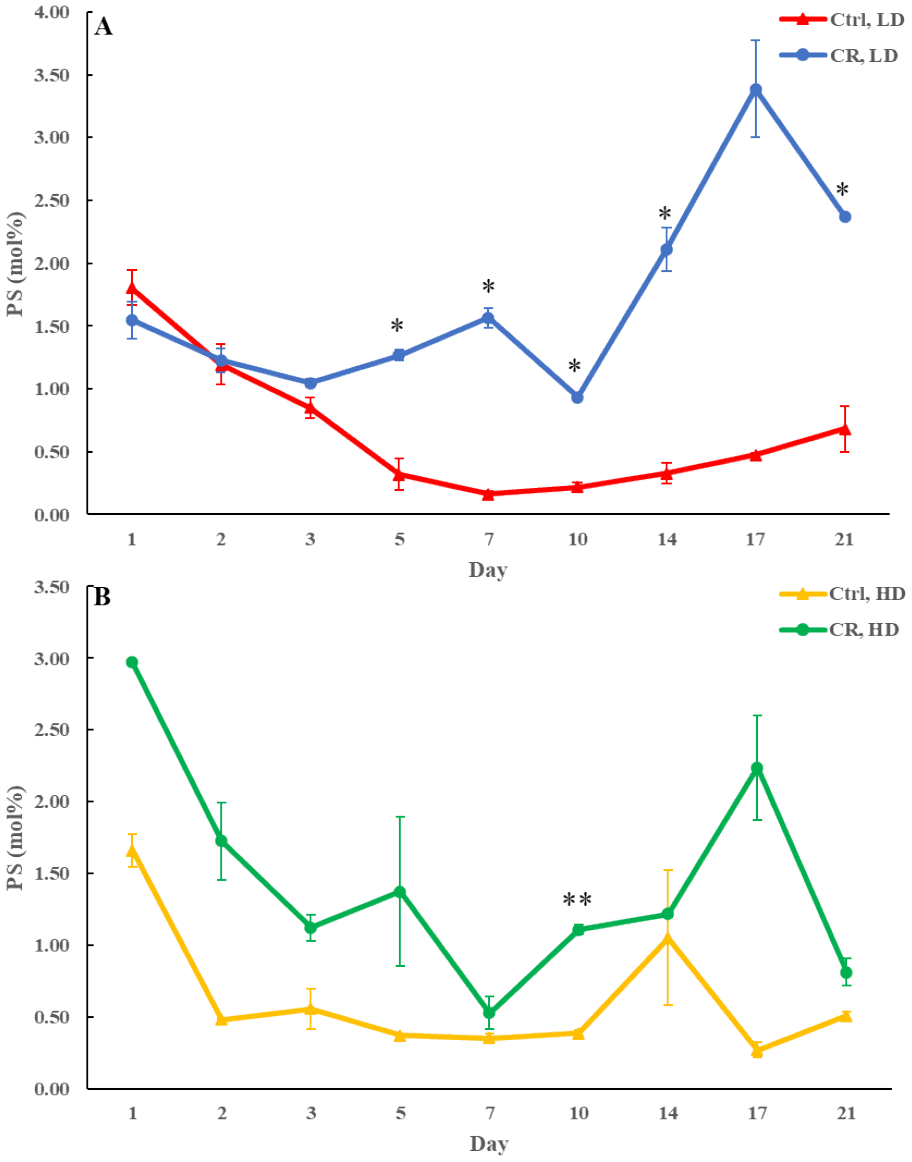

Figure 5.20: PS concentration in the LD cells (and to a lesser extent in HD cells) placed on the CR diet is increased throughout most of the chronological lifespan. WT cells were cultured in the YP medium supplemented with 0.2% glucose (CR conditions) or 2% glucose (control non-CR conditions). Cell aliquots were taken on different days of culturing. The Percoll density gradient centrifugation was used to purify HD and LD cells from these cell aliquots. LC-MS/MS was used to measure PS concentrations in these cells. Data are shown as means ± SD (n = 2; *p < 0.05; **p < 0.01).

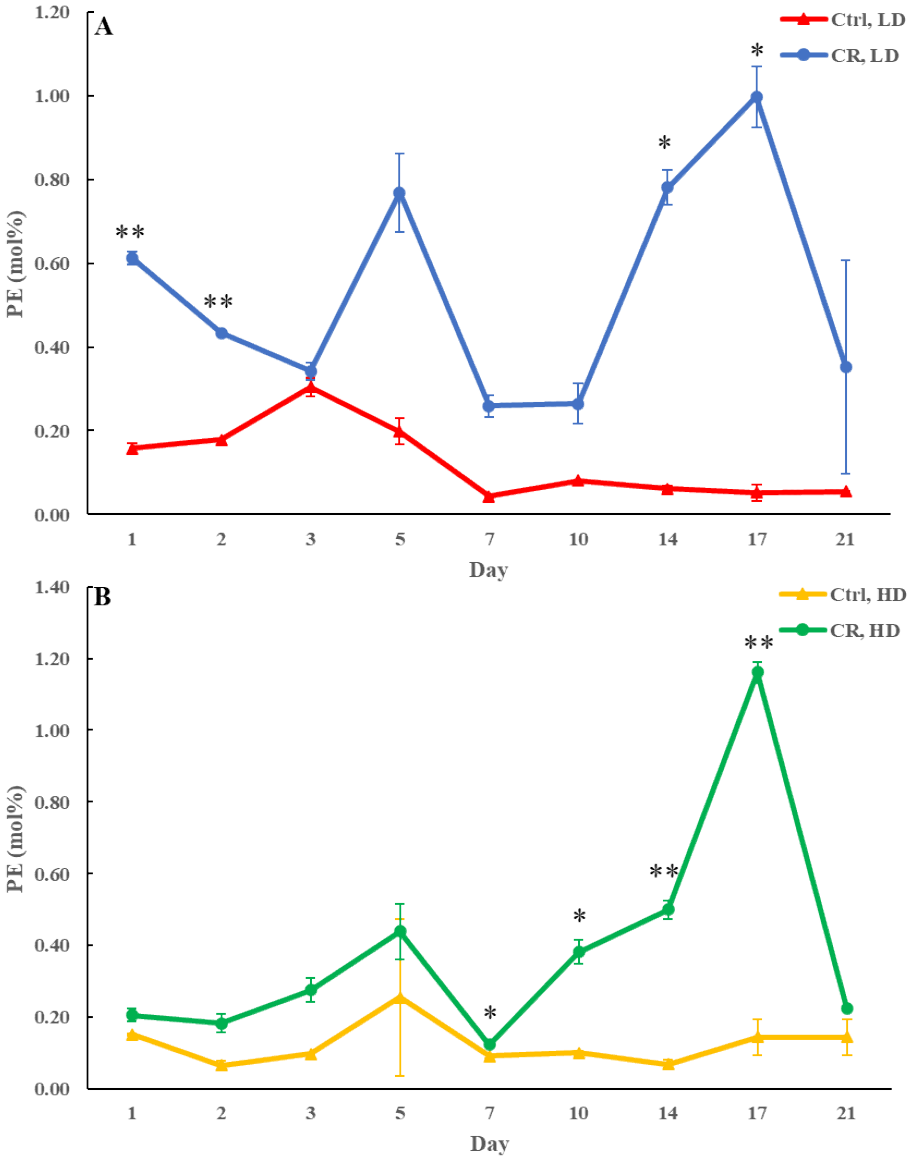

Figure 5.21: PE concentration in the LD cells (and to a lesser extent in HD cells) placed on the CR diet is increased throughout most of the chronological lifespan. WT cells were cultured in the YP medium supplemented with 0.2% glucose (CR conditions) or 2% glucose (control non-CR conditions). Cell aliquots were taken on different days of culturing. The Percoll density gradient centrifugation was used to purify HD and LD cells from these cell aliquots. LC-MS/MS was used to measure PE concentrations in these cells. Data are shown as means ± SD (n = 2; *p < 0.05; **$p < 0.01$; **$p < 0.01$).

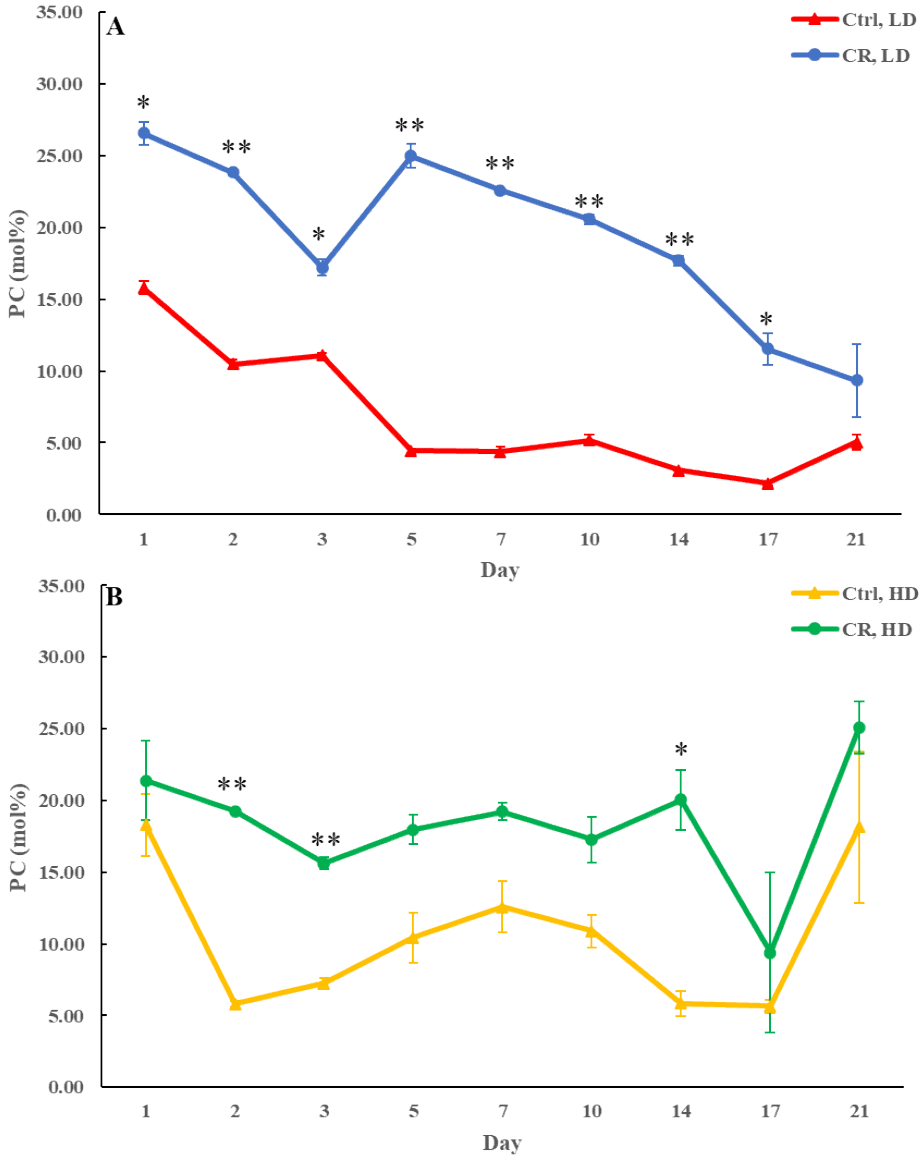

Figure 5.22: PC concentration in the LD cells (and to a lesser extent in HD cells) placed on the CR diet is increased throughout all or most of the chronological lifespan. WT cells were cultured in the YP medium supplemented with 0.2% glucose (CR conditions) or 2% glucose (control non-CR conditions). Cell aliquots were taken on different days of culturing. The Percoll density gradient centrifugation was used to purify HD and LD cells from these cell aliquots. LC-MS/MS was used to measure PC concentrations in these cells. Data are shown as means ± SD (n = 2; *$p < 0.05$; **$p < 0.01$).

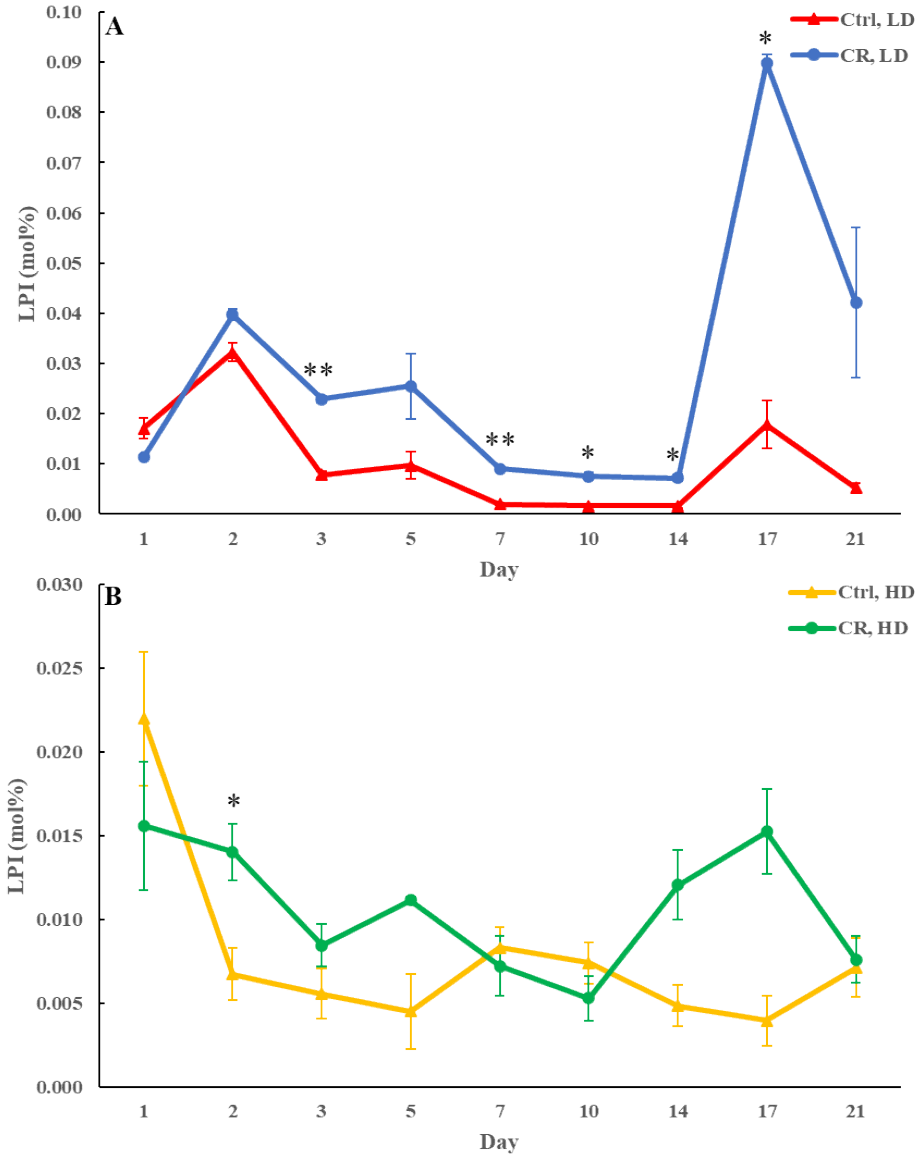

Figure 5.23: LPI concentration in the LD cells (and to a lesser extent in HD cells) placed on the CR diet is increased throughout most of the chronological lifespan. WT cells were cultured in the YP medium supplemented with 0.2% glucose (CR conditions) or 2% glucose (control non-CR conditions). Cell aliquots were taken on different days of culturing. The Percoll density gradient centrifugation was used to purify HD and LD cells from these cell aliquots. LC-MS/MS was used to measure LPI concentrations in these cells. Data are shown as means ± SD (n = 2; *p < 0.05; **$p < 0.01$; **$p < 0.01$).

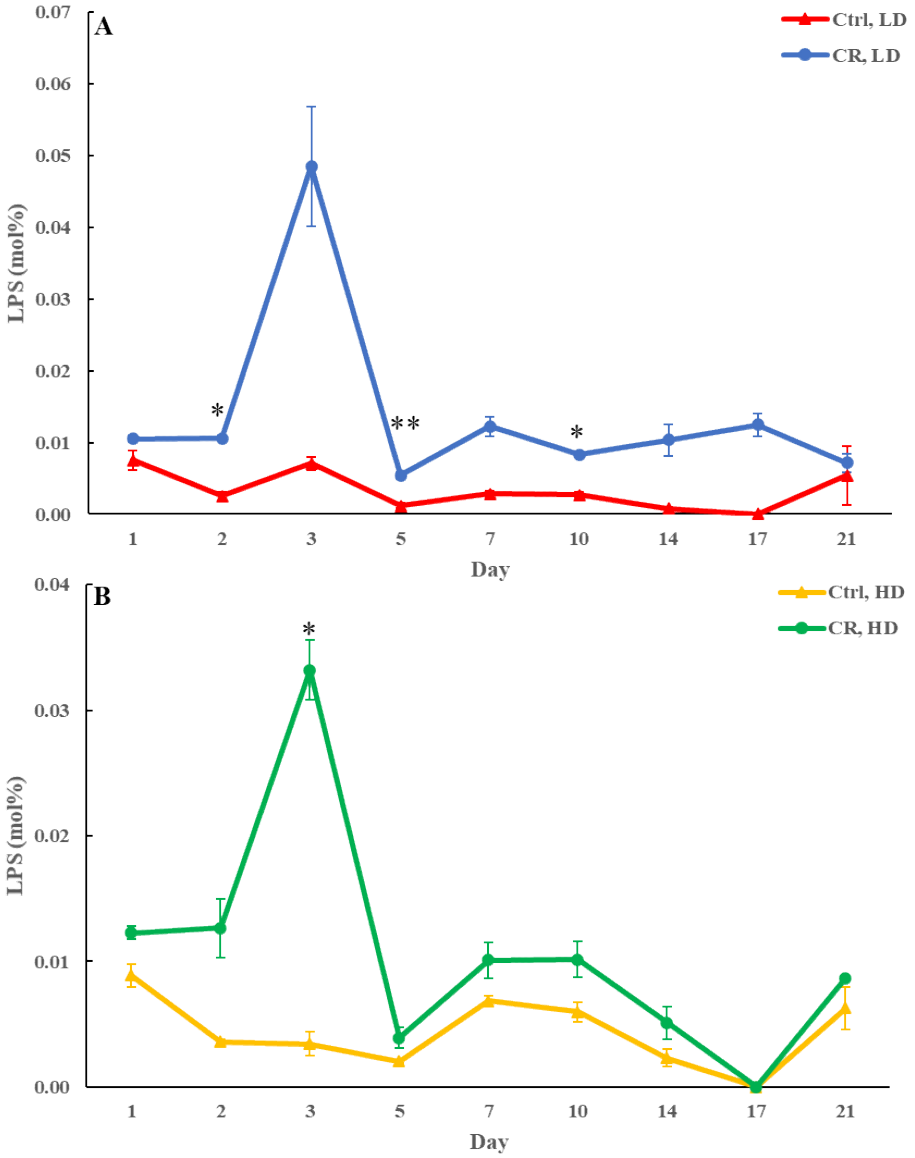

Figure 5.24: LPS concentration in the LD cells (and to a lesser extent in HD cells) placed on the CR diet is increased throughout most of the chronological lifespan. WT cells were cultured in the YP medium supplemented with 0.2% glucose (CR conditions) or 2% glucose (control non-CR conditions). Cell aliquots were taken on different days of culturing. The Percoll density gradient centrifugation was used to purify HD and LD cells from these cell aliquots. LC-MS/MS was used to measure LPS concentrations in these cells. Data are shown as means ± SD (n = 2; *p < 0.05; **$p < 0.01$; **$p < 0.01$).

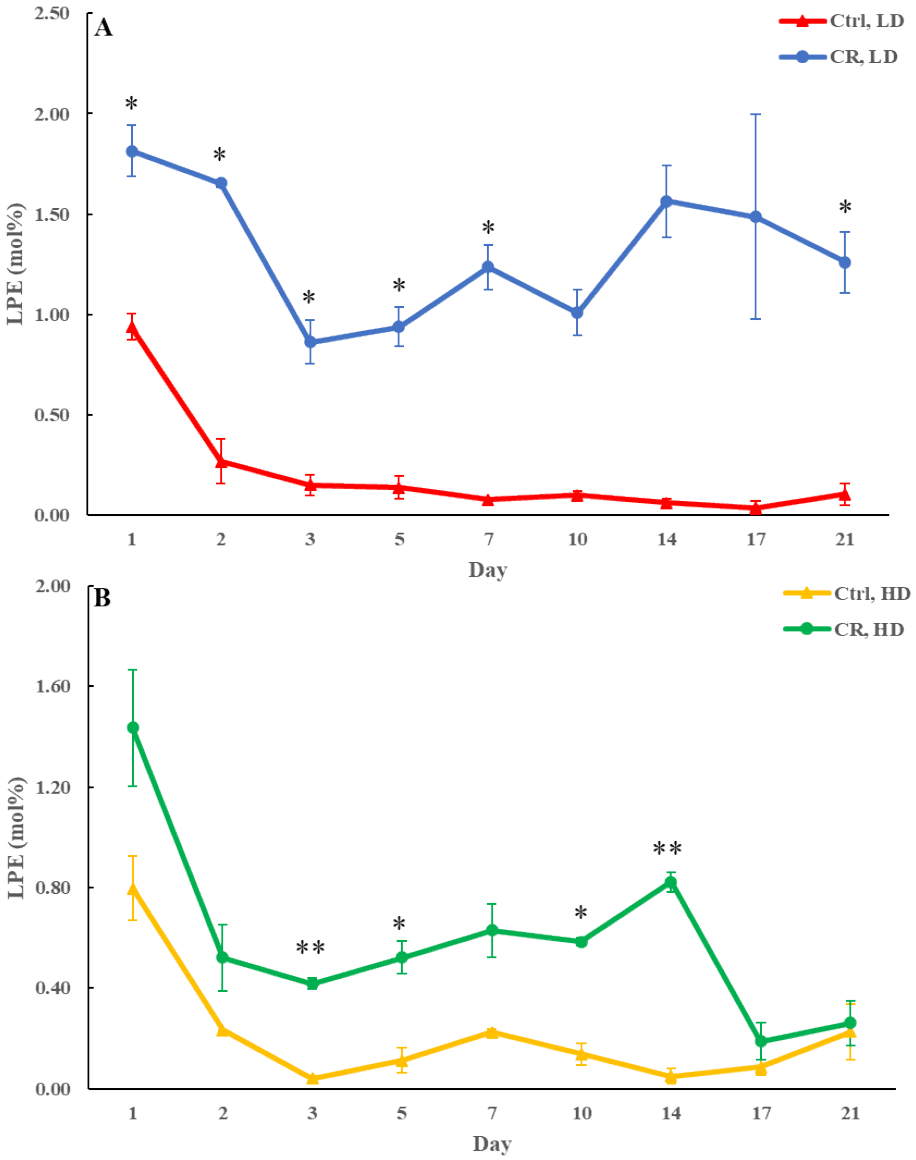

Figure 5.25: LPE concentration in the LD cells (and to a lesser extent in HD cells) placed on the CR diet is increased throughout all or most of the chronological lifespan. WT cells were cultured in the YP medium supplemented with 0.2% glucose (CR conditions) or 2% glucose (control non-CR conditions). Cell aliquots were taken on different days of culturing. The Percoll density gradient centrifugation was used to purify HD and LD cells from these cell aliquots. LC-MS/MS was used to measure LPE concentrations in these cells. Data are shown as means ± SD (n = 2; *$p < 0.05$; **$p < 0.01$; **p < 0.01).

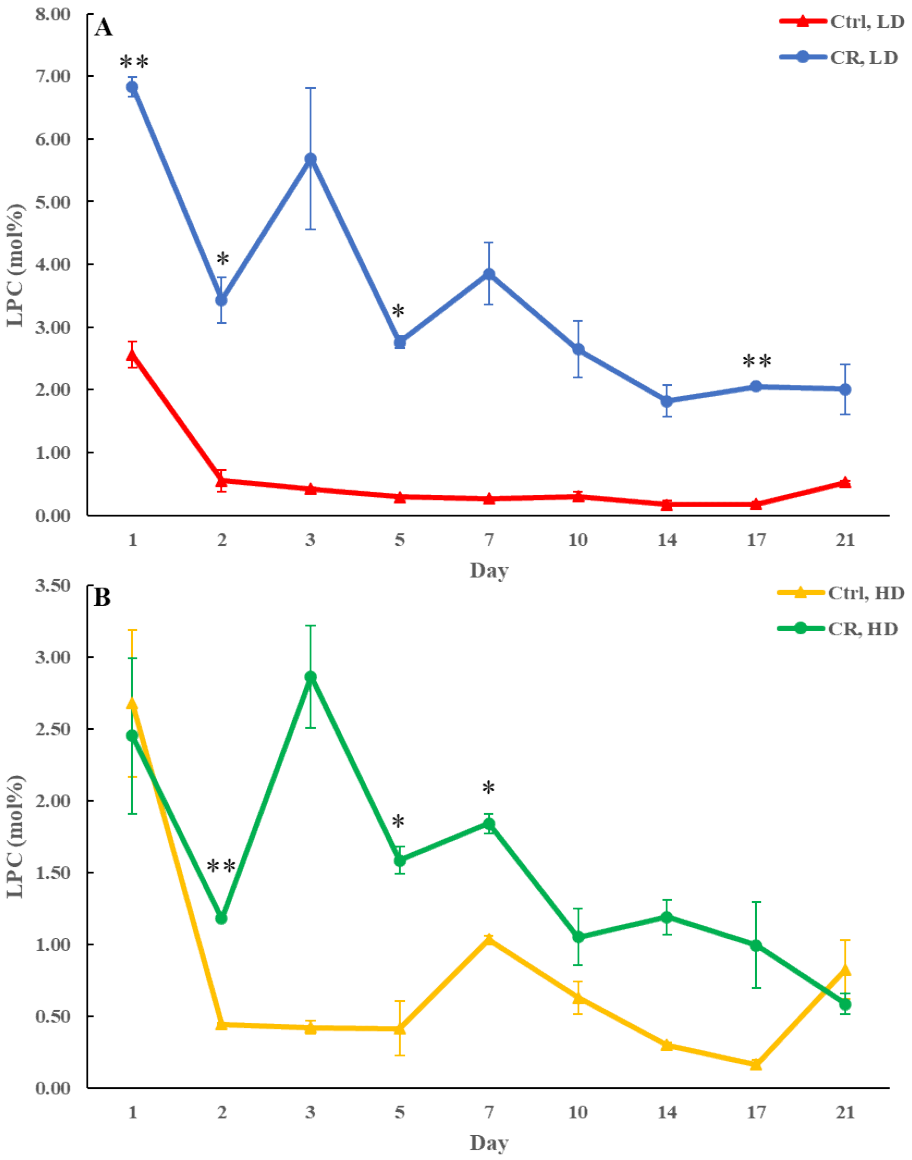

Figure 5.26: LPC concentration in the LD cells (and to a lesser extent in HD cells) placed on the CR diet is increased throughout all or most of the chronological lifespan. WT cells were cultured in the YP medium supplemented with 0.2% glucose (CR conditions) or 2% glucose (control non-CR conditions). Cell aliquots were taken on different days of culturing. The Percoll density gradient centrifugation was used to purify HD and LD cells from these cell aliquots. LC-MS/MS was used to measure LPC concentrations in these cells. Data are shown as means ± SD (n = 2; *$p < 0.05$; **$p < 0.01$; **p < 0.01).

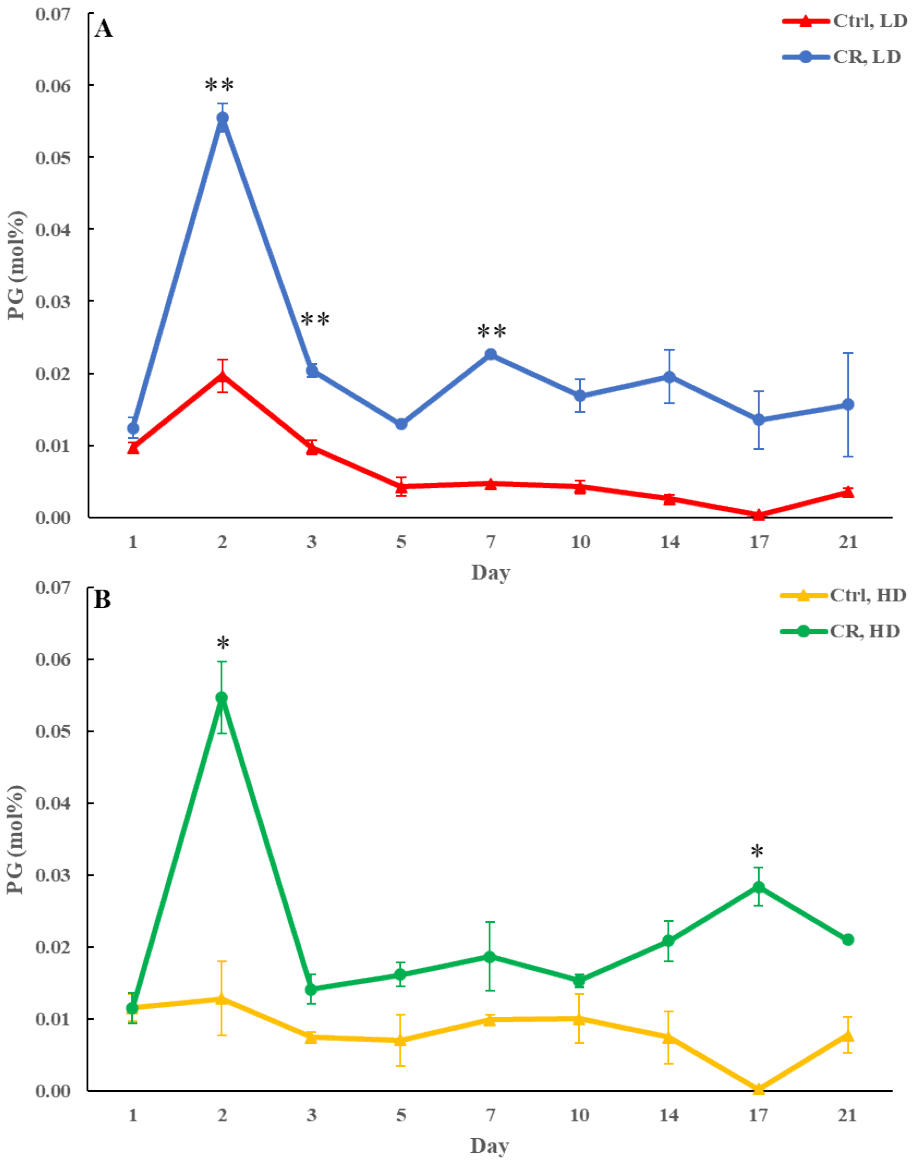

Figure 5.27: PG concentration in the LD and HD cells placed on the CR diet is increased throughout most of the chronological lifespan. WT cells were cultured in the YP medium supplemented with 0.2% glucose (CR conditions) or 2% glucose (control non-CR conditions). Cell aliquots were taken on different days of culturing. The Percoll density gradient centrifugation was used to purify HD and LD cells from these cell aliquots. LC-MS/MS was used to measure PG concentrations in these cells. Data are shown as means ± SD (n = 2; *$p < 0.05$; **$p < 0.01$).

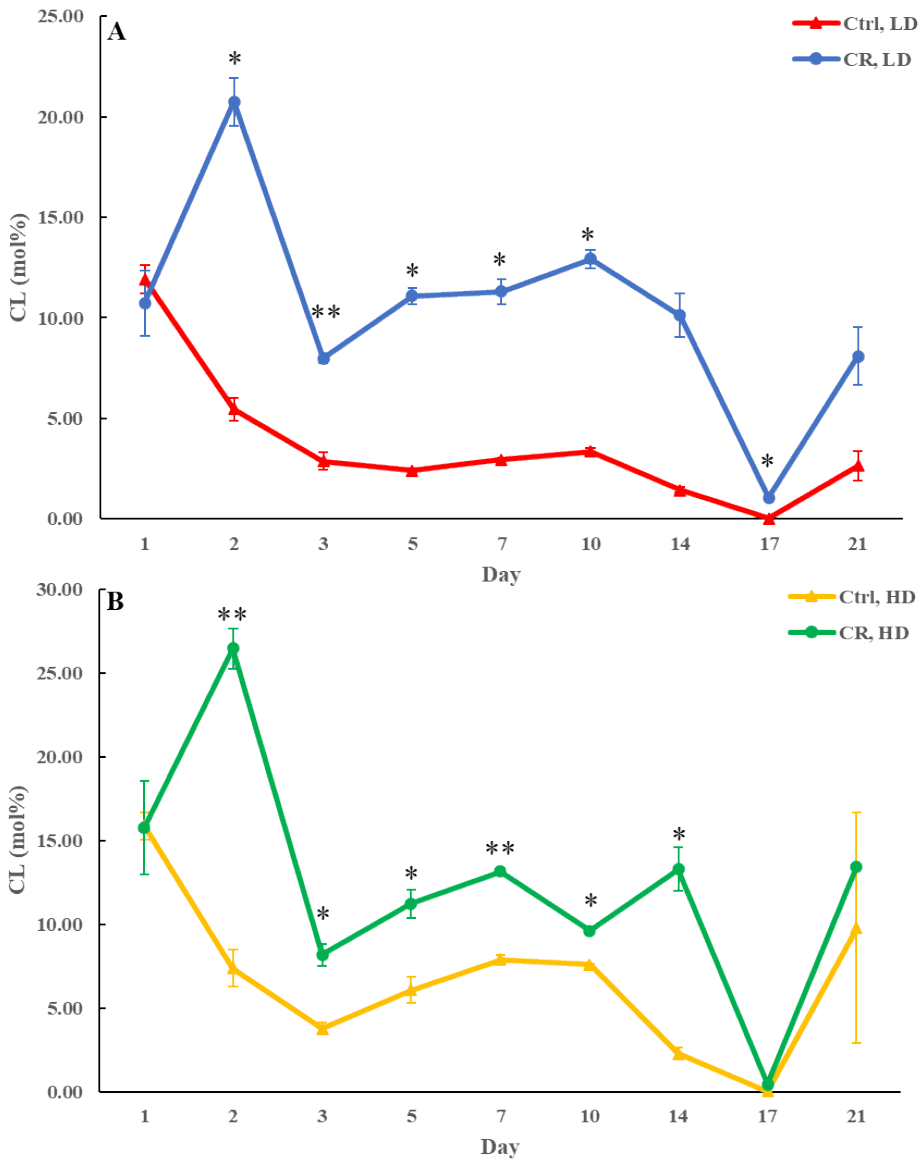

Figure 5.28: CL concentration in the LD cells (and to a lesser extent in HD cells) placed on the CR diet is increased throughout most of the chronological lifespan. WT cells were cultured in the YP medium supplemented with 0.2% glucose (CR conditions) or 2% glucose (control non-CR conditions). Cell aliquots were taken on different days of culturing. The Percoll density gradient centrifugation was used to purify HD and LD cells from these cell aliquots. LC-MS/MS was used to measure CL concentrations in these cells. Data are shown as means ± SD (n = 2; *p < 0.05; **p < 0.01).

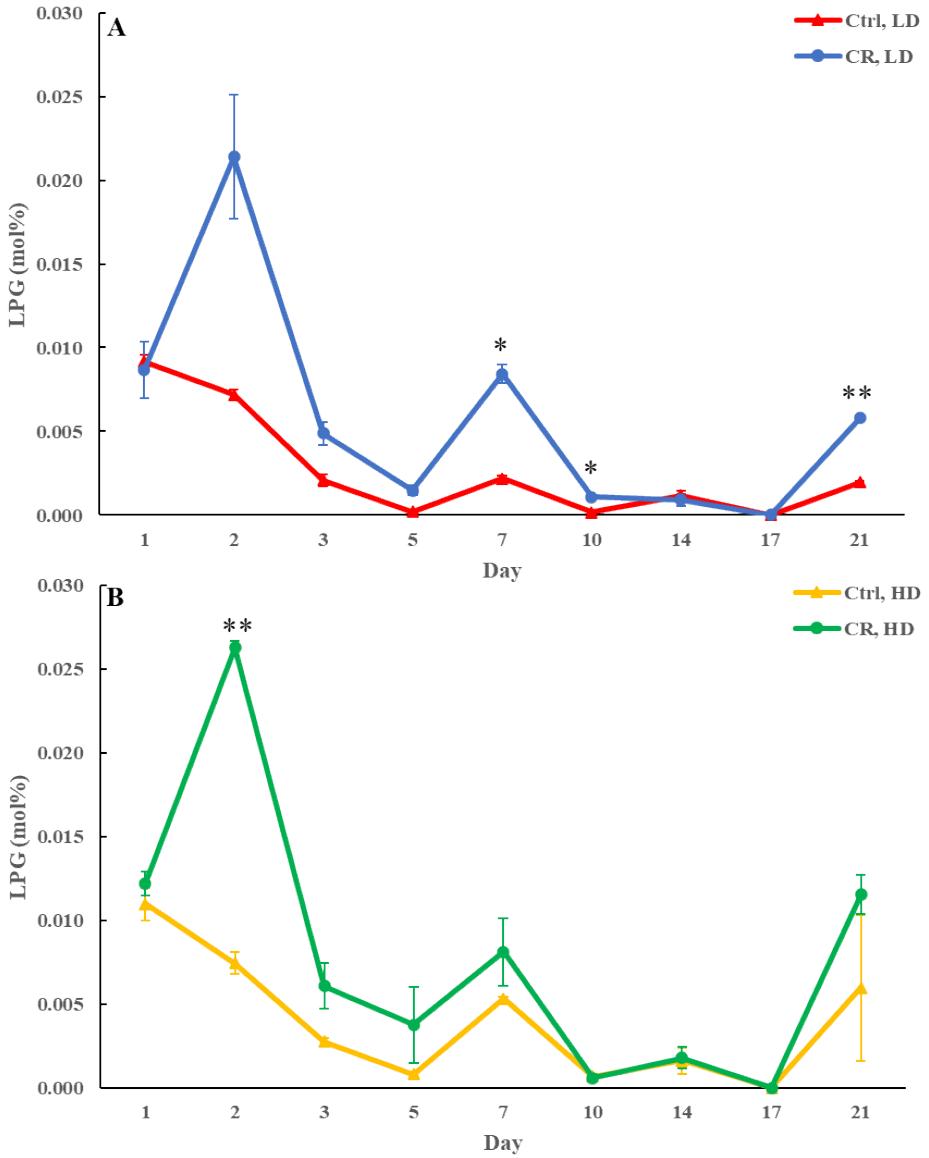

Figure 5.29: LPG concentration in the LD and HD cells placed on the CR diet is increased throughout most of the chronological lifespan. WT cells were cultured in the YP medium supplemented with 0.2% glucose (CR conditions) or 2% glucose (control non-CR conditions). Cell aliquots were taken on different days of culturing. The Percoll density gradient centrifugation was used to purify HD and LD cells from these cell aliquots. LC-MS/MS was used to measure LPG concentrations in these cells. Data are shown as means ± SD (n = 2; *$p < 0.05$; **$p < 0.01$).

5.8 The lipidomes of HD and LD cells are reorganized in budding yeast cultured under CR conditions.

We applied the newly developed LC-MS/MS lipidomics method to measure the age-related changes in the concentrations of 18 lipid classes in HD and LD cells of the WT strain. In the first set of experiments, yeast cells were cultured in a nutrient-rich medium supplemented with 0.2% or 2% glucose (CR or non-CR conditions, respectively) as the only source of carbon. The populations of HD and LD cells were purified using Percoll density gradient centrifugation. The HD cell population on day 1 of culturing includes mainly Q cells [68, 70]. The Q cells in the HD population are comparatively slowly converted into NQ cells [68, 70]. On day 1 of culturing, the LD cell population also contains Q cells primarily [68, 70]. The Q-to-NQ cell conversion within the LD cell population is a comparatively fast process [68, 70].

Using MS/MS to identify and quantitate cellular lipids with the help of a direct-injection method of lipidomics, the Titorenko laboratory has previously revealed that the geroprotective CR diet lowers TAG concentration and rises CL concentration within HD and LD cells [68, 70]. The experiments described in this chapter of my Thesis used the novel method of LC-MS/MS lipidomics to assess how CR influences aging-associated changes in the concentrations of 18 lipid classes (including TAG and CL) within HD and LD cells. We found that CR reorganizes the lipidomes of HD and LD cells by substantially changing the concentrations of 16 out of 18 lipid classes (other than complex SPH and DAG) in both these cell types throughout most of the chronological lifespan. We calculated the concentration of each of the 18 lipid classes in mol% of all lipids to assess the aging-associated changes in the relative concentration of each lipid class. Our findings provide evidence that the lipidomes of HD and LD cells are reorganized in budding yeast cultured under CR conditions. We describe below and schematically show in Figure 5.30 the characteristic CR-dependent reorganization of the lipidomes within chronologically aging HD and LD cells.

A substantial increase in the intracellular FFA observed within HD and LD cells under CR conditions is possibly due to the CR-dependent activation of TAG lipolysis catalyzed by the neutral lipid hydrolases Tgl1, Tgl3, Tgl4, Tgl5 and Yju3 in LD (Figure 5.30). Such CR-dependent activation of TAG lipolysis elicits a substantial increase in the cytosolic concentration of FFA (Figure 5.30). Of note, considering the extending effect of CR on longevity, it is likely that FFA concentration under CR conditions of cell culturing does not exceed a toxic threshold. Our data

indicate that this excessive cytosolic pool of FFA in HD and LD cells under CR is likely incorporated into CER (thus rising CER concentration in the ER) and many phospholipid classes in the ER (Figure 5.30). We found that LPA, PA, PI, PS, PE and PC are the phospholipid classes in the ER whose concentrations rise due to the incorporation of excessive amounts of FFA into phospholipids under CR conditions (Figure 5.30). Our data show that CR not only increases the concentrations of CER, LPA, PA, PI, PS, PE and PC in the ER, but also stimulates the ER-to-mitochondria translocation of PA, PS, PC and PI, and accelerates the mitochondria-to-the ER transport of PE [8]; these movements of phospholipids occur via the mitochondria-ER contact sites [8] (Figure 5.30). The CR-dependent stimulation of the ER-to-mitochondria translocation of PS promotes the conversion of excessive PS into PE, thus increasing the concentration of mitochondrially synthesized PE (Figure 5.30). The CR-driven acceleration of mitochondria-to-the ER transport of PA, PC and PI causes the formation of excessive concentrations of PG and CL in mitochondria (Figure 5.30).

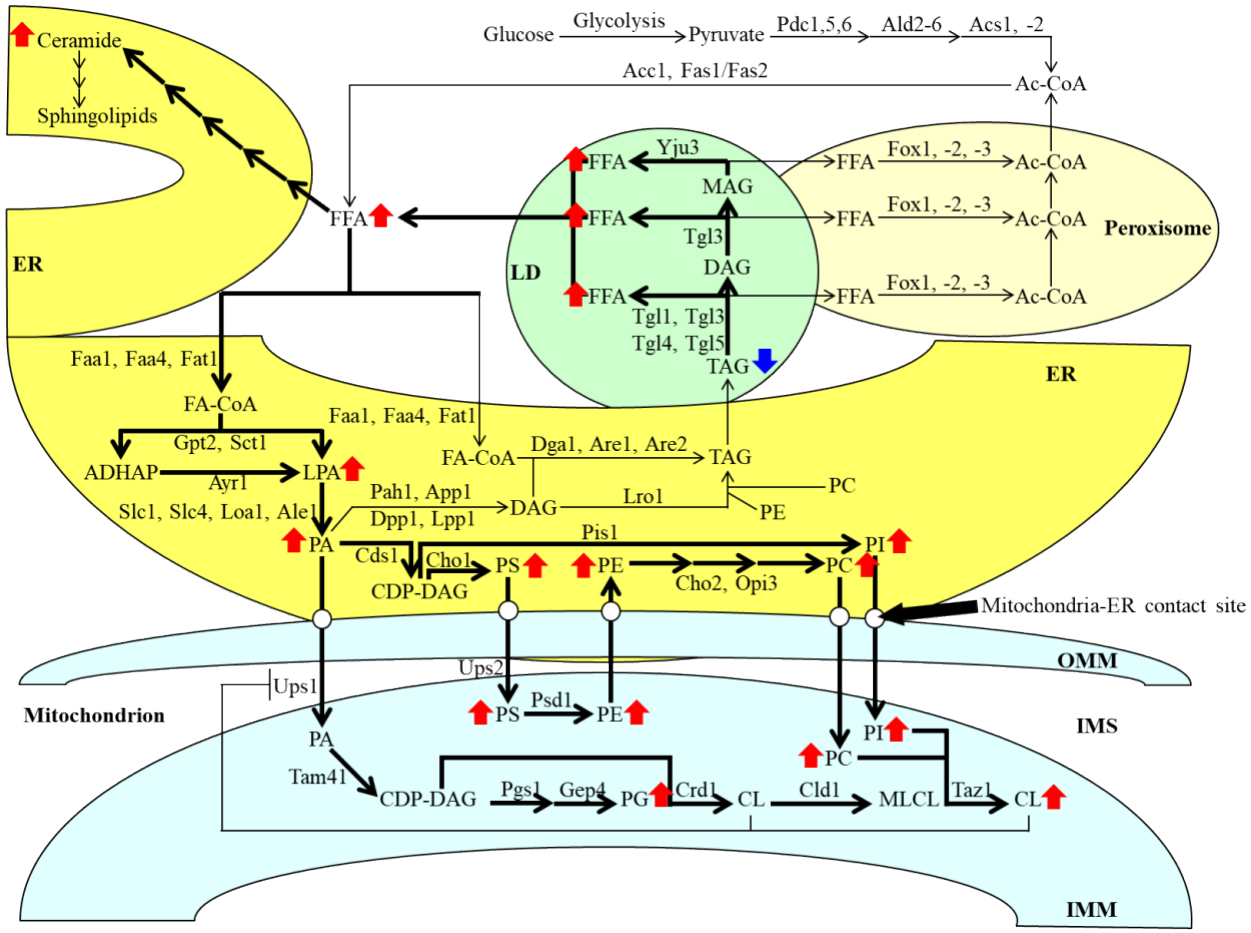

Figure 5.30: CR reorganizes the lipidomes of HD and LD cells by substantially changing the

concentrations of 16 out of 18 lipid classes. A CR-dependent activation of the lipolytic hydrolysis of triacylglycerols (TAG) in LD elicits a substantial rise in the intracellular concentrations of free fatty acids (FFA) within HD and LD cells. The excessive cytosolic pool of FFA in HD and LD cells under CR is incorporated into ceramide (CER) and many phospholipid classes in the ER. See the text for more details. The lipid classes whose concentrations are increased (red arrows) or decreased (blue arrow) in yeast under CR conditions are marked by arrows next to the names of these lipid classes. The efficiencies of TAG lipolysis, FFA-into-phospholipids incorporation and phospholipid transfer via the mitochondria-ER contact sites are proportional to the thickness of black arrows. Other abbreviations: CL, cardiolipin; CDP, cytidine diphosphate; DAG, diacylglycerol; IMM, inner mitochondrial membrane; MLCL, monolysocardiolipin; OMM, outer mitochondrial membrane; PC, phosphatidylcholine; PE, phosphatidylethanolamine; PG, phosphatidylglycerol; PI, phosphatidylinositol; PS, phosphatidylserine.

In the future, it will be important to examine whether the characteristic CR-dependent reorganization of the lipidomes within chronologically aging HD and LD cells contributes to the aging delay and longevity extension by CR. We believe that there might be at least two mechanisms underlying such contribution. These mechanisms are briefly outlined below.

One mechanism is the observed excessive accumulation of phospholipids formed in the ER, which remain there after the formation (Figure 5.30). We propose that the resulting build-up of phospholipids impairs the homeostasis of lipids and proteins in the ER. A disbalance of lipid and protein homeostasis has been shown to initiate a regulatory mechanism known as the unfolded protein response in the ER (UPR^{ER}) [295-325]. The UPR^{ER} is an evolutionarily conserved regulatory mechanism found in many eukaryotes, including budding yeast [295-325]. The initiation of the UPR^{ER} by a disbalanced lipid and protein homeostasis in the ER is aimed at restoring this homeostasis. This restoration is achieved because the UPR^{ER} quality control system slows protein synthesis on the ribosomes attached to the ER, promotes the outward vesicular traffic for taking away the improperly folded proteins from the ER, enhances a refolding of the improperly folded proteins in the ER, stimulates the proteasomal and autophagic degradation of improperly folded proteins, and modulates the synthesis of the ER membrane lipids [315, 319-325]. Because the UPR^{ER} quality control system is an essential contributor to all these processes in the ER, it is involved in sustaining protein and lipid homeostasis within the entire cell and slowing cellular and

organismal aging in all eukaryotes [299, 300, 302, 306, 309, 313-315, 317, 320, 324-341]. Considering all the above, we propose that a build-up of the excessive amounts of phospholipids in the ER of HD and LD cells under CR conditions initiates the UPR^{ER} system as one of the mechanisms for slowing chronological aging and extending the CLS.

We propose that the other mechanism through which the characteristic CR-dependent reorganization of the HD and LD cells' lipidomes might contribute to aging delay under CR conditions is a mechanism linked to the observed rise in the mitochondrial membrane phospholipids PG and CL. The mitochondrial membrane lipidome defines the functional state of mitochondria [83, 95, 142, 146-148, 153, 154, 343, 344], which is an essential longevity-assuring factor in budding yeast and other eukaryotes [83, 95, 142, 146-148, 153, 154, 342-346]. In support of the existence of the mitochondria-based mechanism for the aging delay in calorically restricted HD and LD cells, CR promotes mitochondrial respiration, increases the mitochondrial membrane potential and changes the age-related dynamics of mitochondrial ROS formation in these cells [68, 70]. These three aspects of mitochondrial functionality play an essential role in the longevity assurance of eukaryotic cells, including budding yeast [83, 95, 142, 146-148, 153, 154, 342-346].

The proposed existence of the ER- and mitochondria-based mechanisms for the aging delay in HD and LD cells under CR conditions requires experimental testing in the future. One way of performing these future experiments is to examine the effects of mutations that alter phospholipid metabolism or the UPR^{ER} system on the extent of the CR-driven delay of yeast chronological aging.

One puzzling observation is that the concentrations of several phospholipids (including PI, PS, PE, LPI and LPE) within the Q and NQ cells of a short-lived LD population were higher than those within the Q and NQ cells of a long-lived HD population. The importance of this observation is presently unclear. We hypothesize that there is an optimal threshold in the concentrations of these phospholipids at which they slow yeast chronological aging to the greatest extent and are not toxic to the cell. Our hypothesis posits that the concentrations of the above phospholipid classes within the Q and NQ cells of a long-lived HD population do not exceed the predicted threshold. In our hypothesis, the concentrations of these phospholipid classes within the Q and NQ cells of a short-lived LD population exceed the toxic threshold and decrease the efficiency of chronological aging delay by CR. The critical testing of our hypothesis will require investigating how mutations that alter phospholipid metabolism in the ER affect the CLS of LD cells.

5.9 The *tor1Δ* and LCA geroprotectors influence the lipidomes of HD and LD cells differently than CR.

The second objective of the studies described in this chapter of my Thesis was to compare how CR and two other geroprotective interventions (specifically, the *tor1Δ* mutation and LCA) affect the lipidomes of HD and LD cells retrieved on different days of culturing. We found that the effects of CR on the lipidomes of chronologically aging HD and LD cells differ from those of *tor1Δ* and LCA. Our findings indicate that TAG concentration was substantially decreased in HD and LD cells on most days of the chronological lifespan in WT yeast placed on the CR diet but not in yeast carrying the *tor1Δ* mutation or WT yeast treated with LCA. The other difference was that FFA concentration in HD and LD cells was considerably increased throughout most of the chronological lifespan in calorically restricted WT yeast but not in *tor1Δ* mutant yeast or WT yeast exposed to LCA. A significant rise in CER concentration within HD and LD cells throughout the entire chronological lifespan was observed in WT yeast limited in calorie supply but not in *tor1Δ* mutant yeast or WT yeast treated with LCA. Finally, the concentrations of most ER- and mitochondria-synthesized lipids (other than SPH and DAG) within HD and LD cells were substantially increased on most days of the chronological lifespan in WT yeast placed on the CR diet but not in yeast carrying the *tor1Δ* mutation or WT yeast exposed to LCA.

It needs to be emphasized that my recently published study showed that a global cellular pattern of water-soluble metabolites created by CR in WT cells is different than the ones made by the *tor1Δ* mutation or LCA treatment of WT cells (see chapter 7) [389]. With the findings reported here, a likely consensus is that CR, *tor1Δ* and LCA (and, perhaps, other geroprotectors) establish different patterns of water-insoluble lipidomes and water-soluble metabolomes in budding yeast cells that age chronologically. For example, the geroprotector PE21 weakens TAG synthesis from PA in the ER; this decreases TAG concentration, lowers the concentration of FFA formed via lipolytic hydrolysis of TAG and further increases the intracellular concentration of PA (Figure 3.3). Furthermore, PE21 stimulates the incorporation of PA into the phospholipids synthesized in the ER and mitochondria; this raises the concentrations of PS, PE, PC and PI (Figure 3.3). Moreover, PE21 attenuates the ER-to-mitochondria transport of PA; this causes a decline in the concentration of CL synthesized from PA in a series of reactions confined to the IMM (Figure 3.3).

Chapter 6: Developing a method for the quantitative analysis of budding yeast's water-soluble metabolome using LC-MS/MS.

6.1 Introduction.

As I mentioned in Chapter 4 of my Thesis, the new SOP implemented at the CBAMS instructs that the mass spectrometric analysis of the molecules extracted from biological samples must be preceded by and coupled with a separation of these molecules by liquid chromatography. My research interests include the mechanisms through which the intracellular and extracellular water-soluble metabolites contribute to longevity regulation in chronologically aging budding yeast. A robust, versatile and sensitive LC-MS/MS method for identifying and quantitating water-soluble metabolites is required to dissect such mechanisms. Significant advances have recently been made in employing the LC-MS/MS methods of non-targeted metabolomics to analyze the water-soluble metabolomes of cells and tissues quantitatively. Yet, the presently used LC-MS/MS metabolomics methods have several limitations; I will discuss these limitations in the next section of this chapter. Using some of the currently employed LC-MS/MS metabolomics procedures as prototypes, I developed a novel method for the quantitative analysis of budding yeast's water-soluble metabolome using LC-MS/MS. Sections 2.3, 2.4, 2.10, 2.12-2.14 provide the technical details of the novel LC-MS/MS metabolomics method. This chapter of my Thesis focuses on several important advantages offered by the LC-MS/MS metabolomics method I developed.

6.2 An overview of the use of LC-MS/MS for the identification and quantitation of water-soluble metabolites.

The water-soluble metabolome of a cell includes the low-molecular-weight (under 1500 Daltons) intracellular and extracellular intermediates and products of the catabolic and anabolic pathways of cellular metabolism [390-392]. As discussed in section 1.8 of my Thesis, some water-soluble metabolites are essential contributors to cellular aging [8, 32, 33, 39, 95, 108, 188, 231-238]. Other water-soluble metabolites play essential roles in energy production, macromolecular synthesis, cell proliferation, cell cycle regulation, gene expression control, signal transduction, mitochondrial functionality maintenance, vesicular protein transport, autophagic degradation of macromolecules and organelles, resistance to various cellular and extracellular stresses, and cell death [393-395]. Studies in budding yeast have contributed to the discovery of some of these

cellular functions of water-soluble metabolites [16, 19, 34, 236, 291, 393, 395-402].

Despite recent progress in using the LC-MS/MS methodology for assessing the water-soluble metabolomes in yeast and other organisms [395, 398, 402, 403], there are methodological challenges that need to be addressed [390, 394, 404-411]. The first challenge is that the sensitivity of the currently used LC-MS/MS metabolomics methods is insufficient to detect the cellular concentrations of many water-soluble metabolites. The second challenge is that the existing LC-MS/MS metabolomics methods under-estimate the cellular concentrations of water-soluble metabolites because the efficacy of metabolic activity quenching is insufficiently high, and the magnitude of quenching-related cell leakage of intracellular metabolites is insufficiently low. The third challenge is that the ability of presently used LC-MS/MS metabolomics methods to annotate some metabolites correctly is limited; this is because the current methods are unable to distinguish from each other the structural isomers (whose chemical formulas are identical but atomic connectivities are different) or stereoisomers (whose chemical formulas and atomic connectivities are the same but three-dimensional atomic arrangements differ). The fourth challenge is that the present LC-MS/MS metabolomics methods cannot use the raw LC-MS/MS data to recognize and measure some metabolites because of the incompleteness of the mass spectral online databases of parent ions (MS1) and product ions (MS2) created by these methods. The fifth challenge is that the presently used LC-MS/MS metabolomics methods must employ several types of metabolite extraction to retrieve different classes of water-soluble metabolites. The sixth challenge is that the efficient separation of the complex, multi-class mixtures of water-soluble metabolites by the current LC-MS/MS metabolomics methods requires the use of several types of chromatography columns.

Chapter 6 of my Thesis describes a novel LC-MS/MS method of water-soluble metabolome analysis that I developed to address all these challenges.

6.3 Optimizing the conditions of metabolic activity quenching and reducing the magnitude of quenching-related cell leakage of intracellular metabolites.

As I mentioned before, the improvement of the process of water-soluble metabolites measurement within a yeast cell requires an increase in the efficiency of metabolic activity quenching and a decrease in the magnitude of quenching-related cell leakage of intracellular metabolites. The objective of metabolic activity quenching for water-soluble metabolites

measurement is to arrest all enzymatic reactions within a cell as quickly as possible [391, 407, 412, 413]. A quick process of metabolic activity quenching prevents the under-estimation of metabolite concentrations *in vivo* [391, 407, 412, 413]. Because the plasma membrane (PM) and the cell wall (CW, if present) are damaged during metabolic activity quenching, the intracellular metabolites escape the cell and become undetectable [391, 407, 412, 413]. The method of LC-MS/MS metabolomics that I developed substantially lowers the quenching-associated cell leakage of intracellular metabolites because it uses the conditions of metabolic activity quenching that decrease the extent of PM and CW damage. To optimize conditions for metabolic activity quenching, I performed the following modifications. The existing metabolic activity quenching procedures employ mainly methanol at an organic solvent at the concentrations of 40% (v/v), 60% (v/v), 80% (v/v), or 100% (v/v) [391, 407, 412, 413]. In the currently used procedures for metabolic activity quenching, the cells are incubated at -20 °C, -40 °C or -60 °C in the presence of a buffer or without it [391, 407, 412, 413]. I modified the procedures for metabolic activity quenching by treating the cells with 60% (v/v) methanol at -20 °C in isotonic ammonium bicarbonate (ABC) buffer at pH = 8.0. I assessed how efficiently this modified procedure damages the PM and CW compared with one of the widely used procedures, in which cells are treated with 80% (v/v) methanol at -40 °C without a buffer [413]. I subjected the cells to staining with the fluorescent dye propidium iodide (PID) and used fluorescence microscopy to compare the efficiencies of the modified and the currently used procedures. The intact yeast cells are impermeable to PI, whereas this fluorescent dye can get into the cells whose PM and CW are damaged [414]. After PI gets into the yeast cell through the damaged PM, its binding to DNA or RNA can increase PI's intensity of fluorescence emission by 30-fold [414]. Because the intracellular metabolites can exit the yeast cell only when the PM and CW are damaged, the extent of the metabolic activity quenching-associated cell leakage for intracellular metabolites can be assessed using a PI staining assay [414]. It should be stressed that the software that I used to quantitate the PI staining assay converts the most intense red fluorescence to green fluorescence to distinguish between the strong red fluorescence and mild red fluorescence emissions. When I compared the efficiencies of the modified and the currently used metabolic activity quenching procedures with respect to the degree of PM and CW damage, I concluded that the modified procedure damages the PM and CW to a significantly lower extent than the currently used one (Figure 6.1). My conclusion was based on the fact that almost all cells subjected to the modified procedure of metabolic activity quenching

showed red fluorescence emission (Figure 6.1). Only yeast cells whose PM and CW have not damaged display red fluorescence emission in a PID staining-based cell leakage assay quantitated using the software I mentioned; this software converts the background green fluorescence to red fluorescence [414]. Yet, when I employed the currently used metabolic activity quenching procedure, I found that almost all cells show green fluorescence emission (Figure 6.1). Only yeast cells whose PM and CW have significantly damaged display green fluorescence emission in a PI staining-based cell leakage assay quantitated with the help of the software I mentioned [414].

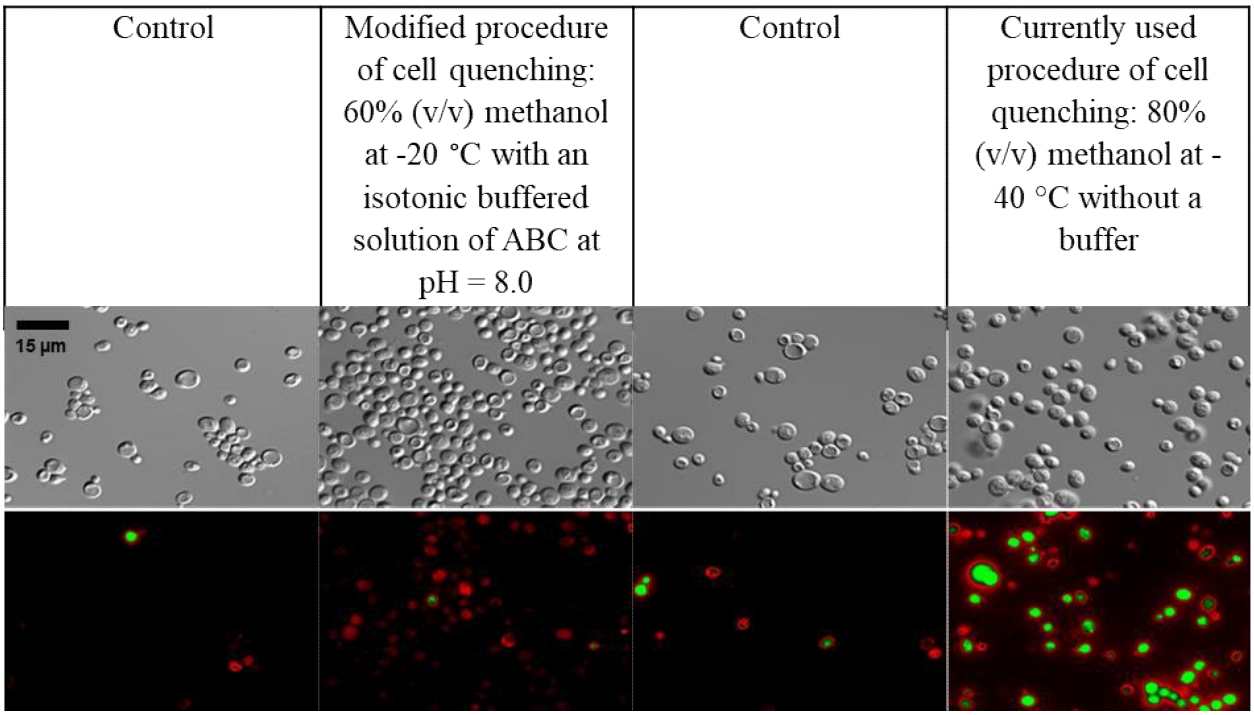

Figure 6.1: Yeast cells subjected to modified or currently used procedure for metabolic activity quenching were incubated with the PID solution for 10 min in the dark on ice. The cells were then visualized using differential interference contrast (DIC; top row) or fluorescence (bottom row) microscopies. Software used to quantitate the PID staining assay converts the most intense red fluorescence to green fluorescence to distinguish between the strong red fluorescence and mild red fluorescence emissions.

I then compared the efficiencies of the modified and the currently used metabolic activity quenching procedures with respect to the magnitude of quenching-related cell leakage of intracellular metabolites. To assess the magnitude of quenching-related cell leakage of intracellular metabolites, I used LC-MS/MS to measure the concentrations of large and small acidic, basic,

neutral-nonpolar, and neutral polar amino acids in the extracellular solution before and after metabolic activity quenching. I found that the modified metabolic activity quenching procedure elicits quite a significantly lower leakage of all these amino acids into the extracellular solution (Figure 6.2) than the currently used one (Figure 6.3).

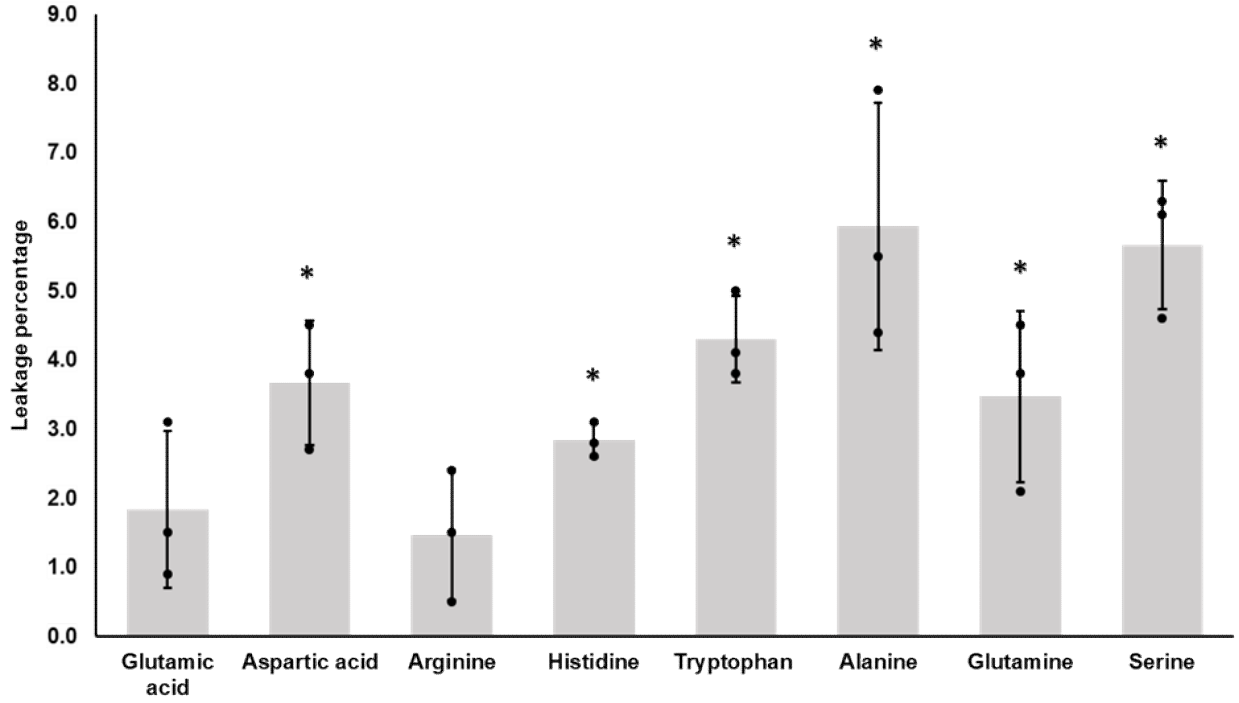

Figure 6.2: The leakage percentage of different classes of amino acids for the modified procedure of metabolic activity quenching. To assess the extent of quenching-related cell leakage of intracellular metabolites, LC-MS/MS was used to measure the concentrations of large and small acidic, basic, neutral-nonpolar, and neutral polar amino acids in the extracellular solution before and after metabolic activity quenching. The mean values ± SD and individual data points are displayed (n = 3). * $p < 0.05$.

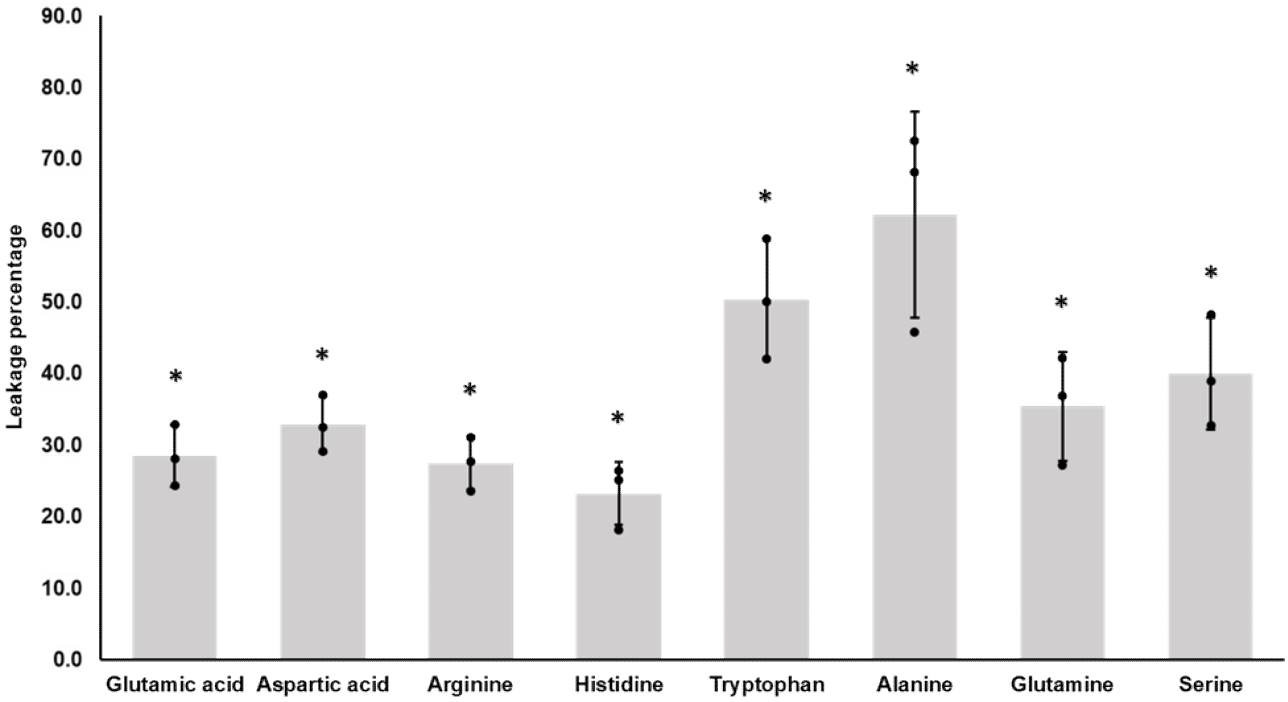

Figure 6.3: The leakage percentage of different classes of amino acids for the currently used procedure of metabolic activity quenching. To assess the extent of quenching-related cell leakage of intracellular metabolites, LC-MS/MS was used to measure the concentrations of large and small acidic, basic, neutral-nonpolar, and neutral polar amino acids in the extracellular solution before and after metabolic activity quenching. The mean values ± SD and individual data points are displayed (n = 3). * $p < 0.05$.

6.4 The novel LC-MS/MS metabolomics method uses a single type of high-performance liquid chromatography (HPLC) column for chromatographic separation of all water-soluble metabolites.

The method I developed uses a single type of HPLC column, namely the zwitterionic-phase column SeQuant ZIC-pHILIC, to separate all water-soluble metabolite classes. The zwitterionic-phase column SeQuant ZIC-pHILIC is used because I found that it much more efficiently separates various classes of water-soluble metabolites than the reverse-phase column ZORBAX Bonus-RP. In fact, the zwitterionic-phase column SeQuant ZIC-pHILIC exhibited much lower retention time (RT) shift values for standards of all water-soluble metabolites (such as NAD+, AMP, GMP, arginine and glutamic acid) than the reverse-phase column ZORBAX Bonus-RP (Table 6.1).

Moreover, the use of the zwitterionic-phase column SeQuant ZIC-pHILIC resulted in significantly sharper peak shapes for all water-soluble metabolites (such as NAD+, AMP, GMP, arginine and glutamic acid) than the use of the reverse-phase column ZORBAX Bonus-RP (Table 6.1).

Table 6.1: Retention Time (RTT) shift values for water-soluble (hydrophilic) and water-insoluble (hydrophobic) metabolites for the zwitterionic-phase column SeQuant ZIC-pHILIC and reverse-phase column ZORBAX Bonus-RP. The metabolites in each sample were extracted from 5.0×10^8 yeast cells. The metabolites were identified by LC-MS/MS. The reported here RT shift values are the means of 20 different samples (n = 20). The samples were analyzed after column equilibration. The *p* values derived from the unpaired *t* test were used to compare the two columns with the equal variance between both sample types.

Metabolites	Zwitterionic-phase column SeQuant ZIC-pHILIC			Reverse phase column ZORBAX Bonus-RP			*p* values
	Mean RT shift (seconds)	Std	Std error	Mean RT shift (seconds)	Std	Std error	
NAD+	7.8	4.5	1	19.2	10.8	2.4	9.80E-05
AMP	6.8	3.5	0.8	21.5	10.3	2.3	5.30E-07
GMP	8.4	4.3	1	16.5	10.2	2.3	2.40E-03
Tryptophan	9.7	4.3	1	9.2	4.7	1	7.50E-01
Arginine	7.8	3.4	0.8	16.3	11.5	2.6	2.90E-03
Glutamate	6.9	4.2	0.9	21	9.9	2.2	9.10E-07
Steric acid	14.6	8.4	1.9	7.7	4.7	1.1	2.70E-03
Lauric Acid	13.8	7.4	1.6	6.1	3.7	0.8	1.60E-04
Decanoic acid	12.9	7.6	1.7	9.1	4.1	0.9	5.80E-02

6.5 A chromatographic procedure used in the novel LC-MS/MS metabolomics method can separate from each other structurally, physically and chemically diverse water-soluble metabolites.

Another advantage of the novel LC-MS/MS metabolomics method is that it uses the chromatographic column and conditions that separate from each other the water-soluble

metabolites exhibiting a wide range of structural, physical and chemical properties. A diverse spectrum of the water-soluble metabolites that can be separated with the help of the developed method includes acidic, basic, neutral polar and non-neutral polar amino acids and their various structural isomers (Figure 6.4). Furthermore, the novel method allows separate different nucleotides and nucleotide derivates involved in vital biological processes (Figure 6.5). Moreover, the developed method can efficiently separate many classes of monosaccharides and different stereoisomeric forms of these monosaccharides (Figure 6.6).

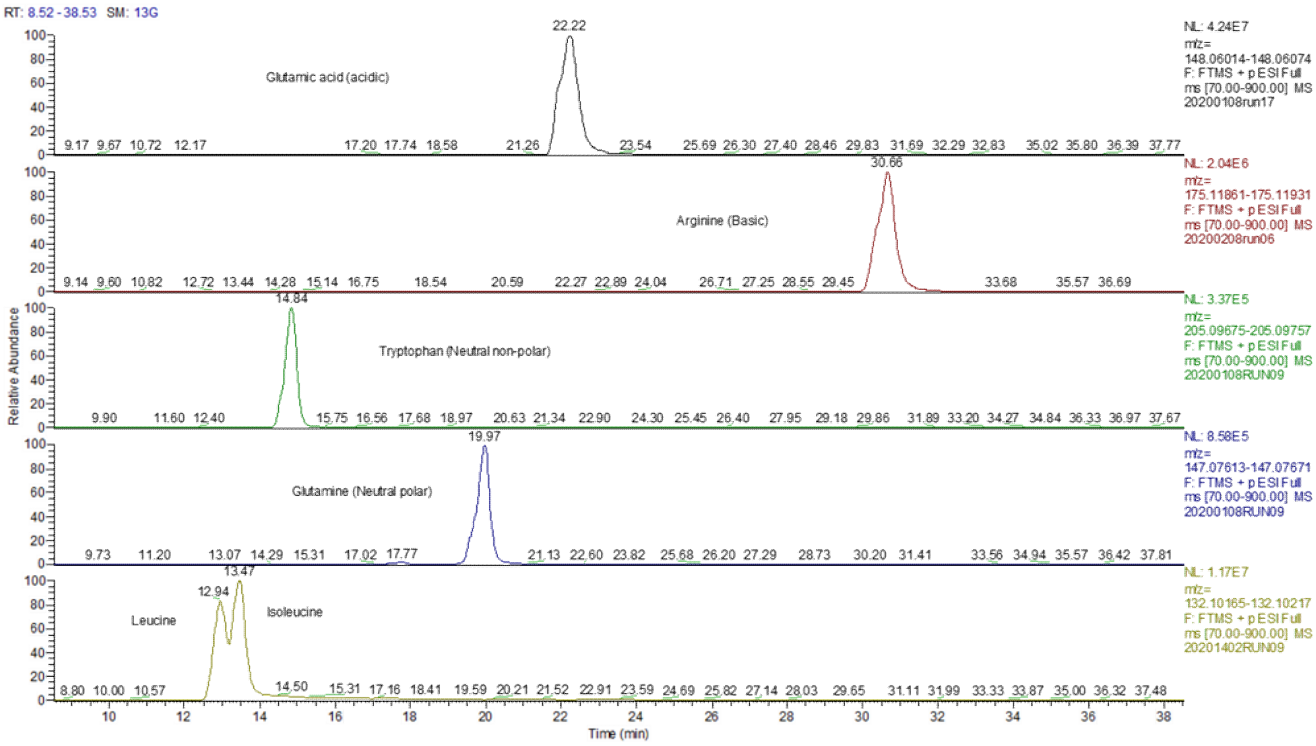

Figure 6.4: The zwitterionic-phase column SeQuant ZIC-pHILIC used in the novel LC-MS/MS metabolomics method efficiently separates from each other acidic, basic, neutral polar and non-neutral polar amino acids and such structural isomers of amino acids as leucine and isoleucine. All amino acid standards are from "Sigma." MS/MS detected all amino acids in the ESI (+) mode. The retention time shifts between 3 independent chromatography runs were less than +/- 10 seconds.

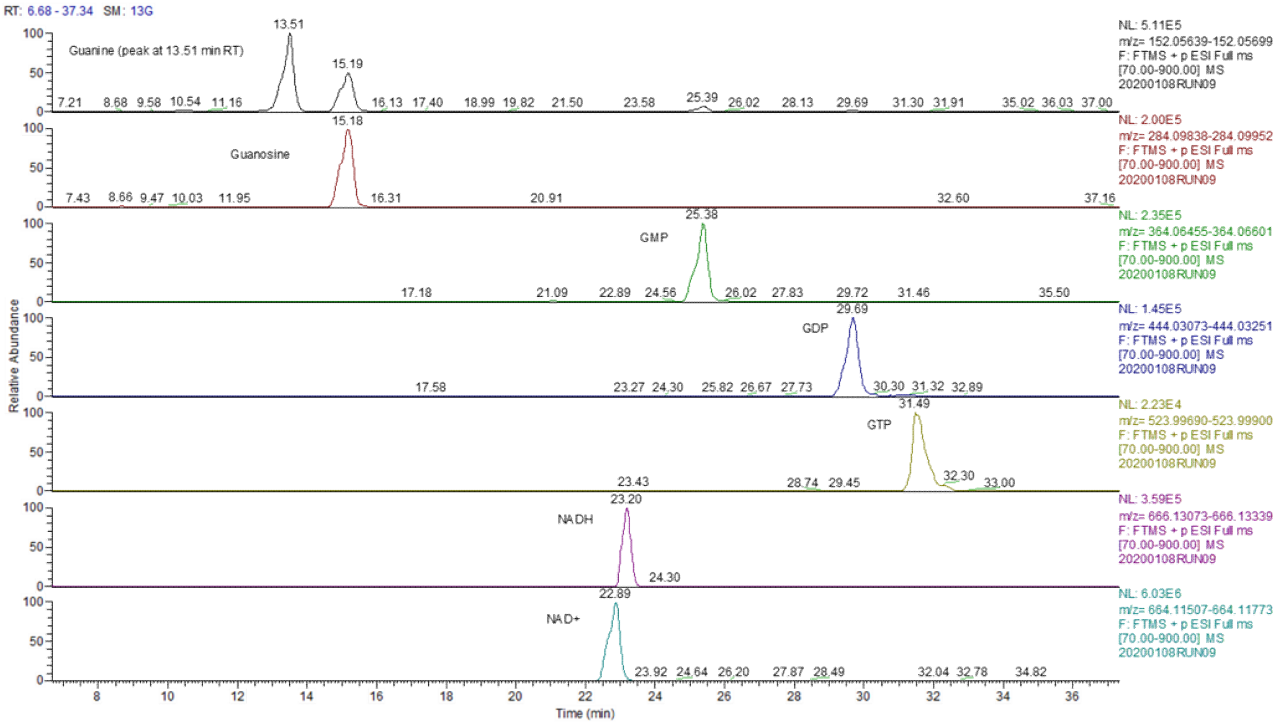

Figure 6.5: The zwitterionic-phase column SeQuant ZIC-pHILIC used in the novel LC-MS/MS metabolomics method efficiently separates from each other different nucleotides and nucleotide derivates involved in vital biological processes. All nucleotide and nucleotide derivate standards are from "Sigma." MS/MS detected all nucleotides and nucleotide derivates in the ESI (+) mode. The retention time shifts between 3 independent chromatography runs were less than +/- 10 seconds.

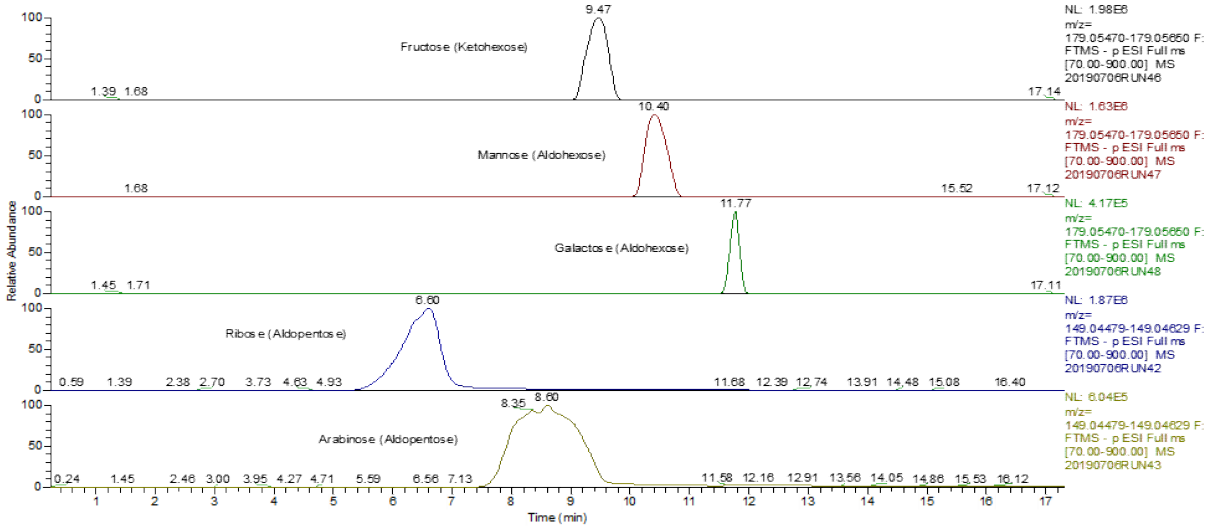

Figure 6.6: The zwitterionic-phase column SeQuant ZIC-pHILIC used in the novel LC-MS/MS metabolomics method efficiently separates from each other many classes of

monosaccharides and different structural isomers and stereoisomeric forms of these monosaccharides. Fructose, mannose and galactose are structural isomers and stereoisomeric forms of aldo- and ketohexoses. Ribose and arabinose are aldopentoses. All monosaccharide standards are from "Sigma." MS/MS detected all monosaccharides in the ESI (+) mode. The retention time shifts between 3 independent chromatography runs were less than +/- 10 seconds.

6.5 The novel LC-MS/MS metabolomics method is robust and versatile.

The robustness of the novel method is underscored by the fact that I was able to use it for the identification and quantitation of as many as 374 water-soluble metabolites of budding yeast cultured in the nutrient-rich YP medium with 2% glucose as a sole carbon source. The method is versatile as these metabolites exhibit diverse structural, physical, chemical and biological properties. The ESI (+, positive) mode was used to detect 240 of these metabolites, whereas 134 water-soluble metabolites were detected in the ESI (-, negative) mode. To confirm the identities of all these water-soluble metabolites, I matched their data-dependent acquisition (DDA) MS2 fragments attained in the ESI (+) and (ESI (-) modes to the MS2 mzCloud online spectral library. The MS2 mzCloud library provides the spectra of metabolite standards with different MS1 and DDA MS2 criteria. In the search for matching between the sample's MS2 spectra and the MS2 spectra provided by the mzCloud library, I used different DDA MS2 criteria. To acquire different features (putative metabolites) present in the same sample, I applied the high-energy-induced-collision-dissociation (HCD) or collision-induced dissociation (CID) fragmentation method, which uses the top 5 MS2 events, 35 collision energy values and 10 ms activation times. This feature acquisition algorithm has led to the identification of almost 6,000 putative metabolites within the same sample. I then filtered the resulting files using > 95% MS2 matching and > 90% MS1 isotopic pattern matching criteria. The file filtering had resulted in the identification of 162 metabolites when the HCD fragmented method was used and 142 metabolites when the CID fragmented method was applied. I found that 81 out of 162 metabolites are unique to the HCD fragmentation method. I also found that 42 out of 142 are unique to the CID fragmentation method. Based on all these findings, I concluded that the use of many different DDA MS2 criteria is essential for the correct annotation of water-soluble metabolites with the help of the novel LC-MS/MS method.

6.6 The novel LC-MS/MS metabolomics method is sensitive and has a wide linear dynamic range.

The novel LC-MS/MS metabolomics method exhibits high sensitivity. I found that its lowest detectable concentration is 0.05 pmol/µl (Table 6.2; see data for phenylalanine), although this value varies significantly for different water-soluble metabolites. The method uses the Thermo Orbitrap Velos MS system. I found that the linear dynamic range of this MS system for measuring the concentrations of various metabolites is at least two orders of magnitude (Figures 6.7 – 6.9).

Table 6.2: The lowest concentrations of different water-soluble metabolites detectable with the help of the novel LC-MS/MS metabolomics method. Commercial standards of different water-soluble metabolites were analyzed. The estimate of the lowest detectable concentration for each metabolite standard is based on the calculation of the MS1 peak area for this metabolite standard. Mean values of two independent experiments, each performed in three technical replicates, are displayed. Notes: 1) although threonine* is detectable, it cannot be quantified because its chemical isomer homoserine co-elutes with threonine; 2) because glucose** creates multiple chromatography peaks, it cannot be identified; and 3) these metabolite standards*** are identifiable and quantifiable only as individual samples, but not in the mixtures with commercial metabolite standards or metabolites extracted from the biological samples.

Std Metabolites	M.W. (g/mole)	[M+H]+1	[M-H]-1	Detection mode	Lowest concentration detected (pmol/µl)
Glycine	75.03203	76.03931	74.02475	Positive	7.43E+00
Tryptophan	204.08988	205.09716	203.0826	Positive	5.56E-02
Phenylalanine	165.07898	166.08626	164.0717	Positive	5.14E-02
Arginine	174.11168	175.11896	173.1044	Positive	7.14E-02
Threonine*	119.05824	120.06552	118.05096	Positive	
Serine	105.04259	106.04987	104.03531	Positive	4.66E+00
Glutamate	147.05316	148.06044	146.04588	Positive	4.20E-01
Methionine	149.05105	150.05833	148.04377	Positive	1.96E+00
Aspartate	133.03751	134.04479	132.03023	Positive	3.75E+00
Valine	117.07898	118.08626	116.0717	Positive	1.49E+00
Isoleucine	131.09463	132.10191	130.08735	Positive	1.84E+00
Leucine	131.09463	132.10191	130.08735	Positive	2.26E+00
Histidine	155.06948	156.07676	154.0622	Positive	2.53E+00
Tyrosine	181.07389	182.08117	180.06661	Positive	8.72E-02

Lysine	146.10553	147.11281	145.09825	Positive	1.43E-01
Alanine	89.04768	90.05496	88.0404	Positive	1.12E+00
Proline	115.06333	116.07061	114.05605	Positive	1.05E+00
Cysteine	121.01975	122.02703	120.01247	Positive	8.22E-01
Asparagine	132.05349	133.06077	131.04621	Positive	1.08E+00
Glutamine	146.06914	147.07642	145.06186	Positive	1.92E+00
Guanine	151.04941	152.05669	150.04213	Positive	5.47E+00
Guanosine	283.09167	284.09895	282.08439	Positive	3.67E-01
GMP	363.058	364.06528	362.05072	Positive	7.17E-01
GDP	443.02434	444.03162	442.01706	Positive	2.57E+00
GTP	522.99067	523.99795	521.98339	Positive	2.27E+00
AMP	347.06309	348.07037	346.05581	Positive	5.25E-01
ADP	427.02942	428.0367	426.02214	Positive	1.32E+00
ATP	506.99575	508.00303	505.98847	Positive	1.77E+00
NADH	665.12478	666.13206	664.1175	Positive	1.47E+00
NAD+	663.10912	664.1164	662.10184	Positive	3.03E+00
Glucose**	180.06339	181.07067	179.05611		
Fructose***	180.06339	181.07067	179.05611	Negative	5.67E-01
Mannose***	180.06339	181.07067	179.05611	Negative	1.05E+00
Galactose***	180.06339	181.07067	179.05611	Negative	9.00E-01
Ribose***	150.05283	151.06011	149.04555	Negative	1.10E+00
Arabinose***	150.05283	151.06011	149.04555	Negative	1.23E+00
Fructose-6-phosphate***	260.02972	261.037	259.02244	Negative	6.60E+00
Glucose-6-phosphate***	260.02972	261.037	259.02244	Negative	4.27E+00
Citric acid	192.12 g	193.034279	191.019726	Negative	9.33E-01
Malic acid	134.09	135.0288	133.014247	Negative	1.23E+00
Pyruvic acid	88.06	89.02332	87.008768	Negative	2.77E+00

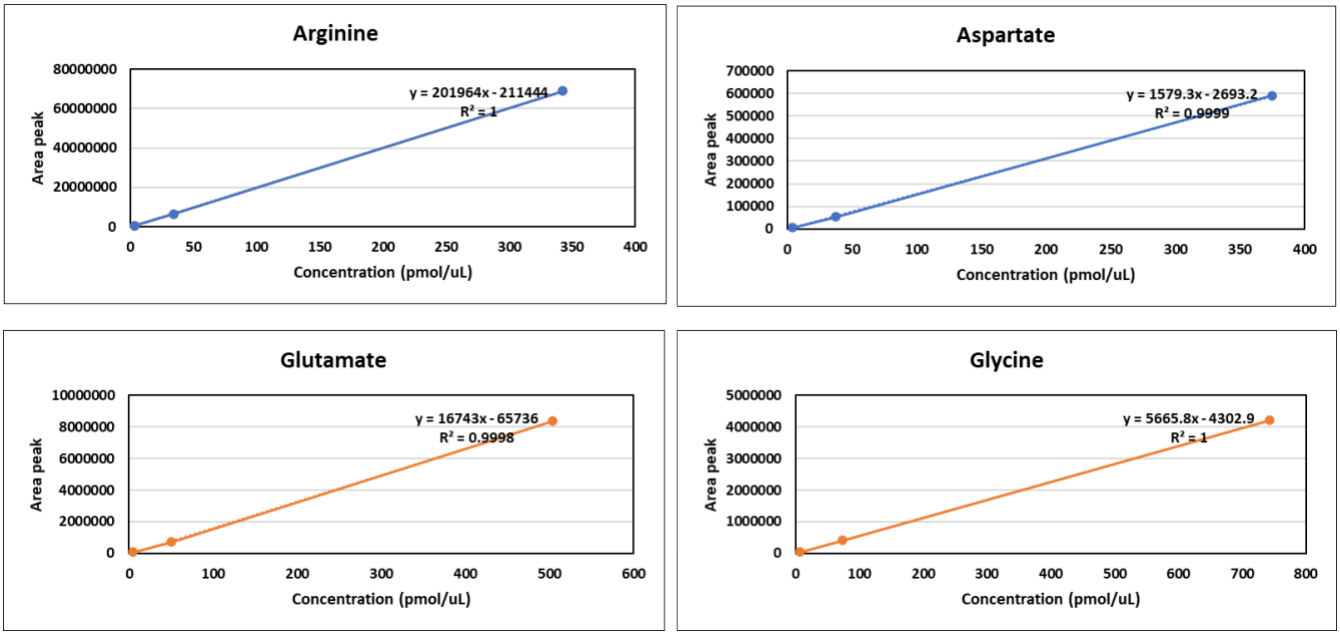

Figure 6.7: A linear dynamic range observed when the concentrations of arginine, aspartate, glutamate or glycine were measured using the Thermo Orbitrap Velos MS system.

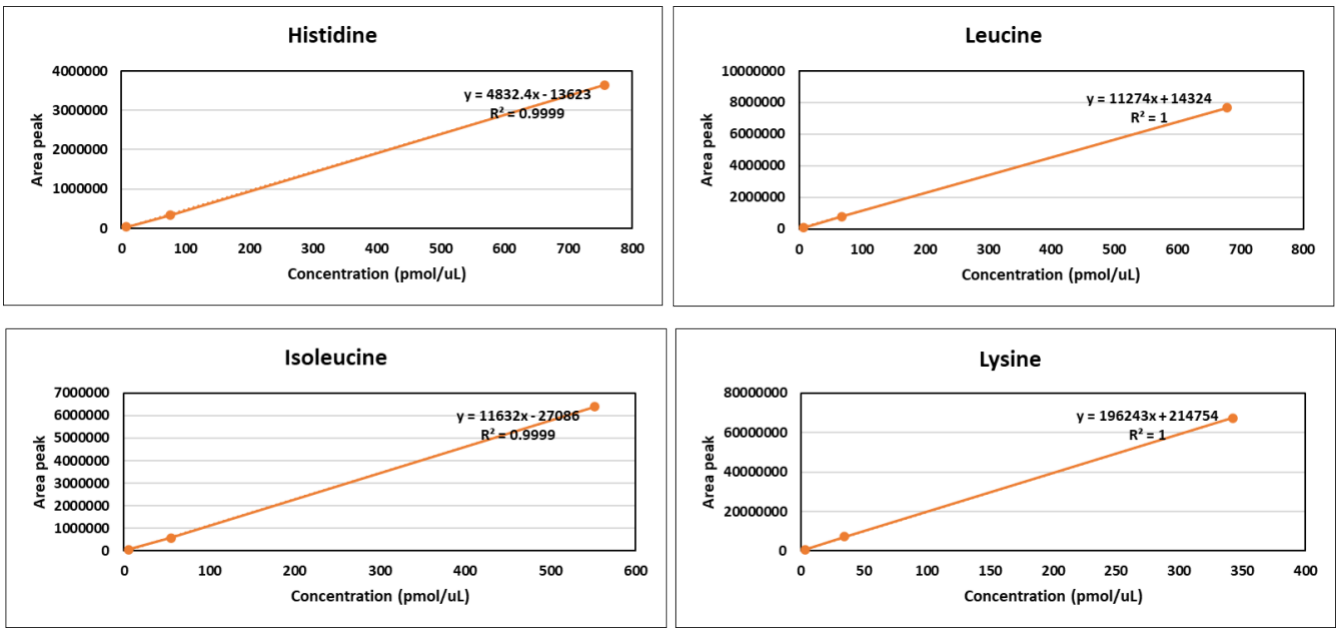

Figure 6.8: A linear dynamic range observed when the concentrations of histidine, leucine, isoleucine or lysine were measured using the Thermo Orbitrap Velos MS system.

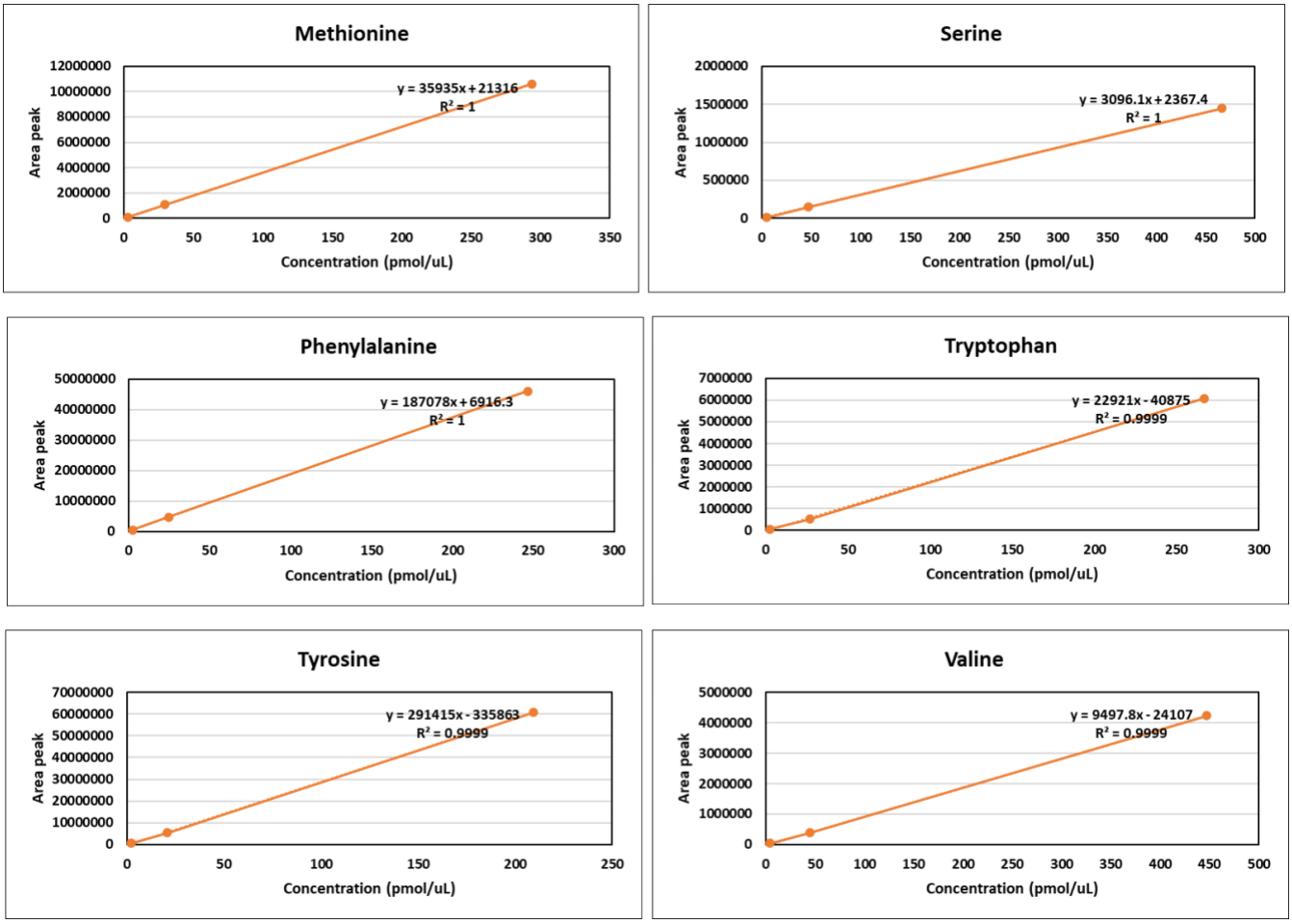

Figure 6.9: A linear dynamic range observed when the concentrations of methionine, serine, phenylalanine, tryptophan, tyrosine or valine were measured using the Thermo Orbitrap Velos MS system.

6.7 A summary of the advantages offered by the novel LC-MS/MS metabolomics method and its comparison with presently used methods.

This Chapter of my Thesis describes a novel LC-MS/MS method of non-targeted metabolomics for the quantitative analysis of many water-soluble metabolites extracted from budding yeast. The described method offers several advantages over the presently used LC-MS/MS methods of non-targeted metabolomics. The first advantage is that the novel method is highly sensitive (the lowest detectable metabolite concentration is 0.05 pmol/µl) and has at least two orders of magnitude linear dynamic range for water-soluble metabolites. The sensitivity of this method exceeds the ones of the presently used methods for non-targeted metabolomics [395, 402-404]. The second advantage is that a metabolic activity quenching procedure designed for the

novel LC-MS/MS metabolomics method causes a substantially lower quenching-related cell leakage of intracellular metabolites than the cell quenching procedures used in the existing LC-MS/MS methods of non-targeted metabolomics [391, 407, 413]. Because the newly designed metabolic activity quenching procedure lowers the quenching-related cell leakage of intracellular metabolites, it decreases the extent to which the current cell quenching procedures under-estimate the intracellular concentrations of water-soluble metabolites. The third advantage is that the novel LC-MS/MS metabolomics method distinguishes between different structural isomers and stereoisomeric forms of many metabolites. In contrast, the currently used LC-MS/MS metabolomics methods do not allow to make such distinction [391, 394, 407]. Many of these structural isomers and stereoisomers are energy carrier molecules, nucleotides, amino acids, monosaccharides, intermediates of glycolysis and tricarboxylic cycle intermediates that perform vital cellular functions. The fourth advantage is that the novel method allowed me to create an extensive mass spectral database of MS1 and MS2 for many water-soluble metabolites not covered in the existing mass spectral online databases [390, 415, 416]. The creation of the extensive mass spectral database of MS1 and MS2 for many new water-soluble metabolites allows their correct identification and quantitation in the future using the raw LC-MS/MS data. The fifth advantage of the novel LC-MS/MS metabolomics method is that it employs a single type of metabolite extraction to retrieve water-soluble metabolites with various structural, physical, chemical and biological properties. The extent of the retrievable metabolites' variety for the metabolite extraction procedure developed here is significantly higher than that for the single-step procedures presently used to extract water-soluble metabolites from budding yeast [395, 402, 403, 417]. The sixth advantage is that the novel LC-MS/MS metabolomics method employs a single type of LC column to separate the water-soluble metabolites exhibiting a wide range of structural and functional properties. The current LC-MS/MS metabolomics methods use more than one type of LC column [395, 402, 418, 419]. One more advantage is that the novel LC-MS/MS metabolomics method allows to identify and quantitate more than 370 water-soluble metabolites extracted from budding yeast, a number of metabolites that exceeds the numbers reported for other LC-MS/MS methods for the quantitative analysis of budding yeast's water-soluble metabolome [395, 402, 403, 420, 421].

6.8 The limitations of the novel LC-MS/MS metabolomics method.

One limitation of the method is that the zwitterionic-phase column SeQuant ZIC-pHILIC used to separate water-soluble metabolites needs extensive re-conditioning after each chromatography run. Another limitation of the method is that it is applicable for the quantitative analysis of only water-soluble, hydrophilic metabolites. A limitation of the method also consists in its inability to quantify different isomeric forms of carbohydrates, including isomers of fructose, glucose and galactose; unfortunately, these carbohydrate isomers cannot be separated from each other using the zwitterionic-phase column SeQuant ZIC-pHILIC when they are present in a mixture with other metabolites. The method's limitation also includes its inability to identify glucose, which creates multiple peaks during chromatography on the zwitterionic-phase column SeQuant ZIC-pHILIC. The method can also not quantify threonine, which co-elutes with its isomer homoserine during chromatography separation on the zwitterionic-phase column SeQuant ZIC-pHILIC.

Chapter 7: Caloric restriction creates a metabolic pattern of chronological aging delay that in budding yeast differs from the metabolic design established by two other geroprotectors, the *tor1Δ* mutation and lithocholic acid.

7.1 Introduction.

A body of evidence indicates that metabolism is an essential contributor to the aging and longevity of eukaryotic organisms across phyla. Indeed, healthy aging of the evolutionarily distant eukaryotes coincides with age-related changes in the concentrations of specific metabolites within cells, tissues, organs and biological fluids [134, 422-435]. These changes are considered metabolic biomarkers characteristic of an aging-associated deterioration in cellular functionality, tissue and organs homeostasis, and organismal health [134, 422-435]. Furthermore, such dietary interventions as caloric restriction (CR), reduced protein intake, a limited supply of single amino acid and, alternating cycles of feeding and fasting are robust geroprotectors that specifically rewire cellular and organismal metabolism in various eukaryotic organisms [285, 436-453]. Moreover, allelic variants of the genes implicated in diverse metabolic pathways delay aging and extend longevity in eukaryotic organisms across species [423, 425, 426, 428, 429, 431, 434, 454-462]. Besides, pharmacological interventions that target distinct aspects of metabolism are potent geroprotectors in diverse eukaryotes; these interventions include metformin, rapamycin, resveratrol, spermidine and others [455, 463-477]. Additionally, it has been emphasized that each of the nine common denominators (hallmarks) of aging is linked to a specific remodeling of metabolism [399, 478]. These aging hallmarks include the damage and repair of nuclear DNA, shortening of telomeres, epigenetic regulation changes, proteotoxic stress, deregulation of nutrient sensing, deterioration of mitochondrial functionality, cellular senescence, the decline in stem cell number and functionality, and changes in intercellular communications [399]. Based on all these observations, the existence of a metabolic “clock,” “signature,” “footprint” or “profile” of aging delay has been proposed [399, 422, 424-426, 428, 440].

It remained unclear if different dietary, genetic and pharmacological anti-aging interventions set up a similar metabolic pattern of aging delay or each of them generates a distinct metabolic profile. In this study, I used non-targeted metabolomics of chronologically aging budding yeast to clarify this issue. I show that three different geroprotectors create distinct metabolic profiles. I identified a unique metabolic pattern established by one of these geroprotectors.

7.2 CR, the *tor1Δ* mutation and lithocholic acid (LCA) extend the longevity of chronologically aging yeast.

The Titorenko laboratory investigated how efficiently CR, the *tor1Δ* mutation and LCA prolong the longevity of chronologically aging wild-type (WT) strain BY4742. WT cells were cultured in the nutrient-rich YP (1% yeast extract and 2% peptone) medium supplemented with glucose as a sole carbon source. The previous studies of the Titorenko laboratory showed that a yeast culture in this nutrient-rich medium provides a beneficial model system for elucidating the chronological aging of multicellular eukaryotes [59].

As I mentioned in Chapter 5, a WT strain cultured in the YP medium that initially contained 2% (w/v) glucose served as a control non-CR culture for examining the CR-dependent longevity extension in chronologically aging yeast [59]. A WT strain culture in the same YP medium, but initially containing 0.2% (w/v) glucose, was used as a model system for studying longevity extension by a CR diet [59].

As I also indicated in Chapter 5, the pro-longevity effect of the *tor1Δ* mutation in the BY4742 genetic background was assessed in the mutant yeast cells cultured in the YP medium supplemented with 2% (w/v) glucose. Under these conditions of culturing (but not if the *tor1Δ* mutant strain was cultured in the YP medium supplemented with 0.2% (w/v) glucose), the *tor1Δ* mutation exhibited the highest longevity-extending efficiency [139].

As I noted in Chapter 5, LCA's greatest beneficial effect on the longevity of chronologically aging WT strain was observed if LCA was used at a final concentration of 50 μM and yeast cells were cultured under CR on 0.2% (w/v) glucose [139]. Under CR conditions on 0.2% (w/v) glucose, a WT strain culture without LCA served as a control for elucidating the LCA-dependent longevity extension. A viability curve of a WT strain cultured with 50 μM LCA under non-CR on 2% (w/v) glucose is provided elsewhere [139].

The Titorenko laboratory found that CR (a dietary geroprotective intervention), the *tor1Δ* mutation (a genetic geroprotective intervention) and LCA (a pharmacological geroprotective intervention) significantly increase the mean and maximum chronological lifespans (CLS) of WT yeast cultured under the above conditions (Figure 5.1).

7.3 CR, the *tor1Δ* mutation and LCA create different metabolic patterns throughout the entire chronological lifespan.

I used a recently developed (see Chapter 6) liquid chromatography coupled with tandem mass spectrometry (LC-MS/MS) method of non-targeted metabolomics [479] to identify and quantitate the intracellular water-soluble metabolites extracted from chronologically aging yeast. Cell aliquots for the metabolomic analysis by LC-MS/MS were collected on days 1, 2, 3, 5, 7, 10, 14, 17 and 21 of culturing (Figure 5.1). A total of 193 metabolites were identified and quantitated in each of the four cultures assessed. These metabolites included AMP, ADP, ATP, FAD^+, FMN, $FADH_2$, NAD^+, NADH, $NADP^+$, NADPH, other nucleotides, amino acids, monosaccharides, intermediates of glycolysis and tricarboxylic cycle intermediates [479].

I found that CR causes extensive remodeling of the water-soluble metabolome within WT cells (Figure 7.2). The CR-dependent remodeling of the water-soluble metabolome was observed throughout the entire chronological lifespan (Figure 7.2). From 14% to 43% of the identified metabolites were downregulated in WT cells recovered on different days of culturing under CR conditions (Figure 7.2). Culturing under CR conditions caused the upregulation of many (from 9% to 46%) of metabolites at various stages of the aging process (Figure 7.2).

Akin to CR, the *tor1Δ* mutation significantly altered the water-soluble metabolome of yeast (Figure 7.3). These *tor1Δ*-driven changes in the spectrum of intracellular water-soluble metabolites were seen on all stages of the chronological aging process in yeast cultured under non-CR conditions (Figure 7.3). The *tor1Δ* mutation elicited a downregulation of 5% to 25% of all intracellular water-soluble metabolites throughout the entire chronological lifespan (Figure 7.3). From 17% to 33% of the water-soluble metabolite pool was upregulated by the *tor1Δ* mutation on different days of chronological aging under non-CR conditions (Figure 7.3).

The intracellular water-soluble metabolome was also considerably changed by LCA (Figure 7.4). I detected the LCA-driven changes in the water-soluble metabolome on all days following LCA addition to WT cells under CR conditions (Figure 7.4). LCA exposure caused downregulation of 5% to 71% of all intracellular metabolites on various days after LCA addition to calorically restricted WT cells (Figure 7.4). Some metabolites (from 3% to 29%) were upregulated on different days following LCA addition to these cells (Figure 7.4).

I normalized the data for the relative concentrations of all 193 water-soluble metabolites identified in age-matched cells cultured under CR conditions, carrying the *tor1Δ* mutation or treated

with LCA. I used these normalized data to compare the metabolic patterns created by the three different geroprotective interventions at various stages of the chronological aging process. Multivariate analysis of the resulting data set using principal component analysis (PCA) demonstrated that the metabolic profiles of the three geroprotectors are very distinct (Figure 7.5). I noticed that these three geroprotector-specific metabolic profiles significantly differ from each other in yeast cells recovered on any day of culturing (Figure 7.5). Indeed, the metabolic patterns specific for CR, *tor1Δ* and LCA were well separated from each other along the PC1 and/or PC2 axes of the PCA plots for various stages of the chronological aging process (Figure 7.5).

In sum, the above findings indicate that CR, the *tor1Δ* mutation and LCA create different metabolic patterns that remain specific for a particular geroprotector throughout the entire chronological lifespan of *S. cerevisiae*.

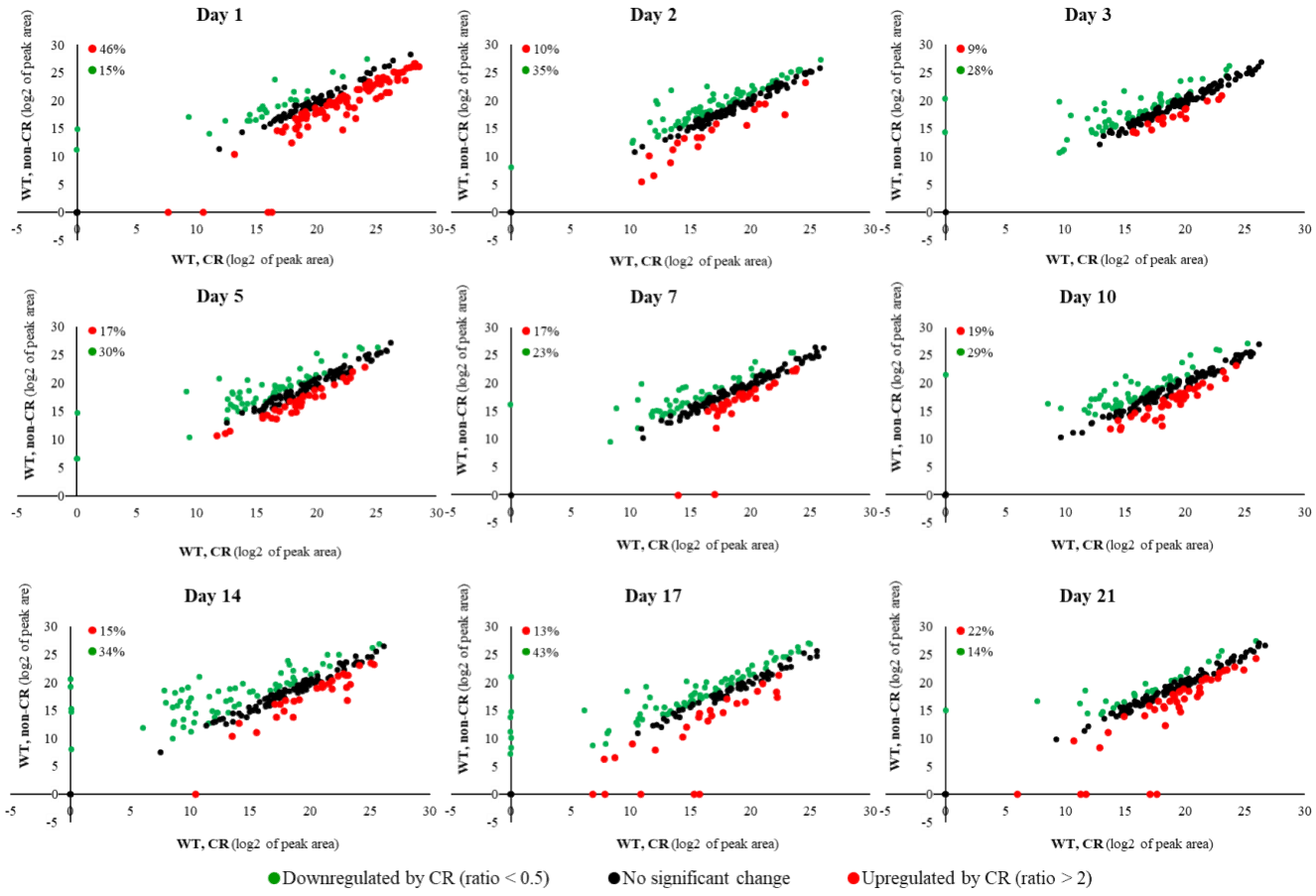

Figure 7.2: CR causes extensive remodeling of the water-soluble metabolome within WT cells. The WT strain BY4742 was cultured in the nutrient-rich YP medium initially containing 0.2% (w/v) glucose (CR conditions) or 2% (w/v) glucose (non-CR conditions). Cell aliquots for

metabolic activity quenching and metabolite extraction were collected on days 1, 2, 3, 5, 7, 10, 14, 17 and 21 of culturing. The use of LC-MS/MS to identify and quantitate the intracellular water-soluble metabolites is described in Materials and Methods. Scatter plots comparing the relative abundance of water-soluble metabolites within WT cells cultured under CR or non-CR conditions are shown. The plots are on a $\log_2$-$\log_2$ scale of mass spectrometric peak areas for different metabolites. The percentage abundance of metabolites that were upregulated (ratio > 2; displayed in red) or downregulated (ratio < 0.5; displayed in green) by CR is provided for each time point.

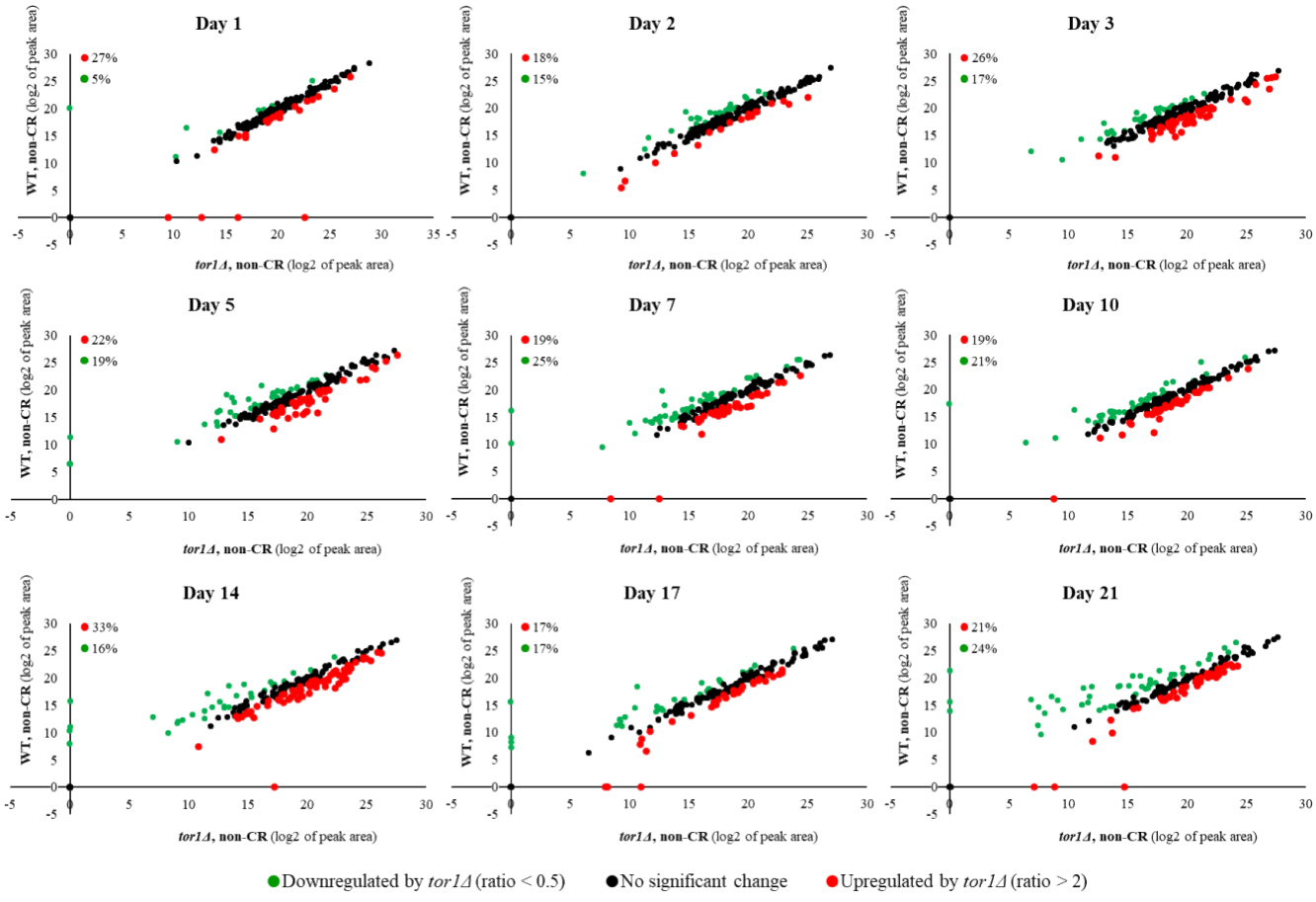

Figure 7.3: The *tor1Δ* mutation elicits significant changes in the water-soluble metabolome of yeast under non-CR conditions. The WT strain BY4742 and the *tor1Δ* single-gene-deletion mutant strain in the BY4742 genetic background were cultured in the nutrient-rich YP medium initially containing 2% (w/v) glucose (non-CR conditions). After being collected on days 1, 2, 3,

5, 7, 10, 14, 17 and 21 of culturing, cell aliquots were subjected to metabolic activity quenching and metabolite extraction (as described in Materials and Methods). According to the procedure outlined in Materials and Methods, LC-MS/MS was then used to identify and quantitate the intracellular water-soluble metabolites. The data on the relative abundance of water-soluble metabolites within WT and *tor1Δ* cells under non-CR conditions were plotted on a $\log_2$-$\log_2$ scale of mass spectrometric peak areas for different metabolites. Each plot provides the percentage abundance of metabolites that were upregulated (ratio > 2; displayed in red) or downregulated (ratio < 0.5; shown in green) by the *tor1Δ* mutation under non-CR conditions of cell culturing.

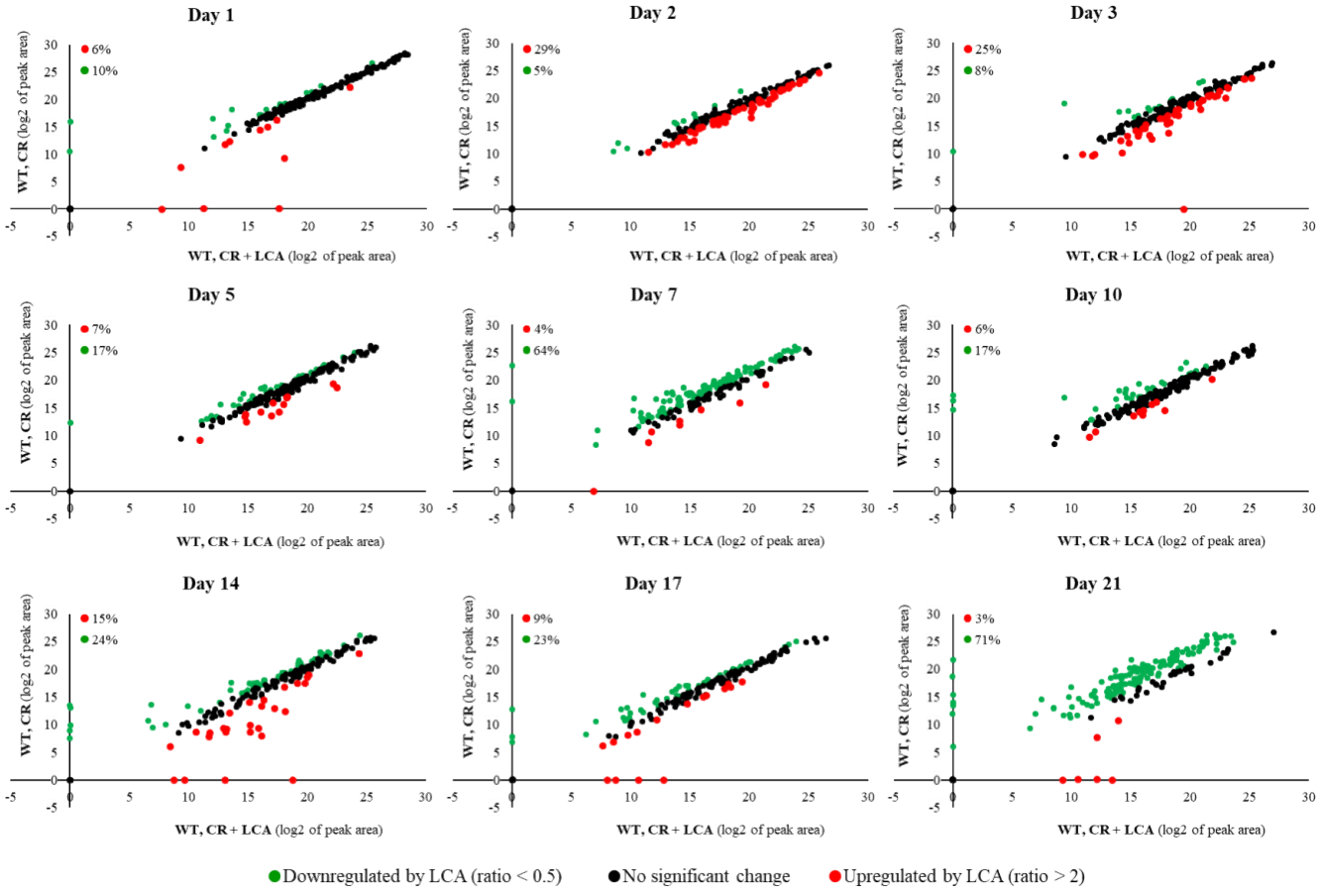

Figure 7.4: LCA added to calorically restricted WT cells considerably alters their intracellular water-soluble metabolome. The WT strain BY4742 was cultured in the nutrient-rich YP medium initially containing 0.2% (w/v) glucose (CR conditions), with 50 µM LCA or without this bile acid. Cell aliquots were collected on days 1, 2, 3, 5, 7, 10, 14, 17 and 21 of culturing. The collected cells were subjected to metabolic activity quenching and metabolite

extraction, followed by metabolite identification and quantitation by LC-MS/MS. All these procedures are described in Materials and Methods. Scatter plots for the relative abundance of water-soluble metabolites within WT cells cultured under CR conditions with or without LCA are presented. These plots are on a $\log_2$-$\log_2$ scale of mass spectrometric peak areas for different metabolites. The percentage abundance of metabolites that were upregulated (ratio > 2; displayed in red) or downregulated (ratio < 0.5; shown in green) by LCA is provided for each time point.

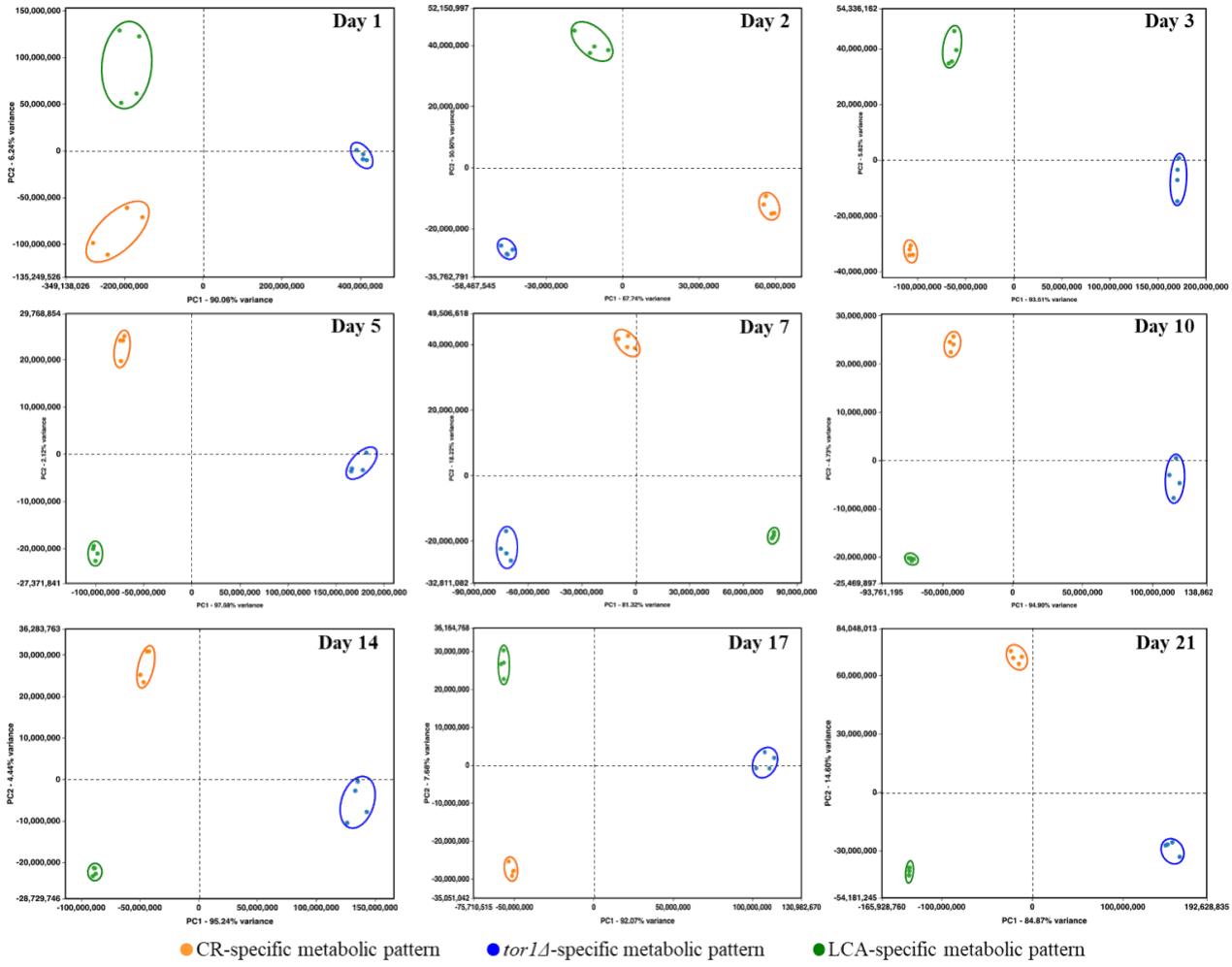

Figure 7.5: CR, *tor1Δ* and LCA generate different metabolic profiles of 193 water-soluble metabolites throughout the entire chronological lifespan of budding yeast. The WT strain BY4742 was cultured in the nutrient-rich YP medium initially containing 2% (w/v) glucose (non-CR conditions), 0.2% (w/v) glucose (CR conditions) or 0.2% (w/v) glucose and 50 μM LCA (CR + LCA conditions). The *tor1Δ* mutant strain in the BY4742 genetic background was cultured in

nutrient-rich YP medium initially containing 2% (w/v) glucose (non-CR conditions). Cell aliquots for metabolic activity quenching and metabolite extraction were collected on days 1, 2, 3, 5, 7, 10, 14, 17 and 21 of culturing. The use of LC-MS/MS to identify and quantitate the intracellular water-soluble metabolites is described in Materials and Methods. A WT strain culture that initially contained 2% (w/v) glucose served as a control non-CR culture for defining the metabolic patterns created by the CR and *tor1Δ* geroprotectors. A WT strain culture that initially contained 0.2% (w/v) glucose without LCA served as a control CR culture for defining the metabolic pattern created by the LCA geroprotector. Normalized data for 193 water-soluble metabolites identified in age-matched cells were used to create the PCA plots for comparing the metabolic patterns created by the three different geroprotectors. Data of 2 independent experiments, each being performed twice, are presented.

7.4 CR creates a unique pattern of the metabolic pathway for sulfur amino acid biosynthesis.

I noticed that CR, but not the *tor1Δ* mutation or LCA, significantly lowers *S*-adenosylmethionine (Sam) concentration in yeast cells recovered on any day of culturing (Figures 7.6A-7.6C and Figure 7.7). Indeed, the intracellular concentration of Sam was decreased in yeast cultured under CR conditions throughout the entire chronological lifespan (Figure 7.6A and Figure 7.7). In contrast, Sam concentrations in yeast cells carrying the *tor1Δ* mutation or treated with LCA fluctuated at various stages of the chronological aging process in a seemingly random manner (Figures 7.6B and 7.6C).

I also found that beginning of day 2 of culturing, CR causes a significant decline in methionine (Met) concentration within yeast cells at various chronological aging phases (Figure 7.6A and Figure 7.8). On the contrary, the *tor1Δ* mutation and LCA elicited alterations in the intracellular concentrations of Met that randomly fluctuated on different days of cell culturing (Figures 7.6B and 7.6C).

Both Sam and Met are the two products of the metabolic pathway for sulfur amino acid biosynthesis from aspartate (Asp), sulfate and 5-methyltetrahydrofolate (5-Mtf) (Figure 7.6D) [480]. This pathway also leads to the biosynthesis of cysteine (Cys) (Figure 7.6D) [480]. I found that CR significantly increases the concentration of Asp throughout the entire chronological lifespan of *S. cerevisiae* (Figure 7.6A and Figure 7.9). CR exhibited the opposite effect on Cys concentration during most days (other than day 21) of yeast cell culturing (Figure 7.6A and Figure

7.10). Akin to the impacts of the *tor1Δ* mutation and LCA on the intracellular concentrations of Sam and Met, these two geroprotectors randomly affected Asp and Cys intracellular concentrations throughout yeast chronological lifespan (Figures 7.6B and 7.6C).

Altogether, the above findings suggest that CR (but not the *tor1Δ* mutation or LCA) regulates the metabolite flow along the metabolic pathway for sulfur amino acid biosynthesis in a specific manner. This geroprotective diet suppresses the biosynthesis of Met, Sam and Cys from Asp, sulfate and 5-Mtf throughout the chronological lifespan (Figure 7.6D).

I normalized the data on the relative concentrations of all four metabolites (i.e., Asp, Cys, Met and Sam) within the sulfur amino acid biosynthetic pathway. This normalization was performed for age-matched cells cultured under CR conditions, carrying the *tor1Δ* mutation or treated with LCA. I then applied multivariate analysis by PCA to compare how the three geroprotectors affect the metabolic pathway for sulfur amino acid biosynthesis on various days of culturing. I found that the pathway patterns specific for CR, *tor1Δ* and LCA are well separated from each other along the PC1 and/or PC2 axes of the PCA plots (Figure 7.11). Notably, these geroprotector-specific patterns were seen at diverse stages of the chronological aging process (Figure 7.11). I concluded that the three geroprotectors differently influence the sulfur amino acid biosynthetic pathway throughout yeast's chronological lifespan.

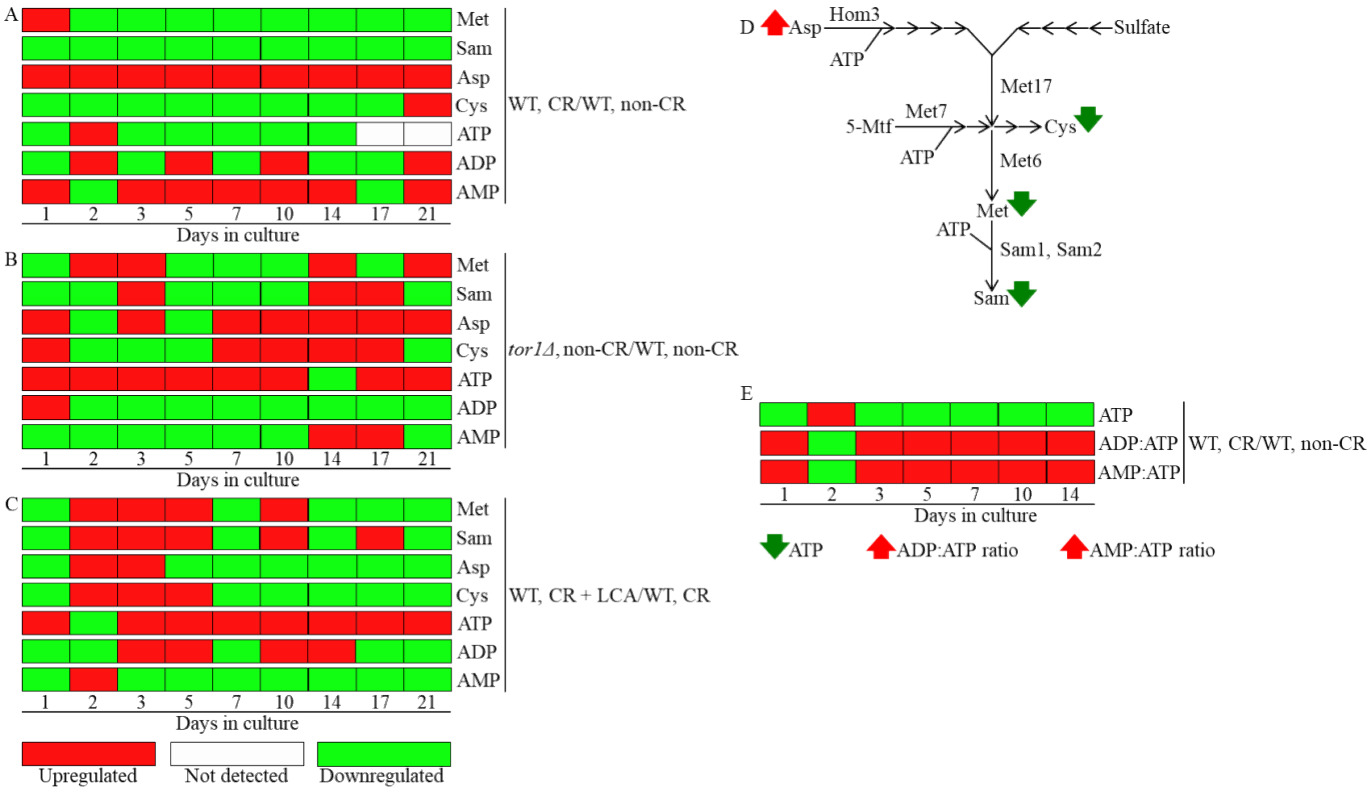

Figure 7.6: CR, the *tor1Δ* mutation and LCA differently influence the concentrations of methionine (Met), S-adenosylmethionine (Sam), aspartate (Asp), cysteine (Cys) and adenosine phosphate nucleotides throughout the chronological lifespan. The WT and *tor1Δ* mutant strains were cultured, cell aliquots were collected and the metabolomic analysis by LC-MS/MS was performed as described in the legend to Figure 7.5. The effects of CR (**A**), the *tor1Δ* mutation (**B**) and LCA (**C**) on the relative intracellular concentrations of Met, Sam, Asp, Cys, ATP, ADP and AMP are shown. CR's effect on the relative intracellular concentration of ATP and the ADP:ATP and AMP:ATP ratios are presented in **E**. The relative concentrations of metabolites that were significantly upregulated (displayed in red) or downregulated (shown in green) are provided for each time point. ATP was not detected in WT cells recovered on days 17 and 21 of culturing under CR or non-CR conditions without LCA. (**D**) A schematic depiction of how CR affects the metabolic pathway for sulfur amino acid biosynthesis from Asp, sulfate and 5-methyltetrahydrofolate (5-Mtf). (**E**) A graphic representation of changes in the intracellular concentration of ATP and in the ADP:ATP and AMP:ATP ratios in chronologically aging yeast limited in calorie supply. Next to metabolites' names, arrows denote those whose concentrations or ratios increase (red arrows) or decrease (green arrows) throughout most or all chronological

lifespan of yeast cultured under CR conditions. Other abbreviations: Hom3, aspartate kinase; Met6, a cobalamin-independent methionine synthase involved (directly or indirectly) in Met and Sam biosynthesis; Met 7, folylpolyglutamate synthetase indirectly involved in Met, Cys and Sam biosynthesis; Met17, an *O*-acetyl homoserine-*O*-acetyl serine sulfhydrylase indirectly involved in Met, Cys and Sam biosynthesis; Sam1 and Sam2, *S*-adenosylmethionine synthetases 1 and 2.

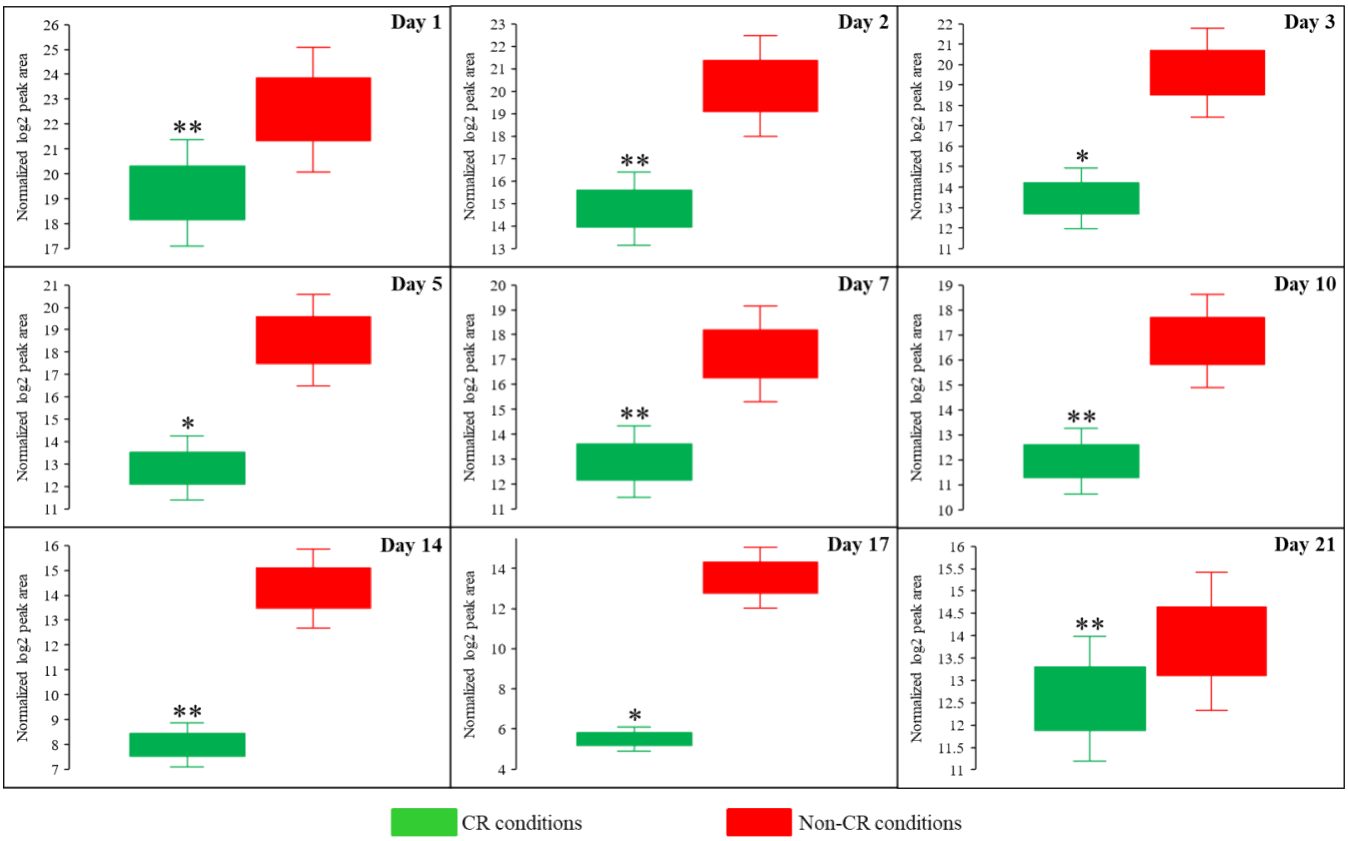

Figure 7.7: CR significantly decreases the intracellular concentration of S-adenosylmethionine (Sam) in yeast cells recovered on any day of culturing. WT strain BY4742 was cultured in the nutrient-rich YP medium initially containing 2% (w/v) glucose (non-CR conditions) or 0.2% (w/v) glucose (CR conditions). Cell aliquots were collected and the metabolomic analysis by LC-MS/MS was performed as described in the legend to Figure 7.5. The concentrations of Sam within WT cells cultured under CR or non-CR conditions are shown as the normalized $\log_2$ values of mass spectrometric peak areas for Sam. The *p* values for comparing the means of two groups were calculated using an unpaired two-tailed *t* test described in Materials and Methods. *$p < 0.05$, **$p < 0.01$ and ***$p < 0.001$. Data of 2 independent experiments, each being

performed twice, are presented.

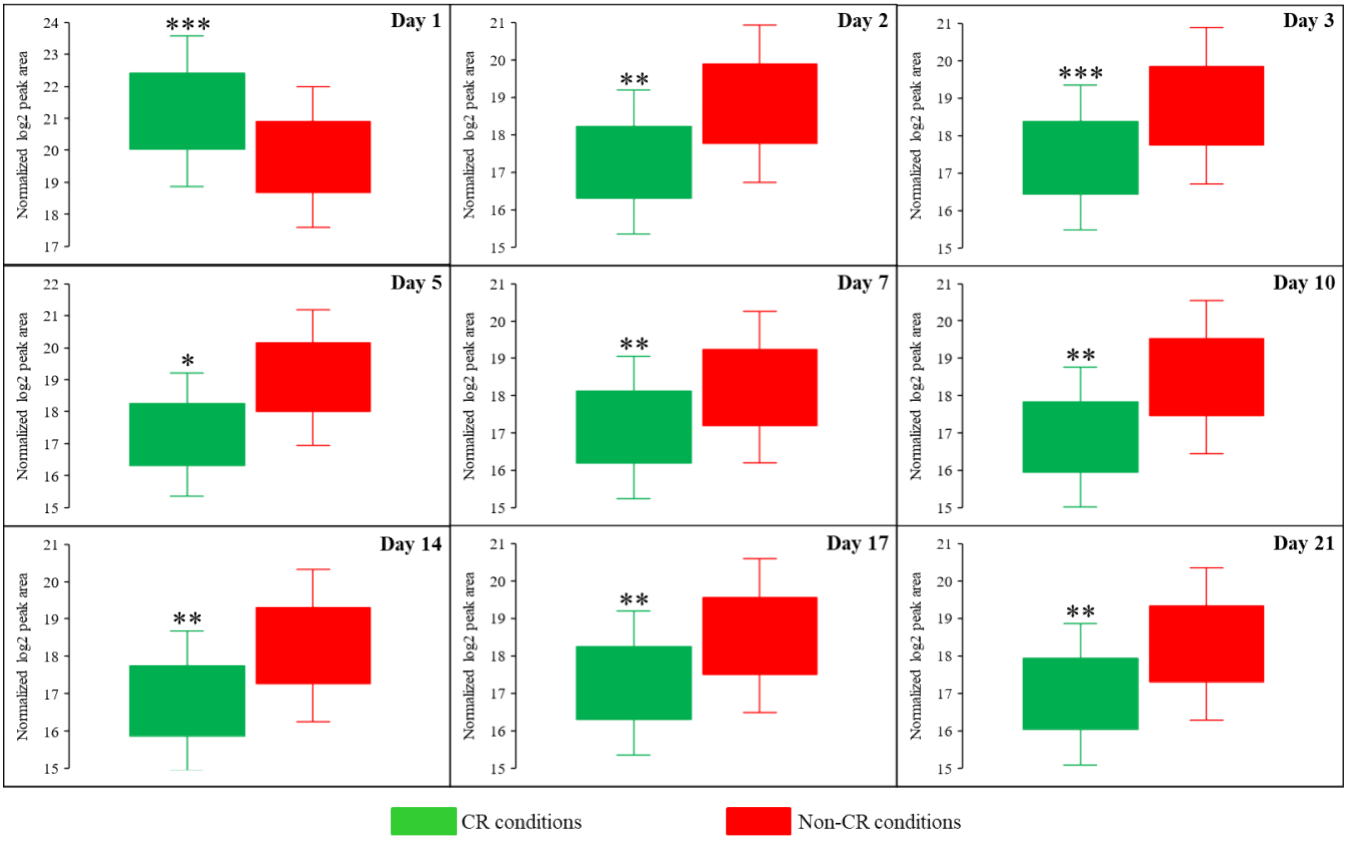

Figure 7.8: CR significantly decreases the intracellular concentration of methionine (Met) during most days of yeast cell culturing. WT strain BY4742 was cultured in the nutrient-rich YP medium initially containing 2% (w/v) glucose (non-CR conditions) or 0.2% (w/v) glucose (CR conditions). Cell aliquots were collected and the metabolomic analysis by LC-MS/MS was performed as described in the legend to Figure 7.5. The concentrations of Met within WT cells cultured under CR or non-CR conditions are shown as the normalized $\log_2$ values of mass spectrometric peak areas for Met. The *p* values for comparing the means of two groups were calculated using an unpaired two-tailed *t* test described in Materials and Methods. *p < 0.05, **p < 0.01 and ***p < 0.001. Data of 2 independent experiments, each being performed twice, are presented.

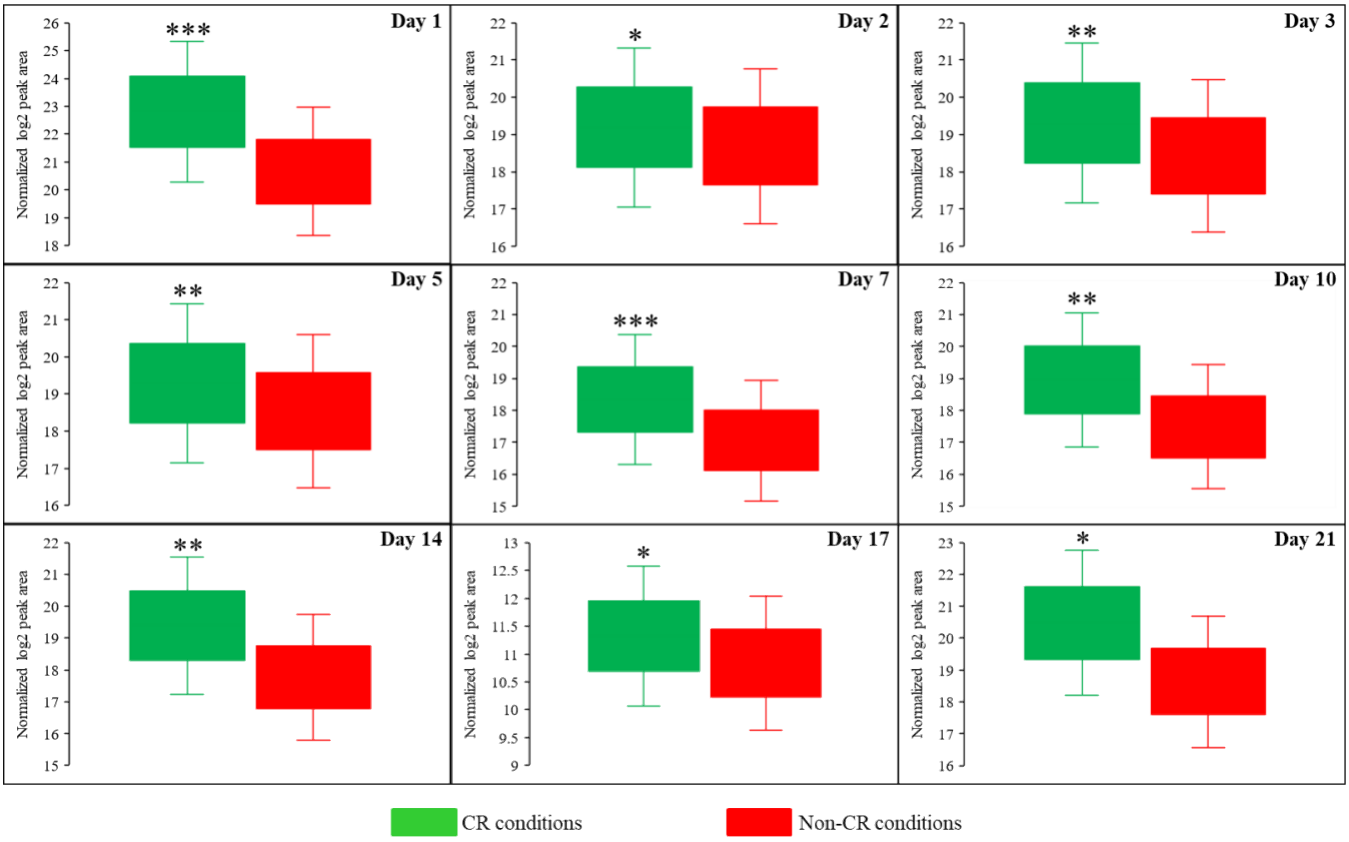

Figure 7.9: CR significantly increases the intracellular concentration of aspartate (Asp) throughout the entire chronological lifespan of budding yeast. WT strain BY4742 was cultured in the nutrient-rich YP medium initially containing 2% (w/v) glucose (non-CR conditions) or 0.2% (w/v) glucose (CR conditions). Cell aliquots were collected and the metabolomic analysis by LC-MS/MS was performed as described in the legend to Figure 7.5. The concentrations of Asp within WT cells cultured under CR or non-CR conditions are shown as the normalized $\log_2$ values of mass spectrometric peak areas for Asp. The *p* values for comparing the means of two groups were calculated using an unpaired two-tailed *t* test described in Materials and Methods. *p < 0.05, **p < 0.01 and ***p < 0.001. Data of 2 independent experiments, each being performed twice, are presented.

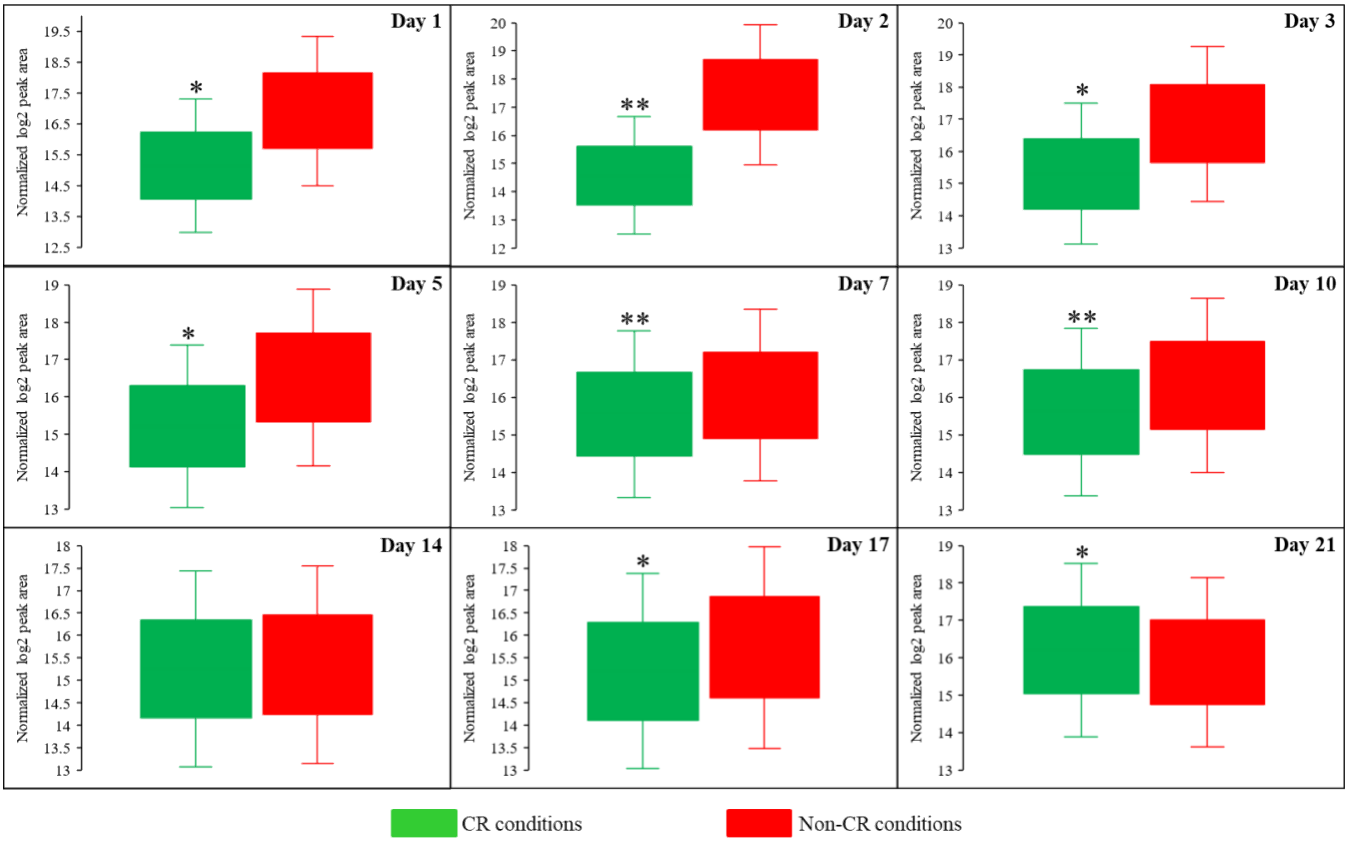

Figure 7.10: CR significantly decreases the intracellular concentration of cysteine (Cys) during most days of yeast cell culturing. WT strain BY4742 was cultured in the nutrient-rich YP medium initially containing 2% (w/v) glucose (non-CR conditions) or 0.2% (w/v) glucose (CR conditions). Cell aliquots were collected and the metabolomic analysis by LC-MS/MS was performed as described in the legend to Figure 7.5. The concentrations of Cys within WT cells cultured under CR or non-CR conditions are shown as the normalized $\log_2$ values of mass spectrometric peak areas for Cys. The *p* values for comparing the means of two groups were calculated using an unpaired two-tailed *t* test described in Materials and Methods. *p < 0.05, **p < 0.01. Data of 2 independent experiments, each being performed twice, are presented.

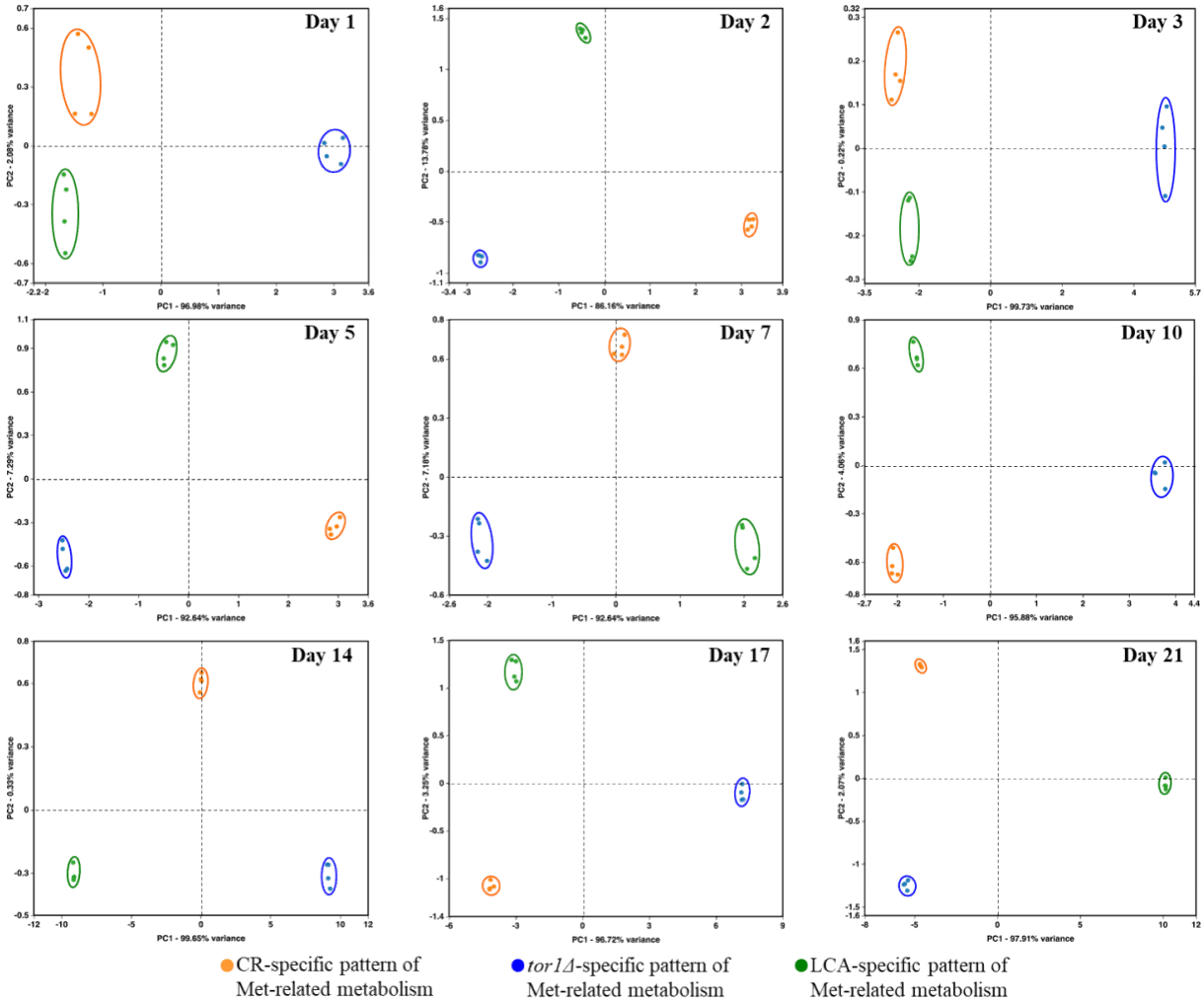

Figure 7.11: CR, *tor1Δ* and LCA differently affect the metabolic pathway for sulfur amino acid biosynthesis on various days of culturing. The WT and *tor1Δ* mutant strains were cultured, cell aliquots were collected and the metabolomic analysis by LC-MS/MS was performed as described in the legend to Figure 7.5. A WT strain culture that initially contained 2% (w/v) glucose served as a control non-CR culture for defining the metabolic patterns created by the CR and *tor1Δ* geroprotectors. A WT strain culture that initially contained 0.2% (w/v) glucose without LCA served as a control CR culture for defining the metabolic pattern created by the LCA geroprotector. The data on the relative concentrations of all four metabolites (i.e., Asp, Cys, Met and Sam) within the sulfur amino acid biosynthetic pathway were normalized in

age-matched cells. Multivariate analysis by PCA was then used to compare how the CR, *tor1Δ* and LCA geroprotectors affect the metabolic pathway for sulfur amino acid biosynthesis on various days of culturing. Data of 2 independent experiments, each being performed twice, are presented.

7.5 CR significantly increases the intracellular ADP:ATP and AMP:ATP ratios.

Three enzymatic reactions of the metabolic pathway for sulfur amino acid biosynthesis from Asp, sulfate and 5-Mtf use ATP as a co-substrate (Figure 7.6D) [480]. These reactions are catalyzed by Hom3, Met7, Sam1 and Sam2 (Figure 7.6D) [480]. Therefore, I expected that the CR-driven remodeling of this metabolic pathway could contribute to a change of ATP, ADP and AMP concentrations within chronologically aging yeast limited in calorie supply. Certainly, any other ATP-, ADP- or AMP-producing or consuming chemical reactions in the cytosol, mitochondria or other cellular locations could contribute to the CR-dependent changes in the concentrations of these adenosyl phosphate nucleotides and their ratios [60]. A genetic analysis similar to that performed in Chapter 3, and the RNA-sequencing analysis, are underway in the Titorenko laboratory to identify the ATP-, ADP- or AMP-producing or consuming chemical reactions that can contribute to the CR-dependent changes in the concentrations of these adenosyl phosphate nucleotides and their ratios

I found that CR, unlike the *tor1Δ* mutation or LCA, significantly decreases the intracellular concentration of ATP on any day of culturing other than day 2 (Figures 7.6A-7.6C; Figure 7.12). I noticed that ATP is not detected in WT cells recovered on days 17 and 21 of culturing under CR conditions without LCA or under non-CR conditions. Unlike CR, the *tor1Δ* mutation and LCA caused a significant rise in ATP concentration during most cell culturing days other than day 14 and day 2, respectively (Figures 7.6B and 7.6C). It remains to be investigated why the *tor1Δ* mutation and LCA extend budding yeast's longevity despite their effects on ATP concentrations differ from those of CR.

I also found that CR significantly alters (i.e., increases or decreases) the intracellular concentration of ADP during most days of yeast culturing (Figure 7.6A and Figure 7.13). Moreover, CR increased AMP concentration within yeast cells on most chronological lifespan days (Figure 7A and Figure 714). Unlike CR, the *tor1Δ* mutation and LCA significantly decreased

ADP and AMP intracellular concentrations at various consecutive phases of chronological aging (compare Figure 7.6A to Figures 7.6B and 7.6C).

I normalized the data on the concentrations of all three adenosine phosphate nucleotides (i.e., ATP, ADP and AMP) within age-matched cells cultured under CR conditions, carrying the *tor1Δ* mutation or treated with LCA. I used multivariate analysis by PCA to compare the normalized data throughout yeast's chronological lifespan. Yeast recovered on days 17 and 21 were not examined by this PCA because ATP was not detected in WT cells cultured under CR conditions without LCA. My PCA revealed that the ATP, ADP and AMP patterns specific for CR, *tor1Δ* and LCA are well separated from each other along the PC1 and/or PC2 axes of the PCA plots (Figure 7.15). Therefore, I concluded that the three geroprotectors differently affect the intracellular concentrations of adenosine phosphate nucleotides at diverse phases of yeast chronological aging.

Due to the above effects of CR on the relative intracellular concentrations of adenosine phosphate nucleotides, this low-calorie diet significantly increased the ADP:ATP and AMP:ATP ratios during most days of yeast cell culturing (Figure 7.6E, Figure 7.12 and Figure 7.13). I applied multivariate analysis by PCA to compare the ADP:ATP and AMP:ATP ratios specific for CR, *tor1Δ* and LCA. Again, the data for yeast recovered on days 17 and 21 were not subject to this PCA because no ATP was detected in WT cells cultured under CR or non-CR conditions in the absence of LCA. My PCA revealed that the normalized data for the ADP:ATP and AMP:ATP ratios specific for CR, *tor1Δ* and LCA are well separated from each other along the PC1 and/or PC2 axes of the PCA plots (Figure 7.18). This separation was observed for all days of cell culturing subjected to PCA (Figure 7.18). Based on these findings, I concluded that the effects of the three geroprotectors on the intracellular ADP:ATP and AMP:ATP ratios differ throughout yeast's chronological lifespan.

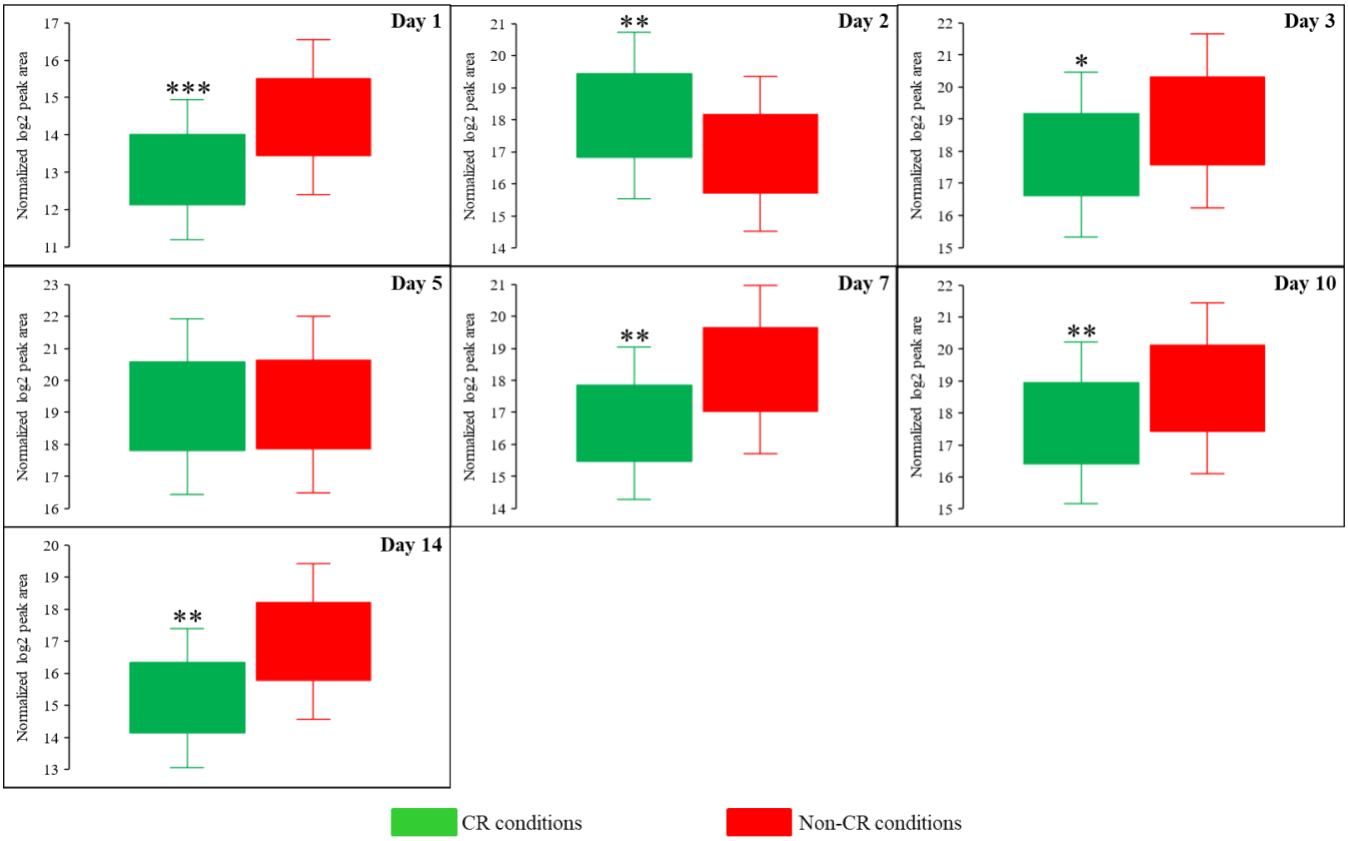

Figure 7.12: CR statistically significantly decreases the intracellular concentration of ATP during most days of yeast cell culturing. WT strain BY4742 was cultured in the nutrient-rich YP medium initially containing 2% (w/v) glucose (non-CR conditions) or 0.2% (w/v) glucose (CR conditions). Cell aliquots were collected and the metabolomic analysis by LC-MS/MS was performed as described in the legend to Figure 7.5. ATP concentrations within WT cells cultured under CR or non-CR conditions are shown as the normalized $\log_2$ values of mass spectrometric peak areas for ATP. No ATP was detected in WT cells recovered on days 17 and 21 of culturing under CR or non-CR conditions. The *p* values for comparing the means of two groups were calculated using an unpaired two-tailed *t* test described in Materials and Methods. *p < 0.05, **p < 0.01 and ***p < 0.001. Data of 2 independent experiments, each being performed twice, are presented.

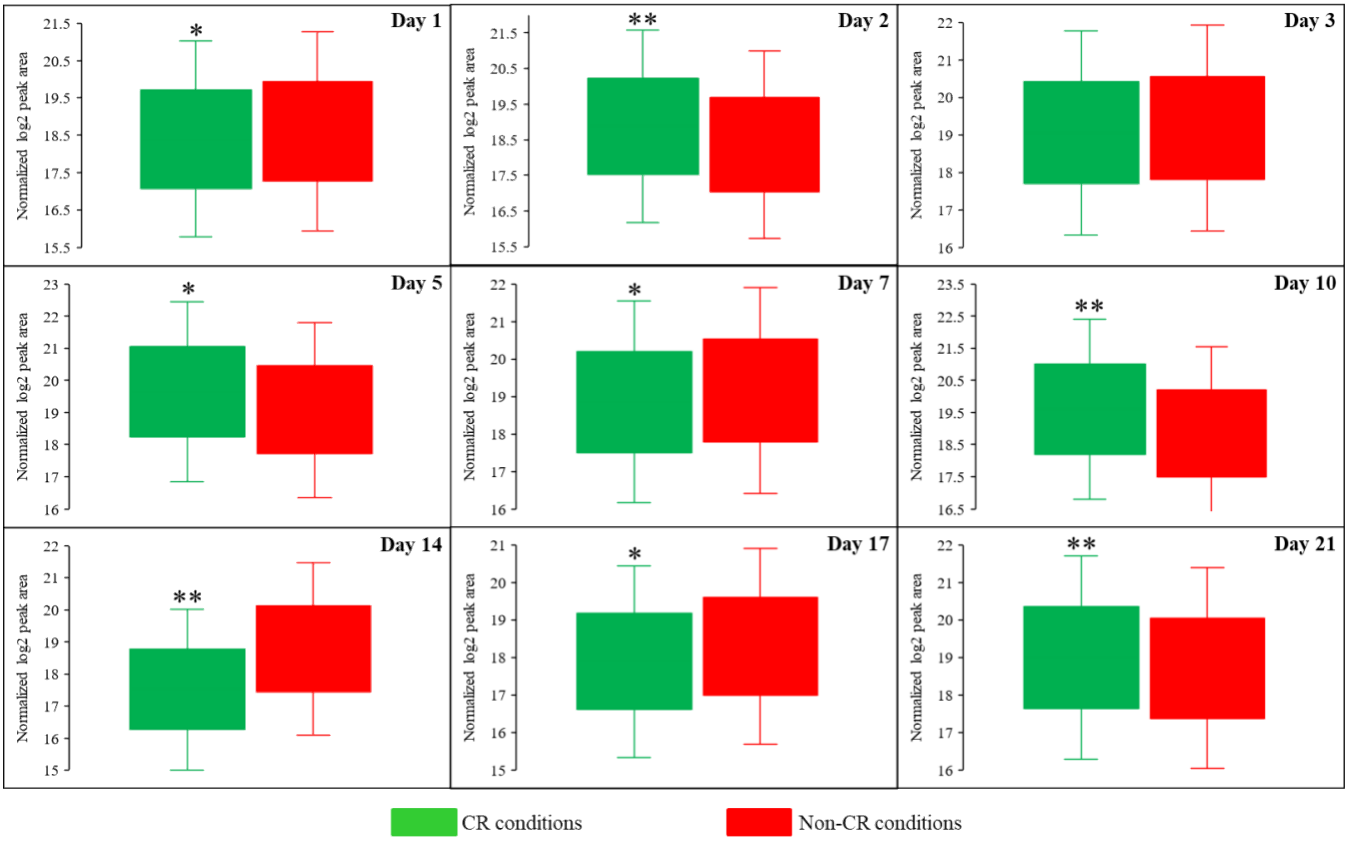

Figure 7.13: CR statistically significantly alters the intracellular concentration of ADP during most days of yeast cell culturing. WT strain BY4742 was cultured in the nutrient-rich YP medium initially containing 2% (w/v) glucose (non-CR conditions) or 0.2% (w/v) glucose (CR conditions). Cell aliquots for metabolic activity quenching and metabolite extraction were collected on days 1, 2, 3, 5, 7, 10, 14, 17 and 21 of culturing. The use of LC-MS/MS to identify and quantitate the intracellular water-soluble metabolites is described in Materials and Methods. ADP concentrations within WT cells cultured under CR or non-CR conditions are shown as the normalized $\log_2$ values of mass spectrometric peak areas for ADP. The *p* values for comparing the means of two groups were calculated using an unpaired two-tailed *t* test described in Materials and Methods. *$p < 0.05$ and **$p < 0.01$. Data of 2 independent experiments, each being performed twice, are presented.

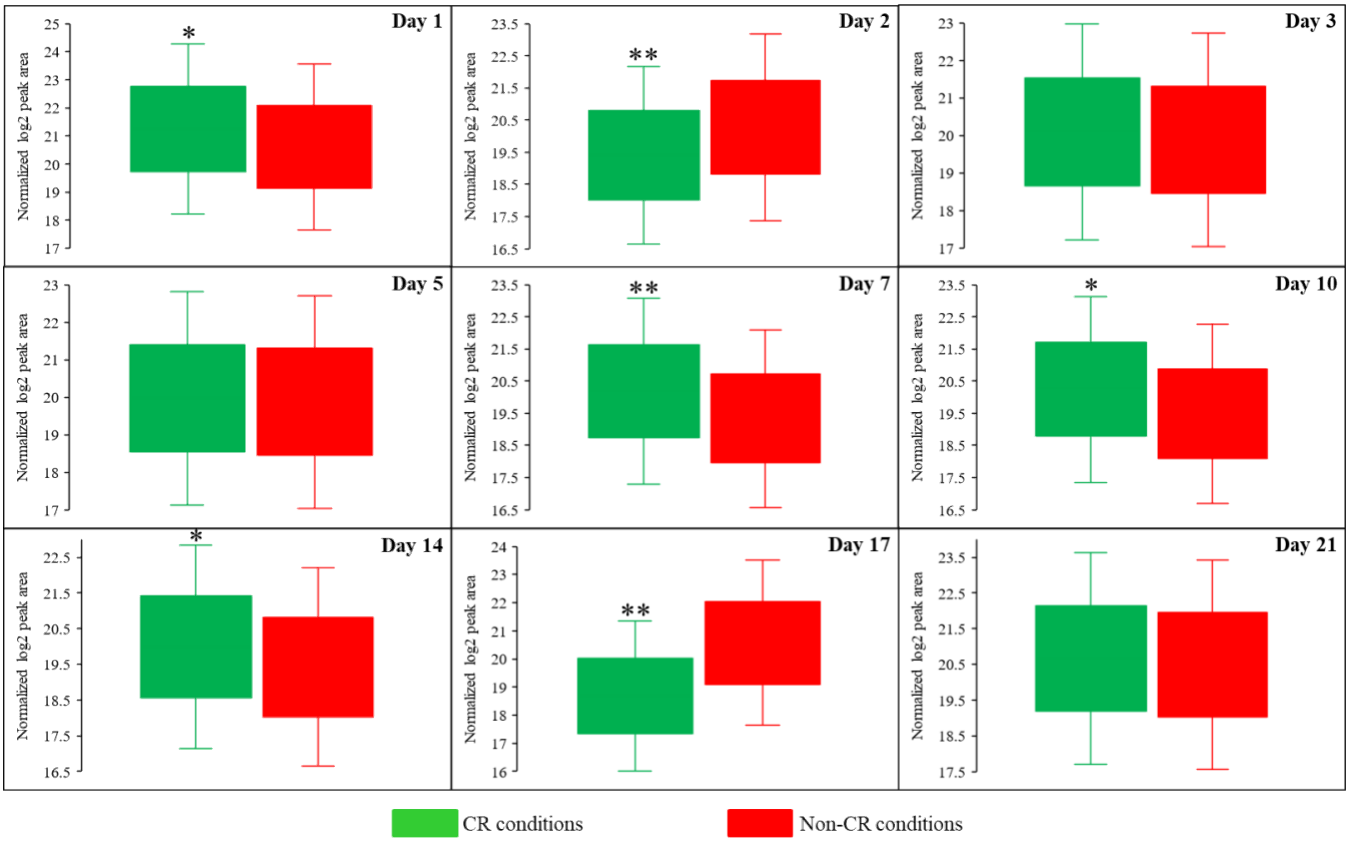

Figure 7.14: CR statistically significantly increases the intracellular concentration of AMP during most days of yeast cell culturing. WT strain BY4742 was cultured in the nutrient-rich YP medium initially containing 2% (w/v) glucose (non-CR conditions) or 0.2% (w/v) glucose (CR conditions). Cell aliquots for metabolic activity quenching and metabolite extraction were collected on days 1, 2, 3, 5, 7, 10, 14, 17 and 21 of culturing. The use of LC-MS/MS to identify and quantitate the intracellular water-soluble metabolites is described in Materials and Methods. AMP concentrations within WT cells cultured under CR or non-CR conditions are shown as the normalized $\log_2$ values of mass spectrometric peak areas for AMP. The *p* values for comparing the means of two groups were calculated using an unpaired two-tailed *t* test described in Materials and Methods. *$p < 0.05$ and **$p < 0.01$. Data of 2 independent experiments, each being performed twice, are presented.

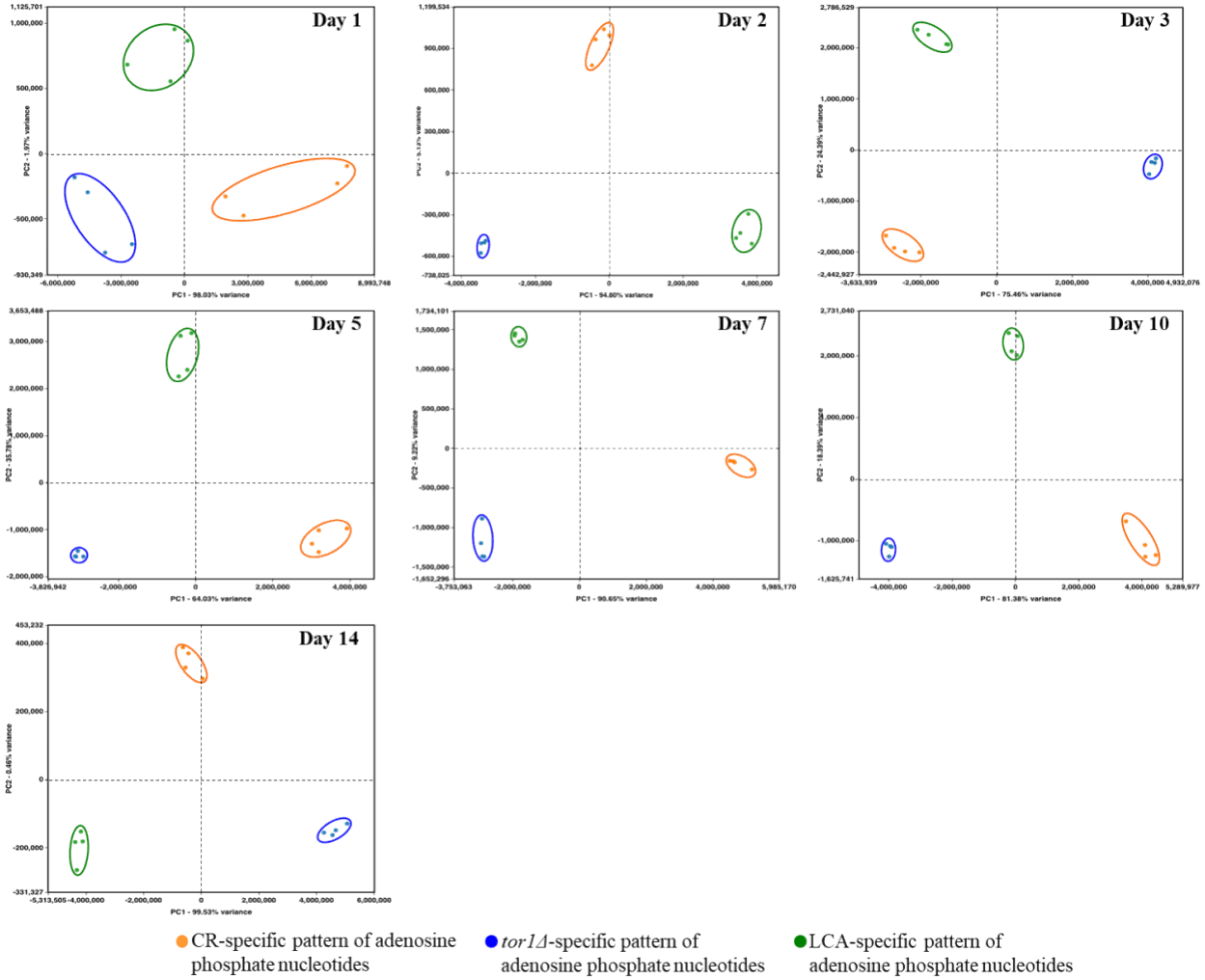

Figure 7.15: CR, *tor1Δ* and LCA differently affect the intracellular concentrations of adenosine phosphate nucleotides (i.e., ATP, ADP and AMP) at diverse phases of yeast chronological aging. The WT strain BY4742 was cultured in the nutrient-rich YP medium initially containing 2% (w/v) glucose (non-CR conditions), 0.2% (w/v) glucose (CR conditions) or 0.2% (w/v) glucose and 50 μM LCA (CR + LCA conditions). The *tor1Δ* mutant strain in the BY4742 genetic background was cultured in nutrient-rich YP medium initially containing 2% (w/v) glucose (non-CR conditions). Cell aliquots for metabolic activity quenching and metabolite extraction were collected on days 1, 2, 3, 5, 7, 10, 14, 17 and 21 of culturing. The use of LC-MS/MS to identify and quantitate the intracellular water-soluble metabolites is described in Materials and Methods. A WT strain culture that initially contained 2% (w/v) glucose served as a control non-CR culture for defining the metabolic patterns created by the CR and *tor1Δ* geroprotectors. A WT strain culture that initially contained 0.2% (w/v) glucose without LCA

served as a control CR culture for defining the metabolic pattern created by the LCA geroprotector. Normalized data for three adenosine phosphate nucleotides (i.e., ATP, ADP and AMP) identified in age-matched cells were used to create the PCA plots comparing the patterns created by the three different geroprotectors. Yeast recovered on days 17 and 21 were not examined by this PCA because ATP was not detected in WT cells cultured under CR conditions without LCA. Data of 2 independent experiments, each being performed twice, are presented.

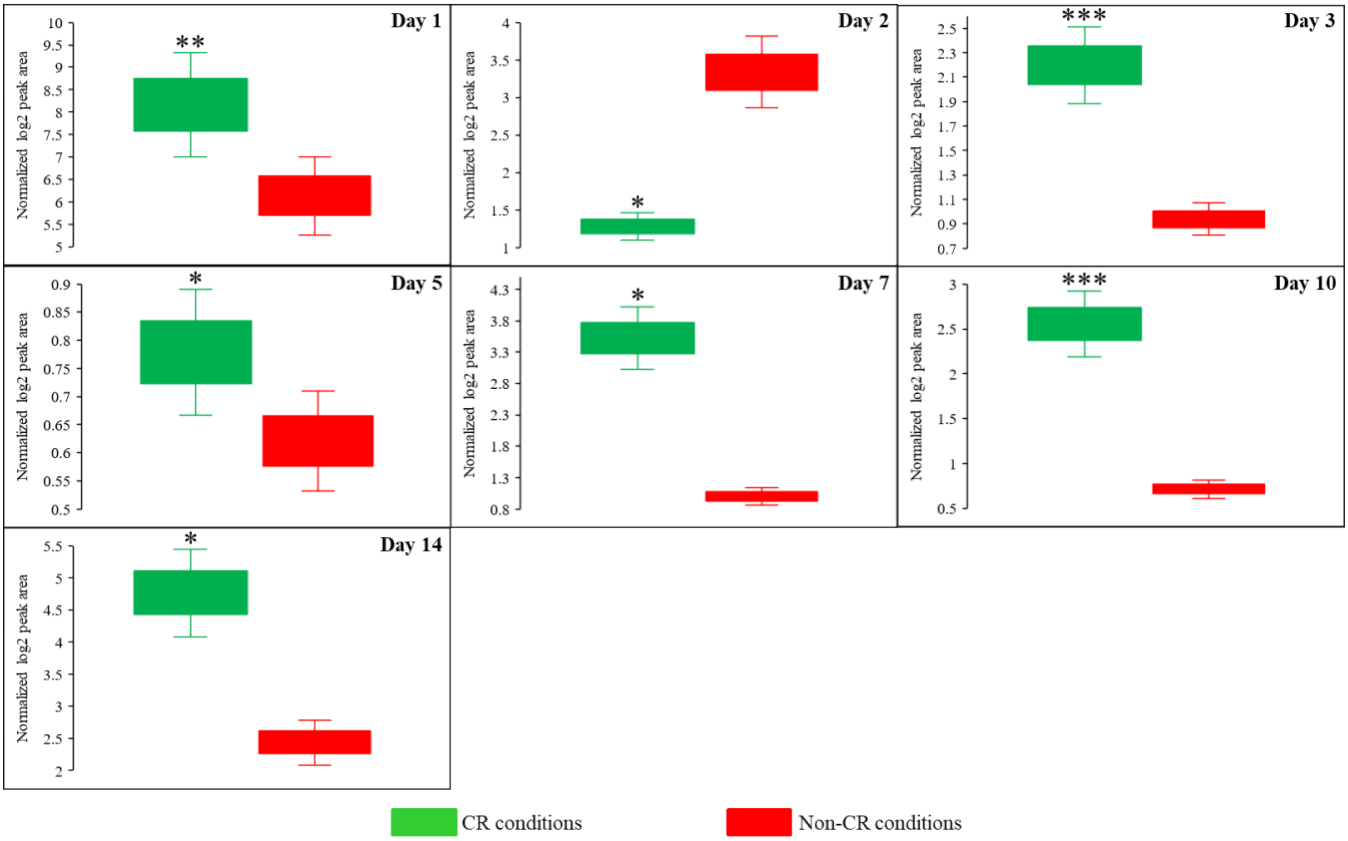

Figure 7.16: CR statistically significantly increases the AMP:ATP ratios during most days of yeast cell culturing. WT strain BY4742 was cultured in the nutrient-rich YP medium initially containing 2% (w/v) glucose (non-CR conditions) or 0.2% (w/v) glucose (CR conditions). Cell aliquots were collected and the metabolomic analysis by LC-MS/MS was performed as described in the legend to Figure 7.5. The AMP:ATP ratios within WT cells cultured under CR or non-CR conditions are shown as the normalized $\log_2$ values of mass spectrometric peak areas for AMP and ATP. The AMP:ATP ratios were not calculated for yeast recovered on days 17 and 21 of culturing because ATP was not detected in WT cells cultured under CR or non-CR conditions without LCA. The *p* values for comparing the means of two groups were calculated using an unpaired two-tailed

t test described in Materials and Methods. *p < 0.05, **p < 0.01, ***p < 0.001. Data of 2 independent experiments, each being performed twice, are presented.

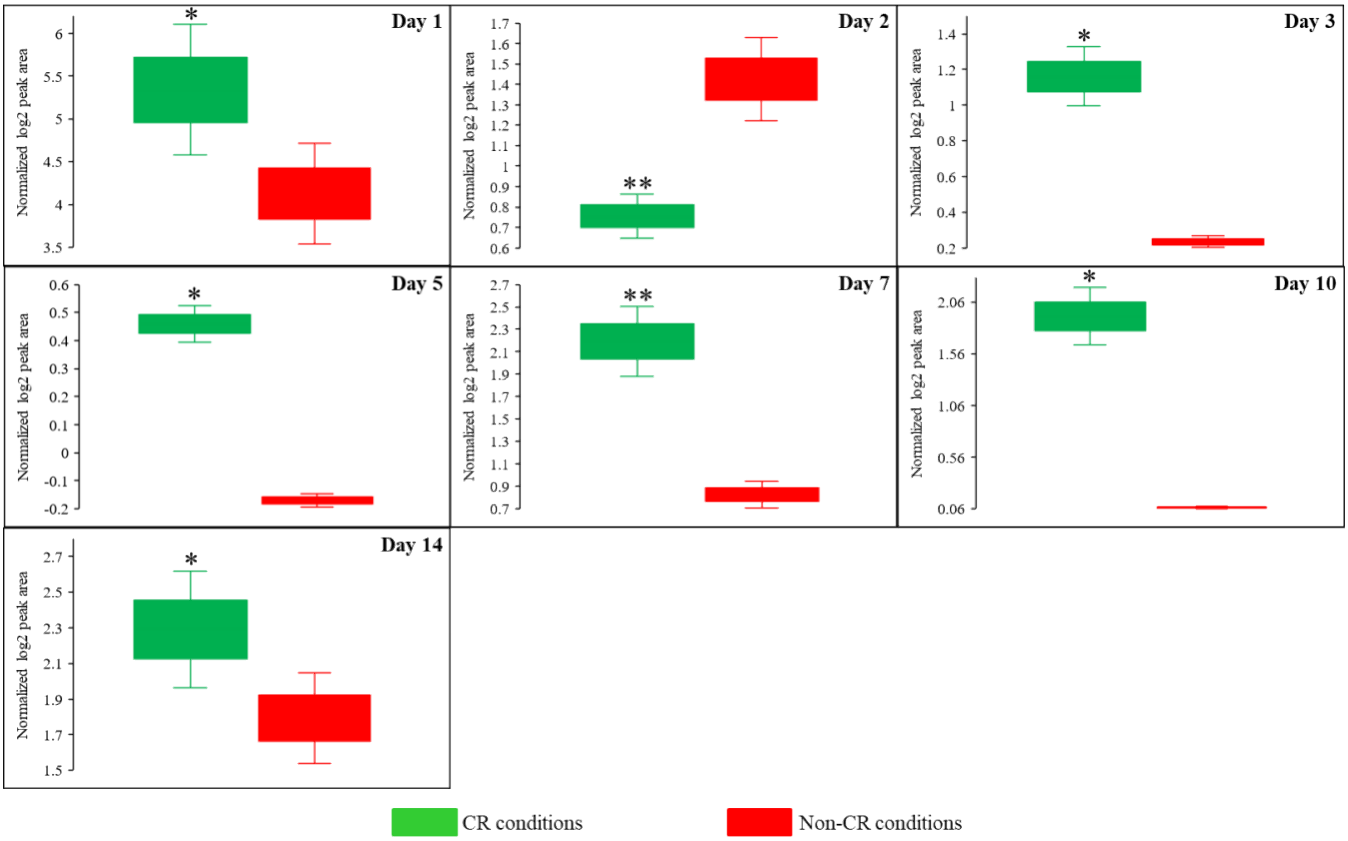

Figure 7.17: CR statistically significantly increases the ADP:ATP ratios during most days of yeast cell culturing. WT strain BY4742 was cultured in the nutrient-rich YP medium initially containing 2% (w/v) glucose (non-CR conditions) or 0.2% (w/v) glucose (CR conditions). Cell aliquots were collected and the metabolomic analysis by LC-MS/MS was performed as described in the legend to Figure 7.5. The ADP:ATP ratios within WT cells cultured under CR or non-CR conditions are shown as the normalized $\log_2$ values of mass spectrometric peak areas for ADP and ATP. The ADP:ATP ratios were not calculated for yeast recovered on days 17 and 21 of culturing because ATP was not detected in WT cells cultured under CR or non-CR conditions without LCA. The *p* values for comparing the means of two groups were calculated using an unpaired two-tailed *t* test described in Materials and Methods. *p < 0.05, **p < 0.01. Data of 2 independent experiments, each being performed twice, are presented.

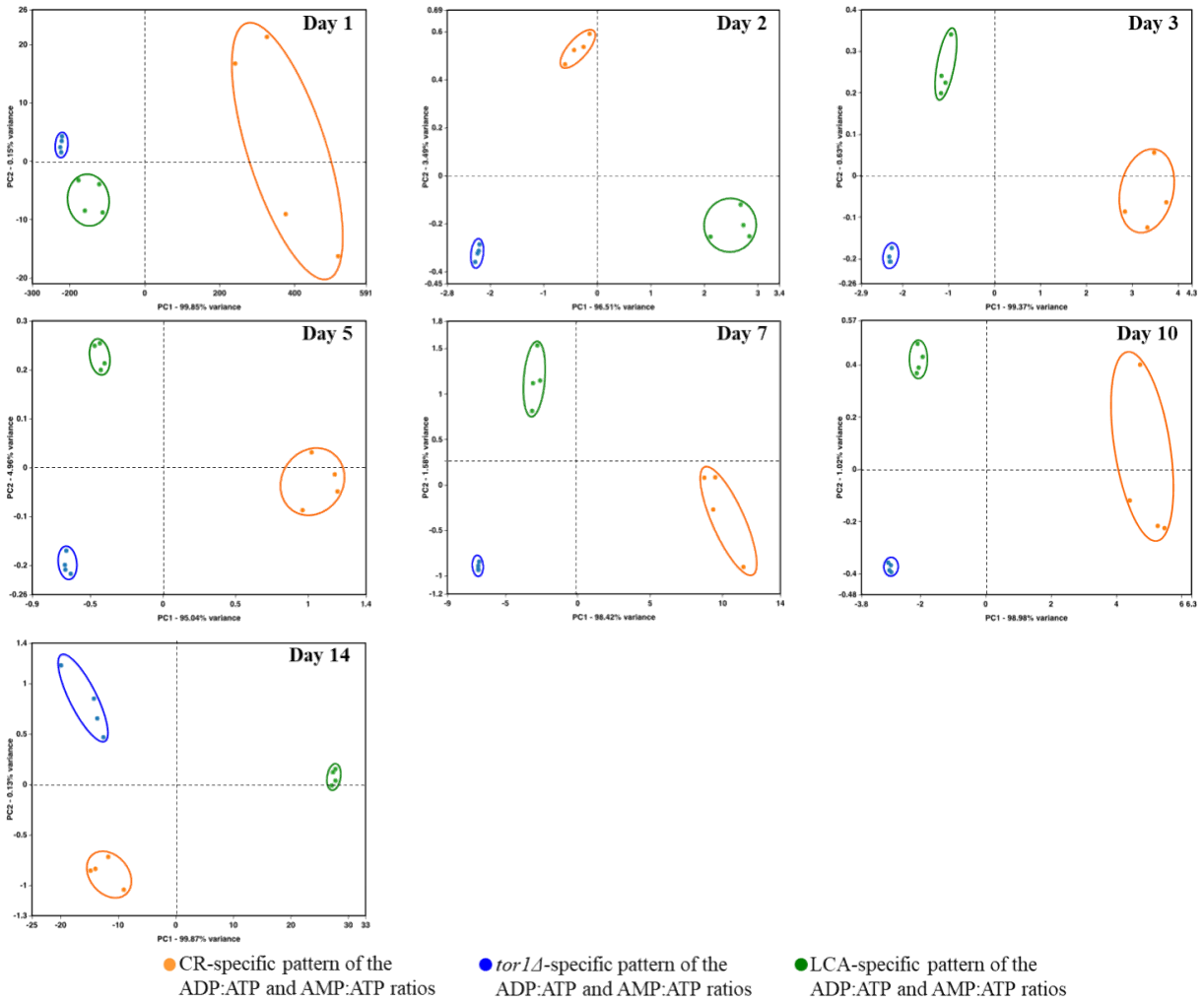

Figure 7.18: CR, *tor1Δ* and LCA differently affect the ADP:ATP and AMP:ATP ratios at diverse phases of yeast chronological aging. The WT strain BY4742 was cultured in the nutrient-rich YP medium initially containing 2% (w/v) glucose (non-CR conditions), 0.2% (w/v) glucose (CR conditions) or 0.2% (w/v) glucose and 50 μM LCA (CR + LCA conditions). The *tor1Δ* mutant strain in the BY4742 genetic background was cultured in nutrient-rich YP medium initially containing 2% (w/v) glucose (non-CR conditions). Cell aliquots for metabolic activity quenching and metabolite extraction were collected on days 1, 2, 3, 5, 7, 10, 14, 17 and 21 of culturing. The use of LC-MS/MS to identify and quantitate the intracellular water-soluble metabolites is described in Materials and Methods. A WT strain culture that initially contained 2% (w/v) glucose served as a control non-CR culture for defining the metabolic patterns created by the CR and *tor1Δ* geroprotectors. A WT strain culture that initially contained 0.2% (w/v) glucose without LCA served as a control CR culture for defining the metabolic pattern created by the LCA geroprotector.

Normalized data for the ADP:ATP and AMP:ATP ratios identified in age-matched cells were used to create the PCA plots comparing the patterns created by the three different geroprotectors. Yeast recovered on days 17 and 21 were not examined by this PCA because ATP was not detected in WT cells cultured under CR or non-CR conditions without LCA. Data of 2 independent experiments, each being performed twice, are presented.

7.6 Discussion.

In this study, I used a recently developed (see Chapter 6) LC-MS/MS method of non-targeted metabolomics to investigate how three different geroprotective interventions affect the intracellular water-soluble metabolome of chronologically aging *S. cerevisiae*. These interventions include CR (a robust dietary geroprotector), the *tor1Δ* mutation (an evolutionarily conserved genetic geroprotector) and LCA (a potent pharmacological geroprotector in yeast). My findings provide the first evidence that the three different geroprotectors create distinct metabolic patterns throughout the budding yeast's entire chronological lifespan.

It needs to be emphasized that my metabolomic analysis of the geroprotector-delayed chronological aging in yeast compared the intracellular concentrations of 193 structurally and functionally diverse water-soluble metabolites. AMP, ADP, ATP, FAD^+, FMN, $FADH_2$, NAD^+, NADH, $NADP^+$, NADPH, other nucleotides, amino acids, monosaccharides, intermediates of glycolysis and tricarboxylic cycle intermediates were among these metabolites. Many of these water-soluble metabolites reside in mitochondria. Thus, the observed geroprotector-specific remodeling of the metabolic pattern affects the major pathways of cellular metabolism in various cellular locations.

My study identified a distinct metabolic pattern created by the CR geroprotector. I found two characteristic features that distinguish the CR-specific metabolic pattern from the cellular metabolism patterns created by the *tor1Δ* and LCA geroprotectors. One characteristic feature that distinguishes the CR-specific metabolic design is CR's ability to suppress the biosynthesis of Met, Sam and Cys from Asp, sulfate and 5-Mtf throughout the chronological lifespan. The other characteristic feature of the CR-specific metabolic pattern is a decline in the intracellular concentration of ATP, a rise in the intracellular concentrations of ADP and ATP, and an increase in the ADP:ATP and AMP:ATP ratios at various consecutive phases of chronological aging.

Notably, both features of the CR-specific remodeling of cellular metabolism are likely to

contribute to yeast chronological aging delay by CR.

Indeed, Met restriction is known to extend longevity in yeast and other evolutionary distant eukaryotes [481-485]. Of note, a possibility remains that the accumulation of Asp in budding yeast mutants deficient in Met biosynthesis (Figure 7.6) may contribute to the longevity extension in the mutants. Therefore, it would be interesting to test whether the addition of exogenous Asp to WT yeast strain could extend its longevity. Furthermore, a recent study revealed that the *met6Δ* and *met17Δ* mutations (Figure 7.6D) decrease the intracellular concentration of Met and extend yeast chronological lifespan under non-CR conditions in a nutrient-limited medium [486]. Moreover, the excessive quantities of exogenously added Met abrogate the CR-dependent extension of yeast CLS in a nutrient-limited medium [486]. Several mechanisms of yeast CLS extension by lowering the intracellular concentration of Met, Sam and Cys have been proposed. One likely mechanism is that a decline in intracellular Met concentration lowers the Met-dependent activation of the pro-aging Tor1 (target of rapamycin complex 1) pathway, thereby suppressing the inhibitory effect of Tor1 on the anti-aging process of autophagy [279]. Another possible mechanism is that a decline in the intracellular concentration of Met activates the anti-aging process for proteasomal degradation of damaged and dysfunctional proteins [486]. Furthermore, a decrease in intracellular Sam concentration can weaken the pro-aging Tor1 pathway because it suppresses the protein phosphatase Ppa2 (inorganic pyrophosphatase 2; a known upstream activator of Tor1) [487]. It needs to be emphasized that SAM is involved in DNA methylation, a well-known aging biomarker [399, 478]. Thus, it is feasible that a decline in intracellular SAM concentration slows aging because it suppresses DNA methylation. Moreover, a decline in the intracellular concentrations of Met and Cys can slow the pro-aging process of protein synthesis because these two sulfur amino acids promote a thiolation-driven tRNA activation [488].

The observed CR-specific remodeling of adenosine phosphate nucleotide metabolism is also a likely contributor to yeast chronological aging delay by CR. Indeed, the increase in the intracellular ADP:ATP and AMP:ATP ratios are known to activate the anti-aging heterotrimeric protein complex Snf1 (sucrose non-fermenting complex 1) [489, 490]. As a member of the family of AMP-activated protein kinases [491], Snf1 is a key energy-sensing regulator that phosphorylates and activates or inactivates several protein targets known for their essential roles in defining yeast CLS [258, 492, 493]. Indeed, in chronologically aging budding yeast that enters the ST phase, Snf1 activates mitochondrial respiration, glyoxylate cycle, gluconeogenesis,

glycogen synthesis and suppresses amino acid synthesis, FFA formation and glycogen degradation; therefore, the knock-out mutation *snf1Δ* eliminates an anti-aging protein and shortens the CLS [137].

These findings suggest a hypothetical model of how the observed CR-specific remodeling of cellular metabolism delays the chronological aging of yeast cultured in the nutrient-rich YP medium. The model is schematically depicted in Figure 7.19. The key aspects of this model are as follows: 1) a life-long decline in the intracellular concentrations of Cys and Met weakens tRNA thiolation, thus slowing down the pro-aging process of protein synthesis, 2) a decrease of intracellular Met throughout the chronological lifespan attenuates a direct Met-driven stimulation of the pro-aging Tor1 pathway, thereby lowering the inhibitory effect of Tor1 on autophagy and other anti-aging processes, 3) a deterioration in intracellular Met concentration at diverse stages of chronological aging also weakens a Met-dependent suppression of the proteasomal degradation of damaged and dysfunctional proteins, a known anti-aging process, 4) a decline in Sam concentration throughout the chronological lifespan lowers the ability of the protein phosphatase Ppa2p to stimulate the pro-aging Tor1 pathway, and 5) a rise in the ADP:ATP and AMP:ATP ratios on most days of yeast chronological lifespan stimulates the anti-aging protein kinase complex Snf1.

The challenge for the future is to test the proposed model. The ongoing studies in the Titorenko laboratory address this challenge. In the future, it would also be interesting to define the metabolic “signatures” specific for other geroprotectors, including the *tor1Δ* mutation and LCA.

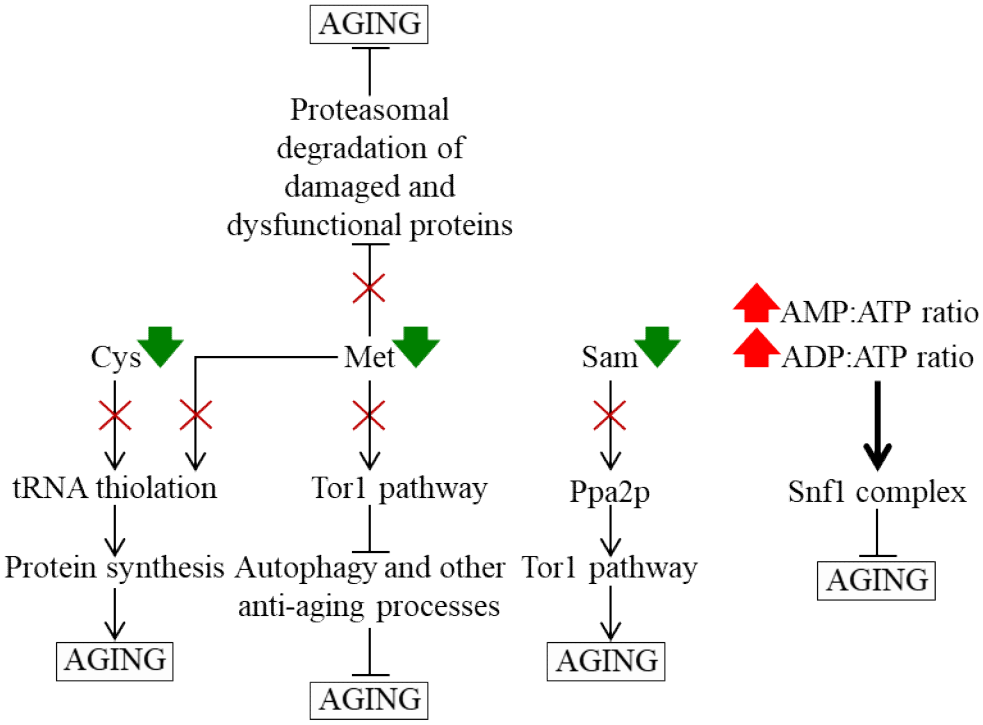

Figure 7.19: A hypothetical model of how a specific remodeling of cellular metabolism by CR slows down yeast chronological aging. See the text for more details. Abbreviations: Cys, cysteine; Met, methionine; Ppa2p, inorganic pyrophosphatase 2; Sam, *S*-adenosylmethionine; Snf1, sucrose non-fermenting complex 1; Tor1, target of rapamycin complex 1.

Chapter 8: General discussion.

In studies presented in this Thesis, I used the existing methods of liquid chromatography coupled with tandem mass spectrometry (LC-MS/MS) as the prototypes to develop the novel LC-MS/MS procedures for identifying and quantifying the intracellular lipidomes and water-soluble metabolomes of budding yeast. The LC-MS/MS lipidomics method I developed exhibits several advantages over the presently used ones. These advantages include the high efficiency of lipid extraction, versatility and robustness, sensitivity, ability to distinguish between isobaric and isomeric lipid species, use of alternative mobile phase additives to enhance ionization of all lipid classes, and increased efficiencies of two different types of precursor ions fragmentation processes. The LC-MS/MS metabolomics method I developed enhances the extent of metabolic activity quenching, reduces the magnitude of quenching-related cell leakage of intracellular metabolites, uses a single type of high-performance liquid chromatography (HPLC) column for chromatographic separation of all water-soluble metabolites, is robust and versatile, exhibits high sensitivity, and has a wide linear dynamic range of detectable metabolites. Because the papers describing both methods had been published, the methods are now available to a broad community of researchers working in science and industry. The feedback that we have received so far indicates that many colleagues are adapting both methods to their research.

In studies described here, I also used tandem mass spectrometry (MS/MS) to investigate how an aging-delaying (geroprotective) extract from *Salix alba's* bark, called PE21, influences the cellular lipidome of chronologically aging budding yeast. My findings provide evidence that PE21 alters the intracellular concentrations of 16 out of 18 lipid classes in chronologically aged budding yeast. Based on these findings, we proposed three mechanisms through which the PE21-driven changes in the cellular lipidome might delay the chronological aging of budding yeast. In one of these mechanisms, I provided evidence that PE21 slows chronological aging because it decreases the intracellular concentration of free fatty acid (FFA). The PE21-dependent FFA decline weakens liponecrotic regulated cell death and delays the age-related onset of liponecrosis, thus increasing the probability of cell survival during the entire process of chronological aging. The challenge for the future is to dissect the molecular mechanism underlying the ability of the excessive concentrations of cellular FFA to commit the chronologically old budding yeast cells to liponecrotic dearth.

Here, I applied my newly developed LC-MS/MS lipidomics method to the quantitative

assessment of how the CR, *tor1Δ* mutation and LCA) geroprotectors influence the lipidomes of chronologically aging quiescent and non-quiescent budding yeast cells. I found that CR reorganizes the lipidomes of quiescent and nonquiescent yeast cells differently than two other geroprotectors. Based on these findings, I proposed a hypothetical model of how the characteristic CR-dependent reorganization of the lipidomes within quiescent and non-quiescent budding yeast cells contributes to the aging delay and longevity extension by CR. The model envisages that there might be at least two mechanisms underlying such contribution. For future research, it would be interesting to test this hypothetical model.

In studies presented in this Thesis, I employed my newly developed LC-MS/MS metabolomics method to compare the effects of the CR, *tor1Δ* and LCA geroprotectors on the water-soluble metabolome of chronologically aging budding yeast. I identified a distinct metabolic pattern created by the CR geroprotector. My PCA, a multivariate type of analysis traditionally used for this purpose, revealed two characteristic features that distinguish the CR-specific metabolic pattern from the cellular metabolism patterns created by the *tor1Δ* and LCA geroprotectors. Thus, both these features are unique for CR. One characteristic feature that distinguishes the CR-specific metabolic design is CR's ability to suppress the biosynthesis of methionine, *S*-adenosylmethionine and cysteine from aspartate, sulfate and 5-methyltetrahydrofolate throughout the chronological lifespan. The other characteristic feature of the CR-specific metabolic pattern is a decline in the intracellular concentration of ATP, a rise in the intracellular concentrations of AMP and ADP, and an increase in the AMP:ATP and ADP:ATP ratios at various consecutive phases of chronological aging. Based on these findings, I proposed a hypothetical model of how the observed CR-specific remodeling of cellular metabolism delays the chronological aging of budding yeast. Future studies will focus on testing this hypothetical model.

An important finding of the studies presented in this Thesis is that budding yeast cells that age chronologically can use multiple strategies for regulating lipid metabolism and transport and the flow of water-soluble metabolites to assure longevity.

As for regulating lipid metabolism and transport to assure budding yeast's longevity, a conclusion about the perceivable multiplicity of strategies might be preliminary. Indeed, the PE21-dependent and CR-driven strategies appear to be similar. They both are aimed at regulating lipid metabolism and transport in the cytosol, LDP, peroxisomes and mitochondria to attain the following three goals: 1) maintain intracellular FFA concentration below toxic but at "hormetic"

level, 2) keep phospholipid concentrations in the ER sufficiently high to sustain the UPR^{ER} highly active but sufficiently low to avoid the toxic effects of excessive phospholipid concentrations in the ER, and 3) retain the concentration of CL in the IMM sufficiently high to maintain mitochondrial functionality but to avoid the toxicity of the excessive CL in the IMM. The ongoing studies in the Titorenko laboratory address the question of what the dynamic range of "hormetic" FFA concentrations is. FFA can still promote the "hormetic" stress response before becoming toxic for the cell at these concentrations. It would be fair to say that we still do not understand the strategies by which the *tor1Δ* mutation and LCA regulate lipid metabolism and transport to assure the longevity of chronologically aging yeast. This is because the occasional significant changes in the concentrations of some lipid classes observed in yeast cells exposed to any of these two geroprotectors are limited to brief periods whose significance as the potential checkpoints in the aging process we yet to appreciate.

As for regulating the flow of water-soluble metabolites to assure budding yeast's longevity, the strategies used by CR, the *tor1Δ* mutation and LCA are different from the point of view of PCA, a formal multivariate statistical analysis traditionally used for the purpose of comparison between multiple datasets. However, we still do not appreciate these differences in terms of underlying molecular and cellular mechanisms.

References.

1. Ackermann M, Chao L, Bergstrom CT, Doebeli M. On the evolutionary origin of aging. Aging Cell. 2007; 6:235-244.

2. Fontana L, Partridge L, Longo VD. Extending healthy life span - from yeast to humans. Science. 2010; 328:321-3266.

3. DiLoreto R, Murphy CT. The cell biology of aging. Mol Biol Cell. 2015; 26:4524-4531.

4. Pitt JN, Kaeberlein M. Why is aging conserved and what can we do about it? PLoS Biol. 2015; 13: e1002131.

5. Flatt T, Partridge L. Horizons in the evolution of aging. BMC Biol. 2018; 16:93.

6. Longo VD, Shadel GS, Kaeberlein M, Kennedy B. Replicative and chronological aging in Saccharomyces cerevisiae. Cell Metab. 2012; 16:18-31.

7. Váchová L, Cáp M, Palková Z. Yeast colonies: a model for studies of aging, environmental adaptation, and longevity. Oxid Med Cell Longev. 2012; 2012:601836.

8. Arlia-Ciommo A, Leonov A, Piano A, Svistkova V, Titorenko VI. Cell-autonomous mechanisms of chronological aging in the yeast Saccharomyces cerevisiae. Microb Cell. 2014; 1:163-178.

9. Denoth Lippuner A, Julou T, Barral Y. Budding yeast as a model organism to study the effects of age. FEMS Microbiol Rev. 2014; 38:300-25.

10. Nyström T, Liu B. Protein quality control in time and space - links to cellular aging. FEMS Yeast Res. 2014; 14:40-8.

11. Kapahi P, Chen D, Rogers AN, Katewa SD, Li PW, Thomas EL, Kockel L. With TOR, less is more: a key role for the conserved nutrient-sensing TOR pathway in aging. Cell Metab. 2010; 11:453-65.

12. Evans DS, Kapahi P, Hsueh WC, Kockel L. TOR signaling never gets old: aging, longevity and TORC1 activity. Ageing Res Rev. 2011; 10:225-37.

13. Jazwinski SM. The retrograde response retrograde response and other pathways of interorganelle communication interorganelle communication in yeast replicative aging. Subcell Biochem. 2012; 57:79-100.

14. Leonov A, Titorenko VI. A network of interorganellar communications underlies cellular aging. IUBMB Life. 2013; 65:665-674.

15. Jazwinski SM. The retrograde response: when mitochondrial quality control is not enough. Biochim Biophys Acta. 2013; 1833:400-409.

16. Minois N, Carmona-Gutierrez D, Madeo F. Polyamines in aging and disease. Aging. 2011; 3:716-32.

17. Hubbard BP, Sinclair DA. Small molecule SIRT1 activators for the treatment of aging and age-related diseases. Trends Pharmacol Sci. 2014; 35:146-54.

18. Sinclair DA, Guarente L. Small-molecule allosteric activators of sirtuins. Annu Rev Pharmacol Toxicol. 2014; 54:363-80.

19. Zimmermann A, Hofer S, Pendl T, Kainz K, Madeo F, Carmona-Gutierrez D. Yeast as a tool to identify anti-aging compounds. FEMS Yeast Res. 2018; 18: foy020.

20. Yalcin G, Lee, C.-K. Recent studies on anti-aging compounds with Saccharomyces cerevisiae as a model organism. Translational Medicine of Aging (2019) 3:109-115.

21. Weissman J, Guthrie C, Fink GR (editors). Guide to Yeast Genetics: Functional Genomics, Proteomics, and Other Systems Analysis. Academic Press:Burlington; 2010. 942 pp.

22. Botstein D, Fink GR. Yeast: an experimental organism for 21st Century biology. Genetics. 2011; 189:695-704.

23. Feldmann H, editor. Yeast: Molecular and Cell Biology. 2nd ed. Weinheim, Germany:Wiley-Blackwell; 2012. 464 pp.

24. Fabrizio P, Longo VD. The chronological life span of Saccharomyces cerevisiae. Methods Mol Biol. 2007; 371:89-95.

25. Piper PW. Maximising the yeast chronological lifespan. Subcell Biochem. 2012; 57:145-159.

26. Hu J, Wei M, Mirisola MG, Longo VD. Assessing chronological aging in Saccharomyces cerevisiae. Methods Mol Biol. 2013; 965:463-472.

27. Burtner CR, Murakami CJ, Kaeberlein M. A genomic approach to yeast chronological aging. Methods Mol Biol. 2009; 548:101-114.

28. Murakami C, Kaeberlein M. Quantifying yeast chronological life span by outgrowth of aged cells. J Vis Exp. 2009; 27:1156.

29. Wu Z, Song L, Liu SQ, Huang D. A high throughput screening assay for determination of chronological lifespan of yeast. Exp Gerontol. 2011; 46:915-922.

30. Longo VD, Kennedy BK. Sirtuins in aging and age-related disease. Cell. 2006; 126:257-68.

31. Longo VD, Fabrizio P. Chronological aging in Saccharomyces cerevisiae. Subcell Biochem. 2012; 57:101-21.

32. Burtner CR, Murakami CJ, Kennedy BK, Kaeberlein M. A molecular mechanism of chronological aging in yeast. Cell Cycle. 2009; 8:1256-1270.

33. Burtner CR, Murakami CJ, Olsen B, Kennedy BK, Kaeberlein M. A genomic analysis of chronological longevity factors in budding yeast. Cell Cycle. 2011; 10:1385-1396.

34. Bitterman KJ, Medvedik O, Sinclair DA. Longevity regulation in Saccharomyces cerevisiae: linking metabolism, genome stability, and heterochromatin. Microbiol Mol Biol Rev. 2003; 67:376-399.

35. Steinkraus KA, Kaeberlein M, Kennedy BK. Replicative aging in yeast: the means to the end. Annu Rev Cell Dev Biol. 2008; 24:29-54.

36. Steffen KK, Kennedy BK, Kaeberlein M. Measuring replicative life span in the budding yeast. J Vis Exp. 2009; 28:1209.

37. Sinclair DA. Studying the replicative life span of yeast cells. Methods Mol Biol. 2013; 1048:49-63.

38. Mirisola MG, Longo VD. Acetic acid and acidification accelerate chronological and replicative aging in yeast. Cell Cycle. 2012; 11:3532-3533.

39. Murakami C, Delaney JR, Chou A, Carr D, Schleit J, Sutphin GL, An EH, Castanza AS, Fletcher M, Goswami S, Higgins S, Holmberg M, Hui J, Jelic M, Jeong KS, Kim JR, Klum S, Liao E, Lin MS, Lo W, Miller H, Moller R, Peng ZJ, Pollard T, Pradeep P, Pruett D, Rai D, Ros V, Schuster A, Singh M, Spector BL, Vander Wende H, Wang AM, Wasko BM, Olsen B, Kaeberlein M. pH neutralization protects against reduction in replicative lifespan following chronological aging in yeast. Cell Cycle. 2012; 11:3087-3096.

40. Polymenis M, Kennedy BK. Chronological and replicative lifespan in yeast: do they meet in

the middle? Cell Cycle. 2012; 11:3531-3532.

41. Delaney JR, Murakami C, Chou A, Carr D, Schleit J, Sutphin GL, An EH, Castanza AS, Fletcher M, Goswami S, Higgins S, Holmberg M, Hui J, Jelic M, Jeong KS, Kim JR, Klum S, Liao E, Lin MS, Lo W, Miller H, Moller R, Peng ZJ, Pollard T, Pradeep P, Pruett D, Rai D, Ros V, Schuster A, Singh M, Spector BL, Wende HV, Wang AM, Wasko BM, Olsen B, Kaeberlein M. Dietary restriction and mitochondrial function link replicative and chronological aging in Saccharomyces cerevisiae. Exp Gerontol. 2013; 48:1006-1013.

42. Carmona-Gutierrez D, Büttner S. The many ways to age for a single yeast cell. Yeast. 2014; 31:289-298.

43. Arlia-Ciommo A, Piano A, Leonov A, Svistkova V, Titorenko VI. Quasi-programmed aging of budding yeast: a trade-off between programmed processes of cell proliferation, differentiation, stress response, survival and death defines yeast lifespan. Cell Cycle. 2014; 13:3336-3349.

44. Molon M, Zadrag-Tecza R, Bilinski T. The longevity in the yeast Saccharomyces cerevisiae: A comparison of two approaches for assessment the lifespan. Biochem Biophys Res Commun. 2015; 460:651-656.

45. Molon M, Panek A, Molestak E, Skoneczny M, Tchorzewski M, Wnuk M. Daughters of the budding yeast from old mothers have shorter replicative lifespans but not total lifespans. Are DNA damage and rDNA instability the factors that determine longevity? Cell Cycle. 2018; 17:1173-1187.

46. Neurohr GE, Terry RL, Sandikci A, Zou K, Li H, Amon A. Deregulation of the G1/S-phase transition is the proximal cause of mortality in old yeast mother cells. Genes Dev. 2018; 32:1075-1084.

47. Lee SS, Avalos Vizcarra I, Huberts DH, Lee LP, Heinemann M. Whole lifespan microscopic observation of budding yeast aging through a microfluidic dissection platform. Proc Natl Acad Sci

USA. 2012; 109:4916-4920.

48. Sutphin GL, Olsen BA, Kennedy BK, Kaeberlein M. Genome-wide analysis of yeast aging. Subcell Biochem. 2012; 57:251-289.

49. Xie Z, Zhang Y, Zou K, Brandman O, Luo C, Ouyang Q, Li H. Molecular phenotyping of aging in single yeast cells using a novel microfluidic device. Aging Cell. 2012; 11:599-606.

50. Zhang Y, Luo C, Zou K, Xie Z, Brandman O, Ouyang Q, Li H. Single cell analysis of yeast replicative aging using a new generation of microfluidic device. PloS One. 2012; 7: e48275.

51. Jo MC, Liu W, Gu L, Dang W, Qin L. High-throughput analysis of yeast replicative aging using a microfluidic system. Proc Natl Acad Sci U S A. 2015; 112:9364-9369.

52. Chen KL, Crane MM, Kaeberlein M. Microfluidic technologies for yeast replicative lifespan studies. Mech Ageing Dev. 2017; 161:262-269.

53. Durán DC, Hernández CA, Suesca E, Acevedo R, Acosta IM, Forero DA, Rozo FE, Pedraza JM. Slipstreaming Mother Machine: A Microfluidic Device for Single-Cell Dynamic Imaging of Yeast. Micromachines (Basel). 2020; 12: 4.

54. Longo VD, Kennedy BK. Sirtuins in aging and age-related disease. Cell. 2006; 126:257-68.

55. Kaeberlein M. Lessons on longevity from budding yeast. Nature. 2010; 464:513-519.

56. Denoth Lippuner A, Julou T, Barral Y. Budding yeast as a model organism to study the effects of age. FEMS Microbiol Rev. 2014; 38:300-325.

57. McCormick MA, Delaney JR, Tsuchiya M, Tsuchiyama S, Shemorry A, Sim S, Chou AC, Ahmed U, Carr D, Murakami CJ, Schleit J, Sutphin GL, Wasko BM, Bennett CF, Wang AM, Olsen B, Beyer RP, Bammler TK, Prunkard D, Johnson SC, Pennypacker JK, An E, Anies A,

Castanza AS, Choi E, Dang N, Enerio S, Fletcher M, Fox L, Goswami S, Higgins SA, Holmberg MA, Hu D, Hui J, Jelic M, Jeong KS, Johnston E, Kerr EO, Kim J, Kim D, Kirkland K, Klum S, Kotireddy S, Liao E, Lim M, Lin MS, Lo WC, Lockshon D, Miller HA, Moller RM, Muller B, Oakes J, Pak DN, Peng ZJ, Pham KM, Pollard TG, Pradeep P, Pruett D, Rai D, Robison B, Rodriguez AA, Ros B, Sage M, Singh MK, Smith ED, Snead K, Solanky A, Spector BL, Steffen KK, Tchao BN, Ting MK, Vander Wende H, Wang D, Welton KL, Westman EA, Brem RB, Liu XG, Suh Y, Zhou Z, Kaeberlein M, Kennedy BK. A comprehensive analysis of replicative lifespan in 4,698 single-gene deletion strains uncovers conserved mechanisms of aging. Cell Metab. 2015; 22:895-906.

58. Kaeberlein M, Burtner CR, Kennedy BK. Recent developments in yeast aging. PLoS Genet. 2007; 3: e84.

59. Goldberg AA, Bourque SD, Kyryakov P, Gregg C, Boukh-Viner T, Beach A, Burstein MT, Machkalyan G, Richard V, Rampersad S, Cyr D, Milijevic S, Titorenko VI. Effect of calorie restriction on the metabolic history of chronologically aging yeast. Exp Gerontol. 2009; 44:555-571.

60. Fraenkel, D.G. Yeast intermediary metabolism; Cold Spring Harbor Laboratory Press: Cold Spring Harbor, NY, USA, 2011; ISBN 978-0-87969-797-6.

61. Broach, J.R. Nutritional control of growth and development in yeast. Genetics 2012, 192, 73-105.

62. Allen C, Büttner S, Aragon AD, Thomas JA, Meirelles O, Jaetao JE, Benn D, Ruby SW, Veenhuis M, Madeo F, Werner-Washburne M. Isolation of quiescent and nonquiescent cells from yeast stationary-phase cultures. J Cell Biol. 2006; 174:89-100.

63. Werner-Washburne M, Roy S, Davidson GS. Aging and the survival of quiescent and non-quiescent cells in yeast stationary-phase cultures. Subcell Biochem. 2012; 57:123-143.

64. De Virgilio C. The essence of yeast quiescence. FEMS Microbiol Rev. 2012; 36:306-339.

65. Aragon AD, Rodriguez AL, Meirelles O, Roy S, Davidson GS, Tapia PH, Allen C, Joe R, Benn D, Werner-Washburne M. Characterization of differentiated quiescent and nonquiescent cells in yeast stationary-phase cultures. Mol Biol Cell. 2008; 19:1271-1280.

66. Davidson GS, Joe RM, Roy S, Meirelles O, Allen CP, Wilson MR, Tapia PH, Manzanilla EE, Dodson AE, Chakraborty S, Carter M, Young S, Edwards B, Sklar L, Werner-Washburne M. The proteomics of quiescent and nonquiescent cell differentiation in yeast stationary-phase cultures. Mol Biol Cell. 2011; 22:988-998.

67. Miles S, Li L, Davison J, Breeden LL. Xbp1 directs global repression of budding yeast transcription during the transition to quiescence and is important for the longevity and reversibility of the quiescent state. PLoS Genet. 2013; 9: e1003854.

68. Leonov A, Feldman R, Piano A, Arlia-Ciommo A, Lutchman V, Ahmadi M, Elsaser S, Fakim H, Heshmati-Moghaddam M, Hussain A, Orfali S, Rajen H, Roofigari-Esfahani N, Rosanelli L, Titorenko VI. Caloric restriction extends yeast chronological lifespan via a mechanism linking cellular aging to cell cycle regulation, maintenance of a quiescent state, entry into a non-quiescent state and survival in the non-quiescent state. Oncotarget. 2017; 8:69328-69350.

69. Sagot I, Laporte D. The cell biology of quiescent yeast - a diversity of individual scenarios. J Cell Sci. 2019; 132: jcs213025.

70. Mohammad K, Baratang Junio JA, Tafakori T, Orfanos E, Titorenko VI. Mechanisms that Link Chronological Aging to Cellular Quiescence in Budding Yeast. Int J Mol Sci. 2020; 21: 4717.

71. Masoro EJ. Caloric Restriction: A Key to Understanding and Modulating Aging. Amsterdam: Elsevier Science; 2002. 192 pp.

72. Fontana L, Partridge L, Longo VD. Extending healthy life span—from yeast to humans.

Science. 2010; 328:321–326.

73. de Cabo R, Carmona-Gutierrez D, Bernier M, Hall MN, Madeo F. The search for antiaging interventions: from elixirs to fasting regimens. Cell. 2014; 157:1515–1526.

74. Colman RJ, Anderson RM, Johnson SC, Kastman EK, Kosmatka KJ, Beasley TM, Allison DB, Cruzen C, Simmons HA, Kemnitz JW, Weindruch R. Caloric restriction delays disease onset and mortality in rhesus monkeys. Science. 2009; 325:201-204.

75. Colman RJ, Beasley TM, Kemnitz JW, Johnson SC, Weindruch R, Anderson RM. Caloric restriction reduces age-related and all-cause mortality in rhesus monkeys. Nat Commun. 2014; 5:3557.

76. Lee C, Longo V. Dietary restriction with and without caloric restriction for healthy aging. F1000Res. 2016; 5:F1000 Faculty Rev-117.

77. Mohammad K, Titorenko VI. Yeast chronological aging is linked to cell cycle regulation. Cell Cycle. 2018; 17:1035-1036.

78. François J, Parrou JL. Reserve carbohydrates metabolism in the yeast Saccharomyces cerevisiae. FEMS Microbiol Rev. 2001; 25:125-145.

79. Kyryakov P, Beach A, Richard VR, Burstein MT, Leonov A, Levy S, Titorenko VI. Caloric restriction extends yeast chronological lifespan by altering a pattern of age-related changes in trehalose concentration. Front Physiol. 2012; 3: 256.

80. Eleutherio E, Panek A, De Mesquita JF, Trevisol E, Magalhães R. Revisiting yeast trehalose metabolism. Curr Genet. 2015; 61:263-274.

81. Babazadeh R, Lahtvee PJ, Adiels CB, Goksör M, Nielsen JB, Hohmann S. The yeast osmostress response is carbon source dependent. Sci Rep. 2017; 7:990.

82. Kohlwein SD, Veenhuis M, van der Klei IJ. Lipid droplets and peroxisomes: key players in cellular lipid homeostasis or a matter of fat--store 'em up or burn 'em down. Genetics. 2013; 193:1-50.

83. Mitrofanova D, Dakik P, McAuley M, Medkour Y, Mohammad K, Titorenko VI. Lipid metabolism and transport define longevity of the yeast Saccharomyces cerevisiae. Front Biosci (Landmark Ed). 2018; 23:1166-1194.

84. Horvath SE, Daum G. Lipids of mitochondria. Prog Lipid Res. 2013; 52:590-614.

85. Mårtensson CU, Doan KN, Becker T. Effects of lipids on mitochondrial functions. Biochim Biophys Acta Mol Cell Biol Lipids. 2017; 1862:102-113.

86. Schlame M, Greenberg ML. Biosynthesis, remodeling and turnover of mitochondrial cardiolipin. Biochim Biophys Acta Mol Cell Biol Lipids. 2017; 1862:3-7.

87. Bonawitz ND, Chatenay-Lapointe M, Pan Y, Shadel GS. Reduced TOR signaling extends chronological life span via increased respiration and upregulation of mitochondrial gene expression. Cell Metab. 2007; 5:265-277.

88. Pan Y, Shadel GS. Extension of chronological life span by reduced TOR signaling requires down-regulation of Sch9p and involves increased mitochondrial OXPHOS complex density. Aging (Albany NY). 2009; 1:131-145.

89. Ocampo A, Liu J, Schroeder EA, Shadel GS, Barrientos A. Mitochondrial respiratory thresholds regulate yeast chronological life span and its extension by caloric restriction. Cell Metab. 2012; 16:55-67.

90. Beach A, Leonov A, Arlia-Ciommo A, Svistkova V, Lutchman V, Titorenko VI. Mechanisms by which different functional states of mitochondria define yeast longevity. Int J Mol Sci. 2015;

16:5528-5554.

91. Giorgio M, Trinei M, Migliaccio E, Pelicci PG. Hydrogen peroxide: a metabolic by-product or a common mediator of ageing signals? Nat Rev Mol Cell Biol. 2007; 8:722-728.

92. Pan Y, Schroeder EA, Ocampo A, Barrientos A, Shadel GS. Regulation of yeast chronological life span by TORC1 via adaptive mitochondrial ROS signaling. Cell Metab. 2011; 13:668-678.

93. Shadel GS. Live longer on MARS: a yeast paradigm of mitochondrial adaptive ROS signaling in aging. Microb Cell. 2014; 1:140-144.

94. Guaragnella N, Coyne LP, Chen XJ, Giannattasio S. Mitochondria-cytosol-nucleus crosstalk: learning from Saccharomyces cerevisiae. FEMS Yeast Res. 2018; 18: foy088.

95. Dakik P, Medkour Y, Mohammad K, Titorenko VI. Mechanisms Through Which Some Mitochondria-Generated Metabolites Act as Second Messengers That Are Essential Contributors to the Aging Process in Eukaryotes Across Phyla. Front Physiol. 2019;10: 461.

96. Ruetenik A, Barrientos A. Exploiting Post-mitotic Yeast Cultures to Model Neurodegeneration. Front Mol Neurosci. 2018; 11: 400.

97. Gladyshev VN. The origin of aging: imperfectness-driven non-random damage defines the aging process and control of lifespan. Trends Genet. 2013; 29:506-512.

98. Ogrodnik M, Salmonowicz H, Gladyshev VN. Integrating cellular senescence with the concept of damage accumulation in aging: Relevance for clearance of senescent cells. Aging Cell. 2019; 18: e12841.

99. Calabrese V, Cornelius C, Cuzzocrea S, Iavicoli I, Rizzarelli E, Calabrese EJ. Hormesis, cellular stress response and vitagenes as critical determinants in aging and longevity. Mol Aspects Med. 2011; 32:279-304.

100. Calabrese V, Cornelius C, Dinkova-Kostova AT, Iavicoli I, Di Paola R, Koverech A, Cuzzocrea S, Rizzarelli E, Calabrese EJ. Cellular stress responses, hormetic phytochemicals and vitagenes in aging and longevity. Biochim Biophys Acta. 2012; 1822:753-783.

101. Gladyshev VN. The free radical theory of aging is dead. Long live the damage theory! Antioxid Redox Signal. 2014; 20:727-731.

102. Herker E, Jungwirth H, Lehmann KA, Maldener C, Fröhlich KU, Wissing S, Büttner S, Fehr M, Sigrist S, Madeo F. Chronological aging leads to apoptosis in yeast. J Cell Biol. 2004; 164:501-507.

103. Fabrizio P, Longo VD. Chronological aging-induced apoptosis in yeast. Biochim Biophys Acta. 2008; 1783:1280-1285.

104. Eisenberg T, Carmona-Gutierrez D, Büttner S, Tavernarakis N, Madeo F. Necrosis in yeast. Apoptosis. 2010; 15:257-268.

105. Laun P, Büttner S, Rinnerthaler M, Burhans WC, Breitenbach M. Yeast aging and apoptosis. Subcell Biochem. 2012; 57:207-232.

106. Richard VR, Beach A, Piano A, Leonov A, Feldman R, Burstein MT, Kyryakov P, Gomez-Perez A, Arlia-Ciommo A, Baptista S, Campbell C, Goncharov D, Pannu S, Patrinos D, Sadri B, Svistkova V, Victor A, Titorenko VI. Mechanism of liponecrosis, a distinct mode of programmed cell death. Cell Cycle. 2014; 13:3707-3726.

107. Sheibani S, Richard VR, Beach A, Leonov A, Feldman R, Mattie S, Khelghatybana L, Piano A, Greenwood M, Vali H, Titorenko VI. Macromitophagy, neutral lipids synthesis, and peroxisomal fatty acid oxidation protect yeast from "liponecrosis", a previously unknown form of programmed cell death. Cell Cycle. 2014; 13:138-147.

108. Falcone C, Mazzoni C. External and internal triggers of cell death in yeast. Cell Mol Life Sci. 2016; 73:2237-2250.

109. Higdon J, Drake VJ. An Evidence-Based Approach to Phytochemicals and Other Dietary Factors. 2nd ed. Thieme: New York, NY, USA, 2012. 328 pp.

110. Harborne JR. Introduction to Ecological Biochemistry. 4th ed. Academic Press; 2014. 384 pp.

111. Wink M. Evolution of secondary metabolites from an ecological and molecular phylogenetic perspective. Phytochemistry. 2003; 64:3-19.

112. Brencic A, Winans SC. Detection of and response to signals involved in host-microbe interactions by plant-associated bacteria. Microbiol Mol Biol Rev. 2005; 69:155-194.

113. Hansen BG, Halkier BA. New insight into the biosynthesis and regulation of indole compounds in Arabidopsis thaliana. Planta. 2005; 221:603-606.

114. Tahara S. A journey of twenty-five years through the ecological biochemistry of flavonoids. Biosci Biotechnol Biochem. 2007; 71:1387-1404.

115. Bednarek P. Sulfur-containing secondary metabolites from Arabidopsis thaliana and other Brassicaceae with function in plant immunity. Chembiochem. 2012; 13:1846-5189.

116. Nwachukwu ID, Slusarenko AJ, Gruhlke MC. Sulfur and sulfur compounds in plant defence. Nat Prod Commun. 2012; 7:395-400.

117. Huot OB, Nachappa P, Tamborindeguy C. The evolutionary strategies of plant defenses have a dynamic impact on the adaptations and interactions of vectors and pathogens. Insect Sci. 2013; 20:297-306.

118. Kazan K, Lyons R. Intervention of Phytohormone Pathways by Pathogen Effectors. Plant

Cell. 2014; 26:2285-2309

119. Burow M, Halkier BA. How does a plant orchestrate defense in time and space? Using glucosinolates in Arabidopsis as case study. Curr Opin Plant Biol. 2017; 38:142-147.

120. Künstler A, Gullner G, Ádám AL, Kolozsváriné Nagy J, Király L. The Versatile Roles of Sulfur-Containing Biomolecules in Plant Defense-A Road to Disease Resistance. Plants (Basel). 2020; 9:1705.

121. Mitrovic P, Djalovic I, Kiprovski B, Veljović Jovanović S, Trkulja V, Jelušić A, Popovic T. Oxidative Stress and Antioxidative Activity in Leaves and Roots of Carrot Plants Induced by Candidatus Phytoplasma Solani. Plants (Basel). 2021; 10:337.

122. Chassagne F, Samarakoon T, Porras G, Lyles JT, Dettweiler M, Marquez L, Salam AM, Shabih S, Farrokhi DR, Quave CL. A Systematic Review of Plants With Antibacterial Activities: A Taxonomic and Phylogenetic Perspective. Front Pharmacol. 2021; 11:586548.

123. Šamec D, Karalija E, Šola I, Vujčić Bok V, Salopek-Sondi B. The Role of Polyphenols in Abiotic Stress Response: The Influence of Molecular Structure. Plants (Basel). 2021; 10:118.

124. Erlund I. Review of the flavonoids quercetin, hesperetin, and naringenin. Dietary sources, bioactivities, bioavailability, and epidemiology. Nutr. Res. 2004; 24:851-874.

125. Belinha I, Amorim MA, Rodrigues P, de Freitas V, Moradas-Ferreira P, Mateus N, Costa V. Quercetin increases oxidative stress resistance and longevity in Saccharomyces cerevisiae. J Agric Food Chem. 2007; 55:2446-2451.

126. Evert RF, Eichhorn SE. Raven biology of plants, 8th ed. W.H. Freeman/Palgrave Macmillan; 2013. 900 pp.

127. Wanke V, Cameroni E, Uotila A, Piccolis M, Urban J, Loewith R, De Virgilio C. Caffeine

extends yeast lifespan by targeting TORC1. Mol Microbiol. 2008; 69:277-285.

128. Deprez MA, Eskes E, Winderickx J, Wilms T. The TORC1-Sch9 pathway as a crucial mediator of chronological lifespan in the yeast Saccharomyces cerevisiae. FEMS Yeast Res. 2018; 18: foy048.

129. Jiang Z, Gao W, Huang L. Tanshinones, Critical Pharmacological Components in Salvia miltiorrhiza. Front Pharmacol. 2019; 10: 202.

130. Wu Z, Song L, Liu SQ, Huang D. Tanshinones extend chronological lifespan in budding yeast Saccharomyces cerevisiae. Appl Microbiol Biotechnol. 2014; 98:8617-8628.

131. Staschke KA, Dey S, Zaborske JM, Palam LR, McClintick JN, Pan T, Edenberg HJ, Wek RC. Integration of general amino acid control and target of rapamycin (TOR) regulatory pathways in nitrogen assimilation in yeast. J Biol Chem. 2010; 285:16893-16911.

132. Hou Y, He W, Hu S, Wu G. Composition of polyamines and amino acids in plant-source foods for human consumption. Amino Acids. 2019; 51:1153-1165.

133. Sagara T, Bhandari DR, Spengler B, Vollmann J. Spermidine and other functional phytochemicals in soybean seeds: Spatial distribution as visualized by mass spectrometry imaging. Food Sci Nutr. 2019; 8:675-682.

134. Eisenberg T, Knauer H, Schauer A, Büttner S, Ruckenstuhl C, Carmona-Gutierrez D, Ring J, Schroeder S, Magnes C, Antonacci L, Fussi H, Deszcz L, Hartl R, Schraml E, Criollo A, Megalou E, Weiskopf D, Laun P, Heeren G, Breitenbach M, Grubeck-Loebenstein B, Herker E, Fahrenkrog B, Fröhlich KU, Sinner F, Tavernarakis N, Minois N, Kroemer G, Madeo F. Induction of autophagy by spermidine promotes longevity. Nat Cell Biol. 2009; 11:1305-1314.

135. Carmona-Gutierrez D, Zimmermann A, Kainz K, Pietrocola F, Chen G, Maglioni S, Schiavi A, Nah J, Mertel S, Beuschel CB, Castoldi F, Sica V, Trausinger G, Raml R, Sommer C, Schroeder

S, Hofer SJ, Bauer MA, Pendl T, Tadic J, Dammbrueck C, Hu Z, Ruckenstuhl C, Eisenberg T, Durand S, Bossut N, Aprahamian F, Abdellatif M, Sedej S, Enot DP, Wolinski H, Dengjel J, Kepp O, Magnes C, Sinner F, Pieber TR, Sadoshima J, Ventura N, Sigrist SJ, Kroemer G, Madeo F. The flavonoid 4,4'-dimethoxychalcone promotes autophagy-dependent longevity across species. Nat Commun. 2019; 10: 651.

136. Courchesne WE, Magasanik B. Regulation of nitrogen assimilation in Saccharomyces cerevisiae: roles of the URE2 and GLN3 genes. J Bacteriol. 1988; 170:708-713.

137. Lutchman V, Dakik P, McAuley M, Cortes B, Ferraye G, Gontmacher L, Graziano D, Moukhariq FZ, Simard É, Titorenko VI. Six plant extracts delay yeast chronological aging through different signaling pathways. Oncotarget. 2016; 7:50845-50863.

138. Dakik P, Rodriguez MEL, Junio JAB, Mitrofanova D, Medkour Y, Tafakori T, Taifour T, Lutchman V, Samson E, Arlia-Ciommo A, Rukundo B, Simard É, Titorenko VI. Discovery of fifteen new geroprotective plant extracts and identification of cellular processes they affect to prolong the chronological lifespan of budding yeast. Oncotarget. 2020; 11:2182-2203.

139. Goldberg AA, Richard VR, Kyryakov P, Bourque SD, Beach A, Burstein MT, Glebov A, Koupaki O, Boukh-Viner T, Gregg C, Juneau M, English AM, Thomas DY, Titorenko VI. Chemical genetic screen identifies lithocholic acid as an anti-aging compound that extends yeast chronological life span in a TOR-independent manner, by modulating housekeeping longevity assurance processes. Aging (Albany NY). 2010; 2:393-414.

140. Thomas C, Pellicciari R, Pruzanski M, Auwerx J, Schoonjans K. Targeting bile-acid signalling for metabolic diseases. Nat Rev Drug Discov. 2008; 7: 678-693.

141. Lefebvre P, Cariou B, Lien F, Kuipers F, Staels B. Role of bile acids and bile acid receptors in metabolic regulation. Physiol Rev. 2009; 89: 147-191.

142. Beach A, Richard VR, Leonov A, Burstein MT, Bourque SD, Koupaki O, Juneau M, Feldman

R, Iouk T, Titorenko VI. Mitochondrial membrane lipidome defines yeast longevity. Aging (Albany NY). 2013; 5:551-574.

143. Tatsuta T, Langer T. Intramitochondrial phospholipid trafficking. Biochim Biophys Acta Mol Cell Biol Lipids. 2017; 1862:81-89.

144. Tamura Y, Kawano S, Endo T. Lipid homeostasis in mitochondria. Biol Chem. 2020; 401:821-833.

145. Arlia-Ciommo A, Piano A, Svistkova V, Mohtashami S, Titorenko VI. Mechanisms underlying the anti-aging and anti-tumor effects of lithocholic bile acid. Int J Mol Sci. 2014; 15:16522-16543.

146. Burstein MT, Titorenko VI. A mitochondrially targeted compound delays aging in yeast through a mechanism linking mitochondrial membrane lipid metabolism to mitochondrial redox biology. Redox Biol. 2014; 2:305-307.

147. Leonov A, Arlia-Ciommo A, Bourque SD, Koupaki O, Kyryakov P, Dakik P, McAuley M, Medkour Y, Mohammad K, Di Maulo T, Titorenko VI. Specific changes in mitochondrial lipidome alter mitochondrial proteome and increase the geroprotective efficiency of lithocholic acid in chronologically aging yeast. Oncotarget. 2017; 8:30672-30691.

148. Medkour Y, Dakik P, McAuley M, Mohammad K, Mitrofanova D, Titorenko VI. Mechanisms Underlying the Essential Role of Mitochondrial Membrane Lipids in Yeast Chronological Aging. Oxid Med Cell Longev. 2017; 2017: 2916985.

149. Vögtle FN, Keller M, Taskin AA, Horvath SE, Guan XL, Prinz C, Opalińska M, Zorzin C, van der Laan M, Wenk MR, Schubert R, Wiedemann N, Holzer M, Meisinger C. The fusogenic lipid phosphatidic acid promotes the biogenesis of mitochondrial outer membrane protein Ugo1. J Cell Biol. 2015; 210:951-960.

150. McMahon HT, Boucrot E. Membrane curvature at a glance. J Cell Sci. 2015; 128:1065-1070.

151. Jarsch IK, Daste F, Gallop JL. Membrane curvature in cell biology: An integration of molecular mechanisms. J Cell Biol. 2016; 214:375-387.

152. Mårtensson CU, Doan KN, Becker T. Effects of lipids on mitochondrial functions. Biochim Biophys Acta Mol Cell Biol Lipids. 2017; 1862:102-113.

153. Beach A, Richard VR, Bourque S, Boukh-Viner T, Kyryakov P, Gomez-Perez A, Arlia-Ciommo A, Feldman R, Leonov A, Piano A, Svistkova V, Titorenko VI. Lithocholic bile acid accumulated in yeast mitochondria orchestrates a development of an anti-aging cellular pattern by causing age-related changes in cellular proteome. Cell Cycle. 2015; 14:1643-1656.

154 Arlia-Ciommo A, Leonov A, Mohammad K, Beach A, Richard VR, Bourque SD, Burstein MT, Goldberg AA, Kyryakov P, Gomez-Perez A, Koupaki O, Titorenko VI. Mechanisms through which lithocholic acid delays yeast chronological aging under caloric restriction conditions. Oncotarget. 2018; 9:34945-34971.

155. Dickson RC. Roles for sphingolipids in Saccharomyces cerevisiae. Adv Exp Med Biol. 2010;688:217-31.

156. Henry SA, Kohlwein SD, Carman GM. Metabolism and regulation of glycerolipids in the yeast Saccharomyces cerevisiae. Genetics. 2012; 190:317-349.

157. Kohlwein SD, Veenhuis M, van der Klei IJ. Lipid droplets and peroxisomes: key players in cellular lipid homeostasis or a matter of fat--store 'em up or burn 'em down. Genetics. 2013; 193:1-50.

158. Klug L, Daum G. Yeast lipid metabolism at a glance. FEMS Yeast Res. 2014; 14:369-388.

159. Mitrofanova D, Dakik P, McAuley M, Medkour Y, Mohammad K, Titorenko VI. Lipid

metabolism and transport define longevity of the yeast Saccharomyces cerevisiae. Front Biosci (Landmark Ed). 2018; 23:1166-1194.

160. Fernández-Murray JP, McMaster CR. Lipid synthesis and membrane contact sites: a crossroads for cellular physiology. J Lipid Res. 2016; 57:1789-1805.

161. Tatsuta T, Langer T. Intramitochondrial phospholipid trafficking. Biochim Biophys Acta Mol Cell Biol Lipids. 2017; 1862:81-89.

162. Csordás G, Weaver D, Hajnóczky G. Endoplasmic Reticulum-Mitochondrial Contactology: Structure and Signaling Functions. Trends Cell Biol. 2018; 28:523-540.

163. Tamura Y, Kawano S, Endo T. Organelle contact zones as sites for lipid transfer. J Biochem. 2019; 165:115-123.

164. Hasslacher M, Ivessa AS, Paltauf F, Kohlwein SD. Acetyl-CoA carboxylase from yeast is an essential enzyme and is regulated by factors that control phospholipid metabolism. J Biol Chem. 1993; 268:10946-10952.

165. Leibundgut M, Maier T, Jenni S, Ban N. The multienzyme architecture of eukaryotic fatty acid synthases. Curr Opin Struct Biol. 2008; 18:714-725.

166. Athenstaedt K, Daum G. Biosynthesis of phosphatidic acid in lipid particles and endoplasmic reticulum of Saccharomyces cerevisiae. J Bacteriol. 1997; 179:7611-7616.

167. Zheng Z, Zou J. The initial step of the glycerolipid pathway: identification of glycerol 3-phosphate/dihydroxyacetone phosphate dual substrate acyltransferases in Saccharomyces cerevisiae. J Biol Chem. 2001; 276:41710-41716.

168. Athenstaedt K, Daum G. 1-Acyldihydroxyacetone-phosphate reductase (Ayr1p) of the yeast Saccharomyces cerevisiae encoded by the open reading frame YIL124w is a major component of

lipid particles. J Biol Chem. 2000; 275:235-240.

169. Benghezal M, Roubaty C, Veepuri V, Knudsen J, Conzelmann A. SLC1 and SLC4 encode partially redundant acyl-coenzyme A 1-acylglycerol-3-phosphate O-acyltransferases of budding yeast. J Biol Chem. 2007; 282:30845-30855.

170. Chen Q, Kazachkov M, Zheng Z, Zou J. The yeast acylglycerol acyltransferase LCA1 is a key component of Lands cycle for phosphatidylcholine turnover. FEBS Lett. 2007; 581:5511-5516.

171. Ayciriex S, Le Guédard M, Camougrand N, Velours G, Schoene M, Leone S, Wattelet-Boyer V, Dupuy JW, Shevchenko A, Schmitter JM, Lessire R, Bessoule JJ, Testet E. YPR139c/LOA1 encodes a novel lysophosphatidic acid acyltransferase associated with lipid droplets and involved in TAG homeostasis. Mol Biol Cell. 2012; 23:233-246.

172. Shen H, Heacock PN, Clancey CJ, Dowhan W. The CDS1 gene encoding CDP-diacylglycerol synthase in Saccharomyces cerevisiae is essential for cell growth. J Biol Chem. 1996; 271:789-795.

173. Oelkers P, Cromley D, Padamsee M, Billheimer JT, Sturley SL. The DGA1 gene determines a second triglyceride synthetic pathway in yeast. J Biol Chem. 2002; 277:8877-8881.

174. Sorger D, Daum G. Synthesis of triacylglycerols by the acyl-coenzyme A:diacyl-glycerol acyltransferase Dga1p in lipid particles of the yeast Saccharomyces cerevisiae. J Bacteriol. 2002; 184:519-524.

175. Oelkers P, Tinkelenberg A, Erdeniz N, Cromley D, Billheimer JT, Sturley SL. A lecithin cholesterol acyltransferase-like gene mediates diacylglycerol esterification in yeast. J Biol Chem. 2000; 275:15609-15612.

176. Athenstaedt K, Daum G. YMR313c/TGL3 encodes a novel triacylglycerol lipase located in

lipid particles of Saccharomyces cerevisiae. J Biol Chem. 2003; 278:23317-23323.

177. Athenstaedt K, Daum G. Tgl4p and Tgl5p, two triacylglycerol lipases of the yeast Saccharomyces cerevisiae are localized to lipid particles. J Biol Chem. 2005; 280:37301-37309.

178. Jandrositz A, Petschnigg J, Zimmermann R, Natter K, Scholze H, Hermetter A, Kohlwein SD, Leber R. The lipid droplet enzyme Tgl1p hydrolyzes both steryl esters and triglycerides in the yeast, Saccharomyces cerevisiae. Biochim Biophys Acta. 2005; 1735:50-58.

179. Kurat CF, Natter K, Petschnigg J, Wolinski H, Scheuringer K, Scholz H, Zimmermann R, Leber R, Zechner R, Kohlwein SD. Obese yeast: triglyceride lipolysis is functionally conserved from mammals to yeast. J Biol Chem. 2006; 281:491-500.

180. Ploier B, Scharwey M, Koch B, Schmidt C, Schatte J, Rechberger G, Kollroser M, Hermetter A, Daum G. Screening for hydrolytic enzymes reveals Ayr1p as a novel triacylglycerol lipase in Saccharomyces cerevisiae. J Biol Chem. 2013; 288:36061-36072.

181. Heier C, Taschler U, Rengachari S, Oberer M, Wolinski H, Natter K, Kohlwein SD, Leber R, Zimmermann R. Identification of Yju3p as functional orthologue of mammalian monoglyceride lipase in the yeast Saccharomyces cerevisiae. Biochim Biophys Acta. 2010; 1801:1063-1071.

182. Huh WK, Falvo JV, Gerke LC, Carroll AS, Howson RW, Weissman JS, O'Shea EK. Global analysis of protein localization in budding yeast. Nature. 2003; 425:686-691.

183. Natter K, Leitner P, Faschinger A, Wolinski H, McCraith S, Fields S, Kohlwein SD. The spatial organization of lipid synthesis in the yeast Saccharomyces cerevisiae derived from large scale green fluorescent protein tagging and high resolution microscopy. Mol Cell Proteomics. 2005; 4:662-672.

184. Binns D, Januszewski T, Chen Y, Hill J, Markin VS, Zhao Y, Gilpin C, Chapman KD, Anderson RG, Goodman JM. An intimate collaboration between peroxisomes and lipid bodies. J

Cell Biol. 2006; 173:719-731.

185. Goldberg AA, Bourque SD, Kyryakov P, Boukh-Viner T, Gregg C, Beach A, Burstein MT, Machkalyan G, Richard V, Rampersad S, Titorenko VI. A novel function of lipid droplets in regulating longevity. Biochem Soc Trans. 2009; 37:1050-1055.

186. Titorenko VI, Terlecky SR. Peroxisome metabolism and cellular aging. Traffic. 2011; 12:252-259.

187. Gao Q, Goodman JM. The lipid droplet-a well-connected organelle. Front Cell Dev Biol. 2015; 3: 49.

188. Dakik P, Titorenko VI. Communications between Mitochondria, the Nucleus, Vacuoles, Peroxisomes, the Endoplasmic Reticulum, the Plasma Membrane, Lipid Droplets, and the Cytosol during Yeast Chronological Aging. Front Genet. 2016; 7: 177.

189. Hanada K. Serine palmitoyltransferase, a key enzyme of sphingolipid metabolism. Biochim Biophys Acta. 2003; 1632:16-30.

190. Dickson RC. Thematic review series: sphingolipids. New insights into sphingolipid metabolism and function in budding yeast. J Lipid Res. 2008; 49:909-921.

191. Dickson RC. Roles for sphingolipids in Saccharomyces cerevisiae. Adv Exp Med Biol. 2010; 688:217-231.

192. Breslow DK, Collins SR, Bodenmiller B, Aebersold R, Simons K, Shevchenko A, Ejsing CS, Weissman JS. Orm family proteins mediate sphingolipid homeostasis. Nature. 2010; 463:1048-1053.

193. Han S, Lone MA, Schneiter R, Chang A. Orm1 and Orm2 are conserved endoplasmic reticulum membrane proteins regulating lipid homeostasis and protein quality control. Proc Natl

Acad Sci USA. 2010; 107:5851-5856.

194. Beeler T, Bacikova D, Gable K, Hopkins L, Johnson C, Slife H, Dunn T. The Saccharomyces cerevisiae TSC10/YBR265w gene encoding 3-ketosphinganine reductase is identified in a screen for temperature-sensitive suppressors of the Ca2+-sensitive csg2Delta mutant. J Biol Chem. 1998; 273:30688-30694.

195. Grilley MM, Stock SD, Dickson RC, Lester RL, Takemoto JY. Syringomycin action gene SYR2 is essential for sphingolipid 4-hydroxylation in Saccharomyces cerevisiae. J Biol Chem. 1998; 273:11062-11068.

196. D'mello NP, Childress AM, Franklin DS, Kale SP, Pinswasdi C, Jazwinski SM. Cloning and characterization of LAG1, a longevity-assurance gene in yeast. J Biol Chem. 1994; 269:15451-15459.

197. Haak D, Gable K, Beeler T, Dunn T. Hydroxylation of Saccharomyces cerevisiae ceramides requires Sur2p and Scs7p. J Biol Chem. 1997; 272:29704-29710.

198. Guillas I, Kirchman PA, Chuard R, Pfefferli M, Jiang JC, Jazwinski SM, Conzelmann A. C26-CoA-dependent ceramide synthesis of Saccharomyces cerevisiae is operated by Lag1p and Lac1p. EMBO J. 2001; 20:2655-2665.

199. Schorling S, Vallée B, Barz WP, Riezman H, Oesterhelt D. Lag1p and Lac1p are essential for the Acyl-CoA-dependent ceramide synthase reaction in Saccharomyces cerevisiae. Mol Biol Cell. 2001; 12:3417-3427.

200. Vallée B, Riezman H. Lip1p: a novel subunit of acyl-CoA ceramide synthase. EMBO J. 2005; 24:730-741.

201. Funato K, Riezman H. Vesicular and nonvesicular transport of ceramide from ER to the Golgi apparatus in yeast. J Cell Biol. 2001; 155:949-959.

202. Kajiwara K, Ikeda A, Aguilera-Romero A, Castillon GA, Kagiwada S, Hanada K, Riezman H, Muñiz M, Funato K. Osh proteins regulate COPII-mediated vesicular transport of ceramide from the endoplasmic reticulum in budding yeast. J Cell Sci. 2014; 127:376-387.

203. Liu LK, Choudhary V, Toulmay A, Prinz WA. An inducible ER-Golgi tether facilitates ceramide transport to alleviate lipotoxicity. J Cell Biol. 2017; 216:131-147.

204. Dickson RC, Lester RL. Sphingolipid functions in Saccharomyces cerevisiae. Biochim Biophys Acta. 2002; 1583:13-25.

205. Dickson RC, Sumanasekera C, Lester RL. Functions and metabolism of sphingolipids in Saccharomyces cerevisiae. Prog Lipid Res. 2006; 45:447-465.

206. Cowart LA, Obeid LM. Yeast sphingolipids: recent developments in understanding biosynthesis, regulation, and function. Biochim Biophys Acta. 2007; 1771:421-431.

207. van Meer G, Voelker DR, Feigenson GW. Membrane lipids: where they are and how they behave. Nat Rev Mol Cell Biol. 2008; 9:112-124.

208. Teixeira V, Costa V. Unraveling the role of the Target of Rapamycin signaling in sphingolipid metabolism. Prog Lipid Res. 2016; 61:109-133.

209. Sawai H, Okamoto Y, Luberto C, Mao C, Bielawska A, Domae N, Hannun YA. Identification of ISC1 (YER019w) as inositol phosphosphingolipid phospholipase C in Saccharomyces cerevisiae. J Biol Chem. 2000; 275:39793-39798.

210. Vaena de Avalos S, Okamoto Y, Hannun YA. Activation and localization of inositol phosphosphingolipid phospholipase C, Isc1p, to the mitochondria during growth of Saccharomyces cerevisiae. J Biol Chem. 2004; 279:11537-11545.

211. Kitagaki H, Cowart LA, Matmati N, Montefusco D, Gandy J, de Avalos SV, Novgorodov SA, Zheng J, Obeid LM, Hannun YA. ISC1-dependent metabolic adaptation reveals an indispensable role for mitochondria in induction of nuclear genes during the diauxic shift in Saccharomyces cerevisiae. J Biol Chem. 2009; 284:10818-10830.

212. Handee W, Li X, Hall KW, Deng X, Li P, Benning C, Williams BL, Kuo MH. An Energy-Independent Pro-longevity Function of Triacylglycerol in Yeast. PLoS Genet. 2016; 12: e1005878.

213. Li X, Handee W, Kuo MH. The slim, the fat, and the obese: guess who lives the longest? Curr Genet. 2017; 63:43-49.

214. Beach A, Titorenko VI. In search of housekeeping pathways that regulate longevity. Cell Cycle. 2011; 10:3042-3044.

215. Beach A, Titorenko VI. Essential roles of peroxisomally produced and metabolized biomolecules in regulating yeast longevity. Subcell Biochem. 2013; 69:153-167.

216. Hiltunen JK, Mursula AM, Rottensteiner H, Wierenga RK, Kastaniotis AJ, Gurvitz A. The biochemistry of peroxisomal beta-oxidation in the yeast Saccharomyces cerevisiae. FEMS Microbiol Rev. 2003; 27:35-64.

217. van der Klei IJ, Yurimoto H, Sakai Y, Veenhuis M. The significance of peroxisomes in methanol metabolism in methylotrophic yeast. Biochim Biophys Acta. 2006; 1763:1453-1462.

218. Aerts AM, François IE, Bammens L, Cammue BP, Smets B, Winderickx J, Accardo S, De Vos DE, Thevissen K. Level of M(IP)2C sphingolipid affects plant defensin sensitivity, oxidative stress resistance and chronological life-span in yeast. FEBS Lett. 2006; 580:1903-1907.

219. Powers RW 3rd, Kaeberlein M, Caldwell SD, Kennedy BK, Fields S. Extension of chronological life span in yeast by decreased TOR pathway signaling. Genes Dev. 2006; 20:174-184.

220. Dickson RC, Nagiec EE, Wells GB, Nagiec MM, Lester RL. Synthesis of mannose-(inositol-P)2-ceramide, the major sphingolipid in Saccharomyces cerevisiae, requires the IPT1 (YDR072c) gene. J Biol Chem. 1997; 272:29620-29625.

221. Thevissen K, Idkowiak-Baldys J, Im YJ, Takemoto J, François IE, Ferket KK, Aerts AM, Meert EM, Winderickx J, Roosen J, Cammue BP. SKN1, a novel plant defensin-sensitivity gene in Saccharomyces cerevisiae, is implicated in sphingolipid biosynthesis. FEBS Lett. 2005; 579:1973-1977.

222. Huang X, Liu J, Dickson RC. Down-regulating sphingolipid synthesis increases yeast lifespan. PLoS Genet. 2012; 8: e1002493.

223. Liu K, Zhang X, Lester RL, Dickson RC. The sphingoid long chain base phytosphingosine activates AGC-type protein kinases in Saccharomyces cerevisiae including Ypk1, Ypk2, and Sch9. J Biol Chem. 2005; 280:22679-22687.

224. Fröhlich F, Moreira K, Aguilar PS, Hubner NC, Mann M, Walter P, Walther TC. A genome-wide screen for genes affecting eisosomes reveals Nce102 function in sphingolipid signaling. J Cell Biol. 2009; 185:1227-1242.

225. Roelants FM, Baltz AG, Trott AE, Fereres S, Thorner J. A protein kinase network regulates the function of aminophospholipid flippases. Proc Natl Acad Sci USA. 2010; 107:34-39.

226. Lavoie H, Whiteway M. Increased respiration in the sch9Delta mutant is required for increasing chronological life span but not replicative life span. Eukaryot Cell. 2008; 7:1127-1135.

227. Pan Y, Shadel GS. Extension of chronological life span by reduced TOR signaling requires down-regulation of Sch9p and involves increased mitochondrial OXPHOS complex density. Aging (Albany NY). 2009; 1:131-145.

228. Fabrizio P, Battistella L, Vardavas R, Gattazzo C, Liou LL, Diaspro A, Dossen JW, Gralla EB, Longo VD. Superoxide is a mediator of an altruistic aging program in Saccharomyces cerevisiae. J Cell Biol. 2004; 166:1055-1067.

229. Fabrizio P, Gattazzo C, Battistella L, Wei M, Cheng C, McGrew K, Longo VD. Sir2 blocks extreme life-span extension. Cell. 2005; 123:655-667.

230. Lutchman V, Medkour Y, Samson E, Arlia-Ciommo A, Dakik P, Cortes B, Feldman R, Mohtashami S, McAuley M, Chancharoen M, Rukundo B, Simard É, Titorenko VI. Discovery of plant extracts that greatly delay yeast chronological aging and have different effects on longevity-defining cellular processes. Oncotarget. 2016; 7:16542-16566.

231. Burhans WC, Weinberger M. Acetic acid effects on aging in budding yeast: are they relevant to aging in higher eukaryotes? Cell Cycle. 2009; 8:2300-2302.

232. Giannattasio S, Guaragnella N, Zdralević M, Marra E. Molecular mechanisms of Saccharomyces cerevisiae stress adaptation and programmed cell death in response to acetic acid. Front Microbiol. 2013; 4: 33.

233. Eisenberg T, Schroeder S, Andryushkova A, Pendl T, Küttner V, Bhukel A, Mariño G, Pietrocola F, Harger A, Zimmermann A, Moustafa T, Sprenger A, Jany E, Büttner S, Carmona-Gutierrez D, Ruckenstuhl C, Ring J, Reichelt W, Schimmel K, Leeb T, Moser C, Schatz S, Kamolz LP, Magnes C, Sinner F, Sedej S, Fröhlich KU, Juhasz G, Pieber TR, Dengjel J, Sigrist SJ, Kroemer G, Madeo F. Nucleocytosolic depletion of the energy metabolite acetyl-coenzyme a stimulates autophagy and prolongs lifespan. Cell Metab. 2014; 19:431-444.

234. Mariño G, Pietrocola F, Eisenberg T, Kong Y, Malik SA, Andryushkova A, Schroeder S, Pendl T, Harger A, Niso-Santano M, Zamzami N, Scoazec M, Durand S, Enot DP, Fernández ÁF, Martins I, Kepp O, Senovilla L, Bauvy C, Morselli E, Vacchelli E, Bennetzen M, Magnes C, Sinner F, Pieber T, López-Otín C, Maiuri MC, Codogno P, Andersen JS, Hill JA, Madeo F, Kroemer G. Regulation of autophagy by cytosolic acetyl-coenzyme A. Mol Cell. 2014; 53:710-725.

235. Schroeder S, Zimmermann A, Carmona-Gutierrez D, Eisenberg T, Ruckenstuhl C, Andryushkova A, Pendl T, Harger A, Madeo F. Metabolites in aging and autophagy. Microb Cell. 2014; 1:110-114.

236. Pietrocola F, Galluzzi L, Bravo-San Pedro JM, Madeo F, Kroemer G. Acetyl coenzyme A: a central metabolite and second messenger. Cell Metab. 2015; 21:805-821.

237. Medkour Y, Svistkova V, Titorenko VI. Cell-Nonautonomous Mechanisms Underlying Cellular and Organismal Aging. Int Rev Cell Mol Biol. 2016; 321:259-297.

238. Mohammad K, Dakik P, Medkour Y, McAuley M, Mitrofanova D, Titorenko VI. Some Metabolites Act as Second Messengers in Yeast Chronological Aging. Int J Mol Sci. 2018; 19: 860.

239. Cai L, Tu BP. Driving the cell cycle through metabolism. Annu Rev Cell Dev Biol. 2012; 28:59-87.

240. Grant CM. Role of the glutathione/glutaredoxin and thioredoxin systems in yeast growth and response to stress conditions. Mol Microbiol. 2001; 39:533-541.

241. Brandes N, Tienson H, Lindemann A, Vitvitsky V, Reichmann D, Banerjee R, Jakob U. Timeline of redox events in aging postmitotic cells. Elife. 2013; 2: e00306.

242. Wei M, Fabrizio P, Madia F, Hu J, Ge H, Li LM, Longo VD. Tor1/Sch9-regulated carbon source substitution is as effective as calorie restriction in life span extension. PLoS Genet. 2009; 5: e1000467.

243. François J, Parrou JL. Reserve carbohydrates metabolism in the yeast Saccharomyces cerevisiae. FEMS Microbiol Rev. 2001; 25:125-145.

244. Samokhvalov V, Ignatov V, Kondrashova M. Reserve carbohydrates maintain the viability of Saccharomyces cerevisiae cells during chronological aging. Mech Ageing Dev. 2004; 125:229-235.

245. Wang J, Jiang JC, Jazwinski SM. Gene regulatory changes in yeast during life extension by nutrient limitation. Exp Gerontol. 2010; 45:621-631.

246. Ocampo A, Liu J, Schroeder EA, Shadel GS, Barrientos A. Mitochondrial respiratory thresholds regulate yeast chronological life span and its extension by caloric restriction. Cell Metab. 2012; 16:55-67.

247. Cao L, Tang Y, Quan Z, Zhang Z, Oliver SG, Zhang N. Chronological Lifespan in Yeast Is Dependent on the Accumulation of Storage Carbohydrates Mediated by Yak1, Mck1 and Rim15 Kinases. PLoS Genet. 2016; 12: e1006458.

248. Svenkrtova A, Belicova L, Volejnikova A, Sigler K, Jazwinski SM, Pichova A. Stratification of yeast cells during chronological aging by size points to the role of trehalose in cell vitality. Biogerontology. 2016; 17: 395-408.

249. Singer MA, Lindquist S. Multiple effects of trehalose on protein folding in vitro and in vivo. Mol Cell. 1998; 1:639-648.

250. Jain NK, Roy I. Effect of trehalose on protein structure. Protein Sci. 2009; 18:24-36.

251. Beach A, Burstein MT, Richard VR, Leonov A, Levy S, Titorenko VI. Integration of peroxisomes into an endomembrane system that governs cellular aging. Front Physiol. 2012; 3: 283.

252. Dakik P, Medkour Y, Mohammad K, Titorenko VI. Mechanisms Through Which Some Mitochondria-Generated Metabolites Act as Second Messengers That Are Essential Contributors to the Aging Process in Eukaryotes Across Phyla. Front Physiol. 2019; 10: 461.

253. Causton HC, Ren B, Koh SS, Harbison CT, Kanin E, Jennings EG, Lee TI, True HL, Lander ES, Young RA. Remodeling of yeast genome expression in response to environmental changes. Mol Biol Cell. 2001; 12:323-337.

254. Fabrizio P, Pozza F, Pletcher SD, Gendron CM, Longo VD. Regulation of longevity and stress resistance by Sch9 in yeast. Science. 2001; 292:288-290.

255. Schroeder EA, Raimundo N, Shadel GS. Epigenetic silencing mediates mitochondria stress-induced longevity. Cell Metab. 2013; 17:954-964.

256. Schroeder EA, Raimundo N, Shadel GS. Epigenetic silencing mediates mitochondria stress-induced longevity. Cell Metab. 2013; 17:954-964.

257. Crespo JL, Powers T, Fowler B, Hall MN. The TOR-controlled transcription activators GLN3, RTG1, and RTG3 are regulated in response to intracellular levels of glutamine. Proc Natl Acad Sci USA. 2002; 99:6784-6789.

258. Conrad M, Schothorst J, Kankipati HN, Van Zeebroeck G, Rubio-Texeira M, Thevelein JM. Nutrient sensing and signaling in the yeast Saccharomyces cerevisiae. FEMS Microbiol Rev. 2014; 38:254-299.

259. Swinnen E, Ghillebert R, Wilms T, Winderickx J. Molecular mechanisms linking the evolutionary conserved TORC1-Sch9 nutrient signalling branch to lifespan regulation in Saccharomyces cerevisiae. FEMS Yeast Res. 2014; 14:17-32.

260. Urban J, Soulard A, Huber A, Lippman S, Mukhopadhyay D, Deloche O, Wanke V, Anrather D, Ammerer G, Riezman H, Broach JR, De Virgilio C, Hall MN, Loewith R. Sch9 is a major target of TORC1 in Saccharomyces cerevisiae. Mol Cell. 2007; 26:663-674.

261. Huber A, Bodenmiller B, Uotila A, Stahl M, Wanka S, Gerrits B, Aebersold R, Loewith R.

Characterization of the rapamycin-sensitive phosphoproteome reveals that Sch9 is a central coordinator of protein synthesis. Genes Dev. 2009; 23:1929-1943.

262. Lee J, Moir RD, Willis IM. Regulation of RNA polymerase III transcription involves SCH9-dependent and SCH9-independent branches of the target of rapamycin (TOR) pathway. J Biol Chem. 2009; 284:12604-12608.

263. Wei Y, Zheng XF. Sch9 partially mediates TORC1 signaling to control ribosomal RNA synthesis. Cell Cycle. 2009; 8:4085-4090.

264. Roosen J, Engelen K, Marchal K, Mathys J, Griffioen G, Cameroni E, Thevelein JM, De Virgilio C, De Moor B, Winderickx J. PKA and Sch9 control a molecular switch important for the proper adaptation to nutrient availability. Mol Microbiol. 2005; 55:862-880.

265. Smets B, Ghillebert R, De Snijder P, Binda M, Swinnen E, De Virgilio C, Winderickx J. Life in the midst of scarcity: adaptations to nutrient availability in Saccharomyces cerevisiae. Curr Genet. 2010; 56:1-32.

266. Eltschinger S, Loewith R. TOR Complexes and the Maintenance of Cellular Homeostasis. Trends Cell Biol. 2016; 26:148-159.

267. Laplante M, Sabatini DM. mTOR signaling in growth control and disease. Cell. 2012; 149:274-293.

268. Alers S, Wesselborg S, Stork B. ATG13: just a companion, or an executor of the autophagic program? Autophagy. 2014; 10:944-956.

269. Yorimitsu T, Zaman S, Broach JR, Klionsky DJ. Protein kinase A and Sch9 cooperatively regulate induction of autophagy in Saccharomyces cerevisiae. Mol Biol Cell. 2007; 18:4180-4189.

270. Stephan JS, Yeh YY, Ramachandran V, Deminoff SJ, Herman PK. The Tor and PKA

signaling pathways independently target the Atg1/Atg13 protein kinase complex to control autophagy. Proc Natl Acad Sci USA. 2009; 106:17049-17054.

271. Stephan JS, Yeh YY, Ramachandran V, Deminoff SJ, Herman PK. The Tor and cAMP-dependent protein kinase signaling pathways coordinately control autophagy in Saccharomyces cerevisiae. Autophagy. 2010; 6:294-295.

278. Johnson JE, Johnson FB. Methionine restriction activates the retrograde response and confers both stress tolerance and lifespan extension to yeast, mouse and human cells. PLoS One. 2014; 9: e97729.

279. Ruckenstuhl C, Netzberger C, Entfellner I, Carmona-Gutierrez D, Kickenweiz T, Stekovic S, Gleixner C, Schmid C, Klug L, Sorgo AG, Eisenberg T, Büttner S, Mariño G, Koziel R, Jansen-Dürr P, Fröhlich KU, Kroemer G, Madeo F. Lifespan extension by methionine restriction requires autophagy-dependent vacuolar acidification. PLoS Genet. 2014; 10: e1004347.

280. Wu Z, Song L, Liu SQ, Huang D. Independent and additive effects of glutamic acid and methionine on yeast longevity. PLoS One. 2013; 8: e79319.

281. Ruckenstuhl C, Netzberger C, Entfellner I, Carmona-Gutierrez D, Kickenweiz T, Stekovic S, Gleixner C, Schmid C, Klug L, Hajnal I, Sorgo AG, Eisenberg T, Büttner S, Marin O G, Koziel R, Magnes C, Sinner F, Pieber TR, Jansen-Dürr P, Fröhlich KU, Kroemer G, Madeo F. Autophagy extends lifespan via vacuolar acidification. Microb Cell. 2014; 1:160-162.

282. Morselli E, Galluzzi L, Kepp O, Criollo A, Maiuri MC, Tavernarakis N, Madeo F, Kroemer G. Autophagy mediates pharmacological lifespan extension by spermidine and resveratrol. Aging (Albany NY). 2009; 1:961-970.

283. Cuevasanta E, Denicola A, Alvarez B, Möller MN. Solubility and permeation of hydrogen sulfide in lipid membranes. PLoS One. 2012; 7: e34562.

284. Hine C, Mitchell JR. Calorie restriction and methionine restriction in control of endogenous hydrogen sulfide production by the transsulfuration pathway. Exp Gerontol. 2015; 68:26-32.

285. Hine C, Harputlugil E, Zhang Y, Ruckenstuhl C, Lee BC, Brace L, Longchamp A, Treviño-Villarreal JH, Mejia P, Ozaki CK, Wang R, Gladyshev VN, Madeo F, Mair WB, Mitchell JR. Endogenous hydrogen sulfide production is essential for dietary restriction benefits. Cell. 2015; 160:132-144.

286. Mohammad K, Dakik P, Medkour Y, McAuley M, Mitrofanova D, Titorenko VI. Yeast Cells Exposed to Exogenous Palmitoleic Acid Either Adapt to Stress and Survive or Commit to Regulated Liponecrosis and Die. Oxid Med Cell Longev. 2018; 2018: 3074769.

287. Madeo F, Fröhlich E, Fröhlich KU. A yeast mutant showing diagnostic markers of early and late apoptosis. J Cell Biol. 1997; 139:729-734.

288. Ingram DK, Zhu M, Mamczarz J, Zou S, Lane MA, Roth GS, deCabo R. Calorie restriction mimetics: an emerging research field. Aging Cell. 2006; 5:97-108.

289. Ingram DK, Roth GS. Calorie restriction mimetics: can you have your cake and eat it, too? Ageing Res Rev. 2015; 20:46-62.

290. Longo VD, Antebi A, Bartke A, Barzilai N, Brown-Borg HM, Caruso C, Curiel TJ, de Cabo R, Franceschi C, Gems D, Ingram DK, Johnson TE, Kennedy BK, Kenyon C, Klein S, Kopchick JJ, Lepperdinger G, Madeo F, Mirisola MG, Mitchell JR, Passarino G, Rudolph KL, Sedivy JM, Shadel GS, Sinclair DA, Spindler SR, Suh Y, Vijg J, Vinciguerra M, Fontana L. Interventions to Slow Aging in Humans: Are We Ready? Aging Cell. 2015; 14:497-510.

291. Carmona-Gutierrez D, Bauer MA, Zimmermann A, Aguilera A, Austriaco N, Ayscough K, Balzan R, Bar-Nun S, Barrientos A, Belenky P, Blondel M, Braun RJ, Breitenbach M, Burhans WC, Büttner S, Cavalieri D, Chang M, Cooper KF, Côrte-Real M, Costa V, Cullin C, Dawes I, Dengjel J, Dickman MB, Eisenberg T, Fahrenkrog B, Fasel N, Fröhlich KU, Gargouri A,

Giannattasio S, Goffrini P, Gourlay CW, Grant CM, Greenwood MT, Guaragnella N, Heger T, Heinisch J, Herker E, Herrmann JM, Hofer S, Jiménez-Ruiz A, Jungwirth H, Kainz K, Kontoyiannis DP, Ludovico P, Manon S, Martegani E, Mazzoni C, Megeney LA, Meisinger C, Nielsen J, Nyström T, Osiewacz HD, Outeiro TF, Park HO, Pendl T, Petranovic D, Picot S, Polčic P, Powers T, Ramsdale M, Rinnerthaler M, Rockenfeller P, Ruckenstuhl C, Schaffrath R, Segovia M, Severin FF, Sharon A, Sigrist SJ, Sommer-Ruck C, Sousa MJ, Thevelein JM, Thevissen K, Titorenko V, Toledano MB, Tuite M, Vögtle FN, Westermann B, Winderickx J, Wissing S, Wölfl S, Zhang ZJ, Zhao RY, Zhou B, Galluzzi L, Kroemer G, Madeo F. Guidelines and recommendations on yeast cell death nomenclature. Microb Cell. 2018; 5:4-31.

292. Rockenfeller P, Gourlay CW. Lipotoxicty in yeast: a focus on plasma membrane signalling and membrane contact sites. FEMS Yeast Res. 2018; 18: foy034.

293. Rockenfeller P, Smolnig M, Diessl J, Bashir M, Schmiedhofer V, Knittelfelder O, Ring J, Franz J, Foessl I, Khan MJ, Rost R, Graier WF, Kroemer G, Zimmermann A, Carmona-Gutierrez D, Eisenberg T, Büttner S, Sigrist SJ, Kühnlein RP, Kohlwein SD, Gourlay CW, Madeo F. Diacylglycerol triggers Rim101 pathway-dependent necrosis in yeast: a model for lipotoxicity. Cell Death Differ. 2018; 25:767-783.

294. Borradaile NM, Han X, Harp JD, Gale SE, Ory DS, Schaffer JE. Disruption of endoplasmic reticulum structure and integrity in lipotoxic cell death. J Lipid Res. 2006; 47:2726-2737.

295. Deguil J, Pineau L, Rowland Snyder EC, Dupont S, Beney L, Gil A, Frapper G, Ferreira T. Modulation of lipid-induced ER stress by fatty acid shape. Traffic. 2011; 12:349-362.

296. Fu S, Yang L, Li P, Hofmann O, Dicker L, Hide W, Lin X, Watkins SM, Ivanov AR, Hotamisligil GS. Aberrant lipid metabolism disrupts calcium homeostasis causing liver endoplasmic reticulum stress in obesity. Nature. 2011; 473:528-531.

297. Promlek T, Ishiwata-Kimata Y, Shido M, Sakuramoto M, Kohno K, Kimata Y. Membrane aberrancy and unfolded proteins activate the endoplasmic reticulum stress sensor Ire1 in different

ways. Mol Biol Cell. 2011; 22:3520-3532.

298. Fu S, Watkins SM, Hotamisligil GS. The role of endoplasmic reticulum in hepatic lipid homeostasis and stress signaling. Cell Metab. 2012; 15:623–634.

299. Thibault G, Shui G, Kim W, McAlister GC, Ismail N, Gygi SP, Wenk MR, Ng DT. The membrane stress response buffers lethal effects of lipid disequilibrium by reprogramming the protein homeostasis network. Mol Cell. 2012; 48:16-27.

300. Cui W, Ma J, Wang X, Yang W, Zhang J, Ji Q. Free fatty acid induces endoplasmic reticulum stress and apoptosis of β-cells by Ca2+/calpain-2 pathways. PLoS One. 2013; 8: e59921.

301. Lagace TA, Ridgway ND. The role of phospholipids in the biological activity and structure of the endoplasmic reticulum. Biochim Biophys Acta. 2013; 1833:2499–2510.

302. Surma MA, Klose C, Peng D, Shales M, Mrejen C, Stefanko A, Braberg H, Gordon DE, Vorkel D, Ejsing CS, Farese R Jr, Simons K, Krogan NJ, Ernst R. A lipid E-MAP identifies Ubx2 as a critical regulator of lipid saturation and lipid bilayer stress. Mol Cell. 2013; 51:519–530.

303. Volmer R, van der Ploeg K, Ron D. Membrane lipid saturation activates endoplasmic reticulum unfolded protein response transducers through their transmembrane domains. Proc Natl Acad Sci USA. 2013; 110:4628–4633.

304. Wu H, Ng BS, Thibault G. Endoplasmic reticulum stress response in yeast and humans. Biosci Rep. 2014; 34: e00118.

305. Volmer R, Ron D. Lipid-dependent regulation of the unfolded protein response. Curr Opin Cell Biol. 2015; 33:67–73.

306. Covino R, Ballweg S, Stordeur C, Michaelis JB, Puth K, Wernig F, Bahrami A, Ernst AM, Hummer G, Ernst R. A Eukaryotic Sensor for Membrane Lipid Saturation. Mol Cell. 2016; 63:49–

59.

307. Akoumi A, Haffar T, Mousterji M, Kiss RS, Bousette N. Palmitate mediated diacylglycerol accumulation causes endoplasmic reticulum stress, Plin2 degradation, and cell death in H9C2 cardiomyoblasts. Exp Cell Res. 2017; 354:85–94.

308. Chen E, Tsai TH, Li L, Saha P, Chan L, Chang BH. PLIN2 is a Key Regulator of the Unfolded Protein Response and Endoplasmic Reticulum Stress Resolution in Pancreatic β Cells. Sci Rep. 2017; 7:40855.

309. Halbleib K, Pesek K, Covino R, Hofbauer HF, Wunnicke D, Hänelt I, Hummer G, Ernst R. Activation of the Unfolded Protein Response by Lipid Bilayer Stress. Mol Cell. 2017; 67:673–684.e8.

310. Covino R, Hummer G, Ernst R. Integrated Functions of Membrane Property Sensors and a Hidden Side of the Unfolded Protein Response. Mol Cell. 2018; 71:458-467.

311. Ho N, Xu C, Thibault G. From the unfolded protein response to metabolic diseases - lipids under the spotlight. J Cell Sci. 2018; 131: jcs199307.

312. Koh JH, Wang L, Beaudoin-Chabot C, Thibault G. Lipid bilayer stress-activated IRE-1 modulates autophagy during endoplasmic reticulum stress. J Cell Sci. 2018; 131: jcs217992.

313. Shyu P Jr, Wong XFA, Crasta K, Thibault G. Dropping in on lipid droplets: insights into cellular stress and cancer. Biosci Rep. 2018; 38: BSR20180764.

314. Almanza A, Carlesso A, Chintha C, Creedican S, Doultsinos D, Leuzzi B, Luís A, McCarthy N, Montibeller L, More S, Papaioannou A, Püschel F, Sassano ML, et al. Endoplasmic reticulum stress signalling - from basic mechanisms to clinical applications. FEBS J. 2019; 286:241–278.

315. Cho H, Stanzione F, Oak A, Kim GH, Yerneni S, Qi L, Sum AK, Chan C. Intrinsic Structural

Features of the Human IRE1α Transmembrane Domain Sense Membrane Lipid Saturation. Cell Rep. 2019; 27:307–320.e5.

316. Fun XH, Thibault G. Lipid bilayer stress and proteotoxic stress-induced unfolded protein response deploy divergent transcriptional and non-transcriptional programmes. Biochim Biophys Acta Mol Cell Biol Lipids. 2020; 1865: 158449.

317. Hariri H, Speer N, Bowerman J, Rogers S, Fu G, Reetz E, Datta S, Feathers JR, Ugrankar R, Nicastro D, Henne WM. Mdm1 maintains endoplasmic reticulum homeostasis by spatially regulating lipid droplet biogenesis. J Cell Biol. 2019; 218:1319–1334.

318. Ron D, Walter P. Signal integration in the endoplasmic reticulum unfolded protein response. Nat Rev Mol Cell Biol. 2007; 8:519–529.

319. Jonikas MC, Collins SR, Denic V, Oh E, Quan EM, Schmid V, Weibezahn J, Schwappach B, Walter P, Weissman JS, Schuldiner M. Comprehensive characterization of genes required for protein folding in the endoplasmic reticulum. Science. 2009; 323:1693–1697.

320. Walter P, Ron D. The unfolded protein response: from stress pathway to homeostatic regulation. Science. 2011; 334:1081–1086.

321. Araki K, Nagata K. Protein folding and quality control in the ER. Cold Spring Harb Perspect Biol. 2011; 3: a007526.

322. Gardner BM, Pincus D, Gotthardt K, Gallagher CM, Walter P. Endoplasmic reticulum stress sensing in the unfolded protein response. Cold Spring Harb Perspect Biol. 2013; 5: a013169.

323. Higuchi-Sanabria R, Frankino PA, Paul JW 3rd, Tronnes SU, Dillin A. A Futile Battle? Protein Quality Control and the Stress of Aging. Dev Cell. 2018; 44:139–163.

324. Karagöz GE, Acosta-Alvear D, Walter P. The Unfolded Protein Response: Detecting and

Responding to Fluctuations in the Protein-Folding Capacity of the Endoplasmic Reticulum. Cold Spring Harb Perspect Biol. 2019; 11: a033886.

325. Salminen A, Kaarniranta K. ER stress and hormetic regulation of the aging process. Ageing Res Rev. 2010; 9:211–217.

326. Hou J, Tang H, Liu Z, Österlund T, Nielsen J, Petranovic D. Management of the endoplasmic reticulum stress by activation of the heat shock response in yeast. FEMS Yeast Res. 2014; 14:481–494.

327. Labunskyy VM, Gerashchenko MV, Delaney JR, Kaya A, Kennedy BK, Kaeberlein M, Gladyshev VN. Lifespan extension conferred by endoplasmic reticulum secretory pathway deficiency requires induction of the unfolded protein response. PLoS Genet. 2014; 10: e1004019.

328. Cui HJ, Liu XG, McCormick M, Wasko BM, Zhao W, He X, Yuan Y, Fang BX, Sun XR, Kennedy BK, Suh Y, Zhou ZJ, Kaeberlein M, Feng WL. PMT1 deficiency enhances basal UPR activity and extends replicative lifespan of Saccharomyces cerevisiae. Age (Dordr). 2015; 37: 9788.

329. Weindling E, Bar-Nun S. Sir2 links the unfolded protein response and the heat shock response in a stress response network. Biochem Biophys Res Commun. 2015; 457:473–478.

330. Piperi C, Adamopoulos C, Papavassiliou AG. XBP1: A Pivotal Transcriptional Regulator of Glucose and Lipid Metabolism. Trends Endocrinol Metab. 2016; 27:119–122.

331. Cohen N, Breker M, Bakunts A, Pesek K, Chas A, Argemí J, Orsi A, Gal L, Chuartzman S, Wigelman Y, Jonas F, Walter P, Ernst R, et al. Iron affects Ire1 clustering propensity and the amplitude of endoplasmic reticulum stress signaling. J Cell Sci. 2017; 130:3222–3233.

332. Guzel E, Arlier S, Guzeloglu-Kayisli O, Tabak MS, Ekiz T, Semerci N, Larsen K, Schatz F, Lockwood CJ, Kayisli UA. Endoplasmic Reticulum Stress and Homeostasis in Reproductive

Physiology and Pathology. Int J Mol Sci. 2017; 18: 792.

333. Martínez G, Duran-Aniotz C, Cabral-Miranda F, Vivar JP, Hetz C. Endoplasmic reticulum proteostasis impairment in aging. Aging Cell. 2017; 16:615–623.

334. Postnikoff SD, Johnson JE, Tyler JK. The integrated stress response in budding yeast lifespan extension. Microb Cell. 2017; 4:368–375.

335. Remondelli P, Renna M. The Endoplasmic Reticulum Unfolded Protein Response in Neurodegenerative Disorders and Its Potential Therapeutic Significance. Front Mol Neurosci. 2017; 10: 187.

336. Moon HW, Han HG, Jeon YJ. Protein Quality Control in the Endoplasmic Reticulum and Cancer. Int J Mol Sci. 2018; 19: 3020.

337. Beaupere C, Labunskyy VM. (Un)folding mechanisms of adaptation to ER stress: lessons from aneuploidy. Curr Genet. 2019; 65:467-471.

338. Chadwick SR, Lajoie P. Endoplasmic Reticulum Stress Coping Mechanisms and Lifespan Regulation in Health and Diseases. Front Cell Dev Biol. 2019; 7: 84.

339. Lehrbach NJ, Ruvkun G. Endoplasmic reticulum-associated SKN-1A/Nrf1 mediates a cytoplasmic unfolded protein response and promotes longevity. Elife. 2019; 8: e44425.

340. Schmidt RM, Schessner JP, Borner GH, Schuck S. The proteasome biogenesis regulator Rpn4 cooperates with the unfolded protein response to promote ER stress resistance. Elife. 2019; 8: e43244.

341. Ha EE, Frohman MA. Regulation of mitochondrial morphology by lipids. Biofactors. 2014; 40:419–424.

342. Valencak TG, Azzu V. Making heads or tails of mitochondrial membranes in longevity and aging: a role for comparative studies. Longev Healthspan. 2014; 3: 3.

343. Vögtle FN, Keller M, Taskin AA, Horvath SE, Guan XL, Prinz C, Opalińska M, Zorzin C, van der Laan M, Wenk MR, Schubert R, Wiedemann N, Holzer M, Meisinger C. The fusogenic lipid phosphatidic acid promotes the biogenesis of mitochondrial outer membrane protein Ugo1. J Cell Biol. 2015; 210:951–960.

344. Medkour Y, Titorenko VI. Mitochondria operate as signaling platforms in yeast aging. Aging (Albany NY). 2016; 8:212–213.

345. Ademowo OS, Dias HK, Burton DG, Griffiths HR. Lipid (per) oxidation in mitochondria: an emerging target in the ageing process? Biogerontology. 2017; 18:859–879.

346. Pollard AK, Ortori CA, Stöger R, Barrett DA, Chakrabarti L. Mouse mitochondrial lipid composition is defined by age in brain and muscle. Aging (Albany NY). 2017; 9:986–998.

347. Zechner R, Zimmermann R, Eichmann TO, Kohlwein SD, Haemmerle G, Lass A, Madeo F. FAT SIGNALS-lipases and lipolysis in lipid metabolism and signaling. Cell Metab. 2012; 15:279–291.

348. Koch B, Schmidt C, Daum G. Storage lipids of yeasts: a survey of nonpolar lipid metabolism in Saccharomyces cerevisiae, Pichia pastoris, and Yarrowia lipolytica. FEMS Microbiol Rev. 2014; 38:892–915.

349. Athenstaedt K, Daum G. Phosphatidic acid, a key intermediate in lipid metabolism. Eur J Biochem. 1999; 266:1-16.

350. Riekhof WR, Wu J, Jones JL, Voelker DR. Identification and characterization of the major lysophosphatidylethanolamine acyltransferase in Saccharomyces cerevisiae. J Biol Chem. 2007; 282:28344–28352.

351. Rajakumari S, Grillitsch K, Daum G. Synthesis and turnover of non-polar lipids in yeast. Prog Lipid Res. 2008; 47:157–171.

352. Kohlwein SD. Triacylglycerol homeostasis: insights from yeast. J Biol Chem. 2010; 285:15663–15667.

353. Kohlwein SD. Obese and anorexic yeasts: experimental models to understand the metabolic syndrome and lipotoxicity. Biochim Biophys Acta. 2010; 1801:222–229.

354. Carman GM, Han GS. Regulation of phospholipid synthesis in the yeast Saccharomyces cerevisiae. Annu Rev Biochem. 2011;80:859-83.

355. Hashemi HF, Goodman JM. The life cycle of lipid droplets. Curr Opin Cell Biol. 2015; 33:119–124.

356. Arlia-Ciommo A, Svistkova V, Mohtashami S, Titorenko VI. A novel approach to the discovery of anti-tumor pharmaceuticals: searching for activators of liponecrosis. Oncotarget. 2016; 7:5204–5225.

357. Köffel R, Tiwari R, Falquet L, Schneiter R. The Saccharomyces cerevisiae YLL012/YEH1, YLR020/YEH2, and TGL1 genes encode a novel family of membrane-anchored lipases that are required for steryl ester hydrolysis. Mol Cell Biol. 2005; 25:1655–1668.

358. Mukaka MM. Statistics corner: A guide to appropriate use of correlation coefficient in medical research. Malawi Med J. 2012; 24:69–71.

359. Medkour Y, Mohammad K, Arlia-Ciommo A, Svistkova V, Dakik P, Mitrofanova D, Rodriguez MEL, Junio JAB, Taifour T, Escudero P, Goltsios FF, Soodbakhsh S, Maalaoui H, Simard É, Titorenko VI. Mechanisms by which PE21, an extract from the white willow *Salix alba*, delays chronological aging in budding yeast. Oncotarget. 2019; 10:5780-5816.

360. Bou Khalil M, Hou W, Zhou H, Elisma F, Swayne LA, Blanchard AP, Yao Z, Bennett SA, Figeys D. Lipidomics era: accomplishments and challenges. Mass Spectrom Rev. 2010; 29:877-929.

361. Shevchenko A, Simons K. Lipidomics: coming to grips with lipid diversity. Nat Rev Mol Cell Biol. 2010; 11:593-5988.

362. Brügger B. Lipidomics: analysis of the lipid composition of cells and subcellular organelles by electrospray ionization mass spectrometry. Annu Rev Biochem. 2014; 83:79-98.

363. Eisenberg T, Büttner S. Lipids and cell death in yeast. FEMS Yeast Res. 2014; 14:179-197.

364. Basu Ball W, Neff JK, Gohil VM. The role of nonbilayer phospholipids in mitochondrial structure and function. FEBS Lett. 2018; 592:1273-1290.

365. Thakur R, Naik A, Panda A, Raghu P. Regulation of Membrane Turnover by Phosphatidic Acid: Cellular Functions and Disease Implications. Front Cell Dev Biol. 2019; 7: 83.

366. Ejsing CS, Sampaio JL, Surendranath V, Duchoslav E, Ekroos K, Klemm RW, Simons K, Shevchenko A. Global analysis of the yeast lipidome by quantitative shotgun mass spectrometry. Proc Natl Acad Sci USA. 2009; 106:2136-2141.

367. Guan XL, Riezman I, Wenk MR, Riezman H. Yeast lipid analysis and quantification by mass spectrometry. Methods Enzymol. 2010; 470:369-391.

368. Guan XL, Cestra G, Shui G, Kuhrs A, Schittenhelm RB, Hafen E, van der Goot FG, Robinett CC, Gatti M, Gonzalez-Gaitan M, Wenk MR. Biochemical membrane lipidomics during Drosophila development. Dev Cell. 2013; 24:98-111.

369. Klose C, Tarasov K. Profiling of Yeast Lipids by Shotgun Lipidomics. Methods Mol Biol.

2016; 1361:309-324.

370. Wang M, Wang C, Han RH, Han X. Novel advances in shotgun lipidomics for biology and medicine. Prog Lipid Res. 2016; 61:83-108.

371. Whitehouse CM, Dreyer RN, Yamashita M, Fenn JB. Electrospray interface for liquid chromatographs and mass spectrometers. Anal Chem. 1985; 57:675-679.

372. Van Pelt CK, Zhang S, Fung E, Chu I, Liu T, Li C, Korfmacher WA, Henion J. A fully automated nanoelectrospray tandem mass spectrometric method for analysis of Caco-2 samples. Rapid Commun Mass Spectrom. 2003; 17:1573-1578.

373. Brügger B, Erben G, Sandhoff R, Wieland FT, Lehmann WD. Quantitative analysis of biological membrane lipids at the low picomole level by nano-electrospray ionization tandem mass spectrometry. Proc Natl Acad Sci USA. 1997; 94:2339-2344.

374. Han X, Gross RW. Electrospray ionization mass spectroscopic analysis of human erythrocyte plasma membrane phospholipids. Proc Natl Acad Sci USA. 1994; 91:10635-10639.

375. Schuhmann K, Herzog R, Schwudke D, Metelmann-Strupat W, Bornstein SR, Shevchenko A. Bottom-up shotgun lipidomics by higher energy collisional dissociation on LTQ Orbitrap mass spectrometers. Anal Chem. 2011; 83:5480-5487.

376. Li J, Hoene M, Zhao X, Chen S, Wei H, Häring HU, Lin X, Zeng Z, Weigert C, Lehmann R, Xu G. Stable isotope-assisted lipidomics combined with nontargeted isotopomer filtering, a tool to unravel the complex dynamics of lipid metabolism. Anal Chem. 2013; 85:4651-4657.

377. Annesley TM. Ion suppression in mass spectrometry. Clin Chem. 2003; 49:1041-1044.

378. Sud M, Fahy E, Cotter D, Brown A, Dennis EA, Glass CK, Merrill AH Jr, Murphy RC, Raetz CR, Russell DW, Subramaniam S. LMSD: LIPID MAPS structure database. Nucleic Acids Res.

2007; 35:D527-D532.

379. Pauling JK, Hermansson M, Hartler J, Christiansen K, Gallego SF, Peng B, Ahrends R, Ejsing CS. Proposal for a common nomenclature for fragment ions in mass spectra of lipids. PLoS One. 2017; 12: e0188394.

380. Mohammad K, Jiang H, Hossain MI, Titorenko VI. Quantitative Analysis of the Cellular Lipidome of Saccharomyces Cerevisiae Using Liquid Chromatography Coupled with Tandem Mass Spectrometry. J Vis Exp. 2020; 157: 60616.

381. Matyash V, Liebisch G, Kurzchalia TV, Shevchenko A, Schwudke D. Lipid extraction by methyl-tert-butyl ether for high-throughput lipidomics. J Lipid Res. 2008; 49:1137-1146.

382. Cequier-Sánchez E, Rodríguez C, Ravelo AG, Zárate R. Dichloromethane as a solvent for lipid extraction and assessment of lipid classes and fatty acids from samples of different natures. J Agric Food Chem. 2008; 56:4297-4303.

383. Casanovas A, Sprenger RR, Tarasov K, Ruckerbauer DE, Hannibal-Bach HK, Zanghellini J, Jensen ON, Ejsing CS. Quantitative analysis of proteome and lipidome dynamics reveals functional regulation of global lipid metabolism. Chem Biol. 2015; 22:412-425.

384. Nie H, Liu R, Yang Y, Bai Y, Guan Y, Qian D, Wang T, Liu H. Lipid profiling of rat peritoneal surface layers by online normal- and reversed-phase 2D LC QToF-MS. J Lipid Res. 2010; 51:2833-2844.

385. Cajka T, Fiehn O. Comprehensive analysis of lipids in biological systems by liquid chromatography-mass spectrometry. Trends Analyt Chem. 2014; 61:192-206.

386. Helmer PO, Nordhorn ID, Korf A, Behrens A, Buchholz R, Zubeil F, Karst U, Hayen H. Complementing Matrix-Assisted Laser Desorption Ionization-Mass Spectrometry Imaging with Chromatography Data for Improved Assignment of Isobaric and Isomeric Phospholipids Utilizing

Trapped Ion Mobility-Mass Spectrometry. Anal Chem. 2021; 93:2135-2143.

387. Züllig T, Trötzmüller M, Köfeler HC. Lipidomics from sample preparation to data analysis: a primer. Anal Bioanal Chem. 2020; 412:2191-2209.

388. Gao X, Zhang Q, Meng D, Isaac G, Zhao R, Fillmore TL, Chu RK, Zhou J, Tang K, Hu Z, Moore RJ, Smith RD, Katze MG, Metz TO. A reversed-phase capillary ultra-performance liquid chromatography-mass spectrometry (UPLC-MS) method for comprehensive top-down/bottom-up lipid profiling. Anal Bioanal Chem. 2012; 402:2923-2933.

389. Mohammad K, Titorenko VI. Caloric restriction creates a metabolic pattern of chronological aging delay that in budding yeast differs from the metabolic design established by two other geroprotectors. Oncotarget. 2021; 12:608-625.

390. Cui L, Lu H, Lee YH. Challenges and emergent solutions for LC-MS/MS based untargeted metabolomics in diseases. Mass Spectrom Rev. 2018; 37:772-792.

391. Gertsman I, Barshop BA. Promises and pitfalls of untargeted metabolomics. J Inherit Metab Dis. 2018; 41:355-366.

392. Ivanisevic J, Want EJ. From Samples to Insights into Metabolism: Uncovering Biologically Relevant Information in LC-HRMS Metabolomics Data. Metabolites. 2019; 9: 308.

393. Hackett SR, Zanotelli VR, Xu W, Goya J, Park JO, Perlman DH, Gibney PA, Botstein D, Storey JD, Rabinowitz JD. Systems-level analysis of mechanisms regulating yeast metabolic flux. Science. 2016; 354: aaf2786.

394. Johnson CH, Ivanisevic J, Siuzdak G. Metabolomics: beyond biomarkers and towards mechanisms. Nat Rev Mol Cell Biol. 2016; 17:451-459.

395. Mülleder M, Calvani E, Alam MT, Wang RK, Eckerstorfer F, Zelezniak A, Ralser M.

Functional Metabolomics Describes the Yeast Biosynthetic Regulome. Cell. 2016; 167:553-565.e12.

396. Carmona-Gutierrez D, Eisenberg T, Büttner S, Meisinger C, Kroemer G, Madeo F. Apoptosis in yeast: triggers, pathways, subroutines. Cell Death Differ. 2010; 17:763-773.

397. Ring J, Sommer C, Carmona-Gutierrez D, Ruckenstuhl C, Eisenberg T, Madeo F. The metabolism beyond programmed cell death in yeast. Exp Cell Res. 2012; 318:1193-1200.

398. Ibáñez AJ, Fagerer SR, Schmidt AM, Urban PL, Jefimovs K, Geiger P, Dechant R, Heinemann M, Zenobi R. Mass spectrometry-based metabolomics of single yeast cells. Proc Natl Acad Sci USA. 2013; 110:8790-8794.

399. López-Otín C, Galluzzi L, Freije JMP, Madeo F, Kroemer G. Metabolic Control of Longevity. Cell. 2016; 166:802-821.

400. Stryeck S, Birner-Gruenberger R, Madl T. Integrative metabolomics as emerging tool to study autophagy regulation. Microb Cell. 2017; 4:240-258.

401. Pedro JMB, Sica V, Madeo F, Kroemer G. Acyl-CoA-binding protein (ACBP): the elusive 'hunger factor' linking autophagy to food intake. Cell Stress. 2019; 3:312-318.

402. Leupold S, Hubmann G, Litsios A, Meinema AC, Takhaveev V, Papagiannakis A, Niebel B, Janssens G, Siegel D, Heinemann M. Saccharomyces cerevisiae goes through distinct metabolic phases during its replicative lifespan. Elife. 2019; 8: e41046.

403. Boer VM, Crutchfield CA, Bradley PH, Botstein D, Rabinowitz JD. Growth-limiting intracellular metabolites in yeast growing under diverse nutrient limitations. Mol Biol Cell. 2010; 21:198-211.

404. Clish CB. Metabolomics: an emerging but powerful tool for precision medicine. Cold Spring

Harb Mol Case Stud. 2015; 1: a000588.

405. Fuhrer T, Zamboni N. High-throughput discovery metabolomics. Curr Opin Biotechnol. 2015; 31:73-78.

406. Liu X, Locasale JW. Metabolomics: A Primer. Trends Biochem Sci. 2017; 42:274-284.

407. Lu W, Su X, Klein MS, Lewis IA, Fiehn O, Rabinowitz JD. Metabolite Measurement: Pitfalls to Avoid and Practices to Follow. Annu Rev Biochem. 2017; 86:277-304.

408. Riekeberg E, Powers R. New frontiers in metabolomics: from measurement to insight. F1000Res. 2017; 6:1148.

409. Gertsman I, Barshop BA. Promises and pitfalls of untargeted metabolomics. J Inherit Metab Dis. 2018; 41:355-366.

410. Ivanisevic J, Want EJ. From Samples to Insights into Metabolism: Uncovering Biologically Relevant Information in LC-HRMS Metabolomics Data. Metabolites. 2019; 9: 308.

411. Srivastava S. Emerging Insights into the Metabolic Alterations in Aging Using Metabolomics. Metabolites. 2019; 9: 301.

412. Chetwynd AJ, Dunn WB, Rodriguez-Blanco G. Collection and Preparation of Clinical Samples for Metabolomics. Adv Exp Med Biol. 2017; 965:19-44.

413. Pinu FR, Villas-Boas SG, Aggio R. Analysis of Intracellular Metabolites from Microorganisms: Quenching and Extraction Protocols. Metabolites. 2017; 7: 53.

414. Zhang N, Fan Y, Li C, Wang Q, Leksawasdi N, Li F, Wang S. Cell permeability and nuclear DNA staining by propidium iodide in basidiomycetous yeasts. Appl Microbiol Biotechnol. 2018; 102:4183-4191.

415. Oberacher H, Reinstadler V, Kreidl M, Stravs MA, Hollender J, Schymanski EL. Annotating Nontargeted LC-HRMS/MS Data with Two Complementary Tandem Mass Spectral Libraries. Metabolites. 2018; 9: 3.

416. Tada I, Tsugawa H, Meister I, Zhang P, Shu R, Katsumi R, Wheelock CE, Arita M, Chaleckis R. Creating a Reliable Mass Spectral-Retention Time Library for All Ion Fragmentation-Based Metabolomics. Metabolites. 2019; 9: 251.

417. Villas-Bôas SG, Højer-Pedersen J, Akesson M, Smedsgaard J, Nielsen J. Global metabolite analysis of yeast: evaluation of sample preparation methods. Yeast. 2005; 22:1155-1169.

418. Crutchfield CA, Lu W, Melamud E, Rabinowitz JD. Mass spectrometry-based metabolomics of yeast. Methods Enzymol. 2010; 470:393-426.

419. Zhang T, Creek DJ, Barrett MP, Blackburn G, Watson DG. Evaluation of coupling reversed phase, aqueous normal phase, and hydrophilic interaction liquid chromatography with Orbitrap mass spectrometry for metabolomic studies of human urine. Anal Chem. 2012; 84:1994-2001.

420. Villas-Bôas SG, Moxley JF, Akesson M, Stephanopoulos G, Nielsen J. High-throughput metabolic state analysis: the missing link in integrated functional genomics of yeasts. Biochem J. 2005; 388:669-677.

421. Buescher JM, Moco S, Sauer U, Zamboni N. Ultrahigh performance liquid chromatography-tandem mass spectrometry method for fast and robust quantification of anionic and aromatic metabolites. Anal Chem. 2010; 82:4403-4412.

422. Fuchs S, Bundy JG, Davies SK, Viney JM, Swire JS, Leroi AM. A metabolic signature of long life in Caenorhabditis elegans. BMC Biol. 2010; 8:14.

423. Yoshida R, Tamura T, Takaoka C, Harada K, Kobayashi A, Mukai Y, Fukusaki E.

Metabolomics-based systematic prediction of yeast lifespan and its application for semi-rational screening of ageing-related mutants. Aging Cell. 2010; 9:616-625.

424. Houtkooper RH, Argmann C, Houten SM, Cantó C, Jeninga EH, Andreux PA, Thomas C, Doenlen R, Schoonjans K, Auwerx J. The metabolic footprint of aging in mice. Sci Rep. 2011; 1:134.

425. Sarup P, Pedersen SM, Nielsen NC, Malmendal A, Loeschcke V. The metabolic profile of long-lived Drosophila melanogaster. PLoS One. 2012; 7: e47461.

426. Butler JA, Mishur RJ, Bhaskaran S, Rea SL. A metabolic signature for long life in the Caenorhabditis elegans Mit mutants. Aging Cell. 2013; 12:130-138.

427. Gonzalez-Covarrubias V, Beekman M, Uh HW, Dane A, Troost J, Paliukhovich I, van der Kloet FM, Houwing-Duistermaat J, Vreeken RJ, Hankemeier T, Slagboom EP. Lipidomics of familial longevity. Aging Cell. 2013; 12:426-434.

428. Tomás-Loba A, Bernardes de Jesus B, Mato JM, Blasco MA. A metabolic signature predicts biological age in mice. Aging Cell. 2013; 12:93-101.

429. Avanesov AS, Ma S, Pierce KA, Yim SH, Lee BC, Clish CB, Gladyshev VN. Age- and diet-associated metabolome remodeling characterizes the aging process driven by damage accumulation. Elife. 2014; 3: e02077.

430. Hertel J, Friedrich N, Wittfeld K, Pietzner M, Budde K, Van der Auwera S, Lohmann T, Teumer A, Völzke H, Nauck M, Grabe HJ. Measuring Biological Age via Metabonomics: The Metabolic Age Score. J Proteome Res. 2016; 15:400-410.

431. Wiley CD, Campisi J. From Ancient Pathways to Aging Cells-Connecting Metabolism and Cellular Senescence. Cell Metab. 2016; 23:1013-1021.

432. Gao AW, Chatzispyrou IA, Kamble R, Liu YJ, Herzog K, Smith RL, van Lenthe H, Vervaart MAT, van Cruchten A, Luyf AC, van Kampen A, Pras-Raves ML, Vaz FM, et al. A sensitive mass spectrometry platform identifies metabolic changes of life history traits in C. elegans. Sci Rep. 2017; 7: 2408.

433. Johnson LC, Martens CR, Santos-Parker JR, Bassett CJ, Strahler TR, Cruickshank-Quinn C, Reisdorph N, McQueen MB, Seals DR. Amino acid and lipid associated plasma metabolomic patterns are related to healthspan indicators with ageing. Clin Sci (Lond). 2018; 132:1765-1777.

434. Ma Z, Wang H, Cai Y, Wang H, Niu K, Wu X, Ma H, Yang Y, Tong W, Liu F, Liu Z, Zhang Y, Liu R, et al. Epigenetic drift of H3K27me3 in aging links glycolysis to healthy longevity in Drosophila. Elife. 2018; 7: e35368.

435. Bunning BJ, Contrepois K, Lee-McMullen B, Dhondalay GKR, Zhang W, Tupa D, Raeber O, Desai M, Nadeau KC, Snyder MP, Andorf S. Global metabolic profiling to model biological processes of aging in twins. Aging Cell. 2020; 19: e13073.

436. D'Antona G, Ragni M, Cardile A, Tedesco L, Dossena M, Bruttini F, Caliaro F, Corsetti G, Bottinelli R, Carruba MO, Valerio A, Nisoli E. Branched-chain amino acid supplementation promotes survival and supports cardiac and skeletal muscle mitochondrial biogenesis in middle-aged mice. Cell Metab. 2010; 12:362-372.

437. Peng W, Robertson L, Gallinetti J, Mejia P, Vose S, Charlip A, Chu T, Mitchell JR. Surgical stress resistance induced by single amino acid deprivation requires Gcn2 in mice. Sci Transl Med. 2012; 4: 118ra11.

438. Sanchez-Roman I, Barja G. Regulation of longevity and oxidative stress by nutritional interventions: role of methionine restriction. Exp Gerontol. 2013; 48:1030-1042.

439. Galluzzi L, Pietrocola F, Levine B, Kroemer G. Metabolic control of autophagy. Cell. 2014; 159:1263-1276.

440. Jové M, Naudí A, Ramírez-Núñez O, Portero-Otín M, Selman C, Withers DJ, Pamplona R. Caloric restriction reveals a metabolomic and lipidomic signature in liver of male mice. Aging Cell 2014; 13:828-837.

441. Solon-Biet SM, McMahon AC, Ballard JW, Ruohonen K, Wu LE, Cogger VC, Warren A, Huang X, Pichaud N, Melvin RG, Gokarn R, Khalil M, Turner N, et al. The ratio of macronutrients, not caloric intake, dictates cardiometabolic health, aging, and longevity in ad libitum-fed mice. Cell Metab. 2014; 19:418-430.

442. Finkel T. The metabolic regulation of aging. Nat Med. 2015; 21:1416-1423.

443. Fontana L, Partridge L. Promoting health and longevity through diet: from model organisms to humans. Cell. 2015; 161:106-111.

444. Madeo F, Zimmermann A, Maiuri MC, Kroemer G. Essential role for autophagy in life span extension. J Clin Invest. 2015; 125:85-93.

445. Bárcena C, Quirós PM, Durand S, Mayoral P, Rodríguez F, Caravia XM, Mariño G, Garabaya C, Fernández-García MT, Kroemer G, Freije JMP, López-Otín C. Methionine Restriction Extends Lifespan in Progeroid Mice and Alters Lipid and Bile Acid Metabolism. Cell Rep. 2018; 24:2392-2403.

446. Brandhorst S, Longo VD. Protein Quantity and Source, Fasting-Mimicking Diets, and Longevity. Adv Nutr. 2019; 10: S340-S350.

447. Canfielda CA, Bradshaw PC. Amino acids in the regulation of aging and aging-related diseases. Transl Med Aging. 2019; 3:70-89.

448. Green CL, Lamming DW. Regulation of metabolic health by essential dietary amino acids. Mech Ageing Dev. 2019; 177:186-200.

449. Kitada M, Ogura Y, Monno I, Koya D. The impact of dietary protein intake on longevity and metabolic health. EBioMedicine. 2019;43: 632-640.

450. Liu YJ, Janssens GE, McIntyre RL, Molenaars M, Kamble R, Gao AW, Jongejan A, Weeghel MV, MacInnes AW, Houtkooper RH. Glycine promotes longevity in Caenorhabditis elegans in a methionine cycle-dependent fashion. PLoS Genet. 2019; 15: e1007633.

451. Mitchell SJ, Bernier M, Mattison JA, Aon MA, Kaiser TA, Anson RM, Ikeno Y, Anderson RM, Ingram DK, de Cabo R. Daily Fasting Improves Health and Survival in Male Mice Independent of Diet Composition and Calories. Cell Metab. 2019; 29:221-228.e3.

452. Aon MA, Bernier M, Mitchell SJ, Di Germanio C, Mattison JA, Ehrlich MR, Colman RJ, Anderson RM, de Cabo R. Untangling Determinants of Enhanced Health and Lifespan through a Multi-omics Approach in Mice. Cell Metab. 2020; 32:100-116.e4.

453. Giese GE, Walker MD, Ponomarova O, Zhang H, Li X, Minevich G, Walhout AJ. Caenorhabditis elegans methionine/S-adenosylmethionine cycle activity is sensed and adjusted by a nuclear hormone receptor. Elife. 2020; 9: e60259.

454. Hansen M, Hsu AL, Dillin A, Kenyon C. New genes tied to endocrine, metabolic, and dietary regulation of lifespan from a Caenorhabditis elegans genomic RNAi screen. PLoS Genet. 2005; 1:119-128.

455. Bitto A, Wang AM, Bennett CF, Kaeberlein M. Biochemical Genetic Pathways that Modulate Aging in Multiple Species. Cold Spring Harb Perspect Med. 2015; 5: a025114.

456. Passarino G, De Rango F, Montesanto A. Human longevity: Genetics or Lifestyle? It takes two to tango. Immun Ageing. 2016; 13: 12.

457. Dato S, Rose G, Crocco P, Monti D, Garagnani P, Franceschi C, Passarino G. The genetics

of human longevity: an intricacy of genes, environment, culture and microbiome. Mech Ageing Dev. 2017; 165:147-155.

458. Giuliani C, Garagnani P, Franceschi C. Genetics of Human Longevity Within an Eco-Evolutionary Nature-Nurture Framework. Circ Res. 2018; 123:745-772.

459. Van Raamsdonk JM. Mechanisms underlying longevity: A genetic switch model of aging. Exp Gerontol. 2018; 107:136-139.

460. Costa D, Scognamiglio M, Fiorito C, Benincasa G, Napoli C. Genetic background, epigenetic factors and dietary interventions which influence human longevity. Biogerontology. 2019; 20:605-626.

461. Dall KB, Færgeman NJ. Metabolic regulation of lifespan from a C. elegans perspective. Genes Nutr. 2019; 14: 25.

462. Morris BJ, Willcox BJ, Donlon TA. Genetic and epigenetic regulation of human aging and longevity. Biochim Biophys Acta Mol Basis Dis. 2019; 1865:1718-1744.

463. Baur JA, Pearson KJ, Price NL, Jamieson HA, Lerin C, Kalra A, Prabhu VV, Allard JS, Lopez-Lluch G, Lewis K, Pistell PJ, Poosala S, Becker KG, et al. Resveratrol improves health and survival of mice on a high-calorie diet. Nature. 2006; 444:337-342.

464. Liu B, Ghosh S, Yang X, Zheng H, Liu X, Wang Z, Jin G, Zheng B, Kennedy BK, Suh Y, Kaeberlein M, Tryggvason K, Zhou Z. Resveratrol rescues SIRT1-dependent adult stem cell decline and alleviates progeroid features in laminopathy-based progeria. Cell Metab. 2012; 16: 738-750.

465. Gomes AP, Price NL, Ling AJ, Moslehi JJ, Montgomery MK, Rajman L, White JP, Teodoro JS, Wrann CD, Hubbard BP, Mercken EM, Palmeira CM, de Cabo R, et al. Declining NAD(+) induces a pseudohypoxic state disrupting nuclear-mitochondrial communication during aging.

Cell. 2013; 155:1624-1638.

466. Harrison DE, Strong R, Allison DB, Ames BN, Astle CM, Atamna H, Fernandez E, Flurkey K, Javors MA, Nadon NL, Nelson JF, Pletcher S, Simpkins JW, et al. Acarbose, 17-α-estradiol, and nordihydroguaiaretic acid extend mouse lifespan preferentially in males. Aging Cell. 2014; 13:273-282.

467. Hernández-Damián J, Andérica-Romero AC, Pedraza-Chaverri J. Paradoxical cellular effects and biological role of the multifaceted compound nordihydroguaiaretic acid. Arch Pharm (Weinheim). 2014; 347:685-697.

468. Weimer S, Priebs J, Kuhlow D, Groth M, Priebe S, Mansfeld J, Merry TL, Dubuis S, Laube B, Pfeiffer AF, Schulz TJ, Guthke R, Platzer M, et al. D-Glucosamine supplementation extends life span of nematodes and of ageing mice. Nat Commun. 2014; 5: 3563.

469. Song YM, Lee YH, Kim JW, Ham DS, Kang ES, Cha BS, Lee HC, Lee BW. Metformin alleviates hepatosteatosis by restoring SIRT1-mediated autophagy induction via an AMP-activated protein kinase-independent pathway. Autophagy. 2015; 11:46-59.

470. Walsh ME, Bhattacharya A, Sataranatarajan K, Qaisar R, Sloane L, Rahman MM, Kinter M, Van Remmen H. The histone deacetylase inhibitor butyrate improves metabolism and reduces muscle atrophy during aging. Aging Cell. 2015; 14:957-970.

471. Jamwal S, Kumar P. Spermidine ameliorates 3-nitropropionic acid (3-NP)-induced striatal toxicity: Possible role of oxidative stress, neuroinflammation, and neurotransmitters. Physiol Behav. 2016; 155:180-187.

472. Lin AL, Jahrling JB, Zhang W, DeRosa N, Bakshi V, Romero P, Galvan V, Richardson A. Rapamycin rescues vascular, metabolic and learning deficits in apolipoprotein E4 transgenic mice with pre-symptomatic Alzheimer's disease. J Cereb Blood Flow Metab. 2017; 37:217-226.

473. Katsyuba E, Mottis A, Zietak M, De Franco F, van der Velpen V, Gariani K, Ryu D, Cialabrini L, Matilainen O, Liscio P, Giacchè N, Stokar-Regenscheit N, Legouis D, et al. De novo NAD+ synthesis enhances mitochondrial function and improves health. Nature. 2018; 563:354-359.

474. Kezic A, Popovic L, Lalic K. mTOR Inhibitor Therapy and Metabolic Consequences: Where Do We Stand? Oxid Med Cell Longev. 2018; 2018: 2640342.

475. Shintani H, Shintani T, Ashida H, Sato M. Calorie Restriction Mimetics: Upstream-Type Compounds for Modulating Glucose Metabolism. Nutrients. 2018; 10: 1821.

476. Bridgeman SC, Northrop W, Melton PE, Ellison GC, Newsholme P, Mamotte CDS. Butyrate generated by gut microbiota and its therapeutic role in metabolic syndrome. Pharmacol Res. 2020; 160: 105174.

477. Smith DL Jr, Orlandella RM, Allison DB, Norian LA. Diabetes medications as potential calorie restriction mimetics-a focus on the alpha-glucosidase inhibitor acarbose. Geroscience. 2020; Epub ahead of print.

478. Catic A. Cellular Metabolism and Aging. Prog Mol Biol Transl Sci. 2018; 155:85-107.

479. Mohammad K, Jiang H, Titorenko VI. Quantitative metabolomics of Saccharomyces cerevisiae using liquid chromatography coupled with tandem mass spectrometry. J Vis Exp. 2020; 166: 62061.

480. Thomas D, Surdin-Kerjan Y. Metabolism of sulfur amino acids in Saccharomyces cerevisiae. Microbiol Mol Biol Rev. 1997; 61:503-532.

481. Lee BC, Kaya A, Gladyshev VN. Methionine restriction and lifespan control. Ann NY Acad Sci. 2016; 1363:116-124.

482. McIsaac RS, Lewis KN, Gibney PA, Buffenstein R. From yeast to human: exploring the

comparative biology of methionine restriction in extending eukaryotic life span. Ann NY Acad Sci. 2016; 1363:155-170.

483. Ables GP, Johnson JE. Pleiotropic responses to methionine restriction. Exp Gerontol. 2017; 94:83-88.

484. Latimer MN, Freij KW, Cleveland BM, Biga PR. Physiological and molecular mechanisms of methionine restriction. Front Endocrinol (Lausanne). 2018; 9: 217.

485. Parkhitko AA, Jouandin P, Mohr SE, Perrimon N. Methionine metabolism and methyltransferases in the regulation of aging and lifespan extension across species. Aging Cell. 2019; 18: e13034.

486. Zou K, Rouskin S, Dervishi K, McCormick MA, Sasikumar A, Deng C, Chen Z, Kaeberlein M, Brem RB, Polymenis M, Kennedy BK, Weissman JS, Zheng J, Ouyang Q, Li H. Life span extension by glucose restriction is abrogated by methionine supplementation: Cross-talk between glucose and methionine and implication of methionine as a key regulator of life span. Sci Adv. 2020; 6: eaba1306.

487. Sutter BM, Wu X, Laxman S, Tu BP. Methionine inhibits autophagy and promotes growth by inducing the SAM-responsive methylation of PP2A. Cell. 2013; 154:403-415.

488. Laxman S, Sutter BM, Wu X, Kumar S, Guo X, Trudgian DC, Mirzaei H, Tu BP. Sulfur amino acids regulate translational capacity and metabolic homeostasis through modulation of tRNA thiolation. Cell. 2013; 154:416-429.

489. Wilson WA, Hawley SA, Hardie DG. Glucose repression/derepression in budding yeast: SNF1 protein kinase is activated by phosphorylation under derepressing conditions, and this correlates with a high AMP:ATP ratio. Curr Biol. 1996; 6:1426-1434.

490. Mayer FV, Heath R, Underwood E, Sanders MJ, Carmena D, McCartney RR, Leiper FC,

Xiao B, Jing C, Walker PA, Haire LF, Ogrodowicz R, Martin SR, Schmidt MC, Gamblin SJ, Carling D. ADP regulates SNF1, the Saccharomyces cerevisiae homolog of AMP-activated protein kinase. Cell Metab. 2011; 14:707-714.

491. Hedbacker K, Carlson M. SNF1/AMPK pathways in yeast. Front Biosci. 2008; 13:2408-2420.

492. Shashkova S, Welkenhuysen N, Hohmann S. Molecular communication: crosstalk between the Snf1 and other signaling pathways. FEMS Yeast Res. 2015; 15: fov026.

493. Coccetti P, Nicastro R, Tripodi F. Conventional and emerging roles of the energy sensor Snf1/AMPK in Saccharomyces cerevisiae. Microb Cell. 2018; 5:482-494.

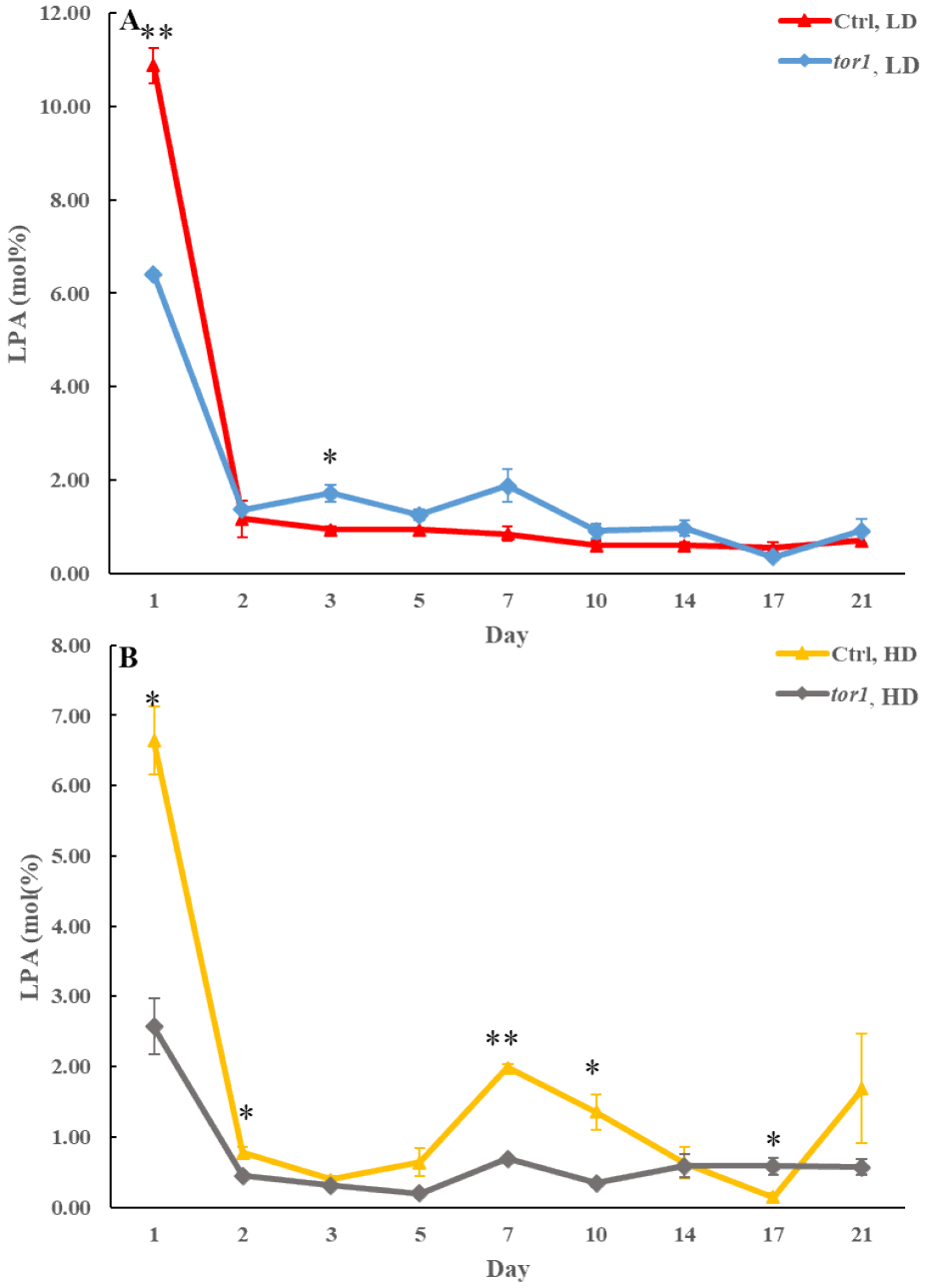

Figure 10.1: No significant and continuing changes in the concentrations of LPA are observed within the HD and LD cell populations carrying the *tor1Δ* mutation. WT and *tor1Δ* cells were cultured in the YP medium supplemented with 2% glucose (non-CR conditions). Cell aliquots were taken on different days of culturing. The Percoll density gradient centrifugation was used to purify HD and LD cells from these cell aliquots. LC-MS/MS was used to assess LPA

concentrations in these cells. Data are shown as means ± SD (n = 2; *$p < 0.05$; **$p < 0.01$).

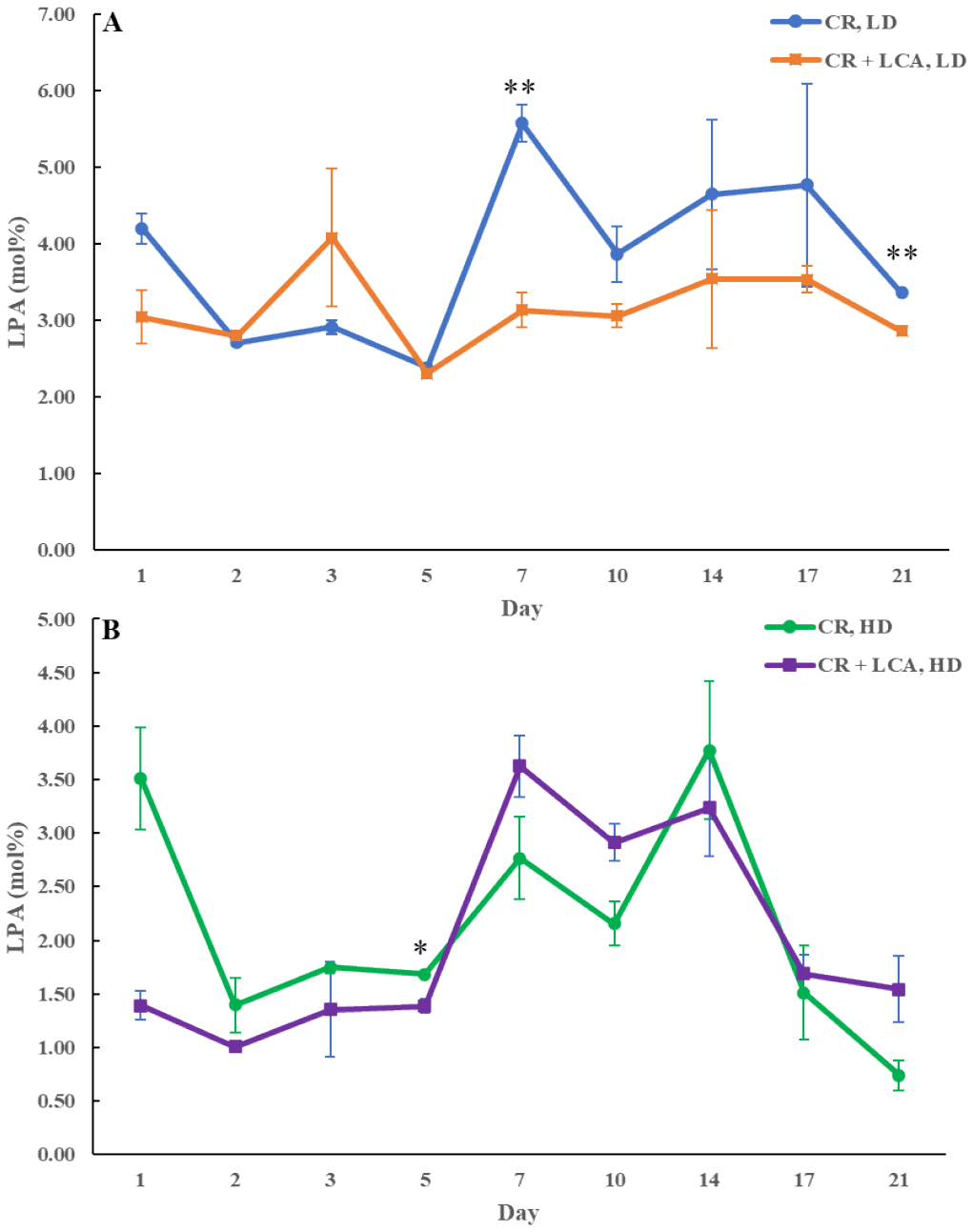

Figure 10.2: No significant and continuing changes in the concentrations of LPA are observed within the HD and LD cell populations treated with LCA. WT cells were cultured in YP medium supplemented with 0.2% glucose (CR conditions) in the presence of 50 µM LCA or its absence. Cell aliquots were taken on different days of culturing. The Percoll density gradient centrifugation was used to purify HD and LD cells from these cell aliquots. LC-MS/MS was used to assess LPA concentrations in these cells. Data are shown as means ± SD (n = 2; *$p < 0.05$; **p

< 0.01).

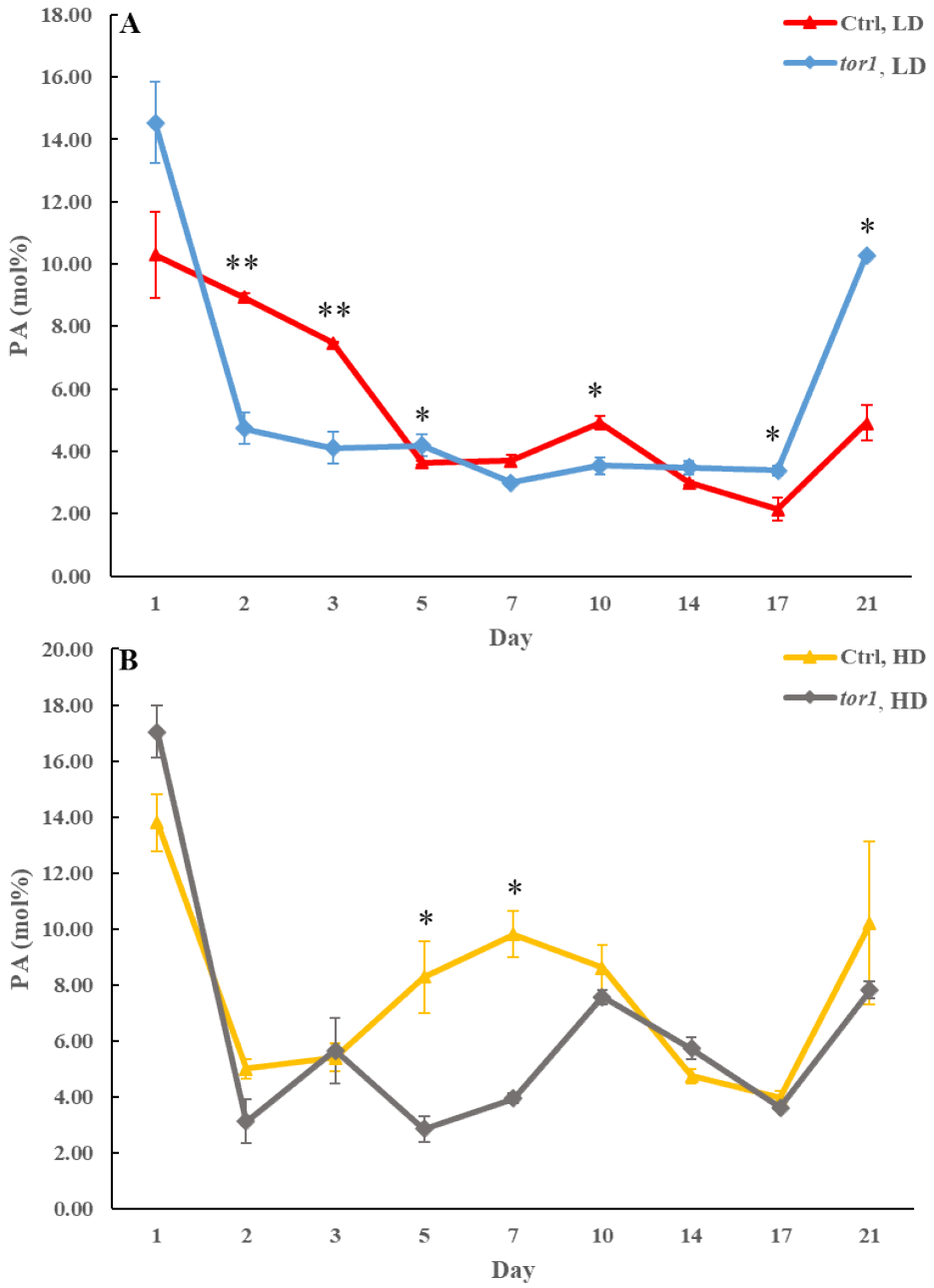

Figure 10.3: No significant and continuing changes in the concentrations of PA are observed within the HD and LD cell populations carrying the *tor1Δ* mutation. WT and *tor1Δ* cells were cultured in the YP medium supplemented with 2% glucose (non-CR conditions). Cell aliquots were taken on different days of culturing. The Percoll density gradient centrifugation was used to purify HD and LD cells from these cell aliquots. LC-MS/MS was used to assess PA concentrations

in these cells. Data are shown as means ± SD (n = 2; *$p < 0.05$; **$p < 0.01$).

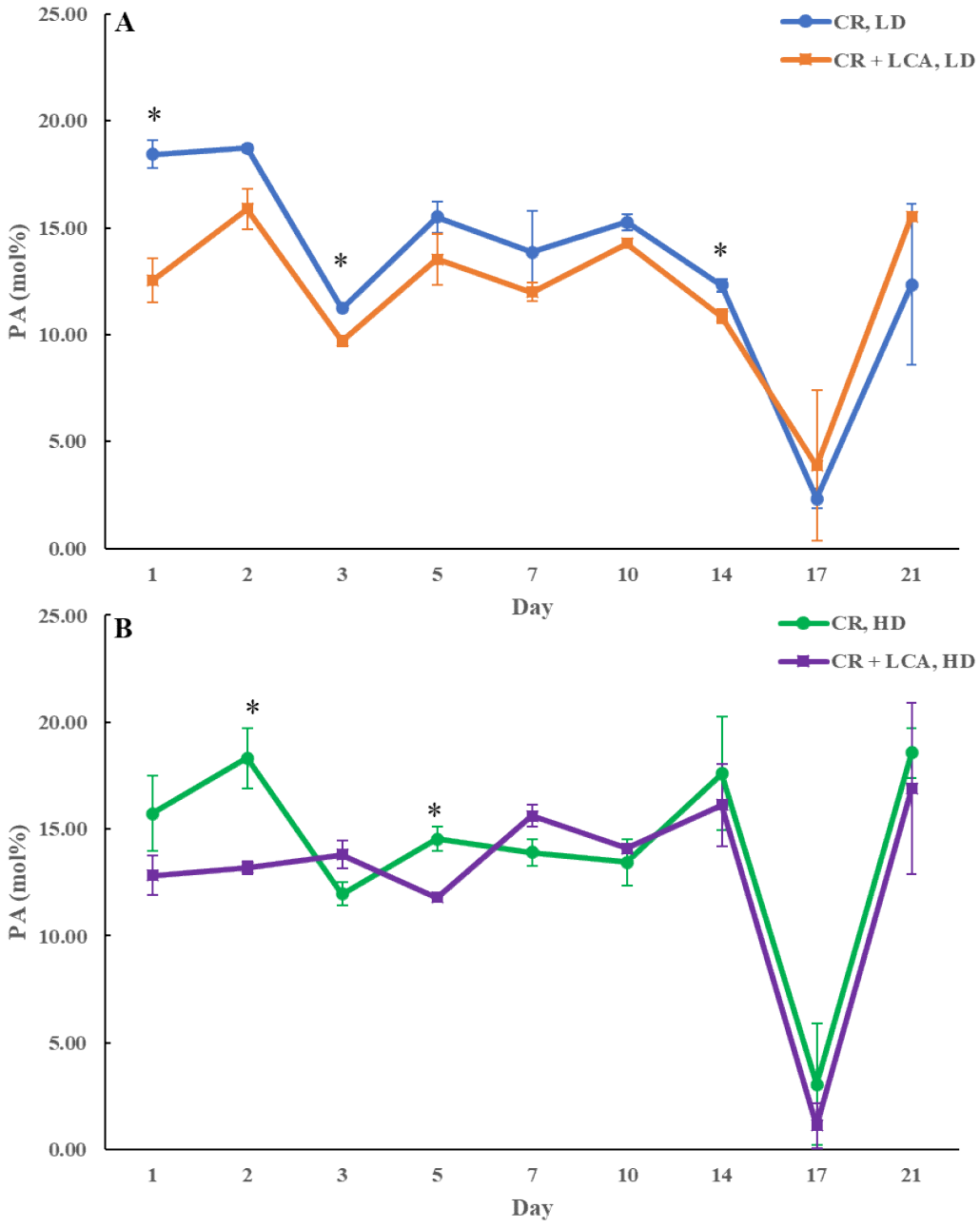

Figure 10.4: No significant and continuing changes in the concentrations of PA are observed within the HD and LD cell populations treated with LCA. WT cells were cultured in YP medium supplemented with 0.2% glucose (CR conditions) in the presence of 50 µM LCA or its absence. Cell aliquots were taken on different days of culturing. The Percoll density gradient centrifugation was used to purify HD and LD cells from these cell aliquots. LC-MS/MS was used to assess PA concentrations in these cells. Data are shown as means ± SD (n = 2; *$p < 0.05$).

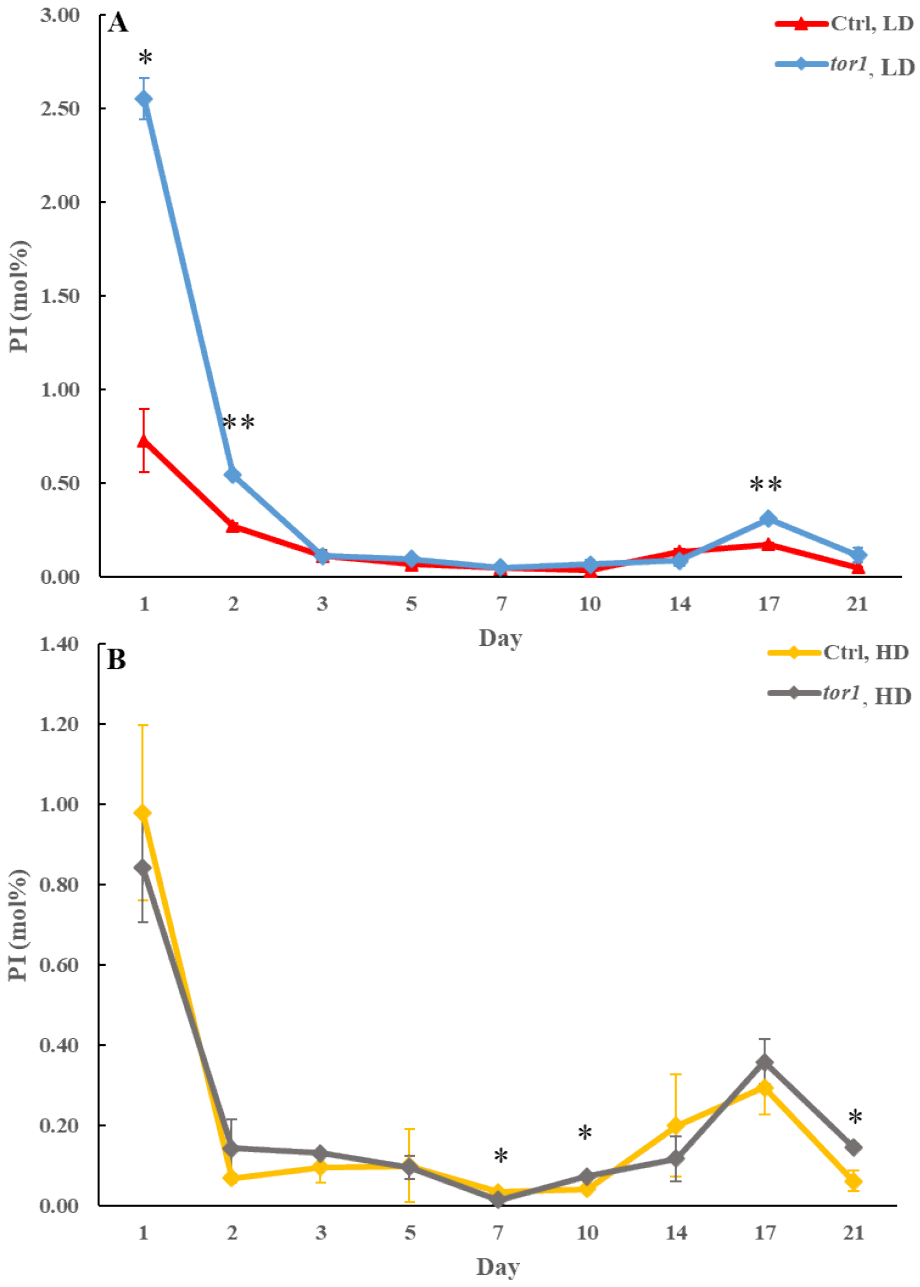

Figure 10.5: No significant and continuing changes in the concentrations of PI are observed within the HD and LD cell populations carrying the *tor1Δ* mutation. WT and *tor1Δ* cells were cultured in the YP medium supplemented with 2% glucose (non-CR conditions). Cell aliquots were taken on different days of culturing. The Percoll density gradient centrifugation was used to purify HD and LD cells from these cell aliquots. LC-MS/MS was used to assess PI concentrations in these cells. Data are shown as means ± SD (n = 2; *$p < 0.05$; **$p < 0.01$).

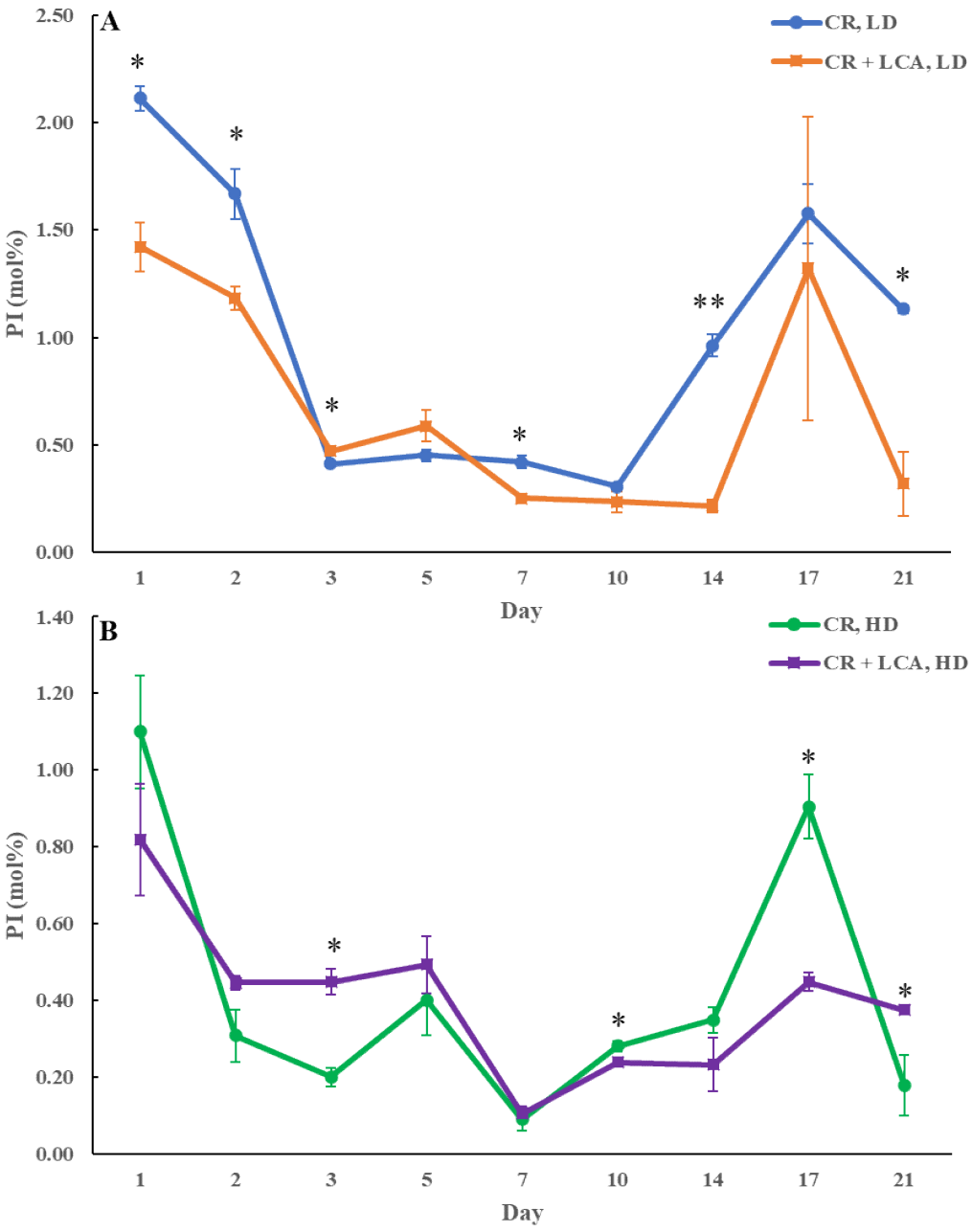

Figure 10.6: No significant and continuing changes in the concentrations of PI are observed within the HD and LD cell populations treated with LCA. WT cells were cultured in YP medium supplemented with 0.2% glucose (CR conditions) in the presence of 50 µM LCA or its absence. Cell aliquots were taken on different days of culturing. The Percoll density gradient centrifugation was used to purify HD and LD cells from these cell aliquots. LC-MS/MS was used

to assess PI concentrations in these cells. Data are shown as means ± SD (n = 2; *$p < 0.05$).

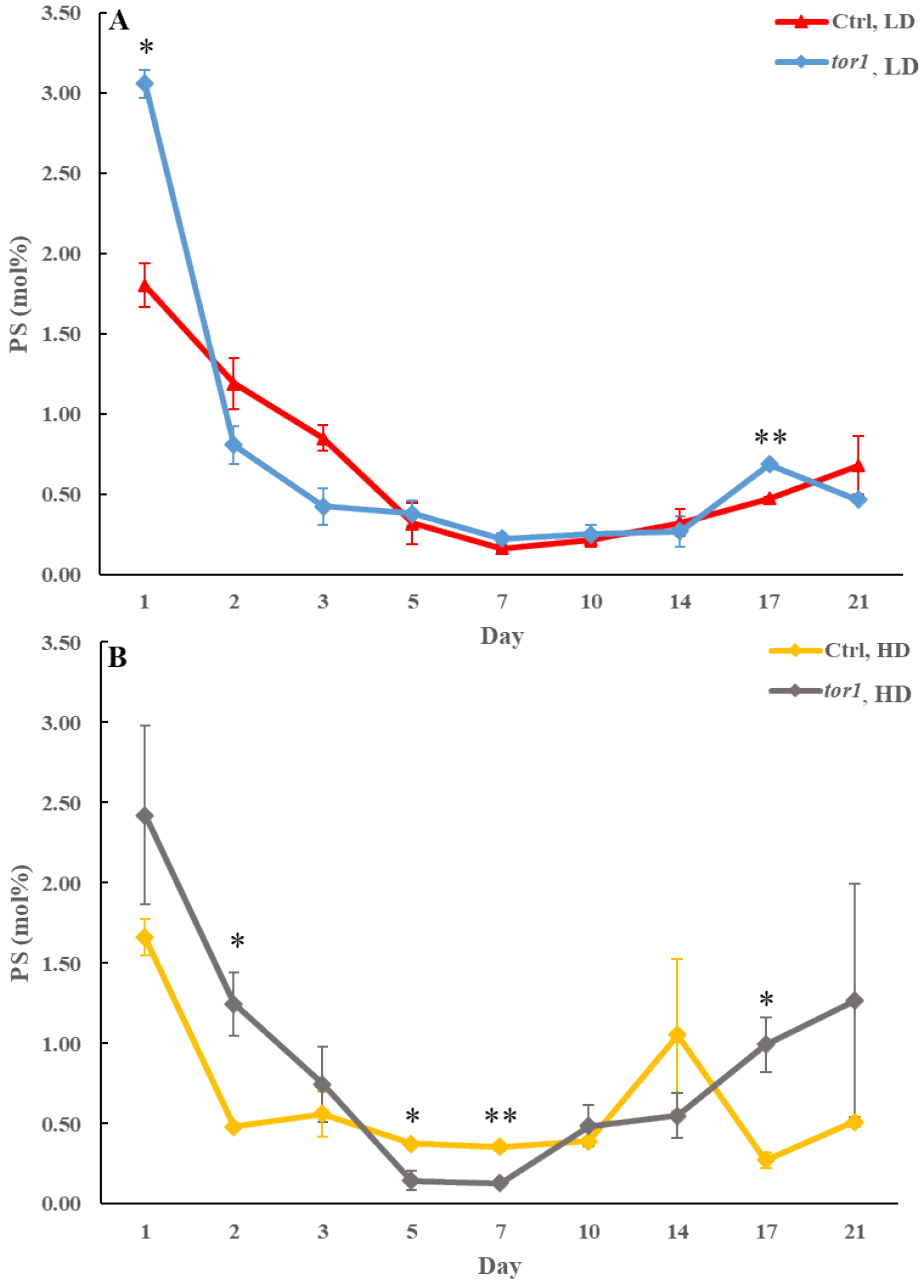

Figure 10.7: No significant and continuing changes in the concentrations of PS are observed within the HD and LD cell populations carrying the *tor1Δ* mutation. WT and *tor1Δ* cells were cultured in the YP medium supplemented with 2% glucose (non-CR conditions). Cell aliquots were taken on different days of culturing. The Percoll density gradient centrifugation was used to purify HD and LD cells from these cell aliquots. LC-MS/MS was used to assess PS concentrations

in these cells. Data are shown as means ± SD (n = 2; *$p < 0.05$; **$p < 0.01$).

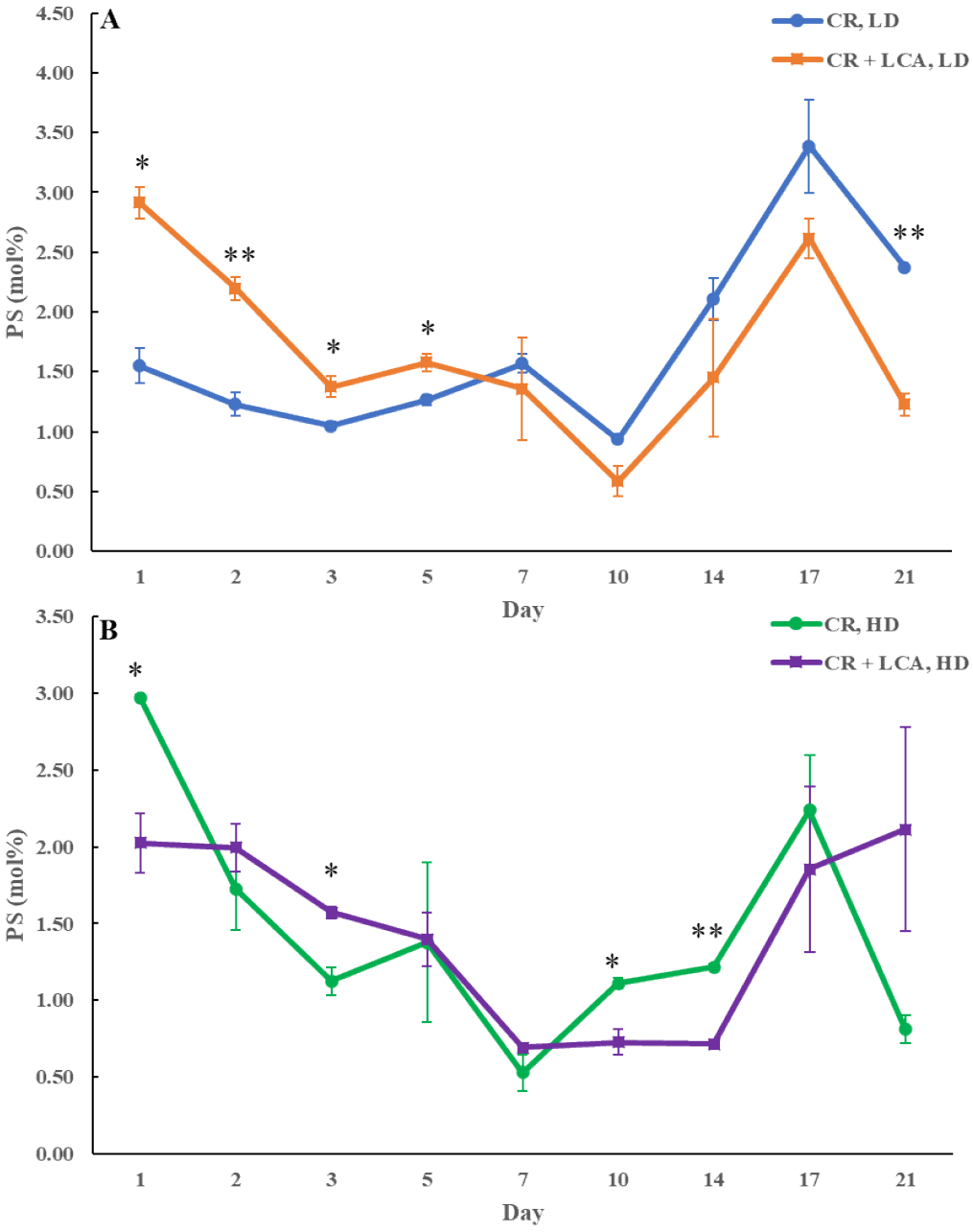

Figure 10.8: No significant and continuing changes in the concentrations of PS are observed within the HD and LD cell populations treated with LCA. WT cells were cultured in YP medium supplemented with 0.2% glucose (CR conditions) in the presence of 50 µM LCA or its absence. Cell aliquots were taken on different days of culturing. The Percoll density gradient centrifugation was used to purify HD and LD cells from these cell aliquots. LC-MS/MS was used to assess PS concentrations in these cells. Data are shown as means ± SD (n = 2; *$p < 0.05$**$p <$

0.01).

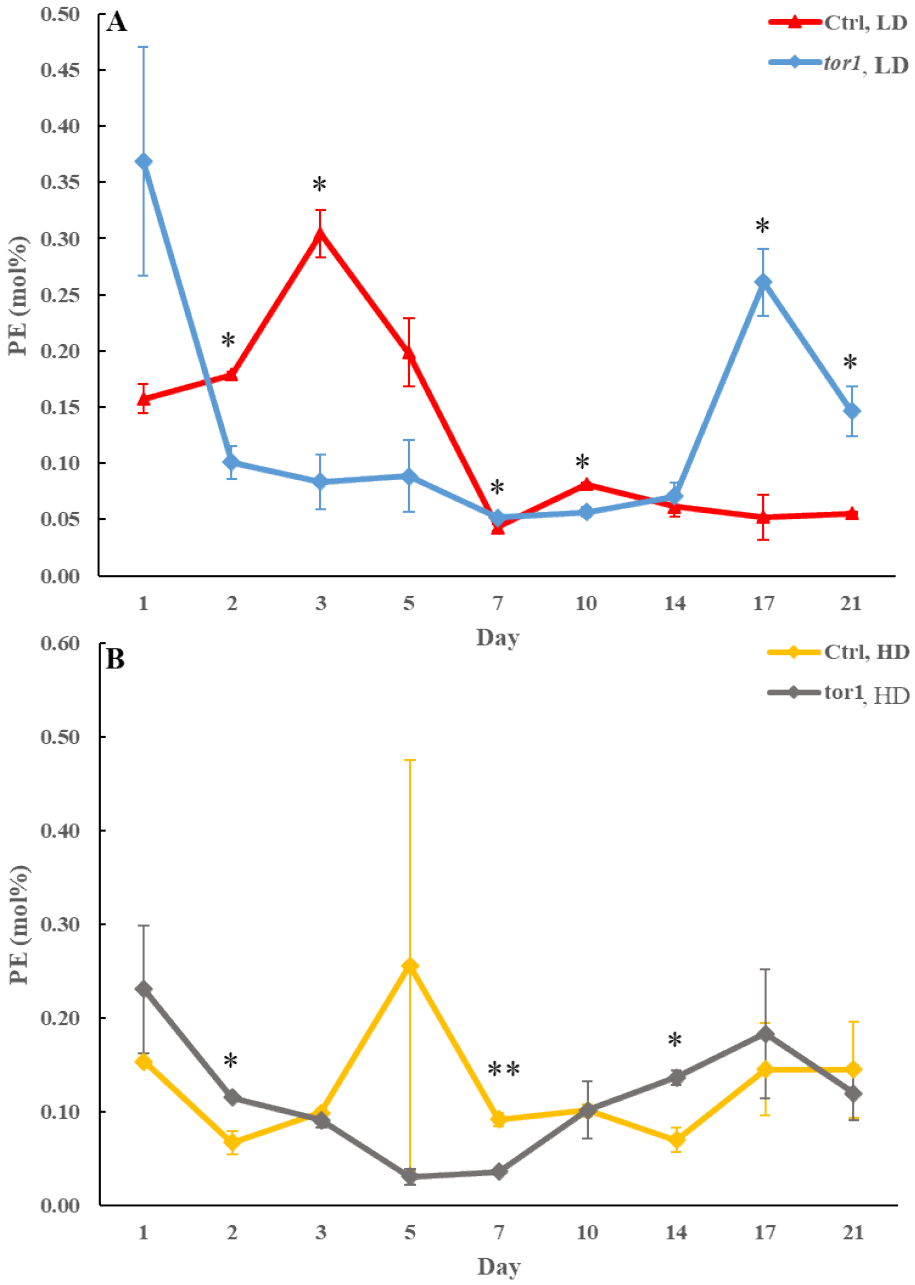

Figure 10.9: No significant and continuing changes in the concentrations of PE are observed within the HD and LD cell populations carrying the *tor1Δ* mutation. WT and *tor1Δ* cells were cultured in the YP medium supplemented with 2% glucose (non-CR conditions). Cell aliquots were taken on different days of culturing. The Percoll density gradient centrifugation was used to purify HD and LD cells from these cell aliquots. LC-MS/MS was used to assess PE concentrations in these cells. Data are shown as means ± SD (n = 2; *$p < 0.05$; **$p < 0.01$).

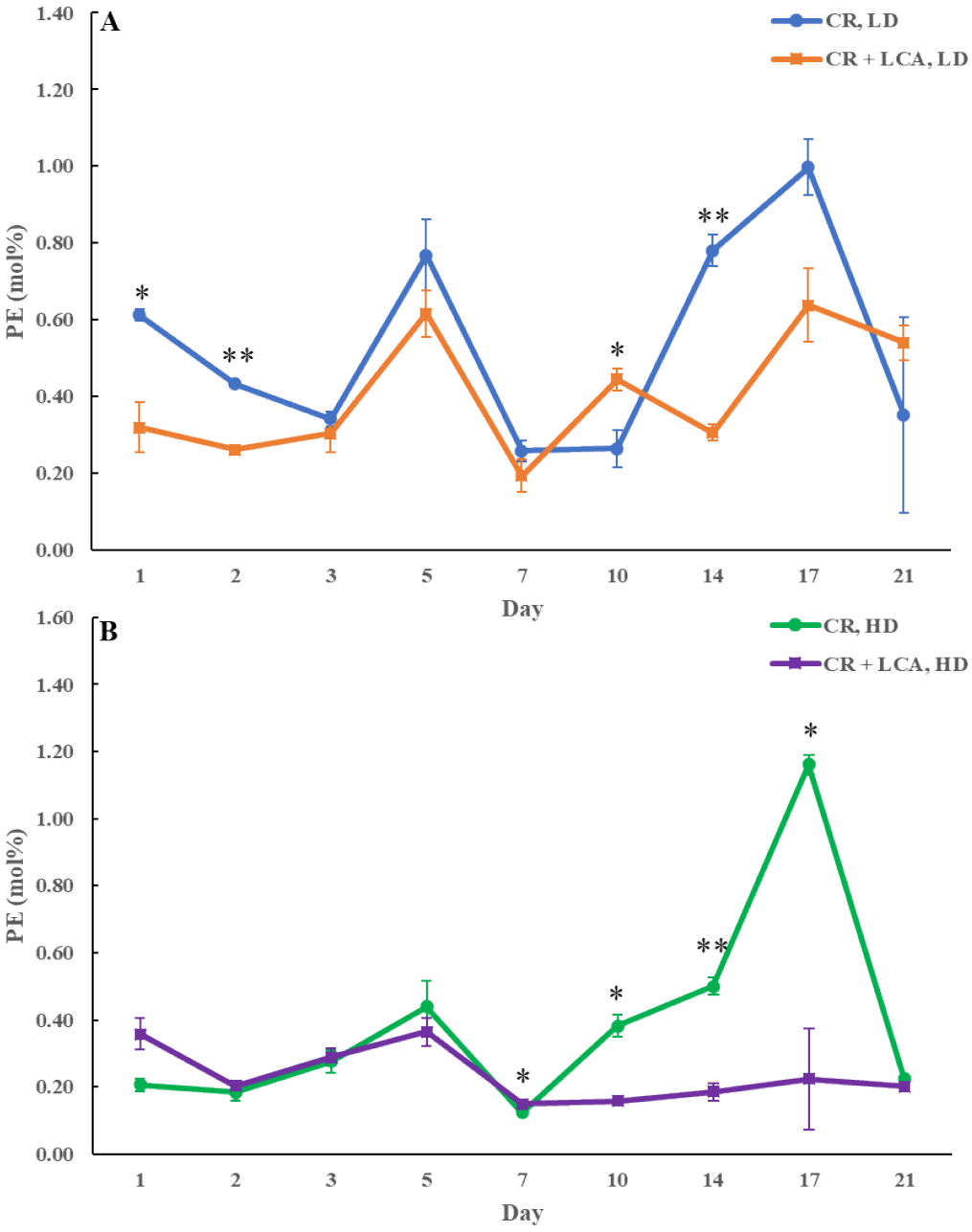

Figure 10.10: No significant and continuing changes in the concentrations of PE are observed within the HD and LD cell populations treated with LCA. WT cells were cultured in YP medium supplemented with 0.2% glucose (CR conditions) in the presence of 50 µM LCA or its absence. Cell aliquots were taken on different days of culturing. The Percoll density gradient centrifugation was used to purify HD and LD cells from these cell aliquots. LC-MS/MS was used to assess PE concentrations in these cells. Data are shown as means ± SD (n = 2; *$p < 0.05$).

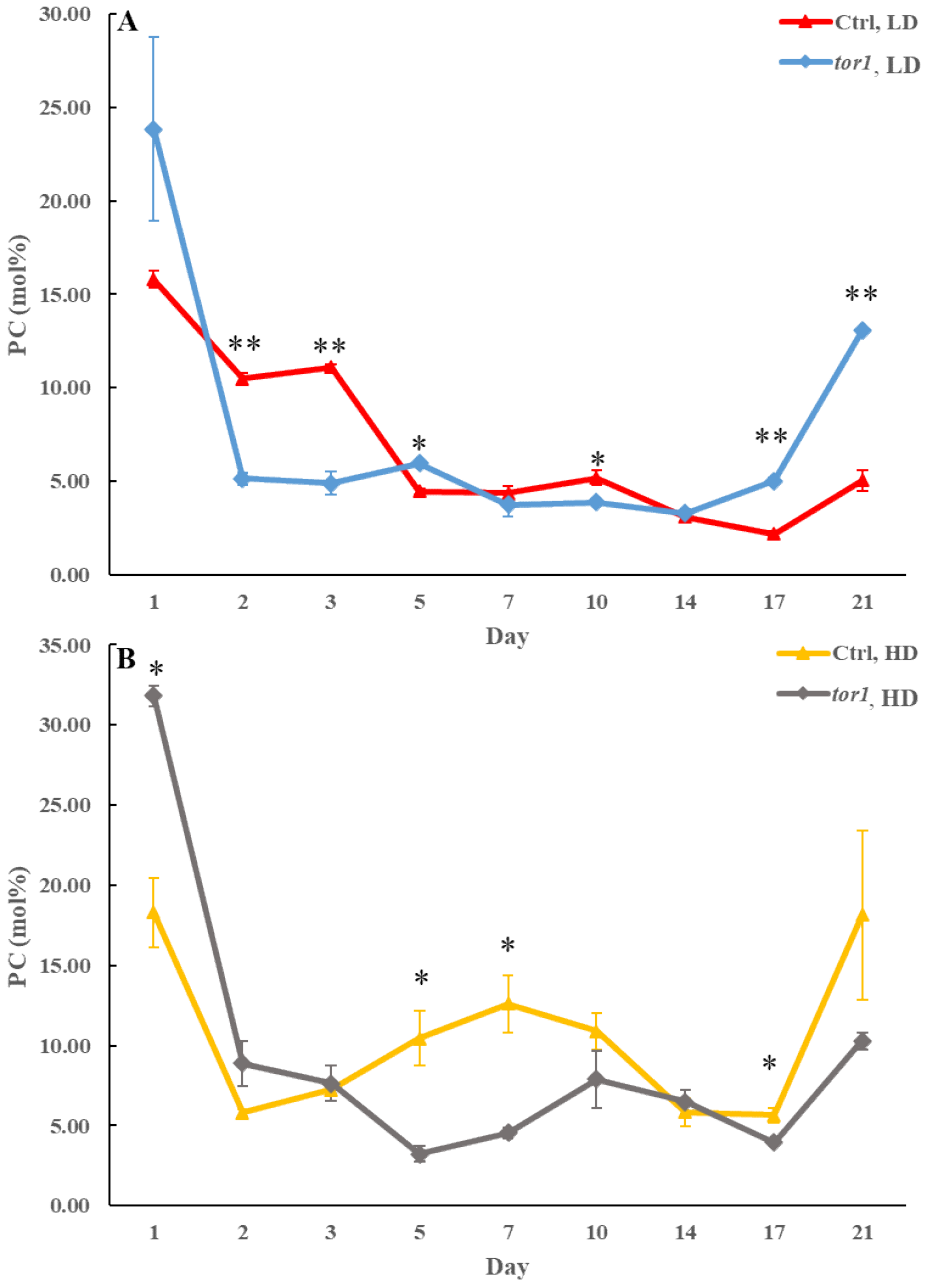

Figure 10.11: No significant and continuing changes in the concentrations of PC are observed within the HD and LD cell populations carrying the *tor1Δ* mutation. WT and *tor1Δ* cells were cultured in the YP medium supplemented with 2% glucose (non-CR conditions). Cell aliquots were taken on different days of culturing. The Percoll density gradient centrifugation was used to purify HD and LD cells from these cell aliquots. LC-MS/MS was used to assess PC concentrations in these cells. Data are shown as means ± SD (n = 2; *$p < 0.05$; **$p < 0.01$).

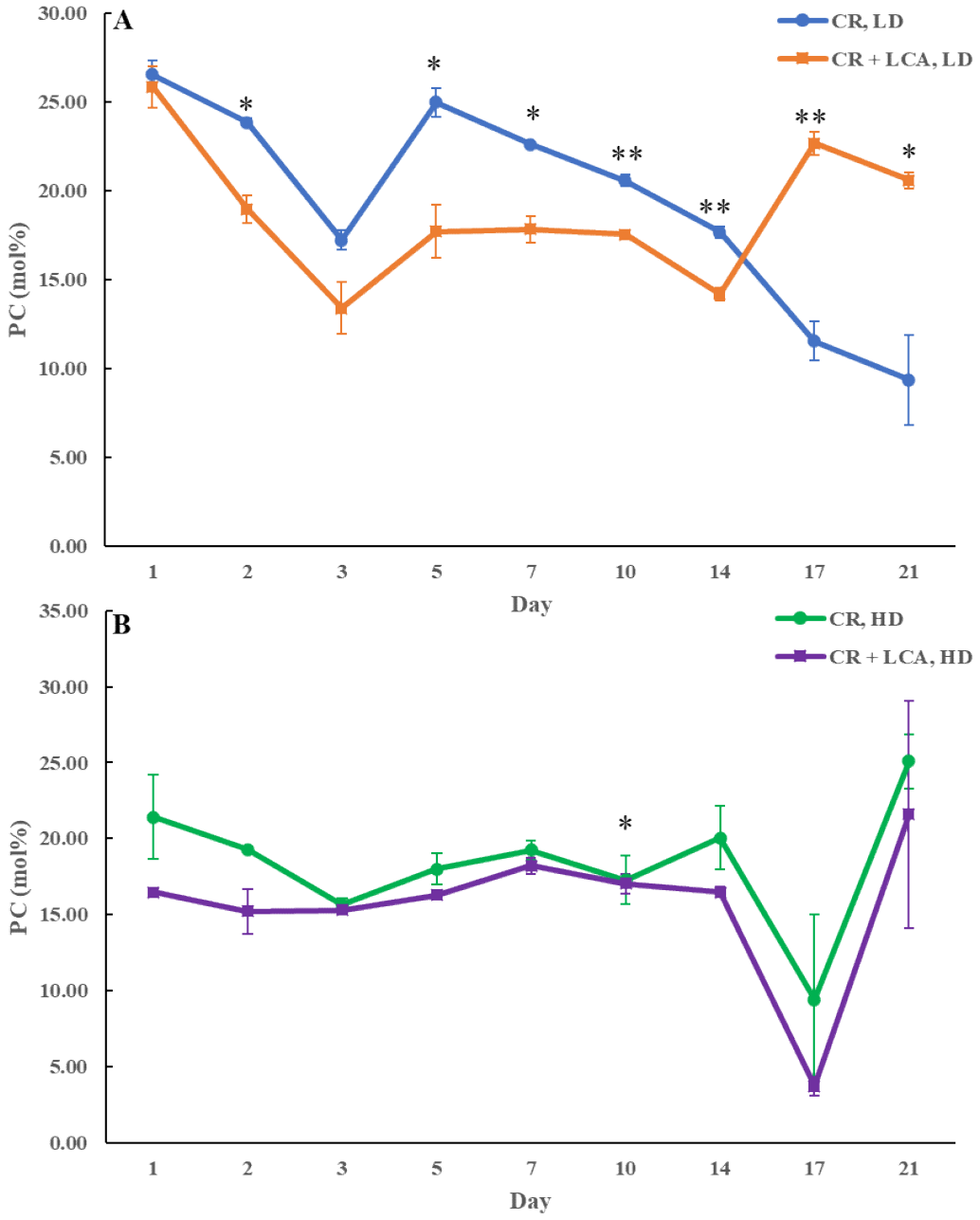

Figure 10.12: No significant and continuing changes in the concentrations of PC are observed within the HD and LD cell populations treated with LCA. WT cells were cultured in YP medium supplemented with 0.2% glucose (CR conditions) in the presence of 50 µM LCA or its absence. Cell aliquots were taken on different days of culturing. The Percoll density gradient centrifugation was used to purify HD and LD cells from these cell aliquots. LC-MS/MS was used to assess PC concentrations in these cells. Data are shown as means ± SD (n = 2; *$p < 0.05$; **$p < 0.01$).

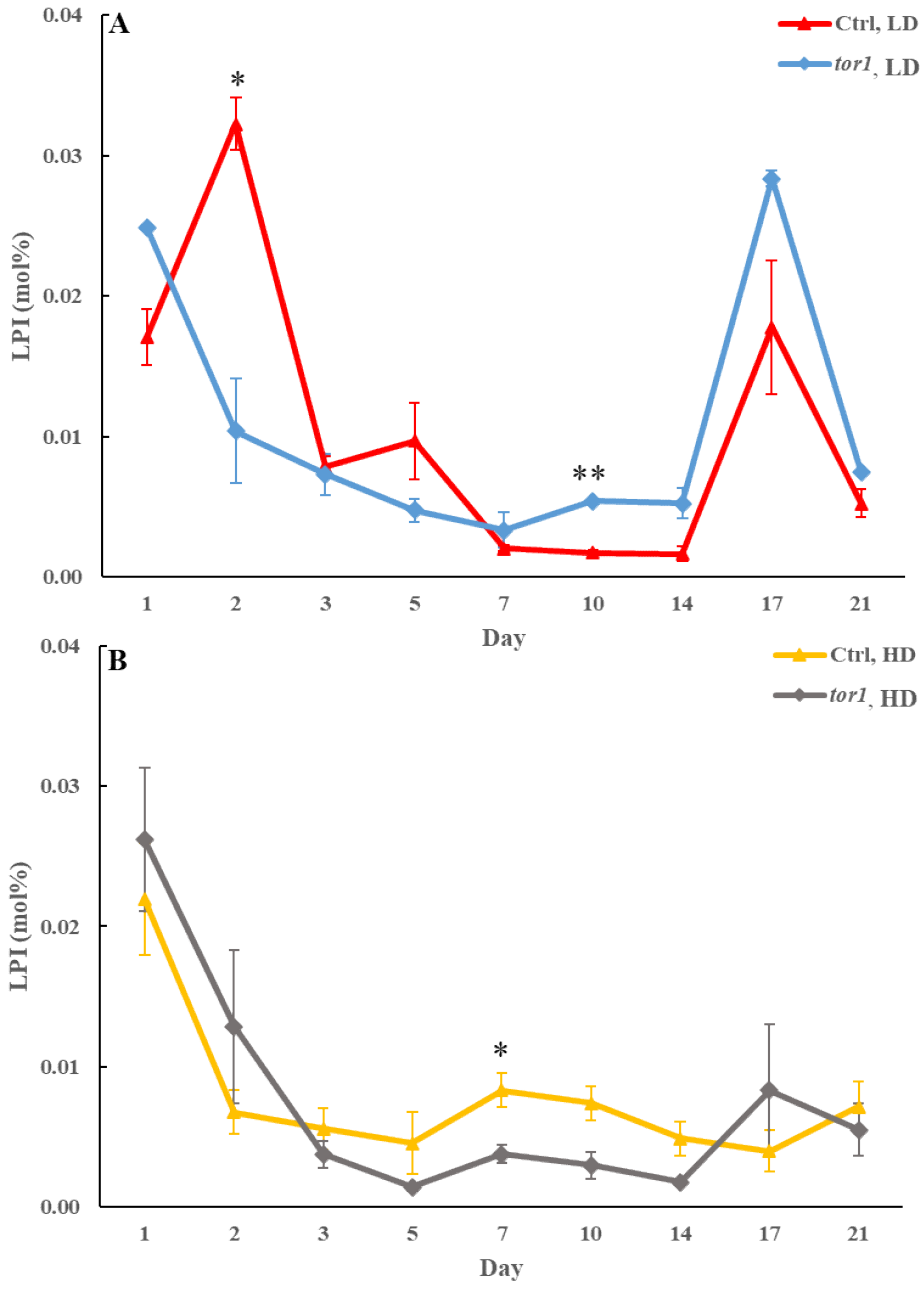

Figure 10.13: No significant and continuing changes in the concentrations of LPI are observed within the HD and LD cell populations carrying the *tor1Δ* mutation. WT and *tor1Δ* cells were cultured in the YP medium supplemented with 2% glucose (non-CR conditions). Cell aliquots were taken on different days of culturing. The Percoll density gradient centrifugation was used to purify HD and LD cells from these cell aliquots. LC-MS/MS was used to assess LPI concentrations in these cells. Data are shown as means ± SD (n = 2; *$p < 0.05$; **$p < 0.01$).

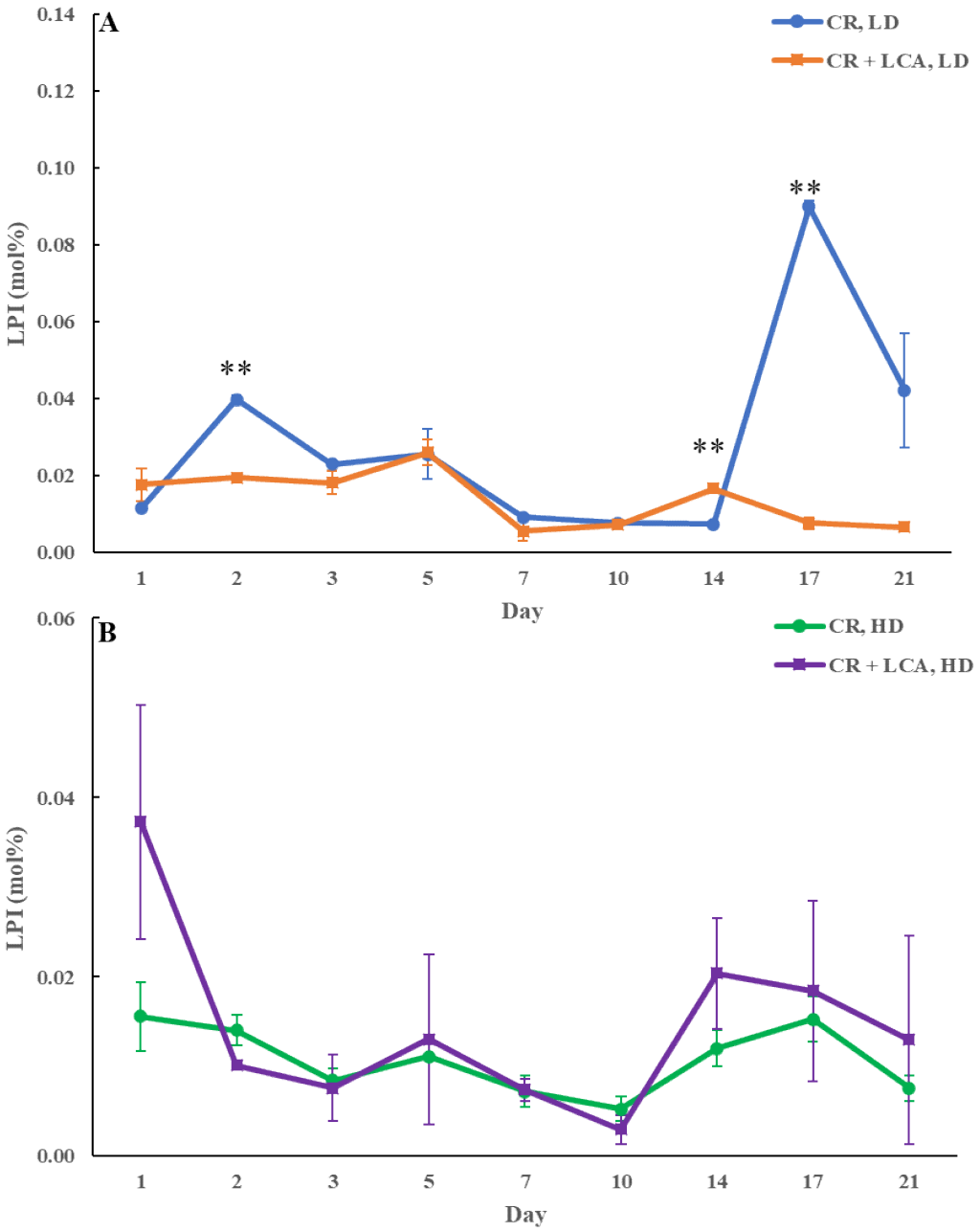

Figure 10.14: No significant and continuing changes in the concentrations of LPI are observed within the HD and LD cell populations treated with LCA. WT cells were cultured in YP medium supplemented with 0.2% glucose (CR conditions) in the presence of 50 µM LCA or its absence. Cell aliquots were taken on different days of culturing. The Percoll density gradient centrifugation was used to purify HD and LD cells from these cell aliquots. LC-MS/MS was used to assess LPI concentrations in these cells. Data are shown as means ± SD (n = 2; $^{**}p < 0.01$).

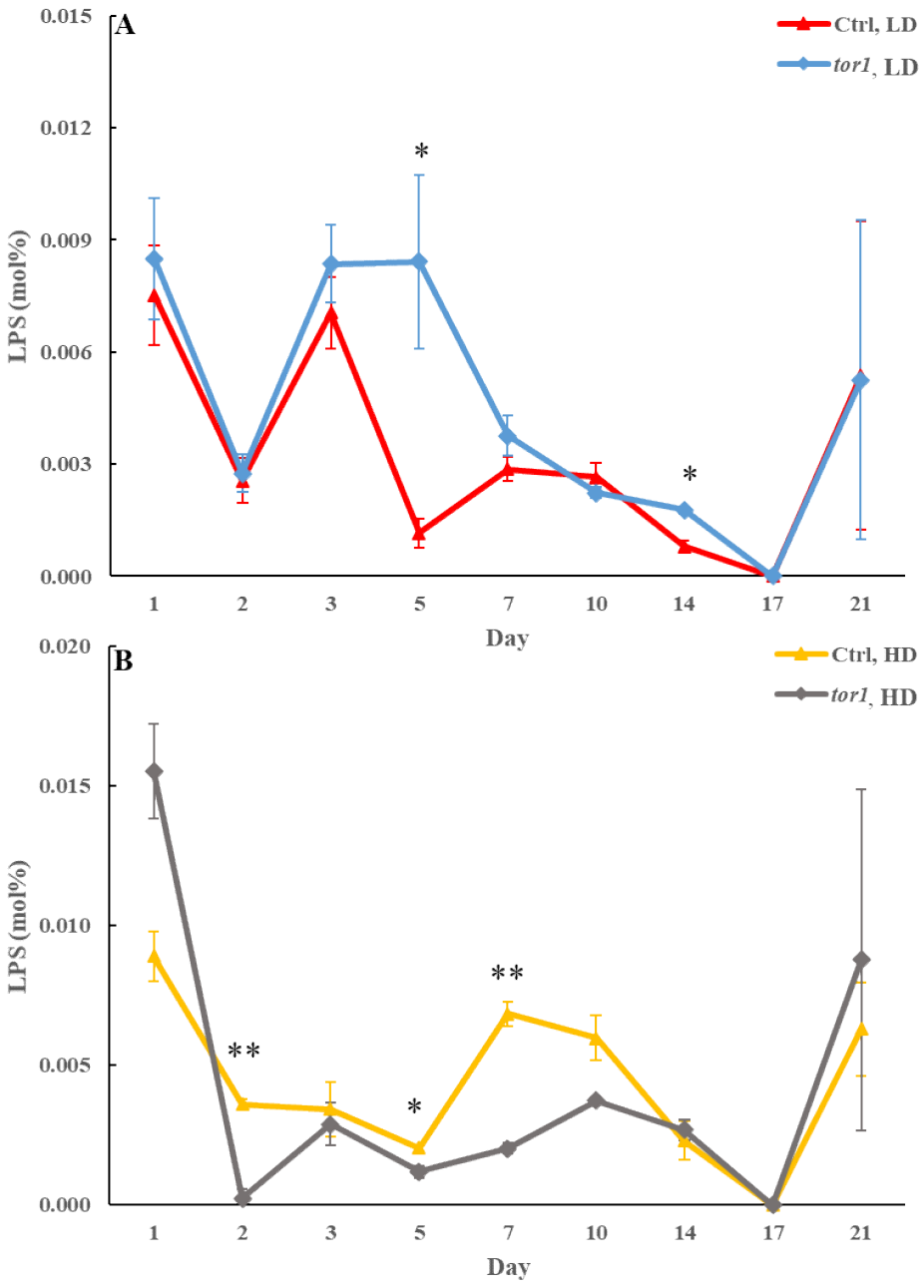

Figure 10.15: No significant and continuing changes in the concentrations of LPS are observed within the HD and LD cell populations carrying the *tor1Δ* mutation. WT and *tor1Δ* cells were cultured in the YP medium supplemented with 2% glucose (non-CR conditions). Cell aliquots were taken on different days of culturing. The Percoll density gradient centrifugation was used to purify HD and LD cells from these cell aliquots. LC-MS/MS was used to assess LPS concentrations in these cells. Data are shown as means ± SD (n = 2; *$p < 0.05$; **$p < 0.01$).

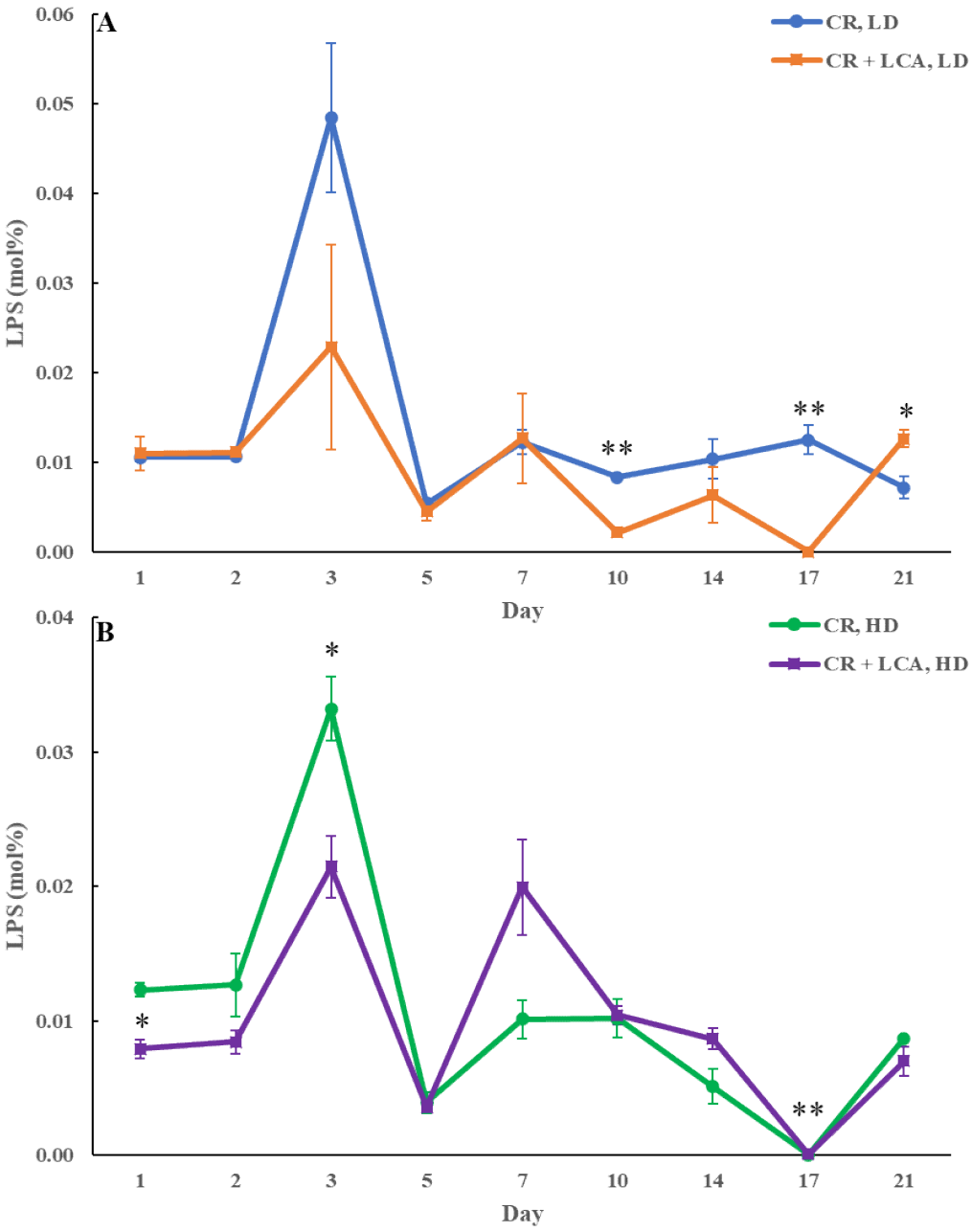

Figure 10.16: No significant and continuing changes in the concentrations of LPS are observed within the HD and LD cell populations treated with LCA. WT cells were cultured in YP medium supplemented with 0.2% glucose (CR conditions) in the presence of 50 µM LCA or its absence. Cell aliquots were taken on different days of culturing. The Percoll density gradient centrifugation was used to purify HD and LD cells from these cell aliquots. LC-MS/MS was used to assess LPS concentrations in these cells. Data are shown as means ± SD (n = 2; *$p < 0.05$; **$p < 0.01$).

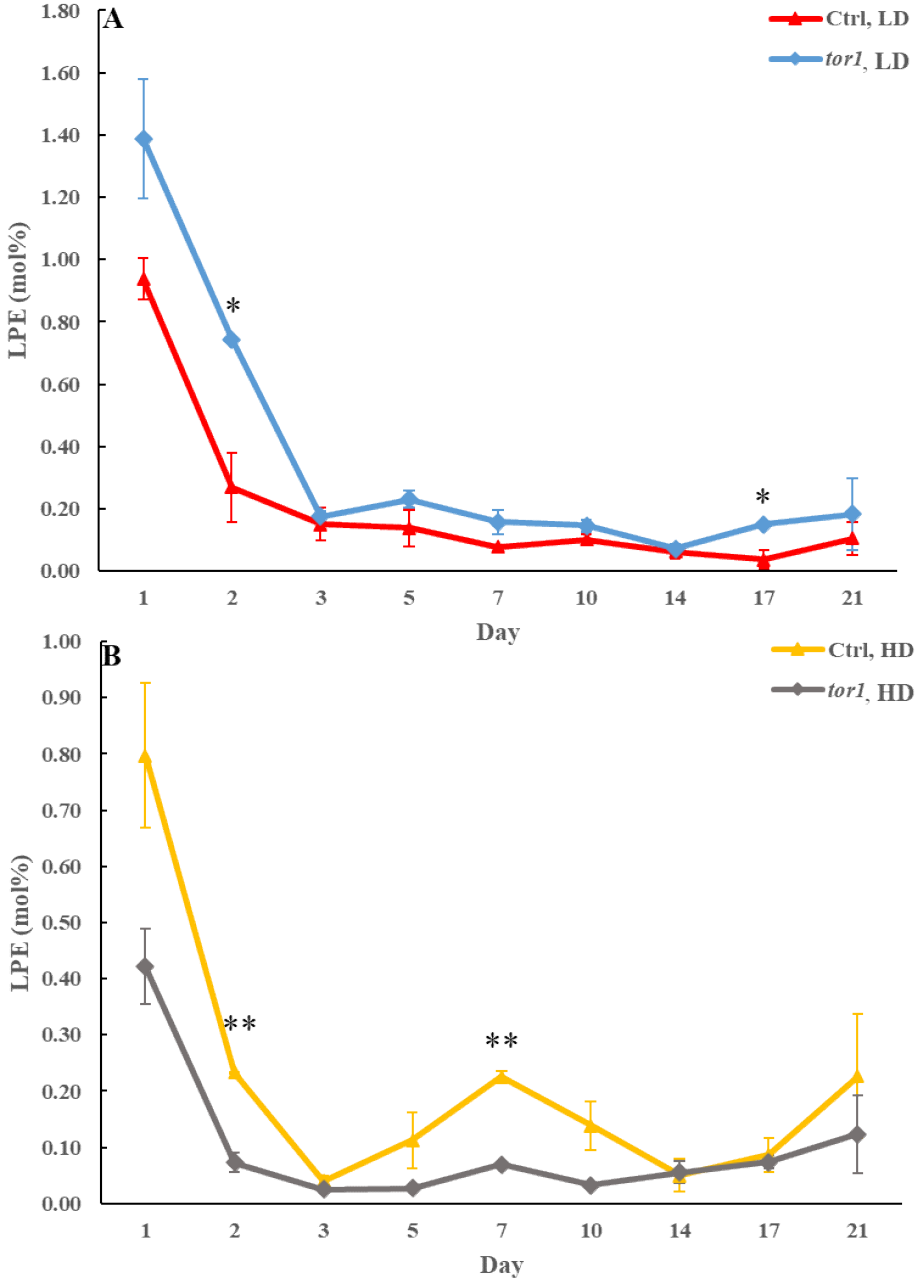

Figure 10.17: No significant and continuing changes in the concentrations of LPE are observed within the HD and LD cell populations carrying the *tor1Δ* mutation. WT and *tor1Δ* cells were cultured in the YP medium supplemented with 2% glucose (non-CR conditions). Cell aliquots were taken on different days of culturing. The Percoll density gradient centrifugation was used to purify HD and LD cells from these cell aliquots. LC-MS/MS was used to assess LPE concentrations in these cells. Data are shown as means ± SD (n = 2; *$p < 0.05$; **$p < 0.01$).

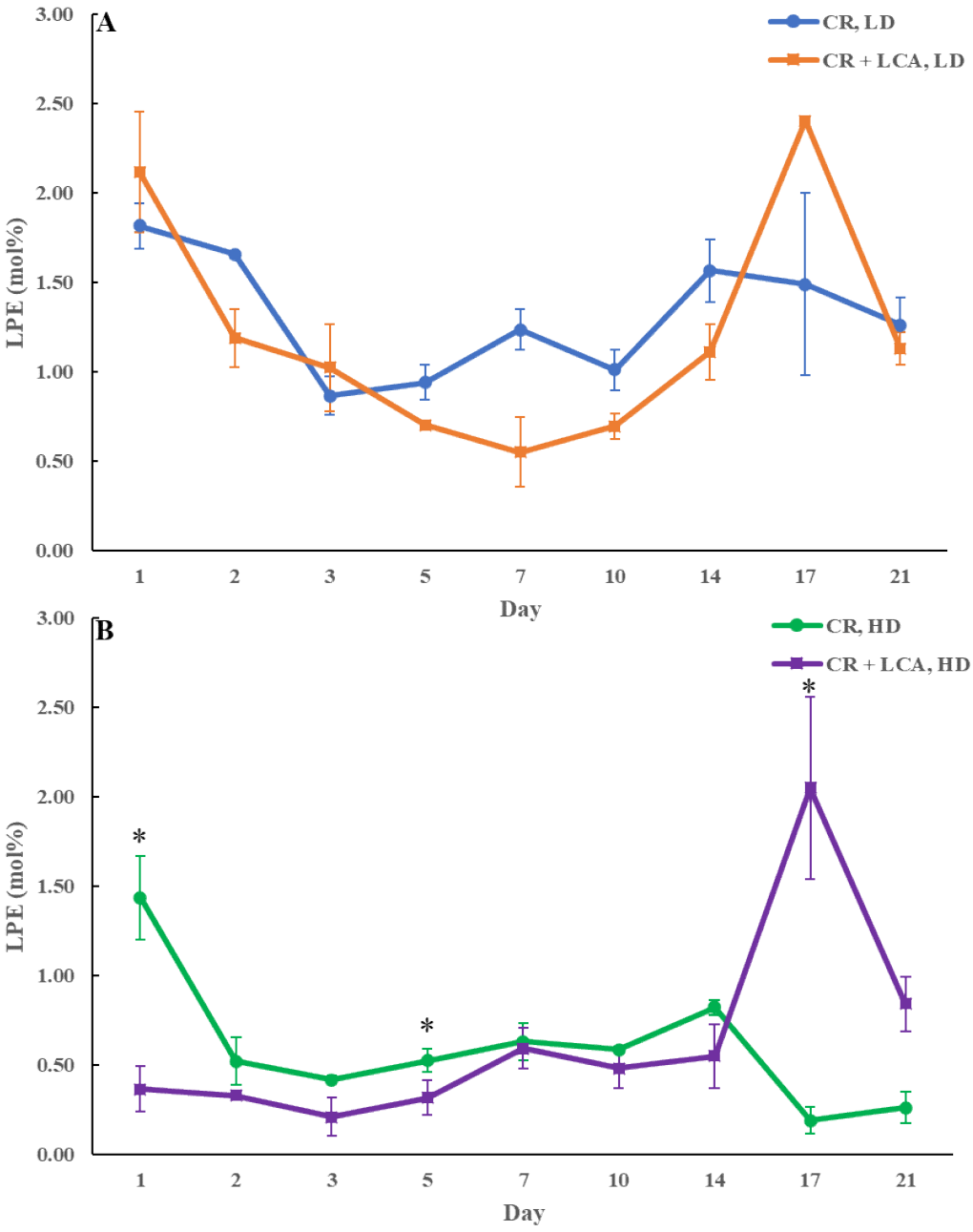

Figure 10.18: No significant and continuing changes in the concentrations of LPE are observed within the HD and LD cell populations treated with LCA. WT cells were cultured in YP medium supplemented with 0.2% glucose (CR conditions) in the presence of 50 µM LCA or its absence. Cell aliquots were taken on different days of culturing. The Percoll density gradient centrifugation was used to purify HD and LD cells from these cell aliquots. LC-MS/MS was used to assess LPE concentrations in these cells. Data are shown as means ± SD (n = 2; *$p < 0.05$; **$p < 0.01$).

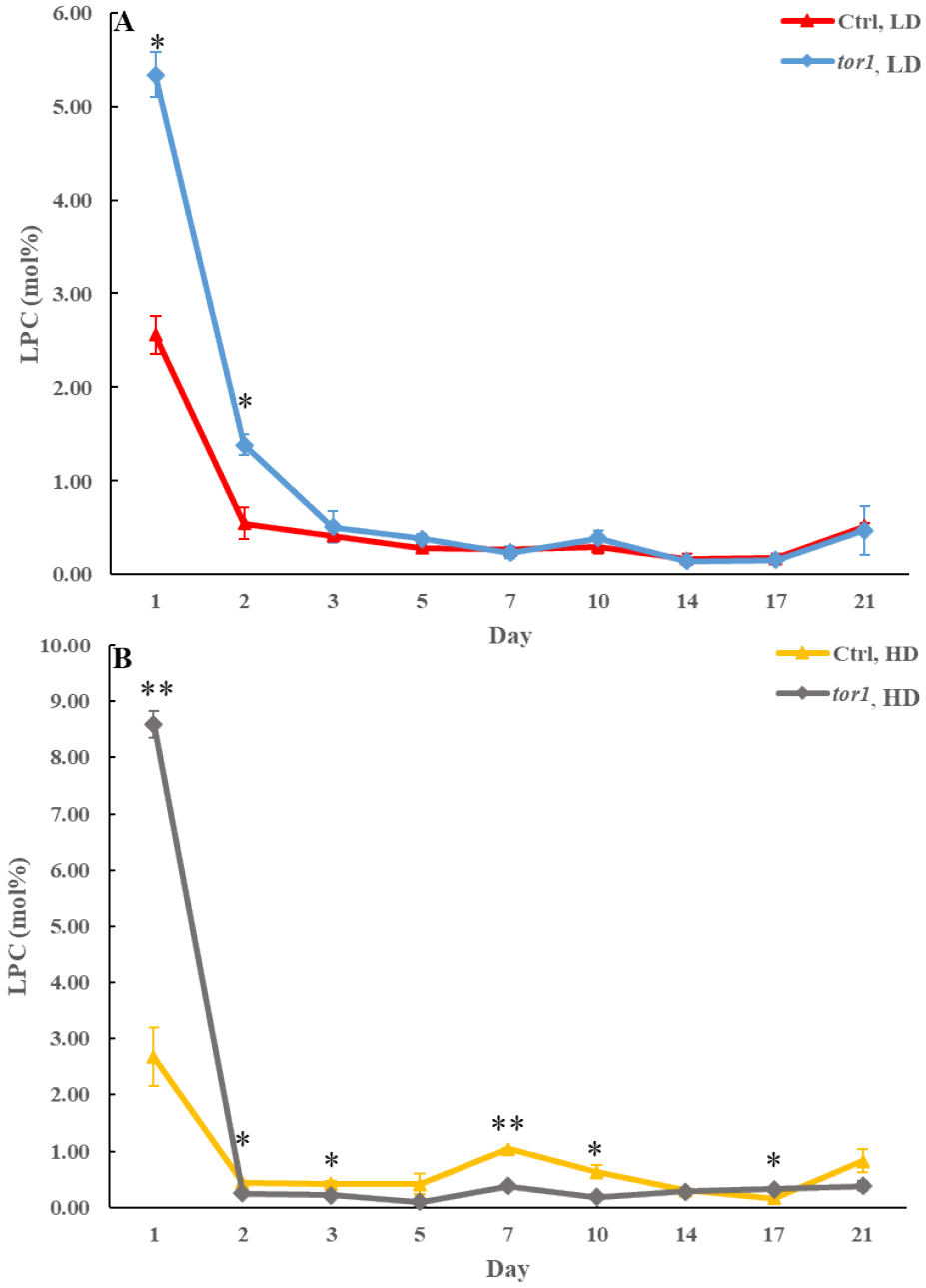

Figure 10.19: No significant and continuing changes in the concentrations of LPC are observed within the HD and LD cell populations carrying the *tor1Δ* mutation. WT and *tor1Δ* cells were cultured in the YP medium supplemented with 2% glucose (non-CR conditions). Cell aliquots were taken on different days of culturing. The Percoll density gradient centrifugation was used to purify HD and LD cells from these cell aliquots. LC-MS/MS was used to assess LPC concentrations in these cells. Data are shown as means ± SD (n = 2; *$p < 0.05$; **$p < 0.01$).

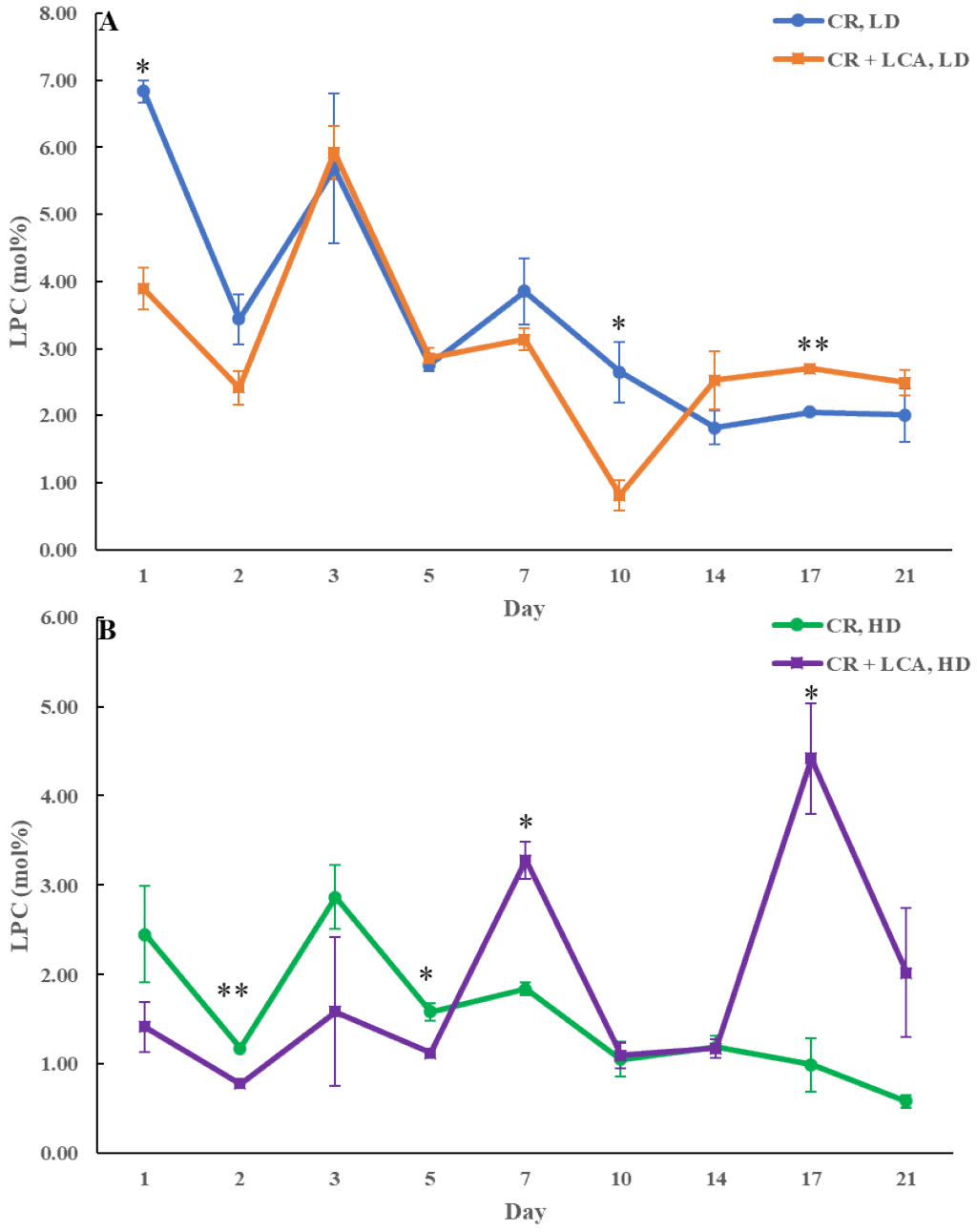

Figure 10.20: No significant and continuing changes in the concentrations of LPC are observed within the HD and LD cell populations treated with LCA. WT cells were cultured in YP medium supplemented with 0.2% glucose (CR conditions) in the presence of 50 µM LCA or its absence. Cell aliquots were taken on different days of culturing. The Percoll density gradient centrifugation was used to purify HD and LD cells from these cell aliquots. LC-MS/MS was used to assess LPC concentrations in these cells. Data are shown as means ± SD (n = 2; *$p < 0.05$; **$p < 0.01$).

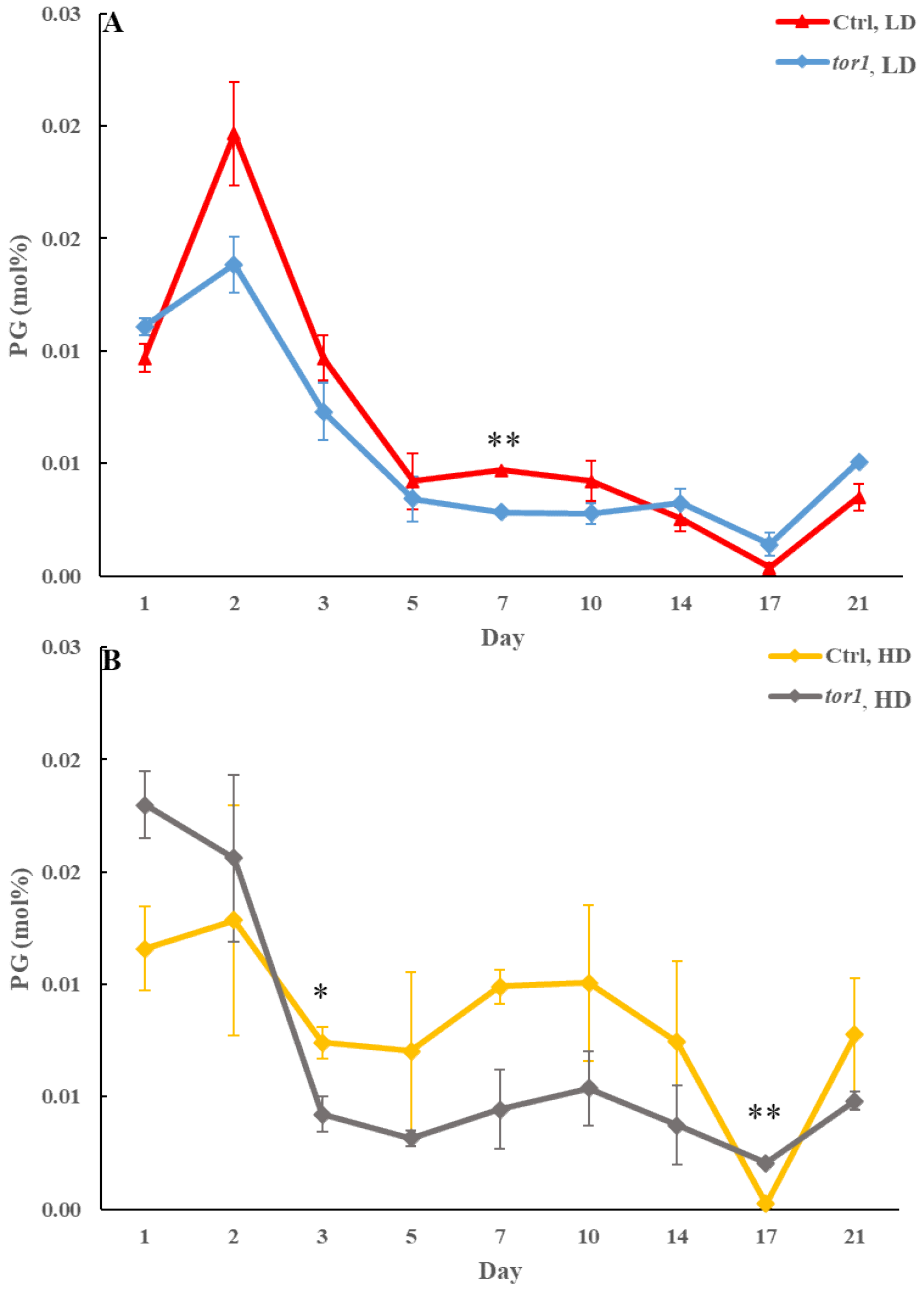

Figure 10.21: No significant and continuing changes in the concentrations of PG are observed within the HD and LD cell populations carrying the *tor1Δ* mutation. WT and *tor1Δ* cells were cultured in the YP medium supplemented with 2% glucose (non-CR conditions). Cell aliquots were taken on different days of culturing. The Percoll density gradient centrifugation was used to purify HD and LD cells from these cell aliquots. LC-MS/MS was used to assess PG concentrations in these cells. Data are shown as means ± SD (n = 2; *$p < 0.05$; **$p < 0.01$).

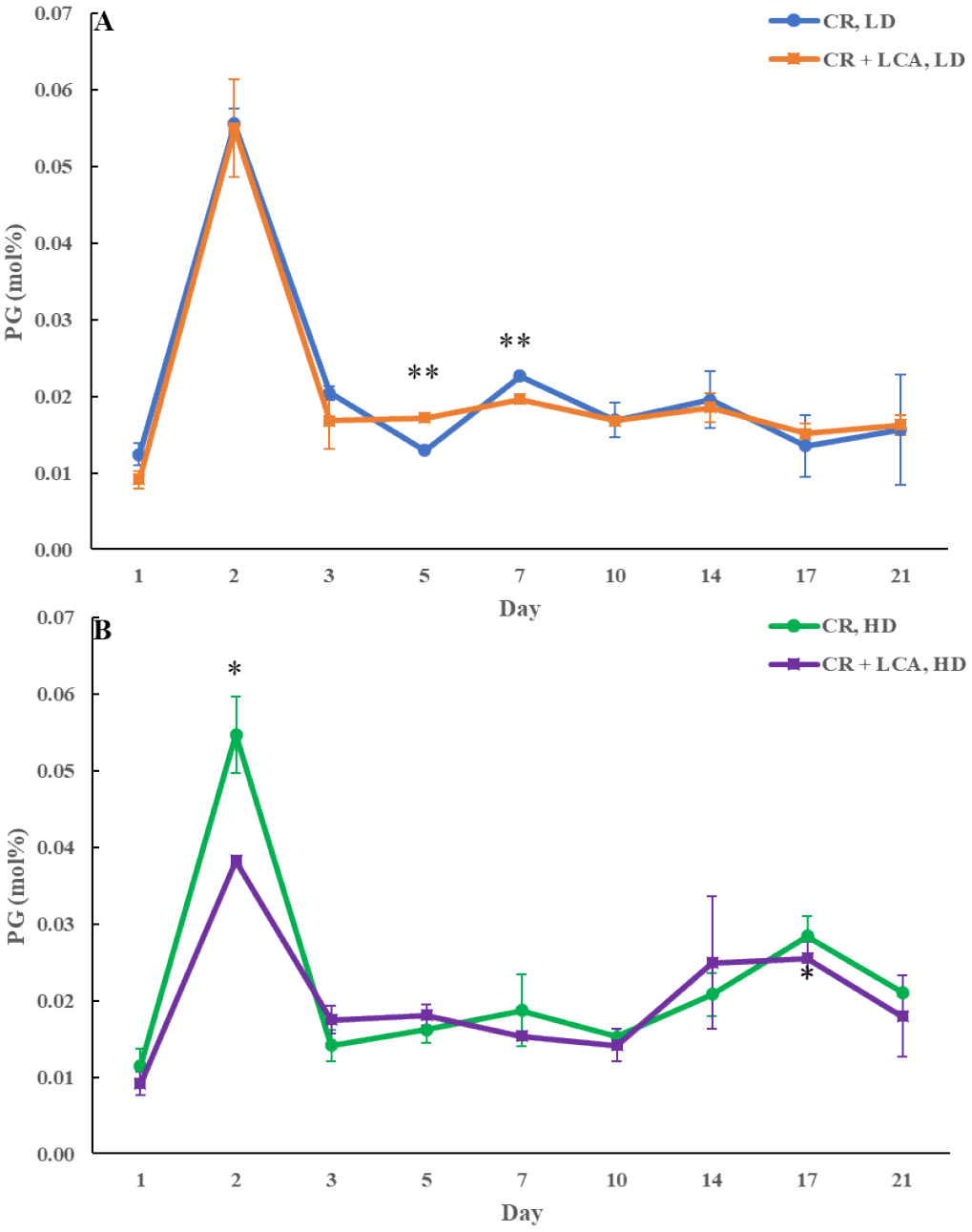

Figure 10.22: No significant and continuing changes in the concentrations of PG are observed within the HD and LD cell populations treated with LCA. WT cells were cultured in YP medium supplemented with 0.2% glucose (CR conditions) in the presence of 50 µM LCA or its absence. Cell aliquots were taken on different days of culturing. The Percoll density gradient centrifugation was used to purify HD and LD cells from these cell aliquots. LC-MS/MS was used to assess PG concentrations in these cells. Data are shown as means ± SD (n = 2; *$p < 0.05$; **$p < 0.01$).

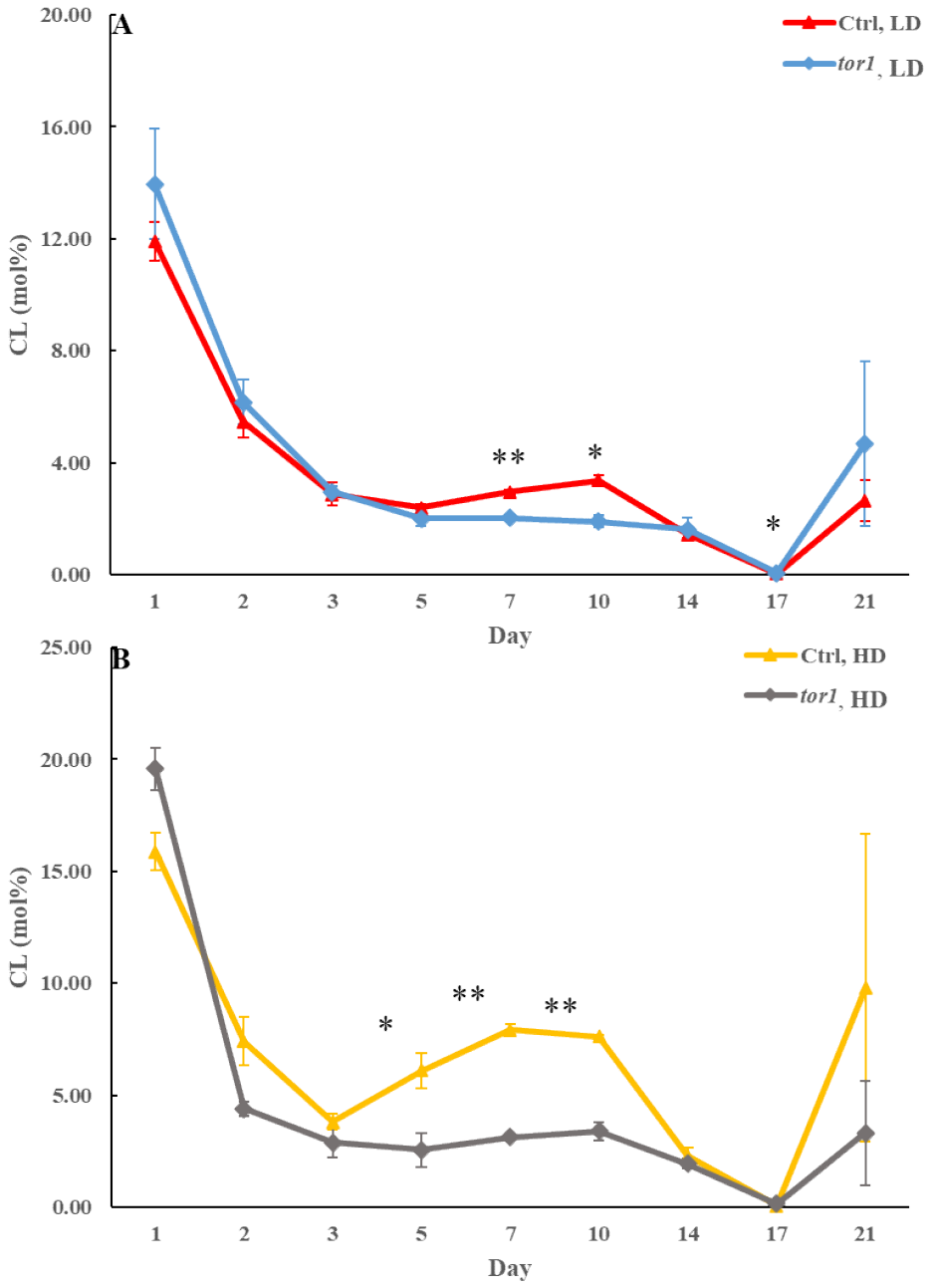

Figure 10.23: No significant and continuing changes in the concentrations of CL are observed within the HD and LD cell populations carrying the *tor1Δ* mutation. WT and *tor1Δ* cells were cultured in the YP medium supplemented with 2% glucose (non-CR conditions). Cell aliquots were taken on different days of culturing. The Percoll density gradient centrifugation was used to purify HD and LD cells from these cell aliquots. LC-MS/MS was used to assess CL concentrations in these cells. Data are shown as means ± SD (n = 2; *$p < 0.05$; **$p < 0.01$).

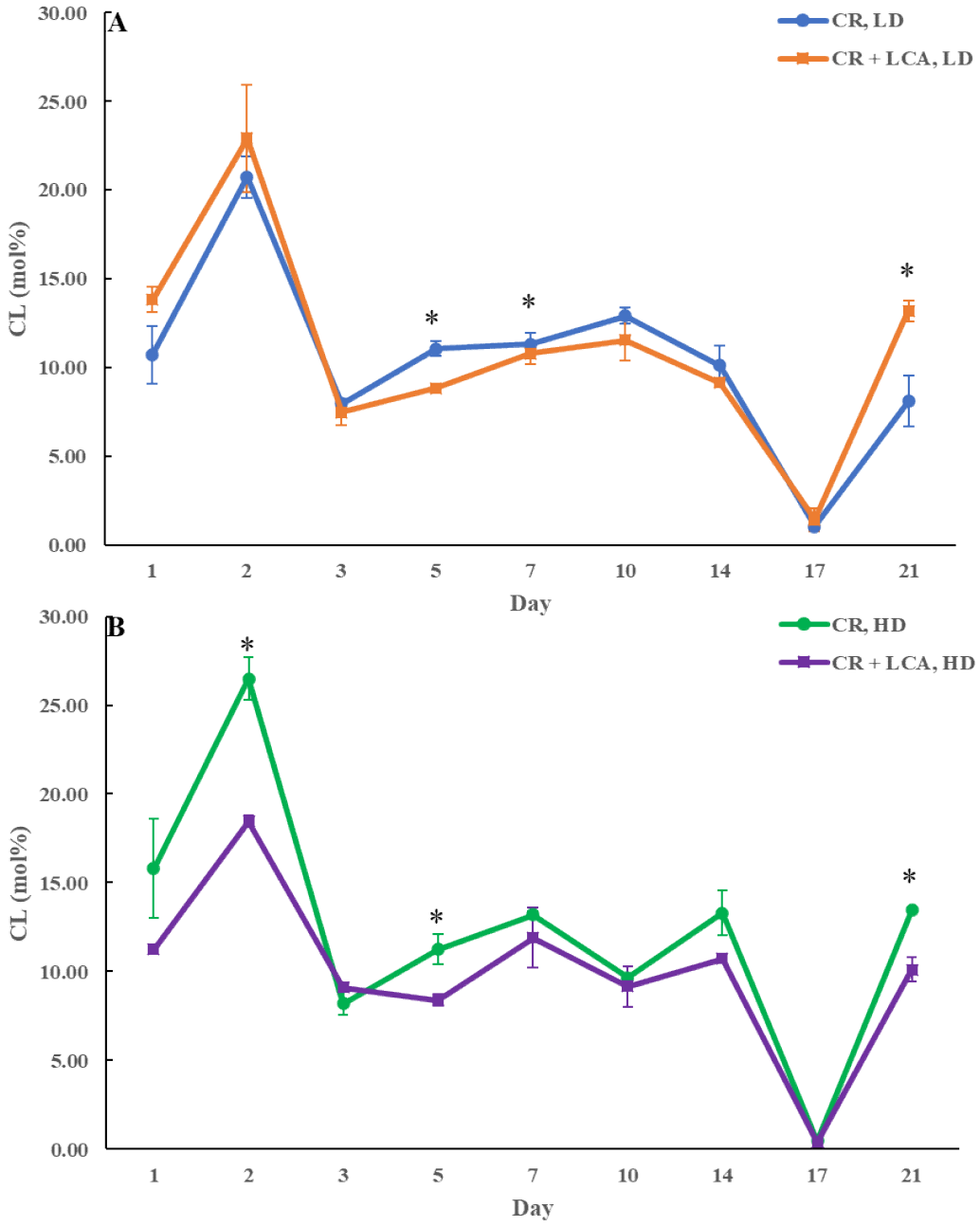

Figure 10.24: No significant and continuing changes in the concentrations of CL are observed within the HD and LD cell populations treated with LCA. WT cells were cultured in YP medium supplemented with 0.2% glucose (CR conditions) in the presence of 50 µM LCA or its absence. Cell aliquots were taken on different days of culturing. The Percoll density gradient centrifugation was used to purify HD and LD cells from these cell aliquots. LC-MS/MS was used to assess CL concentrations in these cells. Data are shown as means ± SD (n = 2; *$p < 0.05$).

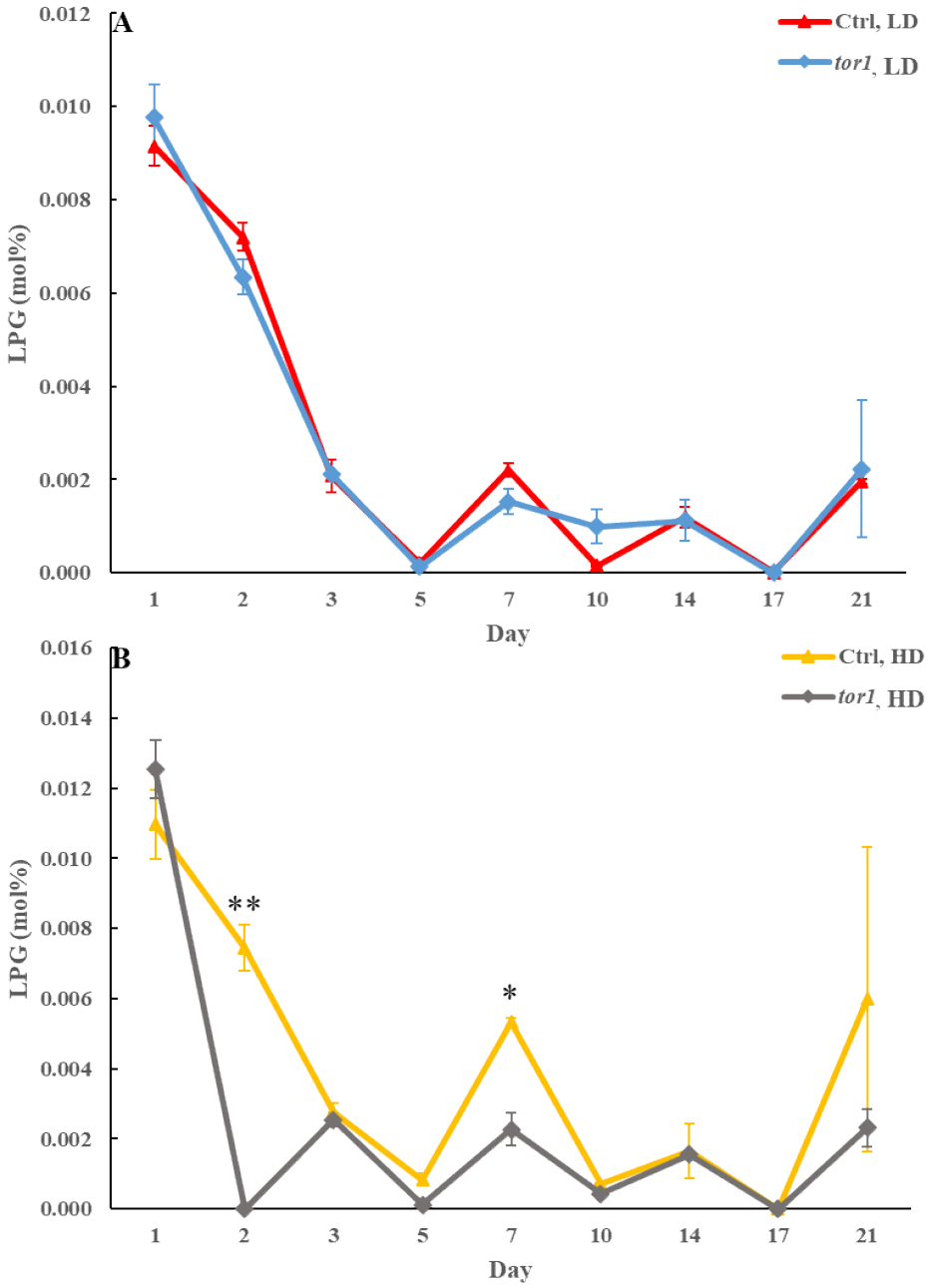

Figure 10.25: No significant and continuing changes in the concentrations of LPG are observed within the HD and LD cell populations carrying the *tor1Δ* mutation. WT and *tor1Δ* cells were cultured in the YP medium supplemented with 2% glucose (non-CR conditions). Cell aliquots were taken on different days of culturing. The Percoll density gradient centrifugation was used to purify HD and LD cells from these cell aliquots. LC-MS/MS was used to assess LPG concentrations in these cells. Data are shown as means ± SD (n = 2; *$p < 0.05$; **$p < 0.01$).

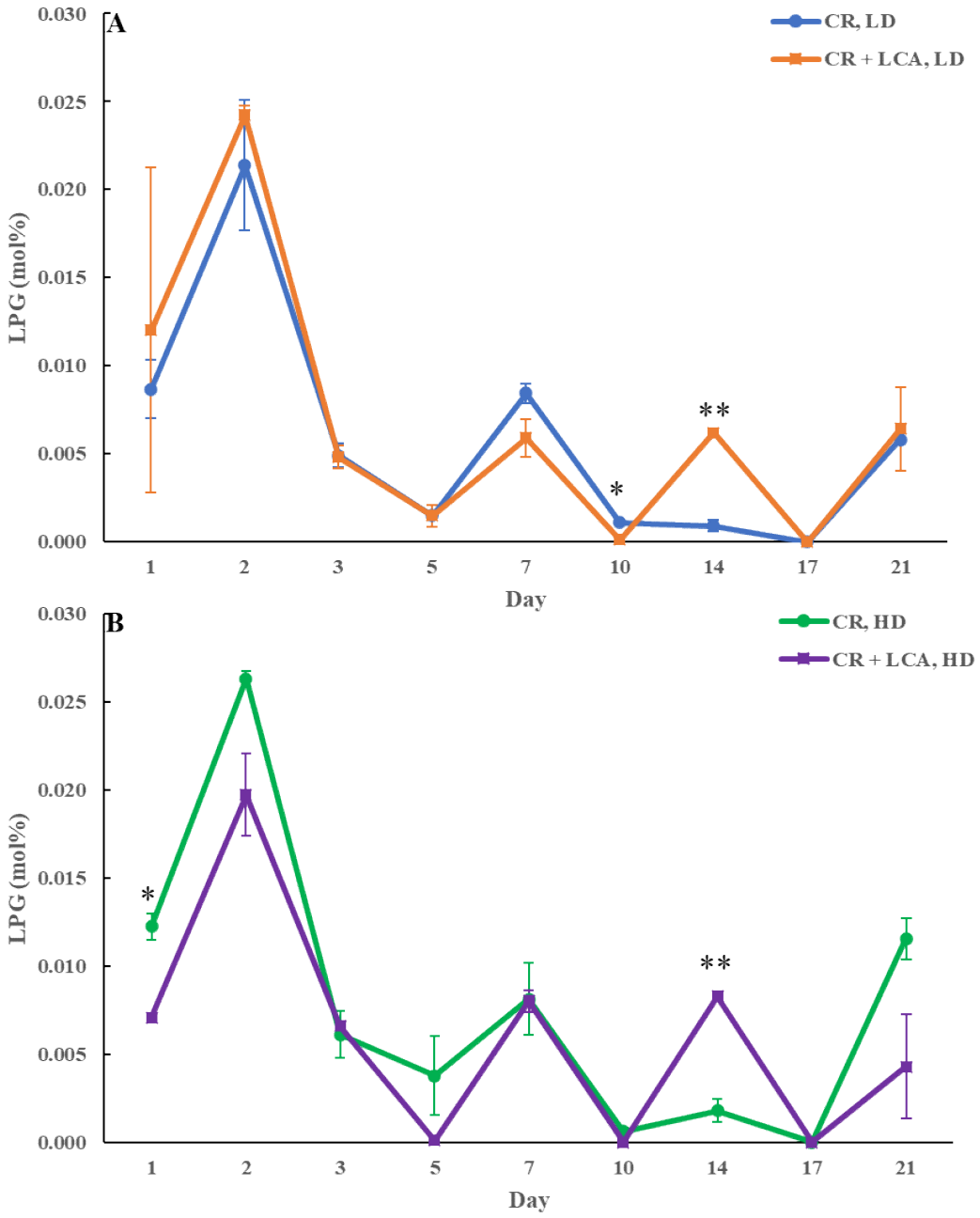

Figure 10.26: No significant and continuing changes in the concentrations of LPG are observed within the HD and LD cell populations treated with LCA. WT cells were cultured in YP medium supplemented with 0.2% glucose (CR conditions) in the presence of 50 µM LCA or its absence. Cell aliquots were taken on different days of culturing. The Percoll density gradient centrifugation was used to purify HD and LD cells from these cell aliquots. LC-MS/MS was used to assess LPG concentrations in these cells. Data are shown as means ± SD (n = 2; *$p < 0.05$; **$p < 0.01$).

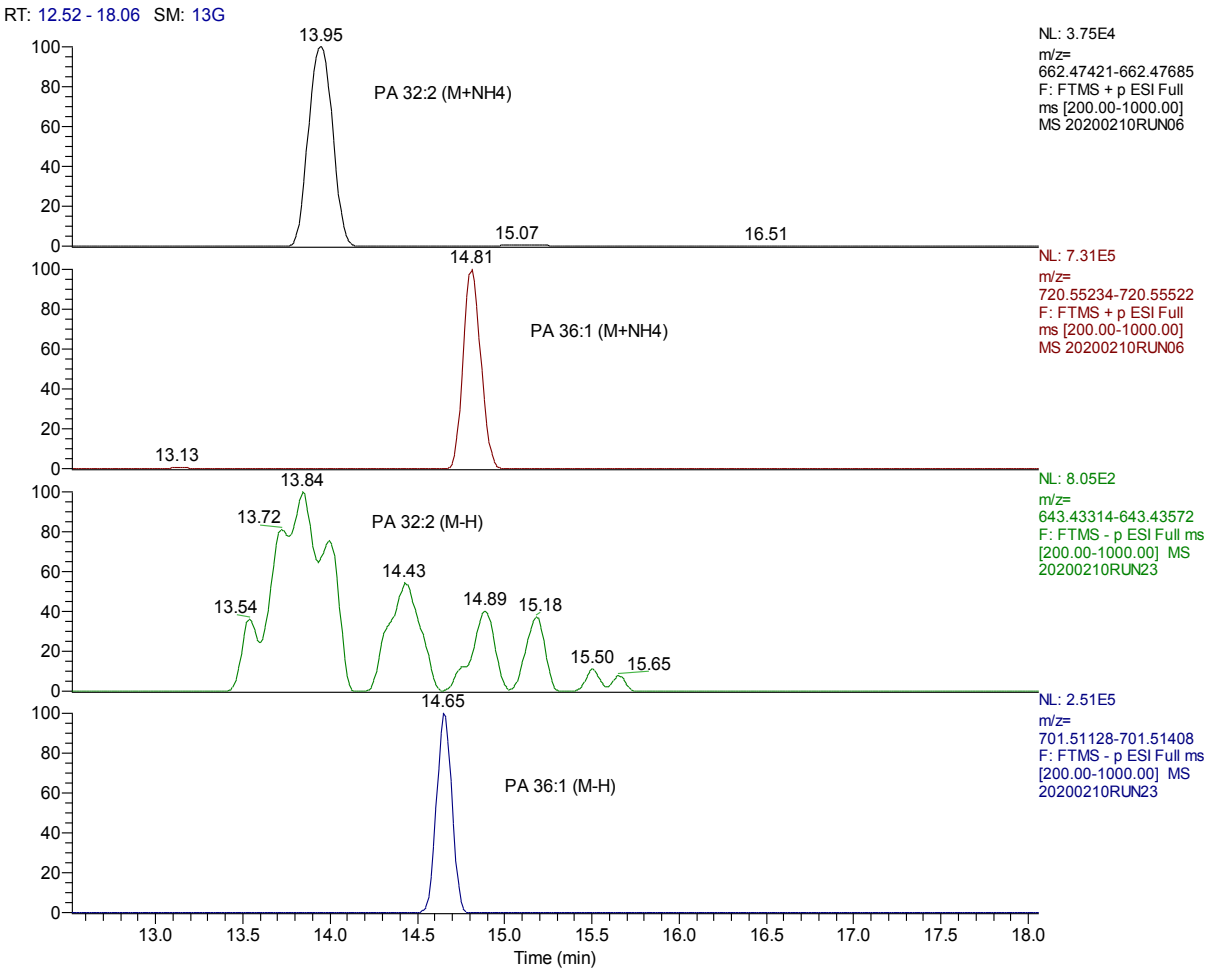

Figure 10.27: Phosphatidic Acid species are better detected in positive mode as an ammonium adduct.

Compound Name	MW	RT (min)	[M+H]+	[M-H]-
dodecatrienol	180.15141	1.4	181.15863	
4-Vinylcyclohexene	108.09381	1.43	109.10108	
Erucamide	337.33443	1.43	338.34177	
Oleamide	281.27181	1.446	282.27911	
Sphingosine (d18:1)	299.28237	1.47	300.28979	
Paradol	278.18712	1.59	279.19443	
16-Hydroxyhexadecanoic acid	272.23466	1.6	271.22726	
Triphenylphosphine oxide	278.08598	1.615	279.09326	
N,N-Dimethylaniline	121.08911	1.64	122.09638	
Triprolidine	278.17864	1.64	279.186	
Ethionine	163.06667	1.68	164.07396	
Palmitoyl ethanolamide	299.28237	1.761	300.28964	
nylon cyclic dimer	226.16844	1.78	227.17572	
7-Oxoheptanoic acid	144.07867	1.8	143.07133	
D-Sphingosine	299.5	1.839	300.28976	
Ripazepam	268.13249	1.89	269.13965	
(Z)-dehydrobutyrine	101.04757	1.91	102.05485	
apronalide	184.12113	1.91	185.12842	
gamma-Aminobutyric acid	103.06322	2.21	104.0705	
Phenethylamine	121.08908	2.26	122.09638	
Ureidoisobutyric acid	146.06914	3.15	147.07642	
trimethadione	143.05828	3.33	144.06546	
N5-METHYLGLUTAMINE	160.08479	3.33	161.0921	
7,8-Diaminononanoic acid	188.15244	3.33	189.15977	
Leucineamide	130.11061	3.51	131.11789	
Pyridoxine	169.07385	3.83	170.08116	
N,N-Dimethylacetamide	87.06825	3.85	88.07554	
5-Aminopentanamide	116.09492	3.89	117.10221	
6-Methyl-2-thiouracil	142.02007	4.33	143.02731	
Vorinostat	264.14748	4.4	265.15488	
1-Vinylimidazole	94.05297	4.746	95.06027	
4-Aminopyridine	94.05297	4.76	95.06024	
3-Hydroxystachydrine	159.08951	5.43	160.09674	
Triethanolamine	149.10508	5.83	150.11243	
2'-Deoxyadenosine	251.10198	6.002	252.10925	
Leu-Leu	244.17875	6.67	245.18605	
Eleganin	434.15865	7.06	435.16625	
Creatinine	113.05887	7.68	114.06615	
Choline O-Sulfate	183.05655	7.83	184.06384	

Adenine	135.05449	8.28	136.0618
Pyridoxal	167.05829	8.8	168.06552
Hypoxanthine	136.03853	8.995	137.0458
Riboflavin	376.13863	9.02	377.1459
4-Nitroaniline	138.04256	9.16	139.04984
7-Methylguanine	165.06516	9.26	166.07246
Biotin	244.08844	9.32	245.09538
Octylamine	129.15193	9.33	130.15916
6-Aminocaproic acid	131.09461	9.789	132.10184
Anabasine	162.11585	10.21	163.12303
Betaine	117.07898	10.28	118.08626
Nornicotine	148.09921	10.604	149.10669
Betahistine	136.10005	10.96	137.10733
Leucylproline	228.14742	11.19	229.15474
4-Methylene-glutamine	158.0692	11.61	159.07648
1-Methylimidazoleacetic acid	140.0586	11.64	141.06584
Inosine	268.08077	11.94	269.08805
Adenosine	267.09667	12.04	268.1041
4'-Phosphopantetheine	358.09587	12.05	359.10272
Acetyl-carnitine	203.11566	12.16	204.12289
2,6-Diaminotoluene	122.08438	12.38	123.09162
Pyridostigmine	180.08997	12.45	181.09717
4-Amino-phenylalanine	180.08997	12.45	181.09726
Benzaldehyde	106.0418	12.86	107.0491
Cytosine	111.04328	12.9	112.05048
Leucine	131.09464	12.94	132.10181
Phenylalanine	165.07903	13.12	166.06623
Nikethamide	178.11069	13.26	179.11768
Amobarbital	226.13141	13.26	227.13869
pentobarbital	226.13192	13.26	227.13916
Guanine	151.04953	13.29	152.05664
Benzamidine	120.06899	13.33	121.07626
Aminocarb	208.12134	13.34	209.12831
Epiguanine	165.06534	13.35	166.07236
Isoleucine	131.09431	13.5	132.10156
AAD	161.06911	13.63	162.07625
Salsolinol	179.09465	14.2	180.10222
5-Hydroxy-tryptophan	220.08518	14.2	221.09253
Proline	115.06319	14.22	116.07058
lentiginosine	157.11035	14.41	158.11765
Methionine	149.05103	14.428	150.0584

2-Aminobutyric acid	103.06336	14.56	104.07043
Pheneturide	206.10565	14.6	207.11316
Indole	117.05797	14.66	118.06509
3-methyleneoxindole	145.05237	14.66	146.05965
8-Hydroxyquinoline	145.05272	14.66	146.05994
2-(Methylamino)isobutyric acid	117.07898	14.669	118.08627
naphthylamine	143.07332	14.69	144.08067
Tryptophan	204.08992	14.69	205.09703
3-Buten-1-amine	71.07329	14.73	72.08057
Valine	117.07862	14.94	118.0857
Crotonoside	283.09142	14.97	284.09875
Carnitine	161.1048	14.99	162.11194
Guanosine	283.09101	15.18	284.09845
Norchelerythrine	333.09938	15.37	334.10672
N-Acetyl-histidine	197.19	15.56	198.08731
Acetylcholine	145.11022	15.7	146.11739
Daminozide	160.08411	15.7	161.09138
Tiglic acid	100.0523	15.72	101.05962
Thiamine	264.10432	15.9	265.11172
Imidazolelactic acid	156.05345	16.15	157.06076
pirsidomine	330.16896	16.26	331.17533
N6-Acetyl-lysine	188.1158	16.55	189.12325
N-(4-Oxobutyl)-glutamine	216.11081	16.59	217.11751
Tyrosine	181.07347	16.75	182.08374
4-Hydroxybenzaldehyde	122.03662	16.85	123.04398
4-Coumaric acid	164.04736	16.85	165.05457
ACETYL PROLINE	157.17	16.99	158.08124
Biocytin	372.18334	17.05	373.19064
14(S)-HDHA	356.24227	17.21	257.24988
N-Acetylornithine	174.10056	17.45	175.10783
(E)-7-(methylsulfanyl)heptanal oxime	175.10369	17.45	176.11104
D-Erythrose 4-phosphate	200.00862	17.5	201.01595
Xanthosine	284.07614	17.54	285.08337
3-Hydroxy-proline	131.05836	17.58	132.06561
4-styrylpyridine	181.08527	17.59	182.09245
1-(4-Aminobutyl)urea	131.10584	17.64	132.11302
Caprolactam	113.08401	17.72	114.09129
Creatine	131.06948	17.77	132.07676
Alanine	89.04769	18	90.05482
Lactamide	89.04763	18	90.05483
Sarcosine	89.04768	18.05	90.05496

Homoserine	119.05824	18.14	120.06552
alpha-Glycerylphosphorylcholine	257.10282	18.24	258.11005
Threonine	119.05814	18.5	120.06546
Flavin mononucleotide (FMN)	456.10451	18.76	457.11179
nicotianamine	303.1429	18.79	304.15018
2-S-Glutathionyl acetate	365.08923	18.8	366.0961
Alanyl-proline	186.10044	18.84	187.10773
pentabamate	204.11072	18.84	205.11824
1-Hydroxycyclohexyl phenyl ketone	204.11101	18.84	205.11827
Acetylarginine	216.12232	18.9	217.12961
4-Guanidinobutyric acid	145.08531	18.93	146.09256
N-α-Acetyl-arginine	216.24	19.066	217.12961
3,4-Diaminopyridine	109.06384	19.17	110.07117
Imidazole-4-acetaldehyde	110.04787	19.17	111.05532
Histamine	111.07954	19.17	112.08686
Histidine	155.06937	19.17	156.07664
Fomepizole	82.05304	19.2	83.06023
2'-Deoxyadenosine 5'-monophosphate (dAMP)	331.06816	19.3	332.07617
S-Adenosyl-homocysteine	384.12159	19.53	385.12887
S-Adenosylhomocysteine	384.12147	19.63	385.12958
Glycine	75.03203	19.66	76.03931
glutaral	100.05225	19.76	101.05965
afegostat	147.08956	19.84	148.09674
Glutamine	146.06925	19.85	147.07651
Pyroglutamic acid	129.04264	19.86	130.04996
5-Aminolevulinate	131.05824	20.06	132.06552
5-Aminolevulinic acid	131.05822	20.14	132.06548
Asparagine	132.05347	20.37	133.06076
Serine	105.04259	20.533	106.0497
Benzimidazole	118.0531	20.62	119.06036
2-Hydroxyfelbamate	254.09039	20.62	255.09764
Nicotinamide	122.04796	20.63	123.05515
1,3-Diphenylacetone	227.13832	20.67	228.14561
Aceglutamide	188.07974	20.76	189.08694
Succinyl proline	215.07935	20.8	216.08685
N-(3-Carboxypropyl)-glutamine	232.10583	20.8	233.11331
Adenosine 5'-monophosphate (AMP)	347.06209	20.8	348.07007
flavin adenine dinucleotide (FAD+)	785.15714	20.94	786.16442
Citrulline	175.09577	21.06	176.10307
Vinylbital	224.11633	21.1	225.12369
Aprobarbital	210.10071	21.13	211.10791

sonedenoson	421.11592	21.34	422.12302
Dopamine 3-O-sulfate	233.03618	21.41	234.04332
Cysteine	121.01986	21.46	122.02703
l-hydroxyvaline	133.07389	21.9	134.08116
sulfacetamide	214.04131	21.94	215.04874
Cysteinylglycine	178.04138	21.96	179.04849
Glutathione (reduced)	307.08342	21.96	308.09094
Aceanthrenequinone	232.05196	21.97	233.05923
Pidotimod	244.05168	21.97	245.05902
Deoxycytidine monophosphate (dCMP)	307.197	21.97	308.064213
ACPC	101.04762	22.03	102.05489
Glutamic acid	147.05308	22.05	148.06038
O-Acetyl-serine	147.05316	22.05	148.06044
Carnosine	226.10675	22.44	227.11368
2-Aminoadipic acid	161.06872	22.49	162.07603
oxazolidinone	87.03181	22.52	88.0391
Nicotinamide adenine dinucleotide (NAD+)	663.10912	22.86	664.1164
β-Nicotinamide mononucleotide	334.05663	22.96	335.06384
inosine 5'-monophosphate (IMP)	348.0471	23.2	349.05438
Nicotinamide adenine dinucleotide (NADH)	665.12478	23.2	666.13206
Fosthiazate	283.04573	23.52	284.0531
Pyridoxamine 5-phosphate	248.05629	23.62	249.06358
D-Glucosamine 6-phosphate	259.04579	23.62	260.05301
3-hydroxykynurenine	224.07981	23.69	225.08701
gamma-Glu-gln	275.11183	23.69	276.11908
Nicotinic acid mononucleotide	335.04024	23.954	336.04788
Gonyautoxin V	379.08995	24.01	380.09653
Cytidine 5'-monophosphate	323.05142	24.15	324.05933
Cytidine 5'-diphosphocholine	488.1071	24.177	489.11462
R-(-)-Phenylephrine	167.09468	24.37	168.10197
1-phenethylamine	121.08901	24.4	122.09628
6-hydroxypseudooxynicotine	194.10576	24.4	195.11298
Butobarbital	212.11637	24.4	213.12381
(alpha)-Kainic Acid	213.10047	24.4	214.10744
Saccharopine	276.13233	24.4	277.13959
lysopine	218.12667	24.43	219.13376
pentahomomethionine	219.13016	24.46	220.13757
2'-Deoxyadenosine 5'-diphosphate (dADP)	411.2	24.71	412.041777
Scillabiose	326.12046	24.87	327.1282
Bromadiolone	526.07842	25.15	527.08612
b-Ala-Lys	217.14281	25.17	218.15009

beta-Alanyl-arginine	245.14897	25.22	246.15613	
Guanosine monophosphate (GMP)	363.05755	25.357	364.06549	
Fosfosal	217.998	25.5	219.00534	
Adenosine diphosphate (ADP)	427.02926	25.6	428.03687	
Cystathionine	222.0675	25.84	223.07489	
N,N-dimethylarginine	202.25	25.883	203.15027	
11-dehydro Thromboxane B2	368.21726	26.07	369.22464	
PPK	340.21156	26.34	341.21838	
Argininosuccinic acid	290.12291	26.49	291.13022	
GPK	300.17989	26.55	301.18741	
N6,N6,N6-Trimethyl-lysine	188.15248	26.65	189.15976	
S-Adenosylmethionine	398.13744	26.7	399.14471	
S-Adenosyl-methionine	398.13724	26.7	399.14452	
N-Methylhexanamide	129.11551	26.85	130.12265	
Deoxyadenosine 5'-triphosphate (dATP)	491.00151	27.2	492.00879	
D-glucose-6-phosphate	260.02963	27.47	261.03708	
Cadralazine	283.16446	27.53	284.17188	
Phosphonoacetate	139.98746	27.76	140.99475	
gamma-Glu-Glu	276.09586	27.8	277.10327	
indospicine	173.11643	28.14	174.12372	
7-(2-aminophenyl)heptanoic acid	203.12699	28.16	204.13438	
Nicotinamide adenine dinucleotide phosphate (NADP+)	743.0755	28.51	744.0827	
Adenosine triphosphate (ATP)	506.99584	28.522	508.0033	
N6-Methyl-lysine	160.12118	28.92	161.12846	
Cytidine diphosphate (CDP)	403.01819	29.12	404.02547	
6-Phosphonoglucono-D-lactone	258.0139	29.22	259.02158	
Nicotinamide adenine dinucleotide phosphate (NADPH)	745.09111	29.83	746.09839	
Pipecolic acid	129.07911	30.08	130.08652	
Lysine	146.10559	30.08	147.11288	
1-Piperideine	83.07343	30.09	84.08065	
Arginine	174.11176	30.33	175.11905	
Prolinamide	114.07945	30.68	115.08669	
1-Nitrosopiperidine (NPIP)	114.07949	30.68	115.08673	
Cytidine 5'-triphosphate	482.98546	30.69	483.99274	
Ornithine	132.08983	30.7	133.09723	
5-Hydroxylysine	162.10044	31.23	163.10757	
Uridine-5'-triphosphate (UTP)	484.14	31.25	484.9758	
Myristyl sulfate	294.18605	1.2		293.17877
2,3-dinor Prostaglandin E1	308.20183	1.21		307.19455
Gingerol	294.18587	1.23		293.1788
4-Dodecylbenzenesulfonic acid	326.19133	1.281		325.184

Cerotic acid	396.69	1.393	395.38959
Lignoceric acid	368.36476	1.4	367.35748
Pentacosanoic acid	382.38069	1.4	381.3732
11(E)-Eicosenoic Acid	310.2863	1.42	309.27936
Arachidic acid	312.5	1.43	311.29532
dilauroyl peroxide	398.33897	1.44	397.33127
Stearic acid	284.27104	1.44	283.26385
Putaminoxin	212.1409	1.45	211.13362
Houttuynin	198.1617	1.46	197.15466
(2Z)-2-Octyl-2-pentenedioic acid	242.15143	1.46	241.14449
Ethyl myristate	256.23967	1.46	255.23216
Palmitoleic acid	254.22409	1.46	253.21687
Margaric acid	270.45	1.468	269.24829
Proximadiol	240.20875	1.47	239.20116
Myristic Acid	228.20839	1.47	227.20132
pentadecanoic acid	242.22401	1.47	241.21674
Tridecylic acid	214.19302	1.493	213.18575
Cycloheximide	186.16176	1.52	185.15448
(R)-2-hydroxystearic acid	300.26567	1.52	299.25833
16-Oxohexadecanoic acid	270.21895	1.52	269.21167
lauric acid	200.17734	1.52	199.1702
Decanoic acid	172.14615	1.57	171.13887
4-Heptylphenol	192.15072	1.59	191.14398
Nonanoic acid	158.1306	1.603	157.12332
[1,1'-biphenyl]-2,2'-dicarboxylic acid	242.06111	1.61	241.05382
2,5-di-tert-Butylhydroquinone	222.1617	1.63	221.15442
Embelin	294.18306	1.63	293.17578
2-Ethylhexanoic acid	144.11517	1.64	143.10776
Caprylic acid	144.11502	1.657	143.10774
Clomipramine	314.15465	1.66	313.14713
2-Hydroxymyristic acid	244.20367	1.68	243.1964
10-oxocapric acid	186.12546	1.71	185.11818
n-heptanoic acid	130.09935	1.71	129.09207
12-Hydroxydodecanoic acid	216.17232	1.723	215.16504
3-oxolauric acid	214.1566	1.73	213.14938
3-Hydroxydecanoic acid	188.14117	1.755	187.1339
9-Oxononanoic acid	172.10982	1.76	171.10254
10-Hydroxydecanoic acid	188.14146	1.761	187.13419
Dodecanedioic acid	230.15138	1.764	229.14413
Valeric acid	102.06806	1.773	101.06078
Sesamex	298.14119	1.8	297.13416

Hydrocinnamic acid	150.06799	1.8	149.06071
(Hydroxyethyl)methacrylate	130.06294	1.82	129.05574
8-Hydroxyoctanoic acid	160.21	1.843	159.10294
Ethyl acetate	88.05254	1.89	87.04539
Isobutyric acid	88.05258	1.9	87.04531
Sinapyl alcohol	210.0889	1.91	209.08188
2,5-Dioxopentanoic acid	130.02643	2.17	129.01915
Itaconic acid	130.02672	2.17	129.0193
2-Naphthalenesulfonic acid	208.01903	2.4	207.01175
Succinic anhydride	100.01619	2.59	99.00891
4-Thiapentanoic acid	120.02451	2.79	119.01744
Benzoic acid	122.03705	3.2	121.02964
Azelaic acid	188.10507	4.867	187.09764
4-Aminobenzoic acid	137.04725	5.315	136.04007
4-Nitrotoluene	137.04747	5.35	136.0401
Salicylamide	137.04745	5.35	136.04007
5-Aminonicotinic acid	138.04292	5.67	137.03532
N-Acetyl-phenylalanine	207.08916	6.6	206.0822
2-Aminooctanedioic acid	189.10021	6.93	188.09285
N-Acetyl-methionine	191.0614	7.2	190.05412
N-Acetyl-cysteine	163.03041	8.08	162.02309
(S)-(-)-pipecolic acid	129.07905	8.23	128.07178
Vigabatrin	129.07915	8.23	128.07172
Picolinic acid	123.03212	8.26	122.02492
Nicotinic acid	123.03208	8.32	122.02483
Mevalonic acid	148.07336	8.45	147.06642
Lactic acid	90.0319	8.64	89.02462
Uridine	244.06904	8.771	243.06197
Erythritol	122.05794	9.03	121.05066
Pantothenic acid	219.11064	9.18	218.10295
Xanthine	152.03317	10.34	151.02585
anthopleurine	177.09996	10.49	176.09283
Metronidazole	171.06433	10.86	170.05695
Ethenzamide	165.07886	12.87	164.0714
Succinic acid	118.02659	12.87	117.01929
Penicillamine	149.05099	14.26	148.0437
Dulcitol	182.07889	14.497	181.07159
Mannitol	182.07887	14.55	181.07158
5-Aminovaleric acid	117.07882	14.62	116.07164
2-Oxobutyric acid	102.03171	15.02	101.02443
metioprim	306.11522	15.06	307.1225

N-Acetyl-glutamine	188.18	15.438	187.07295
Dihydroorotic acid	158.03245	15.5	157.02518
Threonic acid	136.03705	16.18	135.02994
Glycyl-leucine	188.11578	16.42	187.10864
2-Hydroxyphenylalanine	181.107416	16.7	180.06656
Orotidine	288.05855	17.81	287.05164
3-Hydroxy-3-methylglutaric acid	162.05275	18.09	161.04536
Cytidine	243.08565	18.5	242.07907
2-Isopropylmalic acid	176.06814	18.6	175.06104
(Hydroxymethyl)phosphonic acid	111.99257	19.09	110.98529
Isoniazid	137.05879	19.31	136.05151
4-Aminonicotinic acid	138.04274	19.32	137.03549
D-Xylonic acid	166.04814	19.58	165.04066
5-Nitrilonorvaline	128.05879	19.86	127.05143
Glutamine	146.06903	19.86	145.0618
2'-Deoxyguanosine 5'-monophosphate (dGMP)	347.06245	20.278	346.05518
beta-D-Mannopyranose	180.06329	20.54	179.05595
Hexose	180.06332	20.54	179.05602
Sucrose	342.11573	21.09	341.10846
α,α-Trehalose	342.11579	21.09	341.10858
Citrulline	175.09558	21.29	174.0883
Prolylglycine	172.08471	21.48	171.07762
Nicotinuric acid	180.05359	21.89	179.04602
Zalcitabine	211.09544	21.91	210.08817
Glycerol 3-phosphate	172.01352	22.14	171.00632
Uridine monophosphate (UMP)	324.03486	22.15	323.02811
Aspartic acid	133.03742	22.2	132.03012
glyceraldehyde 3-phosphate	169.99794	22.45	168.99066
N-Acetyl-glutamic acid	189.0636	22.48	188.05632
Formylpyruvate	116.01092	22.5	115.00378
N-Acetyl-aspartic acid	175.0479	22.5	174.0406
Cyclic ADP-ribose	541.06044	22.53	540.05267
Malic acid	134.0214	24.31	133.01421
Tenuazonic acid	197.10486	24.43	196.09779
Maleic acid	116.01103	25.58	115.00376
Maleamic acid	115.02692	25.6	114.0197
Uridine 5'-diphosphate (UDP)	404.00166	27.3	402.99432
3-Phosphoglyceric acid	185.99305	27.76	184.98582
2-Furoic acid	112.01612	27.894	111.00881
Phosphoenolpyruvic acid	167.98225	28.37	166.97499
Orotidine 5'-monophosphate	368.02424	28.63	367.01715

Deoxyguanosine diphosphate (dGDP)	427.02775	28.646	426.02103
Glutathione oxidized	612.15122	29.4	611.14343
Guanosine 5'-diphosphate (GDP)	443.0236	29.4	442.01633
homoisocitric acid	206.04236	29.43	205.03508
Ornithine	132.08969	30.5	131.08244
α-D-Glucose-1,6-bisphosphate	339.99483	30.63	338.98752
Guanosine triphosphate (GTP)	522.98933	31.4	521.98224

Figure 10.28: 370 metabolites were separated and detected by the new developed LC-MS/MS method. The annotation and the retention times of all the metabolites were confirmed by MS2 spectra match.